Membrane-Supported Hydrogen/Syngas Production using Reactive H_2O/CO_2 Splitting for Energy Storage

By
Xiaoyu Wu

S.M. Thermal Engineering,
Zhejiang University (2012)
B.S. Energy & Environment System Engineering,
Zhejiang University (2009)

Submitted to the Department of Mechanical Engineering
in partial fulfillment of the requirements for the degree of
Doctor of Philosophy in Mechanical Engineering
at the
MASSACHUSETTS INSTITUTE OF TECHNOLOGY

June 2017

Signature of Author: _____
Department of Mechanical Engineering
May 12, 2017

Certified by: _____
Professor Ahmed F. Ghoniem
Ronald C. Crane (1972) Professor of Mechanical Engineering
Thesis Supervisor

Accepted by: _____
Professor Rohan Abeyaratne
Professor of Mechanical Engineering
Chairman, Department Committee on Graduate Students

This page is intentionally left blank

Membrane-Supported Hydrogen/Syngas Production using Reactive H_2O/CO_2 Splitting for Energy Storage

By
Xiaoyu Wu

Submitted to the Department of Mechanical Engineering
on May 12 2017 in partial fulfillment of the
requirements for the degree of Doctor of Philosophy in
Mechanical Engineering

Abstract

Energy storage technologies are crucial for supporting the fast expansion of intermittent renewable energy at the grid scale. One such technology is the efficient and economic conversion of H_2O and CO_2 into fuels utilizing excess thermal energy at intermediate temperatures. This thesis explores fuel production using oxygen permeable membranes. $La_{0.9}Ca_{0.1}FeO_{3-\delta}$ (LCF-91) perovskite is used to develop a framework for reactor design based on a careful assessment of fuel production rates on the membrane design and operating conditions. This material exhibits strong chemical stability but relatively low permeability.

Hydrogen production from water splitting is investigated using CH_4 to increase the chemical potential gradient across the membrane. Analysis shows that oxygen consumption on the sweep-side is the rate limiting step, and the addition of a nickel catalyst on a porous LCF-91 layer on that side raises the hydrogen production rate from water splitting by two orders of magnitude, reaching 0.37 μmol/cm^2•s. Raising the oxygen flux suppresses carbon deposition and achieves optimum syngas composition for gas-to-liquid. CO_2 splitting was also demonstrated on the same membrane material, with similar enhancement as fuel is introduced and porous layers are added on both sides, but at measurably lower rates than water splitting.

Based on the experimental data, an oxygen flux model incorporating the surface kinetics and ion transport is developed, in which the oxygen direct-incorporation kinetics are used on the feed-side, and the Mars-van Krevelen (MvK) mechanism for fuel (H_2, CO or CH_4) oxidation reactions are applied on the sweep-side. The data show that H_2 has the lowest activation energy for oxidation among the three fuels, and hence, leads to the highest oxygen flux for H_2O/CO_2 splitting. Moreover, while the limiting step is always the fuel oxidation in water splitting, it changes from CO formation reactions on the feed-side to fuel oxidation reactions on the sweep-side as the temperature is raised in CO_2 splitting.

A monolith membrane reactor model based on the reaction kinetics is developed for hydrogen and syngas production from water splitting and partial oxidation of methane,

respectively. Results show that the efficiency is ~2% points higher than the conventional steam-methane reforming, when high-purity hydrogen (>99%) is produced. Sensitivity analysis shows that, for the best performance, it is critical to maintain high operating temperatures and high catalytic reactivity for methane oxidation.

Thesis supervisor: Professor Ahmed F. Ghoniem
Title: Ronald C. Crane (1972) Professor of Mechanical Engineering

Doctoral Thesis Committee
Professor Ahmed F. Ghoniem
Ronald C. Crane (1972) Professor of Mechanical Engineering
Committee chair

Professor Harry L. Tuller
Professor of Ceramics and Electronic Materials
Committee member

Professor Alexie Kolpak
Rockwell International Career Development Professor
Committee member

Acknowledgements

I would like to thank all the people who have supported me through my PhD. Without you all, this thesis would not have been possible. In particular, I would like to express my deepest appreciation to a few people.

My utmost thanks and sincere gratitude go to my supervisor Professor Ahmed Ghoniem, for his time and efforts in helping me in this thesis. I am very grateful to have the opportunity to work with him at MIT on this membrane project. Professor Ghoniem is the person who I can always learn from and more importantly, who I always trust.

Next, I would like to thank my committee members Professor Harry Tuller and Professor Alexie Kolpak for all their guidance along the way. I appreciate Professor Tuller's insights on the ceramic materials and his valuable suggestions in understanding the oxygen transport process. I am also grateful to Professor Kolpak for introducing me the density functional theory and for being a successful example of young faculty.

I would also like to thank all the RGD lab members, especially those who were in the membrane group: Dr. Mruthunjaya Uddi, Dr. Jongsup Hong, Dr. Anton Hunt, Dr. Georgios Dimitrakopoulos and Mr. Le Chang. And I also thank Dr. Katherine Ong for reviewing parts of this thesis.

Next, I would like to thank all my friends and family. I owe a debt of gratitude to my parents who always love me. And I am grateful to my friends and family in China for their support. I'd also like to thank my friends who I met in the US for their kindness and companionship.

Lastly, I would like to thank both Shell and the King Abdullah University of Science and Technology (KAUST) for funding this research. I am also grateful to Dr. Chiang Chen and Chiang Chen Industrial Charity Foundation for their generous fellowship support.

This page is intentionally left blank

Table of Contents

List of Figures

List of Tables

Chapter 1

Introduction

1.1 Background

The year 2016 was the hottest year on record and the global temperature has observably increased in the past few decades [1, 2]. Even though global CO_2 emissions have leveled off in 2014 and 2015 [3], the accumulation of greenhouse gases (mainly CO_2 and CH_4) in the atmosphere keeps rising, and the global average atmospheric CO_2 concentration is currently above 400 ppm [4]. In 2015, the first universal climate agreement was adopted by 195 countries to keep global warming below 2 ℃ in the 2015 Paris Climate Conference [5]. Concerted efforts from various countries and sectors are required to keep global warming within the safety limit of 2^oC [6, 7].

Increasing CO_2 emission can, however, also be viewed as an opportunity to utilize this abundant C1 carbon source [8]. In 2015, global CO_2 emissions were 32.1 Gt [3], which contained 8.75 Gt of carbon. Utilizing CO_2 to produce value-added chemicals such as CO, urea, salicylic acid and polyurethanes is an essential step towards a carbon free economy [8, 9].

Electricity demand and generation also vary on a daily basis, especially with the fast expand of intermittent renewable energy (e.g., solar and wind power) at the grid scale [10]. For example, as is shown in Figure 1.1, on March 7 2017 in New England, the electricity demand ramped up around 7 am, remained high during the day, reached a peak around 6 pm and then went down and remained low during the night. As a result, fossil fuel power plants were required to follow the demand and operate at conditions below the design load at lower efficiency or were even shut down. In another example in Germany on May 8 2016, the renewable power plants supplied about 87% of the electricity demand at around 1 pm on that day causing instability in the electricity market [10].

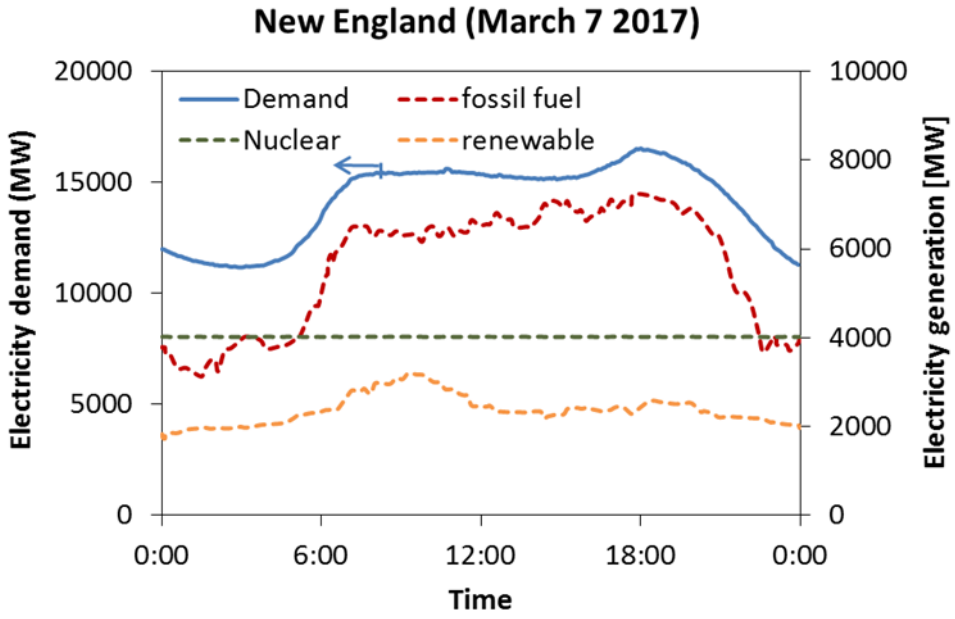

Figure 1.1 Electricity demand and generation by source on a regular day (March 7 2017) in New England, US [11]

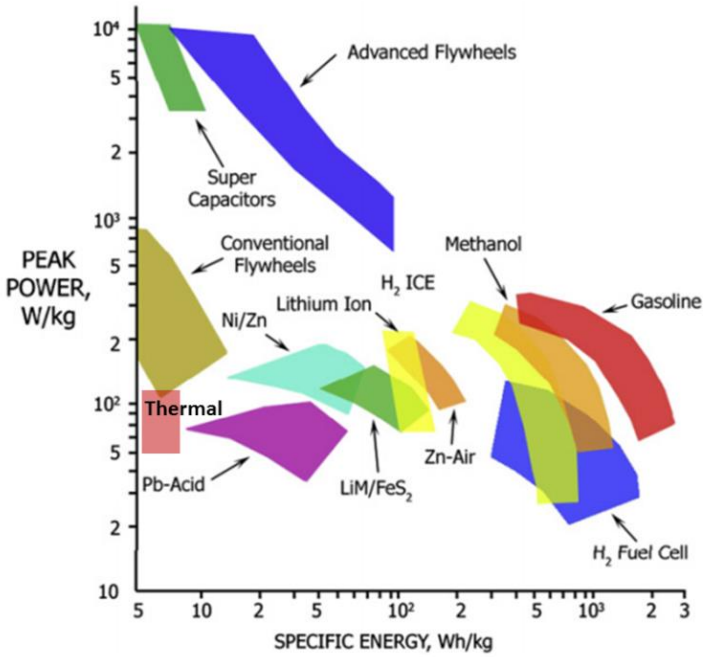

Figure 1.2 Ragone chart comparing the power density and energy density of different energy storage techniques (reproduced from [12])

In order to integrate the intermittent renewable energy sources while maintaining fossil fuel power production, energy storage technologies are required to store the excess energy for later use. Several technologies are proposed in the literature and compared using criteria such as the Ragone chart (Figure 1.2) and the roundtrip efficiency (Figure 1.3). The Ragone chart compares the power density and energy density of different storage technologies, while the roundtrip efficiency is defined as the ratio of the energy put into storage to the energy retrieved from storage. Both Figure 1.2 and Figure 1.3 indicate that storing energy in the forms of chemical bonds (e.g., hydrogen and natural gas) has high specific energy, low installation cost and good power density. However, the roundtrip efficiency to generate hydrogen and synthetic natural gas is still low. Therefore, research efforts are needed to increase the roundtrip efficiency of storing energy in chemical bonds.

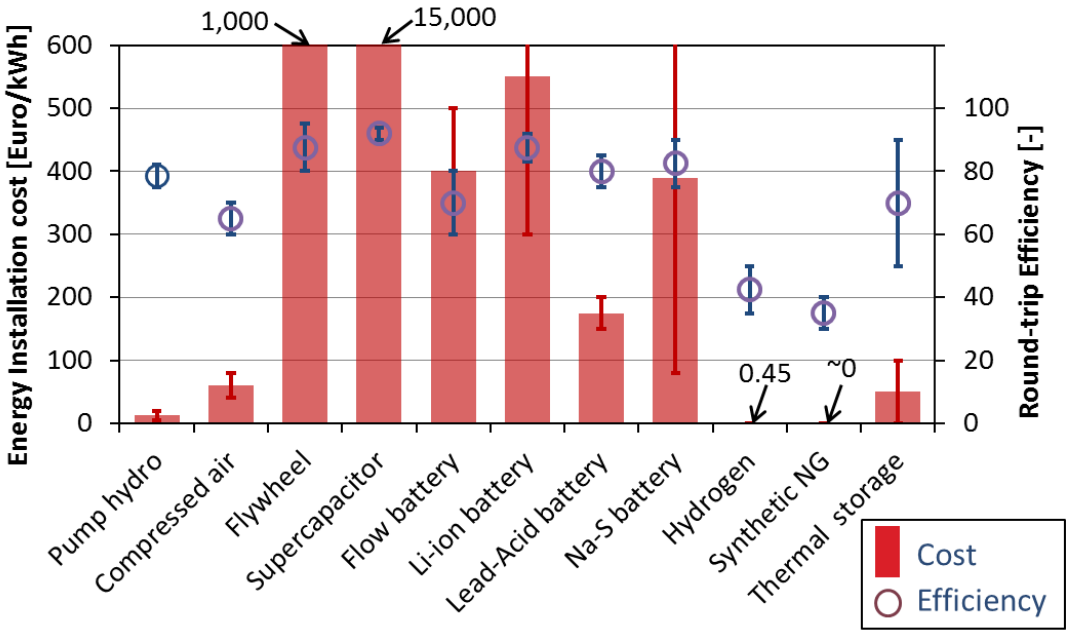

Figure 1.3 Comparison of the cost and roundtrip efficiency among various energy technologies proposed in the literature (bars are energy installation costs and the circles are roundtrip efficiencies) [13]

Hence, this thesis focuses on hydrogen/syngas production technology using reactive H_2O/CO_2 splitting as an intensified CO_2 utilization and energy storage

technology. A schematic of this process is shown in Figure 1.4. Combustion products from fossil fuel power plants (i.e., H_2O and CO_2) are captured and then converted to H_2, CO or synthesis gas (syngas) by utilizing excess thermal energy from renewable sources. Furthermore, this technology can also be intensified with hydrocarbon partial oxidation to utilize the oxygen from H_2O/CO_2 splitting to produce syngas. Syngas is a mixture of H_2 and CO that can either be used directly as a fuel or converted into value-added chemicals like ammonia and methanol that are among the top ten chemicals produced annually in the world [9, 14].

This proposed technology enables the continual use of cheap, plentiful fossil fuels while mitigating their negative impacts on the environment. Besides, H_2O/CO_2 is converted to value-added products by storing the excess heat in the form of chemical bonds. There are three main methods to convert H_2O/CO_2 into syngas (electrolysis, photoelectrolysis and thermolysis) as summarized and compared in Table 1.1. Except alkaline H_2O electrolysis, these technologies are all demonstrated in lab-scaled and breakthroughs such as efficiency improvement and cost reduction are required before industrial applications. In this thesis, only the reactive H_2O/CO_2 splitting from thermal dissociation is discussed, which falls under the category of thermolysis. In this technology, heat is directly converted to chemical energy.

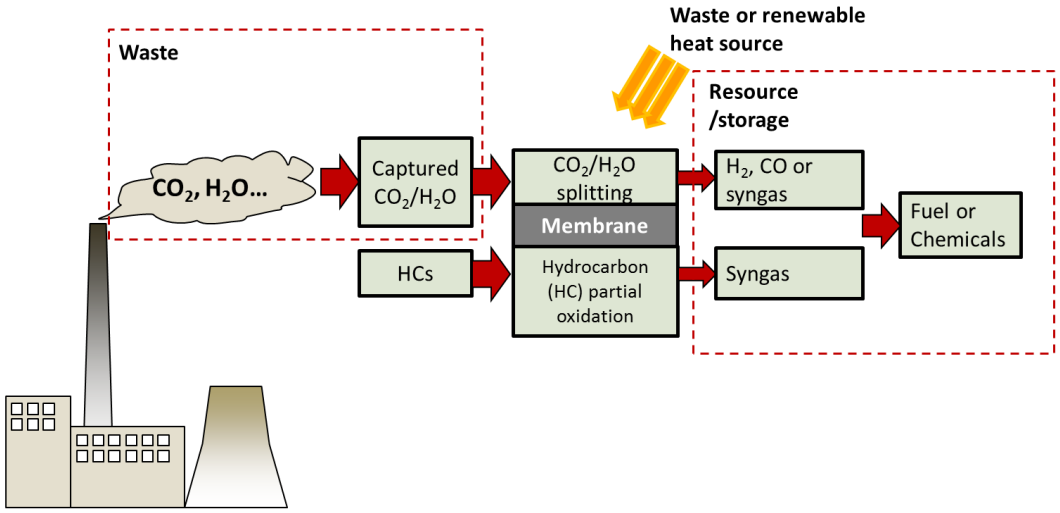

Figure 1.4 Flow diagram of capturing and reusing the combustion products using membrane-supported H_2O/CO_2 splitting

Table 1.1 Comparison between three H_2O/CO_2 to fuel technologies

	Electrolysis	**Photoelectrolysis**	**Thermolysis (membrane)**
Early ideas	Discovered by Deimann and Troostwyk in 1789 [15]	Demonstrated by Fujishima and Kenichi in 1972 [16]	Proposed by Fletcher [17] and Browall [18] in 1977
Energy input	Electricity and/or heat	Photon (solar)	Heat
Operating Temperature	Alkaline & proton exchange membrane electrolyzer: 60 – 90^{o}C Solid oxide electrolyzer: 500 – 900^{o}C	Room temperature	Elevated temperature 800 - 1000^{o}C
Main Advantages	Alkaline water electrolysis is a mature technology contributing to ~4% of global hydrogen production [19]	Clean and direct utilization of solar energy	Direct storage of heat from various sources in chemical bonds; heat is a cheaper form of energy than electricity
Main Disadvantages	Electricity consumption, which is expensive	1. Expensive catalyst 2. Partial utilization of solar radiation spectrum 3. Low production rate	High temperature heat source
Latest reviews on this topic	[9] [20] [21] [22] [23] [24] [25]	[9] [22] [26] [27]	[9] [28] [29]

Membrane-supported H_2O/CO_2 splitting is proposed as a clean way to produce fuel from H_2O/CO_2 when utilizing solar or nuclear heat [17, 18]. Elevated temperatures, however, are required to overcome high activation energy for surface reactions as well as bulk diffusion in the membrane [30]. Furthermore, in order to prevent the thermolysis products from recombining, methods such as quenching [31, 32], heat-exchanger-loop [30], and perm-selective membranes [30-33] are needed. Quenching and heat-exchanger-loops have the disadvantages of high entropy generation and low efficiency. High-temperature perm-selective membranes, on the other hand, can *in situ* separate the products during the splitting process. The development of oxygen permeable membranes at medium temperatures in the range of 700 – 1000^{o}C, in particular, draws researchers' interest for H_2O/CO_2 splitting applications [28, 29].

In this chapter, I first discuss the thermodynamics of H_2O/CO_2 thermolysis. Then the studies on membrane-supported H_2O/CO_2 splitting are summarized in sections 1.3 and 1.4. Membrane materials, categorized into single phase (fluorite or perovskite) and mixed phase materials, are discussed separately. Intensification of hydrocarbon partial oxidation in the membrane reactor is then discussed. Next, the oxygen diffusion models are summarized in section 1.5, and the interaction (adsorption and reaction) between H_2O/CO_2 and solid surface are discussed in section 1.6. However, as the mechanisms and kinetics are still not well understood for this process, larger scale demonstrations of this technology haven't been carried out to this date. More studies are needed, especially on the kinetics of the splitting reaction, the selection of materials, and system-scale analysis, so that this technology can be implemented.

1.2 Thermodynamic discussion

1.2.1 Thermodynamic analysis

Water and carbon dioxide dissociation reactions are highly endothermic,

$$H_2O \rightarrow H_2 + \frac{1}{2}O_2 \qquad \Delta H^o_{298K} = 241.8 \text{ kJ/mol} \tag{1-1}$$

$$CO_2 \rightarrow CO + \frac{1}{2}O_2 \qquad \Delta H^o_{298K} = 282.9 \text{ kJ/mol} \tag{1-2}$$

Lede et al. [32] summarized the homogeneous H_2O splitting mechanism into four steps:

$$H_2O + M \leftrightarrow H + OH + M \qquad \Delta H^o_{298K} = 500 \text{ kJ/mol} \qquad (1\text{-}3)$$

$$H + H_2O \leftrightarrow H_2 + OH \qquad \Delta H^o_{298K} = 60.1 \text{ kJ/mol} \qquad (1\text{-}4)$$

$$H + OH \leftrightarrow H_2 + O \qquad \Delta H^o_{298K} = 8.4 \text{ kJ/mol} \qquad (1\text{-}5)$$

$$O + OH \leftrightarrow O_2 + H \qquad \Delta H^o_{298K} = -65 \text{ kJ/mol} \qquad (1\text{-}6)$$

where *M* is a carrier gas. The rate constants for each step are shown in Table 1.2.

Water and carbon dioxide are stable molecules: the average H-O and C=O bond energies are 464 kJ/mol and 805 kJ/mol, respectively [34]. The bond cleavage is usually the first step for the splitting reaction, as is shown in (1-3), and its activation energy is the highest among the four steps. In order to increase the splitting rate, catalysts are used to decrease the activation energy and hence, facilitate the reactions. Experiments were carried out to study water thermal dissociation on Pt and Ir catalysts at 1300 – 1400^{o}C and 1700^{o}C, respectively, and the reactions proceeded faster on the precious metal catalysts; however, less than 1% of water was split due to the equilibrium constraint [30].

The thermodynamic equilibrium of H_2O/CO_2 thermolysis is modeled by the Cantera software package [35] using the GRI-Mech 3.0 mechanism [36], and the equilibrium constants are summarized in Table 1.3. As shown in Figure 1.5, the mole fractions for H_2 and CO at equilibrium at 1000^{o}C are $X_{H_2} = 1.81 \times 10^{-5}$ and $X_{CO} = 2.49 \times 10^{-5}$, respectively. Due to the low equilibrium constants, homogeneous thermal dissociation requires very high temperature to produce observable amount of H_2/CO and O_2.

Table 1.2 Rate constants for homogeneous water thermolysis [32]

Rate constant	Units	M
$k_3 = 1.3\times10^{9}\exp(-52900/T)$	$m^3mol^{-1}s^{-1}$	Ar
$k_{-3} = 8.4\times10^{9}T^{-2}$	$m^6mol^{-1}s^{-1}$	Ar
$k_3 = 2.2\times10^{10}\exp(-52900/T)$	$m^3mol^{-1}s^{-1}$	H_2O
$k_{-3} = 1.4\times10^{11}T^{-2}$	$m^6mol^{-1}s^{-1}$	H_2O
$k_4 = 9\times10^{7}\exp(-10250/T)$	$m^3mol^{-1}s^{-1}$	H_2O
$k_{-4} = 2.2\times10^{7}\exp(-2590/T)$	$m^3mol^{-1}s^{-1}$	H_2O
$k_5 = 8.3\times10^{3}T\exp(-3500/T)$	$m^3mol^{-1}s^{-1}$	H_2O
$k_{-5} = 1.8\times10^{4}T\exp(-4480/T)$	$m^3mol^{-1}s^{-1}$	H_2O
$k_6 = 2\times10^{7}$	$m^3mol^{-1}s^{-1}$	H_2O
$k_{-6} = 2.2\times10^{8}\exp(-8420/T)$	$m^3mol^{-1}s^{-1}$	H_2O
Note: k_i and k_{-i} are the reaction rate constants for the forward and reverse reactions (1-3) to (1-6)		

Table 1.3 Thermodynamics equilibrium constants for H_2O/CO_2 thermolysis reactions, derived from the GRI-Mech 3.0 mechanism [36]

Reaction	Thermodynamics equilibrium constant
$H_2O \leftrightarrow H_2 + \frac{1}{2}O_2$	$K_{eq,H_2O} = 982.5e^{-30069/T}$
$CO_2 \leftrightarrow CO + \frac{1}{2}O_2$	$K_{eq,CO_2} = 26676.4e^{-33682/T}$

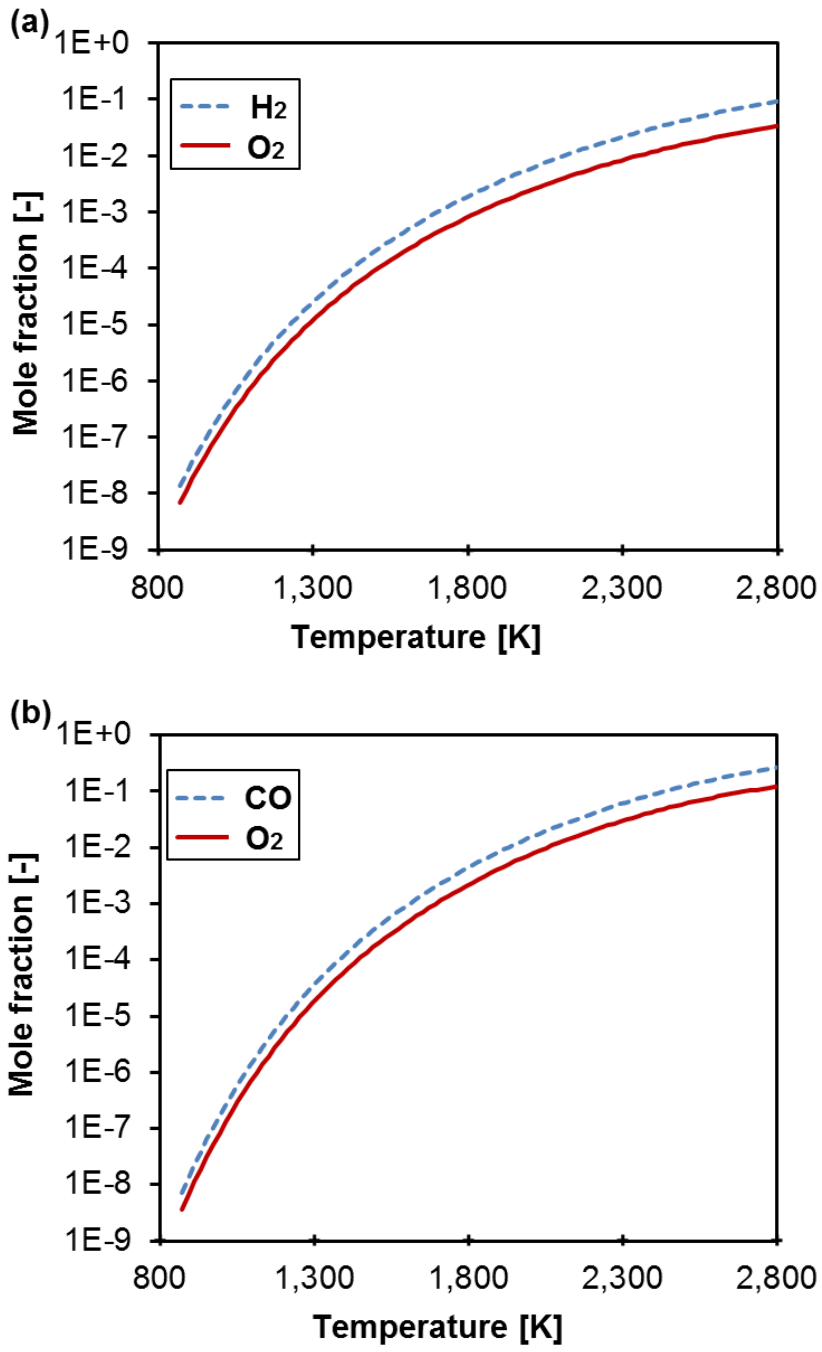

Figure 1.5 Thermodynamics equilibrium of the products from (a) water, and (b) CO_2 homogeneous dissociation vs. temperatures

1.2.2 Membrane reactor to shift equilibrium

In order to achieve higher dissociation ratios, it is desirable to separate the products and shift the thermodynamic equilibrium of these splitting reactions. In 1977 two different groups proposed to incorporate separation method with H_2O splitting: Fletcher [17] suggested to use a porous membrane with pore sizes in the order of magnitude of the mean free path of the gas molecules to separate products, while Browall [18] explicitly proposed a doped yttria-stabilized zirconia (YSZ) dense membrane to separate oxygen as the doped YSZ membrane has oxygen permeability. Since then, several other methods were proposed to break the equilibrium, such as quenching [31, 32] and heat-exchanger-loop [30]. However, the perm-selective permeable membrane reactor attracts the most attention due to its advantages of *in situ* separation of products and continuous fuel production from splitting.

Several types of perm-selective membranes can be used to separate the reaction products (i.e., H_2 and O_2 or CO and O_2). Table 1.4 summarizes three different perm-selective membranes in the literature. Only oxygen or hydrogen permeable membranes are listed, as CO permeable membranes are unavailable in the literature as far as the author knows. However, the available hydrogen permeable membranes (e.g., Pd-alloy membrane or mixed ionic-protonic conducting membrane) would suffer the degradation from exposure to oxygen, water and carbon monoxide, so these membranes are not applicable in H_2O/CO_2 splitting processes. Hence, the mixed ionic-electronic conducting (MIEC) membrane for oxygen permeation is chosen as an appropriate perm-selective membrane to enhance hydrogen/syngas production from H_2O/CO_2 splitting. In the MIEC membrane, lattice oxygen diffuses across without applied electric potential, as the driving force is the chemical potential gradients across the dense membrane.

The first proof-of-concept study on this MIEC membrane is dated back to 1982, when Lede et al. [32, 37] from the French National Center for Scientific Research used a $0.9ZrO_2$-0.1CaO tubular membrane to split water vapor at temperatures up to 1800^oC, and the hydrogen production rate measured was as high as 2.2 μmol/s. The extremely high operating temperature makes this demonstration difficult for industrial applications due to the very high solar concentration ratios and low heat adsorption efficiency [38]. However, more membrane materials that work at lower temperatures (around 900^oC)

have since been developed and reported, so these studies will be summarized in the following chapters.

Figure 1.6 illustrates the schematic for this membrane-supported H_2O/CO_2 splitting process. There are five steps: (1) H_2O/CO_2 diffuses onto the membrane in the gas phase; (2) H_2O/CO_2 react with oxygen vacancies on the membrane surface and H_2/CO is produced; (3) lattice oxygen permeates through the membrane, driven by chemical partial pressure gradients; (4) Lattice oxygen recombines into oxygen molecules, or lattice oxygen reacts with fuel to produce syngas; and (5) The products on both sides leave the membrane surfaces by diffusion.

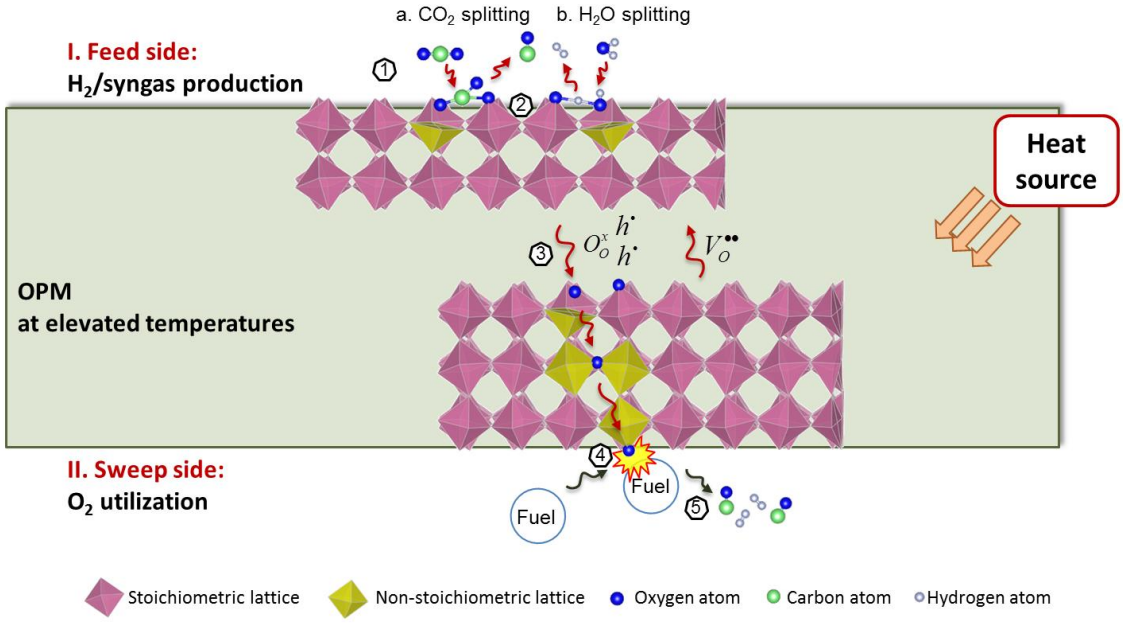

Figure 1.6 Schematic diagram shows the oxygen transport process in an oxygen permeable membrane with H_2O/CO_2 thermolysis on the feed side and oxygen utilization on the sweep side

The figures of merits (FOM) of such an oxygen permeable membrane are summarized as follows:

(1) High oxygen permeability: the oxygen permeability is directly proportional to the H_2 or CO production rate, and oxygen permeation depends on the ambipolar diffusion of ions and electrons/holes across the membrane;

(2) High active surface area: surface reactions are important steps on both sides of the membrane; the overall H_2O/CO_2 splitting performance depends on the surface reactions such as the adsorption/desorption and heterogeneous gas-solid reactions;

(3) Good chemical and mechanical stabilities: as the oxygen permeable membrane operates at elevated temperatures and under redox reactions on different surfaces, the stability of the membrane materials during heating/cooling and under long term operations is of great importance for industrial applications;

(4) Low cost: In order to increase the overall production rate, huge membrane surface areas are required. The membrane materials should be easily derived and the cost of the membrane fabrication and assembly at large scale must be competitively low;

(5) Low operating temperature: High operating temperature leads to higher surface reaction kinetics and better oxygen permeability. But it also means higher maintenance and operational costs. Better and more insulation materials are required to decrease the heat lost from the hot devices. Nevertheless, optimization is required to have the reactor operating at appropriate temperatures to achieve the best performances.

In the following chapters, the studies on membrane-supported hydrogen/syngas production from H_2O/CO_2 splitting are summarized with a focus on membrane preparations, splitting rate and stability.

Table 1.4 Comparison between three perm-selective membranes from the literature

	MIEC membrane	**Metal membrane**	**MPEC membrane**
Temperature	700 – 1000°C	300 – 600°C	700 – 1000°C
Conduction	Vacancies ($V_O^{\bullet\bullet}$), electrons (e') or electron holes ($h^{\bullet}$)	Hydrogen atom (H)	Protons ($OH^{\bullet}$), $V_O^{\bullet\bullet}$, e' or $h^{\bullet}$
Materials	Perovskite/fluorite/dual-phase	Pd/Pd-alloy	Mainly $ACeO_3$, A = La, Sr, Ba
Flux	~5 μmol/cm^2•s [39]	~10 μmol/cm^2•s [40]	~1 μmol/cm^2•s [41]
Stability	Some perovskites, especially Sr- and Ba- based perovskites suffer from poisonous gases such as CO_2, H_2O, H_2S, SO_2 [39]	Hg vapor, H_2S, SO_2, thiophene, arsenic, unsaturated hydrocarbons, chlorine carbons will all contaminate Pd membranes [40]	$BaCeO_3$-derived compounds are unstable in CO_2 or H_2O environments [42]
Main Disadvantages	Activity and stability couldn't be both optimized easily; cobalt based materials are unstable under reducing environments	Precious metal palladium is used (but efforts have been done to reduce Pd usage by using Pd alloys)	1. Low hydrogen permeability; 2. Vulnerability in H_2O and CO_2 environment
Commercial applications	Air products and Chemicals, Inc [43] and Praxair, Inc. [44] both have pilot scaled demonstration projects for oxygen separation	In 1964, a dense 23 wt% Pd-Ag membrane was used for purifying a H_2 rich stream by Johnson Matthey [40]	/
MIEC: Mixed Ionic-Electronic Conductive; MPEC: Mixed Protonic-Electronic Conductive			

1.3 Current status of membrane-supported H_2O splitting

The oxygen permeable membranes are generally categorized as single-phase (fluorite or perovskite) or mixed-phase membranes. Fluorites or perovskites are popular MIEC materials for single-phase oxygen permeable membranes at elevated temperatures. By doping different cations into the lattice, the material properties (i.e., conductivity and reactivity) are modified and optimized. Meanwhile, mixed-phase materials are also studied, as the properties of the different phases can be optimized separately. However, these phases should have similar thermal and chemical expansion properties, as the interconnections among them are important and need to be maintained intact during heating/cooling operations and reactions. The membrane materials for oxygen separation application (air as the oxygen source) have been reviewed before [39, 45]. In this section, the oxygen permeable membrane materials for water splitting are reviewed. A non-exhaustive summary of the literature is listed in Table 1.5. Most of the membranes operated at temperatures around 900 - 1000^{o}C, and hydrogen production rates on the orders of 0.01 – 10 μmol/cm^2•s were reported.

In the following, material synthesis and membrane fabrication for these oxygen permeable membranes are firstly summarized. Then the performances of these membranes, transport process, co-production and material stability are discussed.

1.3.1 Fabrications

1.3.1.1 Powder synthesis

To synthesize the solid powders of each phase is the first step. There are generally five methods to prepare ceramic powders [46]: solid state reaction, co-precipitation, sol-gel, hydrothermal synthesis, and spray/freeze drying. The first three are the more conventional methods, and almost all the membranes listed in Table 1.6 adopted these three methods. Therefore, only these three particle synthesis methods are summarized here. More information about other methods can be found in the review [46].

While preparation methods can impact the performances of oxygen permeation with air as the feed gas [39], no similar studies are available to compare the water splitting rate of the same membrane materials prepared by different synthesis methods.

(1) Solid state reaction

Solid state reaction, or the mixed-powders technique, is the most common approach to produce ceramic particles [39]. Oxides, carbonates, hydroxides or salts are weighed according to cation stoichiometric ratios and then mixed and ball-milled up to two days. Organic liquids, such as methanol [47] and isopropyl alcohol [48] can be applied to the solid mixture to increase its homogeneity. After milling, the dried mixture is calcined at high temperatures. During this process, the cations diffuse in the mixture to form the desired thermodynamically stable crystals [49]. The particle size distribution is usually wide and ball-milling is required to make finer ceramic particles for further processes. However, the homogeneity and purity of the ceramic powders prepared by the solid state reaction method are usually poor [46]. Besides, the energy consumption is intense due to the ball-milling and high temperature calcination for solid reactions.

(2) Co-precipitation

This is one of the oldest methods to prepare crystals with particle sizes generally on the scale of nanometers. The desired amount of cation precursors are dissolved and mixed with the precipitating agent. After this, a series of processes (e.g., filtration, drying and thermal decomposition) are carried out to achieve the desired ceramic powders. For example, Jeon et al. [50] prepared $LaNiO_{4+\delta}$ (LNO) powders from lanthanum acetate hydrate and nickel acetate tetrahydrate, and ammonium hydroxide was added to adjust the pH values. They also used thermogravimetric analysis to determine the thermal decomposition temperature [51]. The particle morphology and purities can be well controlled by the pH, mixing rate, thermal decomposition temperature, and cation concentrations in the solution. Doping agents can also be added to avoid the inhomogeneity in the composition [39]. Additionally, as the temperatures for co-precipitation are lower than the solid-state reactions, less energy is consumed for particle synthesis.

(3) Sol-gel method

The sol-gel method for non-silicate ceramics has been under development since 1948 to prepare functional oxides such as titanate or mixed cation perovskites [39]. It

provides excellent composition control and the ceramic particles prepared in the sol-gel method are with very high purity. Different routes are adopted such as the all-alkoxide method, alkoxide-salt citrate-type method and hydrous oxide solutions [46]. Generally, an amorphous gel is produced from the cation precursors (i.e., metal nitrates and metal alkoxides), with the addition of a chelating agent, such as citric acid. Polymerization promoters such as ethylene glycol can also be applied to control the gel formation. After the gel is formed, it is dehydrated at low temperature and then calcined at high temperature. Sol-gel method has been successfully applied to produce functional oxides with high purity, such as the $BaCo_xFe_yZr_{1-x-y}O_{3-\delta}$ (BCoFZ) [52] and $La_{0.3}Sr_{0.7}FeO_{3-\delta}$ (LSF-37) [53] membranes for water splitting applications.

1.3.1.2 Membrane Fabrication

Various configurations of ceramic membranes are studied in the literature for water splitting (i.e., tubular, planar or thin film membranes). The dense part thickness varies from 0.02 mm to 1.5 mm, as shown in Table 1.5. In order to achieve high mechanical strength, thin film membranes are always supported by thicker porous layers which can be made of the same material with the dense membrane [54, 55], or different materials to catalyze the surface reactions [56, 57].

Several methods are applied to prepare the green membranes, such as pressing, plastic extrusion, phase-inversion spinning or painting. The as-produced green membrane is then sintered in air or a reducing environment (if one phase is metal) at high temperatures to achieve the densification. During the sintering process, the green membrane may shrink: Schiestel et al. [58] found that after sintering the BCoFZ tubular membrane shrank 34% in length and 50% in diameter compared to the green membrane. Therefore, green membranes with larger dimensions are prepared by design to achieve desired membrane dimensions.

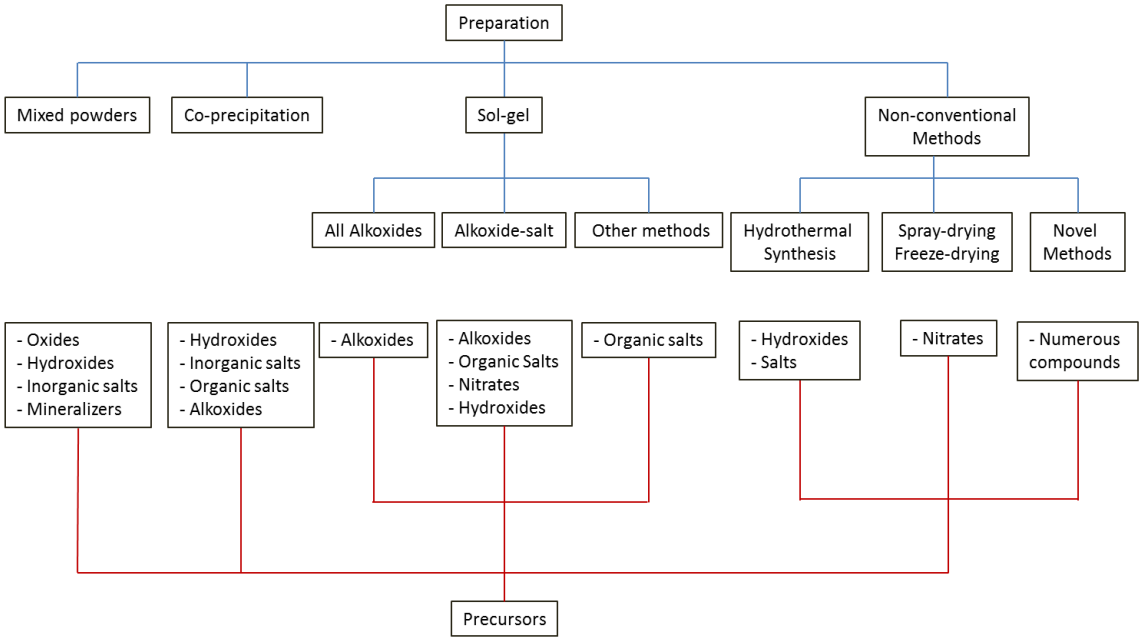

Figure 1.7 Preparation methods and the corresponding precusors for ceramic powder synthsis (reproduced from [46])

(1) Pressing

Pressing is a straightforward method to prepare green membranes with simple geometries such as plates and closed-one-end (COE) tubes. The as-synthesized particles are ground and pressed in a cold isostatic press in a mold (rubber or stainless steel) into desired tubes or plates [54, 59]. For two-phase membranes, mixing of different phases is required before being ground and pressed, and binders such as polyninyl alcohol can also be added [53]. In order to make a porous surface, graphite or organic particles are mixed with the functional material particles [60]. Wu et al. [60] prepared a porous $La_{0.9}Ca_{0.1}FeO_{3-\delta}$ (LCF-91) layer by mixing LCF-91 powers with graphite powders (<20μm, Sigma-Aldrich®) at 50 vol% with a mortar and pestle for twenty minutes, and then compressing the mixture into a flat circular plate at 10 metric ton-force for 1 minute. After sintering at 1450^{o}C for 30 minutes, a porous substrate with pores of several micrometers was produced as is shown in Figure 1.8.

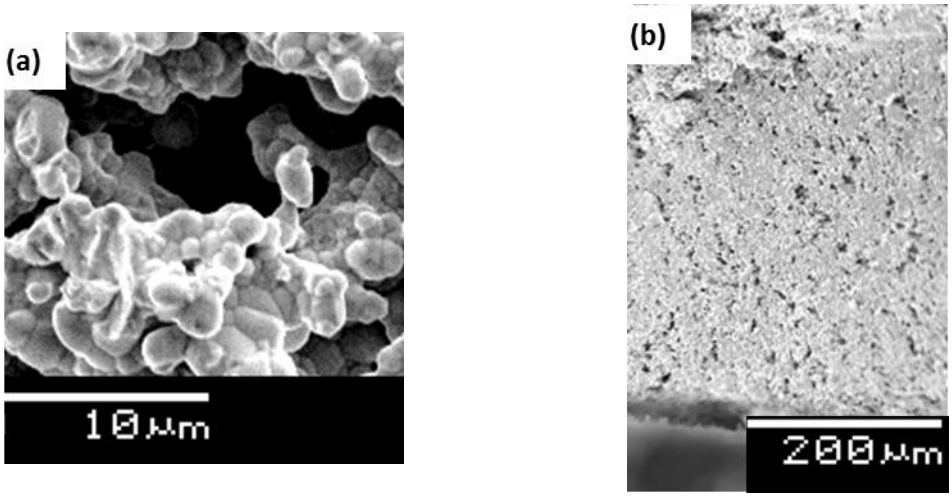

Figure 1.8 The SEM images of the LCF-91 porous layer on a membrane (a) Porous membrane surface shows the large pores (sizes are several micrometers); (b) The cross-section of the porous membrane shows the pores along the thickness of the membrane [60]

(2) Plastic extrusion

The plastic extrusion method is usually applied to fabricate tubular membranes. First, a mixture with good plasticity, known as a 'slip' consisting of ceramic particles and organic additives (i.e. a solvent, a dispersant, a binder and a plasticizer) is prepared [61]. Then the slip undergoes solvent evaporation and extrusion to form tubular membranes. Zhu et al. [62] prepared a 0.3 mm thick tubular $SrCo_{0.4}Fe_{0.5}Zr_{0.1}O_{3-\delta}$ (SCoFZ) membrane for water splitting using a slip with a mixture of 76 wt% SCoFZ powder, 10 wt% polyvinyl alcohol solution, 10 wt% dextrin and 4 wt% Tung oil.

(3) Phase-inversion spinning

Phase-inversion spinning is similar to plastic extrusion, as both are derived from polymer fabrications and both are applied to prepare tubular membranes. In this method, the ceramics powders are mixed with organic solutions to form slurry, which is spun through a spinneret to form green tubular membranes [52, 58]. Jiang et al. [52] prepared 0.17 mm thick hollow fiber tubular BCoFZ membranes using this method: they first mixed BCoFZ with a solution of polysulfone in 1-methyl-2-pyrrolidone and ball-milled the mixture for 16 hours; and then the slurry was spun through and the green BCoFZ

perovskite fiber obtained was cut into 0.5 m pieces and sintered in a hanging geometry at 1320 ℃ for 5 h. After sintering, a thin dense membrane with porous support is shown in Figure 1.9.

(4) Painting

Painting or coating is an effective approach to fabricate thin film membranes on a porous support, while the porous support is prepared by sintering a mixture of ceramic particles and combustible particles using the methods above. The slurry for painting usually consists of the functional oxide powders, a binder, a plasticizer, poly-vinyl butyral, α-terpineol [57]. After the slurry is painted onto the substrate, the asymmetric membrane is dried and sintered to form a dense thin film on the porous support. Park et al. [57] painted a 0.05 mm thick dense $La_{0.7}Sr_{0.3}Cu_{0.2}Fe_{0.8}O_{3-\delta}$ (LSCuF-7328) thin film membrane on the porous substrates with the same perovskite material. The sample was then dried at 80^{o}C for 1 hour and heated at 1100–1140^{o}C for 10 h in air. SEM images show that dense thin film was successfully fabricated, as shown in Figure 1.10.

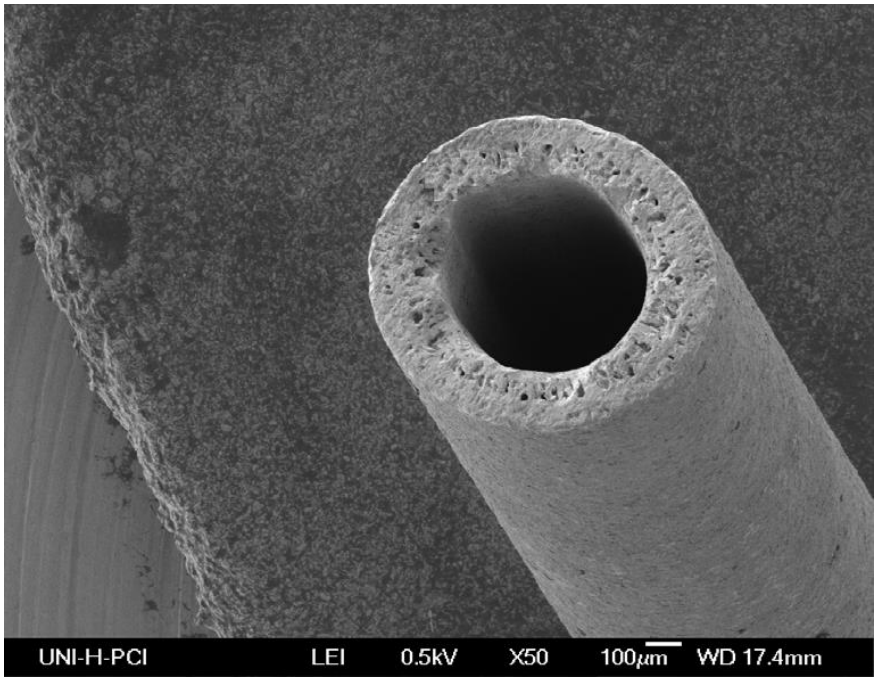

Figure 1.9 SEM pictures of the cross-section of the fresh hollow fiber membranes with an asymmetric structure made by phase-inversion spinning [52]

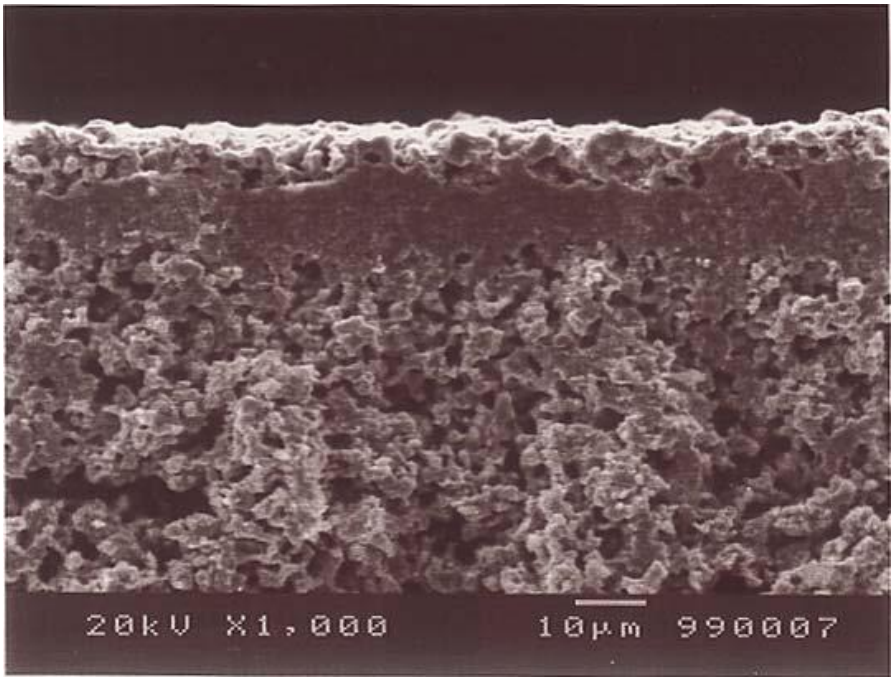

Figure 1.10 Micrograph of the cross-section of LSCuF-7328 thin film prepared by painting [57]

1.3.2 Single phase membranes

1.3.2.1 Fluorite membranes

Stabilized zirconia was an attractive candidate for the oxygen permeable membrane for water dissociation in early attempts due to its high ionic conductivity and high melting points. Dopants such as CaO and Y_2O_3 are essential for the stability of the cubic phase of zirconia, while others such as CeO_2 and TiO_2 can enhance the electronic conductivity of the oxide to make it mixed ionic-electronic conductive for oxygen permeation [39].

Cales et al. [37] studied water splitting on a $(ZrO_2)_{0.9}$-$(CaO)_{0.1}$ closed-one-end tube with 50 % CO on the sweep side at temperatures as high as 1400 – 1800 K. The oxygen permeation rate is fitted as

$$J_{O_2} = A\left(p''^{-1/4}_{O_2} - p'^{-1/4}_{O_2} \right) e^{-\frac{E_a}{kT}} \qquad (1\text{-}7)$$

where A is a fitted constant, k is the gas constant, T is temperature and E_a is activation energy (390 kJ/mol for their experiments). p'_{O_2} and p''_{O_2} are the oxygen partial pressures calculated by thermodynamic equilibrium in the gas phase on the feed and sweep sides, respectively. Later the same group carried out more extensive investigations on these $(ZrO_2)_{0.9}$-$(CaO)_{0.1}$ tubular membranes and achieved hydrogen production rate from water splitting as high as 2.2 μmol/s [32]. The hydrogen production rate is thought to be limited by the low electronic conductivities of this Ca-doped stabilized ZrO_2 tube.

Later, Naito and Arashi [47] doped TiO_2 into $(ZrO_2)_{0.9}$-$(Y_2O_3)_{0.1}$ (YSZ) to enhance the electronic conductivity. They compared the performances of both doped and undoped membranes for water splitting with H_2-CO_2 mixture as the sweep gas, and found that the doped membrane had higher performances than the undoped ones at 1600 – 1700^{o}C. This is due to the TiO_2 dopant increases the electronic conductivity of YSZ, which was the bottleneck for oxygen permeation in YSZ membranes. The highest hydrogen production rate on the doped membrane was 0.4 μmol/cm^2•s at 1683 ^{o}C when the oxygen partial pressure on the sweep side is 10^{-7} Pa based on the thermodynamic equilibrium in the gas phase.

However, the total conductivity of doped fluorite materials is still very low (as shown later in Figure 1.14). Therefore, for such a membrane, the bulk diffusion of oxygen ions is limited by the electronic conduction [39]. Later researches were focused on mixing better electronic conductive materials with these fluorite materials to overcome the limiting step of electronic conduction. These mixed phase membranes will be discussed later in this chapter.

1.3.2.2 Perovskite membranes

Mixed ionic-electronic conductive perovskites ($ABO_{3-\delta}$) are attractive candidates for oxygen permeation, and better oxygen flux is usually achieved on perovskite membranes than on fluorite membranes when air is the feed gas [39]. Various combinations of A and B cations change the conductivity and catalytic activities of the material. The perovskite is expected to be stable if the Goldschmidt tolerance factor, T_G, is in the range of

$$0.8 < T_G = \frac{r_A + r_O}{\sqrt{2}\left(r_B + r_O\right)} < 1 \qquad (1\text{-}8)$$

where r_A, r_B and r_O are the radius of ions A, B and O, respectively. Usually, alkaline-earth metal ions are doped in A site to create oxygen vacancies, while transition metal ions in B sites to improve the electronic properties [39]. Oxygen ion diffuses through hopping mechanism in the oxygen vacancies while electronic conduction is usually attributed to the B^{n+}-O-$B^{(n+1)+}$ pairs [63]. In the following, we use A site alkaline-earth metal ions to categorize the perovskite membranes for facilitating water splitting.

(1) Barium based perovskite

The oxygen fluxes through a 300 μm thick hollow fiber $Ba_xCo_{1-x}Fe_yZr_{1-y}O_{3-\delta}$ (BCoFZ) membrane were as high as 5.6 μmol/cm^2•s at 900^{o}C when air was the feed gas and inert gas as the sweep gas [64]. This high oxygen permeability attracts researchers to investigate water splitting on this BCoFZ membrane and high hydrogen production rates were achieved [52, 54, 56, 65, 66].

Jiang et al. carried out extensive studies on 0.17 mm thick BCoFZ tubular membranes (dense part was 0.05 – 0.1 mm thick) for enhanced water splitting and they incorporated partial oxidation of methane [52, 56, 66] or oxidative dehydrogenation of ethane [65] on the sweep side to co-produce syngas and ethylene, respectively. The highest hydrogen production rates achieved on this BCoFZ membrane for methane and ethane sweep cases were 3.4 μmol/cm^2•s at 950^{o}C with 10% CH_4 (Ni/Al_2O_3 catalysts) and 0.6 μmol/cm^2•s at 800^{o}C with 20% C_2H_6 on the sweep side, respectively. Increasing temperature or hydrocarbon concentrations both increased the hydrogen production rate from water splitting. Ni/Al_2O_3 and Pd doped BCoFZ catalysts were also compared for the methane partial oxidation on the sweep side [52, 56]. However, when inert gas was used as the sweep gas, hardly any hydrogen production could be observed from water splitting on the feed side [66].

Although BCoFZ has excellent performances for water splitting, the membrane suffers from cobalt segregation to the surface under reducing environment, which may lead to potential membrane failure [56, 65]. In order to avoid cobalt segregation, Park et al. [54] in Argonne National Laboratory tested the cobalt-free $BaFe_{0.9}Zr_{0.1}O_{3-\delta}$ (BFZ)

membrane with the gasification products of coal (mainly CO and CO_2) as the sweep gas. On a 1.6 mm thick BFZ membrane, hydrogen production rates as high as 0.2 μmol/cm^2•s were achieved at 900^{o}C (80% CO sweep and 49% H_2O feed).

(2) Strontium based perovskite

Strontium based perovskite is another popular oxygen permeation material due to its high oxygen permeability. $SrCo_{0.4}Fe_{0.5}Zr_{0.1}O_{3-\delta}$ (SCoFZ-451) has a high oxygen flux and good chemical stability for air separation [67]. When it is under water splitting with ethanol steam reforming conditions, hydrogen production rates increased from 0.97 to 2.53 μmol/cm^2•s as temperature rised from 750 to 900^{o}C when 6% ethanol was on the sweep side and 69% water on the feed side [62]. Ni/Al_2O_3 catalysts were packed on the sweep side to promote ethanol oxidation.

Electron donors such as lanthanum can be doped into the Sr-based perovskites to modify the valence of the B site transition metal and the concentration of oxygen vacancies. A 0.25 mm thick $La_{0.6}Sr_{0.4}Co_{0.2}Fe_{0.8}O_{3-\delta}$ (LSCoF-6428) membrane was tested, and hydrogen production as high as 0.21 μmol/cm^2•s was achieved with 5% methane on the sweep side at 900^{o}C [68]. It was also found that methane can activate water dissociation on the feed side: when the methane stream is switched to an inert gas stream on the sweep side, water splitting rate can be maintained at high values, which is greater than that of inert sweep case before the introduction of methane to that side.

However, similar to the Ba-based perovskites discussed before, cobalt is an undesired dopant on the B site, as it is likely to segregate and migrate to the surface and thus, lead to membrane failure under reducing environment [39]. Therefore, materials without cobalt were investigated. One example is $La_{0.3}Sr_{0.7}FeO_{3-\delta}$ (LSF-37), and the hydrogen production rates were 0.01 and 0.04 μmol/cm^2•s at 860 and 900^{o}C, respectively on a 3 mm thick LSF-97 membrane with CO on the sweep side [53, 69]. Similar to the LSCoF-6428 membranes in [68], the LSF-37 membrane can also be activated by the reducing gas on the sweep side. And the hydrogen production with CO sweep was 7.5 times higher than the value with inert sweep case after activation [69].

Cobalt free LSF membranes have lower performance for water splitting as shown in [53, 69]. In order to improve its performance while maintaining the stability, copper

was doped in the B site. The $La_{0.7}Sr_{0.3}Cu_{0.2}Fe_{0.8}O_{3-\delta}$ (LSCuF-7328) membranes were tested extensively in the literature with three different configurations (planar, thin films on porous support, and close-one-end tubes) and with either H_2 or CO on the sweep side.

For a planar LSCuF-7328 membrane, hydrogen production rate from water splitting rose at higher water concentrations and smaller membrane thickness [57]. The highest hydrogen production of 1.4 μmol/cm^2•s was achieved for a 0.33 mm thick membrane at 900^{o}C with 80% H_2 sweep and 79% H_2O feed. However, the 0.33 mm thick LSCuF-7328 membrane had slightly lower performances than a 0.97 mm mixed phase Ni/CGO membrane, even though the thickness of LSCuF-7328 membrane was smaller [57]. Moreover, at 900^{o}C with H_2 sweep, a 0.05 mm thick thin film with Pt porous support showed a 7.8 μmol/cm^2•s hydrogen production rate as the maximum reported value [57], and on a 0.022 mm thick thin film without Pt on the support, the maximum value reported was 6.8 μmol/cm^2•s [48]. These exceptional performances shed lights on these ultra-thin membranes as potential membrane configurations for better performances of water splitting.

When the water concentration on the feed side was higher than 7%, the water splitting rate decreased in the order of: 80% H_2 > 100% CO > 50% CO+CO_2 in the sweep gas on the LSCuF-7328 thin-film membrane. However, when the water concentration is in the range of 3 – 7%, 80% H_2 and 100% CO sweep cases showed almost the same performances [48]. Additionally, Park et al. [48] compared He and CO_2 as diluents in the CO sweep gas and found that at the same CO concentration at the inlet, the cases with CO+He mixtures on the sweep side led to higher hydrogen production rates than those with CO+CO_2 mixtures. This can be due to the CO_2 reaction on the membrane to form carbonates on the surface that block the effective surface area.

The LSCuF-7328 membrane was also studied by a different group as in [70], and the hydrogen production rate was 0.09 μmol/cm^2•s for a 0.36 mm thick membrane with 80%CO on the sweep side and 49% H_2O on the feed side at 900^{o}C. They also reported the expansion coefficient of the membrane: 13×10^{-6} K^{-1} below 973 K and 20×10^{-6} K^{-1} between 1073 and 1273K. The former expansion rate at low temperature is mainly due to thermal expansion, while the latter one at high temperature is attributed to both thermal and chemical expansion from oxygen vacancy formation. As oxygen vacancy formation

and destruction lead to higher expansion coefficients, careful operation is required to maintain membrane stability under chemical reactions.

(3) Calcium based perovskite

Ca based perovskites show smaller oxygen fluxes than Sr or Ba based perovskites under the same operating conditions for air separation [71]. However, due to its high resistance to carbonate formation and stability under CO_2 environments, Ca-based membranes are more attractive than Sr and Ba based membranes for CO_2 reuse applications [39]. Wu et al. [60, 72] studied $La_{0.9}Ca_{0.1}FeO_{3-\delta}$ (LCF-91) membrane for water splitting, and achieved hydrogen production rate as high as 0.37 μmol/cm^2•s with CH_4 sweep on a 0.9 mm thick LCF-91 membrane with a Ni/LCF-91 porous layer on the methane side, which is two orders of magnitude higher compared to the case without the porous layer when 5% methane on the sweep side at 990^{o}C [60]. The sweep side surface reaction was found to be the rate limiting step under the operating conditions in their experiments. No carbon deposition was found on either side of the membrane surface after experiments, and syngas with H_2/CO ratio of 2 was produced at the outlet of the membrane reactor.

1.3.3 Mixed phase membranes

A mixed phase membrane consists of multiple phases: at least one phase exhibits high ionic conductivity and another high electronic conductivity. Since fluorite conductors have high ionic conductivity but are limited by the low electronic conductivity, attempts have been made to mix them with a good electronic conductor, either metal or oxides to achieve high mixed conductivity.

On a 0.09-mm thick gadolinium-doped ceria (CGO)/NiO membranes with porous supports made of the same mixed phase materials, Balachandran et al. [59, 73] measured the hydrogen production rate from water splitting as high as 6.3 μmol/cm^2•s at 900^{o}C when 80% H_2 is on the sweep side and 49% H_2O on the feed side. This high performance was attributed to the fact that nickel boosts electronic conductivity of a CGO membrane [73]. They also found that CGO/NiO membranes had finer surface and larger surface area

than the CGO/Ni membranes, so the former showed higher performances for water splitting [73].

Besides, Cu has also been mixed with CGO to achieve high mixed conductivity. Song et al. [74] studied the CGO/Cu dual phase membrane and reported the hydrogen production rate as high as 1.71 μmol/cm^2•s at 900^{o}C for a 0.48 mm membrane with 80% H_2 on the sweep side and 50% H_2O on the feed. The hydrogen production rate increases linearly with $\log\left(p_{H_2}\right)$ on the sweep side or $\log\left(p_{H_2O}\right)$ on the feed side.

Another electronic conductor $Gd_{0.08}Sr_{0.88}Ti_{0.95}Al_{0.05}O_{3\pm\delta}$ (GSTA) is mixed with CGO, and the hydrogen production rate from water splitting was reported to be as high as 7.3 μmol/cm^2•s at 900^{o}C on a 0.025 mm CGO/GSTA thin-film membrane [75]. This thin-film membrane was supported on a 2-mm thick porous layer of 35% porosity, which was made of the same CGO/GSTA material. GSTA is an n-type electronic conductor with negligible oxygen ionic conductivity under the operating conditions in this paper, and its electronic conductivity is much higher than that of the CGO. However, the conductivity of the CGO/GSTA mixture is susceptible to the oxidizing environment, and the overall conductivity decreases with increasing oxygen partial pressure. Therefore, a small amount of H_2 (0.2%) was added on the feed side to avoid the conductivity degradation from the oxidization.

Moreover, a mixed phase material $SrFeCo_{0.5}O_{3-\delta}$ (SFC2) was developed in Argonne national laboratory [55, 73] and has been applied to both oxygen separation and membrane-supported water splitting. SFC2 consists of an intergrowth ($Sr_4Fe_{6-x}Co_xO_{13\pm\delta}$), perovskite ($SrFe_{1-x}Co_xO_{3-\delta}$) and spinel ($Co_{3-x}Fe_xO_4$) phases [76]. Hydrogen production rates as high as 11.9 μmol/cm^2•s were measured at 900 ^{o}C on a 0.02 mm SFC2 thin film with porous support on the sweep side when 80% H_2 was on the sweep side and 49% H_2O on the feed side [55]. They also compared the performances of a 1.04 mm planar membrane and a 0.02 mm thin film and found that hydrogen production rate increases with water partial pressure on both membranes; when the water concentration on the feed side is as low as 3%, the performances on both membranes were very close.

Most of the mixed membranes have two phases randomly distributed along the thickness. Yet Jeon et al. [50] layered the mixed ionic-electronic conductor $LaNiO_{4+\delta}$ (LNO) onto an oxygen ionic conductor CGO; LNO was on the water side, while CGO

was on the sweep side. The reason for this arrangement is that LNO degrades at low oxygen partial pressure and CGO exhibits electronic conductivity at low oxygen partial pressure. The highest hydrogen production rate measured on this 0.3 mm thick membrane (CGO 0.008 mm and LNO 0.292 mm) was 0.09 μmol/cm^2•s at 900^{o}C with 23.25% CO on the sweep side. This is twice as high as that for a 0.36 mm LSCuF-7328 membrane at the same sweep condition [70].

1.3.4 Rate limiting steps and critical thickness

The oxygen transport process through the oxygen permeable membrane consists of five steps as is shown in Figure 1.11: two mass transfer steps in the gas phase (*a* and *e*), two surface reaction steps between gas species and the membrane surface (*b* and *d*), and one bulk diffusion step through the membrane (*c*). The oxygen species here are the oxygen atoms in either H_2O/CO_2 molecules or oxide lattices. If the membrane surface is porous, the mass transfer processes can be further modelled as two sub-steps: one in the open space and the other in the porous substrate.

The mass diffusion in the gas phase and the solid/solid or solid/gas interactions can be modelled separately. The gas phase transport in the open space can be modelled using Fick's law with diffusion coefficients. In the porous substrates, either the dusty-gas model [77] or the advective-diffusive model [78] can be used. On the other hand, the solid/solid or solid/gas interactions involve heterogeneous surface reactions, electron transfer and ionic and electronic conduction. In the literature, the mass diffusion resistance in the gas phase is usually neglected, and the experimental measurements taken far away from the membrane surface are assumed to be representative of the species on membrane surfaces. However, this assumption is not always valid, especially when there is the surface reaction rate is faster than the mass diffusion, which usually leads to the polarization of concentration in the gas phase. Moreover, the gas phase reactions from the membrane surface to the outlet of the membrane can't be ignored at high temperature operations. Therefore, Ghoniem's group proposes that gas phase samples in the vicinity of the membrane surface rather than the bulk values should be used to describe the surface reaction resistances, and both experimental and numerical studies have verified that the local sample measurements describe the transport resistances better [60, 79-81].

But in the following, we summarize the transport discussions in the literature by assuming that the bulk gas species measurements in the corresponding experiments can be the same as the local values.

To compare the effects of the surface reactions and bulk diffusion, a critical thickness is generally identified such that when the membrane is thicker than the critical thickness, the bulk diffusion is the only rate limiting step. For example, for the CGO/NiO membranes with hydrogen sweep, by comparing the membranes with or without porous supports, Balachandran et al. [59] found that the critical thickness was 0.5 mm. The porous support couldn't increase the hydrogen production rate once the membrane was thicker than 0.5 mm (feed side P_{H2O} = 0.03 – 0.5 atm, sweep side P_{H2} = 0.01 – 0.05 atm). This was also verified by the linear dependence of hydrogen production rate on $\log\left({p'_{O_2}}/{p''_{O_2}} \right)$ for a 0.91 mm thick membrane. Because of this membrane is in the bulk diffusion limiting region, the surface reactions can be assumed to be in thermodynamic equilibrium, and the oxygen partial pressure on each side can be evaluated from gas phase equilibrium values [59]. On the other hand, when the membrane is thinner than 0.5 mm, the surface kinetics is important and the surface morphology affects the performances. As a result, the CGO/NiO membrane that had finer surfaces and larger surface area than the CGO/Ni membrane led to a higher hydrogen production rate from water splitting [73].

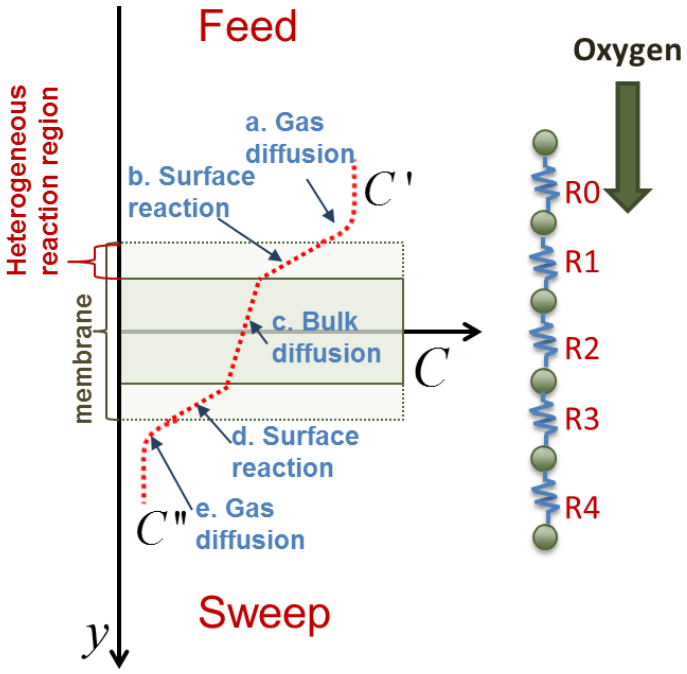

Figure 1.11 Oxygen (or oxygen species) transport process in an oxygen permeable membrane can be divided into five steps: two mass-transfer, two surface-reaction and one bulk-diffusion processes

The critical thickness depends on both the membrane materials and operating conditions. Wang et al. [75] found that the critical thickness of a flat CGO-GSTA membrane is 1.2 mm (feed side P_{H2O} = 0.03 – 0.25 atm, sweep side P_{H2} = 1 atm). Therefore, when the membrane is 0.025 mm thick with a 2 mm porous support, both surface reactions and bulk diffusion affects the water splitting rate. On the other hand, the bulk diffusion was found to be the limiting step for a 0.46 mm thick CGO/Cu membrane at 900°C with 80% H_2 in the sweep gas, as the hydrogen production rate increased linearly with $\log p_{H_2O}$ on the feed side [74]. But for the SFC2 membranes, even when the membrane was as thick as 1 mm, the surface reactions could not be ignored, which was indicated by that the hydrogen production rate did not increase linearly with $\log\left(p'_{O_2}/p''_{O_2}\right)$ [55, 73] (feed side P_{H2O} = 0.49 atm, sweep side P_{H2} = 0.04 – 0.8 atm).

For LSCuF-7328 membranes, the critical thickness is 0.75 mm, as it was found that Pt catalytic support hardly enhanced the hydrogen production rate from water splitting when the membrane thickness was larger than 0.75 mm [57] (feed side P_{H2O} = 0.03 – 0.79 atm, sweep side P_{H2} = 0.8 atm). For a 3 mm thick LSF membrane, Evdou et al. [53] and Nalbandian et al. [69] proposed that bulk diffusion was the limiting step (feed side P_{H2O} = 0.025 atm, sweep side P_{CO} = 1 atm). But for a 0.3 mm thick SCFZ-451 membrane with Ni/Al_2O_3 catalysts on the sweep side, water splitting was proposed to be the rate limiting step [62] (feed side P_{H2O} = 0.69 atm, sweep side P_{EtOH} = 0.06 atm)..

Wu et al. [60, 72] identified the surface reaction on the sweep side as the rate limiting step for a 0.9 mm thick LCF-91 membrane using a resistance model, when a fuel (i.e., H_2 or CH_4) is used as the sweep gas (feed side P_{H2O} = 0.5 atm, sweep side P_{fuel} = 0.01 – 0.05 atm). This was confirmed by that the surface modifications on the sweep side (e.g., adding a porous layer and catalysts) improved the performances by two orders of magnitude compared with the unmodified membranes [60].

1.3.5 Sweep side: fuel and catalysts

Adding reducing gases (i.e., fuels) into the sweep side can improve the oxygen flux in two ways. First, it reduces the oxygen chemical potential on the sweep side and the chemical potential difference across the membrane increases as a result. Second, the heterogeneous reactions between fuels and the lattice oxygen have faster kinetics than the oxygen evolution reaction [82]. As a result, the water splitting rate with fuels on the sweep side is usually much higher than those values with inert on the sweep side [68, 69, 72]. For example, for a 3 mm thick LSF-37 membrane, Evdou et al. [53] found that the water splitting rate with argon sweep was 3 times lower than that with CO and Ar mixture sweep. Therefore, in order to enhance the water splitting rate, fuels such as hydrogen [73, 74], carbon monoxide [48, 50], methane [52], ethane [65] or ethanol [62] have been investigated in the literature.

Due to the various reactivity with the lattice oxygen, different fuels on the sweep side result in different water splitting rates even when the fuel concentrations at the inlet are the same. For the 0.9 mm LCF-91 membrane at 990^{o}C, methane was found to be less effective in enhancing water dissociation rate than H_2 [60, 72]. Similarly, for the 0.46 mm

thick CGO/NiO membrane with 49% H_2O on the feed side, the water splitting rate with 5% CH_4 in the sweep side was 4 times less than that with 5% H_2 [59]. And on a 0.022 mm LSCF-7328 thin film membrane with a LSCF-7328 porous support, the water splitting rate decreased in the order of sweep gases: pure H_2 > pure CO > $CO+CO_2$ mixture [48].

Although hydrocarbons have slower kinetics than hydrogen, water dissociation intensified with hydrocarbon upgradation on the sweep side is more practical and economically favorable. Therefore, catalysts such as Ni [52, 60, 62], Pt [57] and Pd doped perovskite [56] are applied on the fuel side to increase the reactivity and selectivity to the desired products. Wu et al. [60] applied nickel catalysts on the porous LCF-91 layer on a 0.9-mm thick dense LCF-91 membrane using wet impregnation method and found that the hydrogen production rate from water splitting further increases by a factor of two compared to unmodified membranes. However, if the limiting step is not on the sweep side surface reaction, the catalysts couldn't enhance the water splitting rate. For example, the porous CGO/NiO layer [59, 73] or porous Pt catalyst [57] couldn't increase the water splitting on a CGO/NiO membrane thicker than 0.5 mm as the bulk diffusion was the limiting step under their experimental conditions.

1.3.5.1 Methane partial oxidation

Methane partial oxidation can be incorporated into the membrane sweep side to produce syngas. Syngas, a mixture of H_2 and CO, is an important feedstock for various synthetic fuels and chemicals such as methanol and ammonia that are among the top ten chemicals produced annually in the world [9, 14]. The H_2/CO ratio is an important parameter for the syngas quality. An optimum feedstock syngas H_2/CO ratio is required for each chemical [83]. For example, $H_2/CO \approx 2.0$ is preferred for methanol production and partial oxidation of methane (POM) on the sweep side of the membrane gives such a H_2/CO ratio of 2,

$$CH_4 + \frac{1}{2}O_2 \leftrightarrow CO + 2H_2 \quad \Delta H_{298}^0 = -36kJ/mol \tag{1-9}$$

As a result, the intensification of water splitting and POM on an oxygen permeable membrane reactor has been investigated.

BCoFZ [52, 56, 66], LSCoF-6428 [68], LCaF-91 [60] and GDC/Ni [59] membranes were tested in the literature with syngas production from POM on the sweep side, as is summarized in Table 1.7. For a BCoFZ membrane reactor, both nickel and Pd doped-BCoFZ catalysts were applied, and nickel was found to have higher activity than Pd doped-BCoFZ under the reported operating conditions [52, 56].

The conversion of methane is related to the CH_4/O_2 ratio on the sweep side. Both Jiang et al. [52] and Wu et al. [60] found that the CH_4/O_2 ratio on the sweep side decreased with increasing CH_4 concentration at the inlet on the sweep side, and the conversion ratio of methane dropped as a result. For the BCoFZ membrane with Ni/Al_2O_3 catalysts in [52], when CH_4 concentration at the inlet increased from 1 to 10%, its conversion decreased from ~100% to ~60% [52]. And for the LCF-91 membrane with Ni/ LCF-91 porous catalytic layer on the sweep side conversion ratio decreased from ~80% to ~20% when CH_4 concentration at the inlet was raised from 1 to 5% [60].

Additionally, selectivity to CO/H_2 is also related to CH_4/O_2 ratio. First, higher CH_4/O_2 ratio leads to partial oxidation to CO and H_2. It is shown in [52] that CO selectivity increased from 3% to 45% when the CH_4/O_2 ratio increased. On the other hand, high CH_4/O_2 ratio also increases the tendency to coke formation at high temperature at 950 ^oC on Ni catalysts, and coke formation decreases both the selectivity to CO and the conversion of CH_4 [52]. And adding CO_2 on that side can decrease coke formation by reverse Boudouard reaction [84].

Three pathways for carbon reaction are proposed on the surface depending on the available lattice oxygen on the sweep side: methane deposition, partial oxidation and full oxidation, as shown in Figure 1.12. As the oxygen flux is determined by CH_4 concentration, membrane configuration, catalysts as well as operating conditions, a detailed study or model is required to optimize the syngas production and water dissociation in the reactor based on the methane oxidation mechanism.

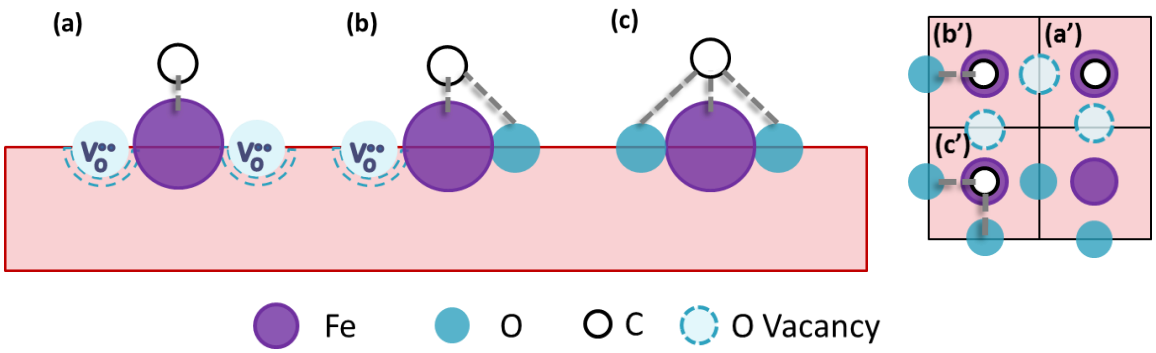

Figure 1.12 Pathways for carbon on surface LCF-91 lattice: (a) solid carbon depostion; (b) partial oxidation; (c) complete oxidation; (a') (b') and (c') are top views of the absorbed carbons on FeO_2 terminated LCF-91 lattice (modified from [60])

1.3.5.2 Higher hydrocarbon processing

Higher hydrocarbons processing (e.g., oxidative dehydrogenation of ethane or oxidative steam reforming of ethanol) was studied on the sweep side of the membrane to produce value-added products [85]. However, this is still at the stage of proof-of-concept and more studies are required to understand the coupling effects among the water splitting, oxygen permeation and hydrocarbon reactions.

One example is to incorporate oxidative dehydrogenation of ethane (ODE) for ethylene production to utilize the oxygen on the sweep side. ODE is an exothermic reaction, and the overall ethylene production process by ODE is estimated to consume only 35% of the energy of the industrialized ethane cracking [86].

Ethane cracking: $C_2H_6 \rightarrow C_2H_4 + H_2 \qquad \Delta H^0_{298K} = 136kJ/mol$ (1-10)

ODE: $C_2H_6 + 1/2O_2 \rightarrow C_2H_4 + H_2O \qquad \Delta H^0_{298K} = -105.5kJ/mol$ (1-11)

Jiang et al. [65] studied the intensification of water splitting and ODE on a BCoFZ membrane reactor. The selectivity to ethylene was as high as 89% at 800 ^oC with 59% ethane on the sweep side, and the hydrogen production on the feed side was as high as 0.6 μmol/cm^2•s, which was on the same order of magnitude with the values under the methane sweep case [65]. However, after the experiments, cobalt in the perovskite phase was reduced and segregated onto the membrane surface, which made BCoFZ membrane unstable for this application.

Another example is oxidative steam reforming (OSR) of ethanol on the sweep side to generate hydrogen, and the reaction on the sweep side is

$$C_2H_5OH + 2H_2O + O_O^X + 2h^{\bullet\bullet} \rightarrow 2CO_2 + 5H_2 + V_O^{\bullet\bullet} \quad \Delta H_{298K}^0 = -68.3kJ/mol \text{ (1-12)}$$

Zhu et al. [62] studied water splitting with OSR of bio-ethanol on a 0.3-mm thick SCoFZ-451 membrane with Ni/Al_2O_3 catalysts on the sweep side for ethanol reaction and found that the selectivity to H_2 on the sweep side didn't depend on the temperature, while the selectivity to CO increased from 64% to 76% when temperature was raised from 700 to 900^{o}C [62]. Very little amount of methane was produced especially when the temperature is higher than 800^{o}C.

1.3.6 Stability

As the oxygen partial pressure is very low during water splitting on both sides of the membrane, the stability of the materials under reducing environments is important for this application. Long term stability tests are required to verify the stability of the membranes. So far, the longest study on membrane-supported water splitting is a 260 h test on a LSCoF-4628 membrane; but segregation of SrO and La_2O_3 was found on the water side and Co segregation and cracks were found on the fuel side after the experiments [68].

Other cobalt containing membranes suffer similar problems of element segregation. When ethane was used as the sweep gas, the BCoFZ surface was eroded to a depth of 10 μm after 100 h, but no cracks were formed; and cobalt was reduced and segregated from the membrane [65]. Similarly on a Pd doped BCoFZ membrane, Co and Pd atoms are found to be distributed non-homogeneously on the surface after experiments, but the authors suggest that this segregation leads to better catalytic effects [56].

For cobalt-free materials, surfaces morphology changes were found. Isolated pores and carbon deposition were identified on both the BFZ and the LSCuF-7328 membranes after CO sweep experiments [54]. Surface morphology changes as well as impurities were found on LCF-91 membranes when the sweep gas was hydrogen [72]. However, morphology changes are less detrimental than element segregation. Long term stability tests on the LCF-91 membrane showed an almost constant oxygen flux with either air or water vapor as the oxygen sources despite of these surface morphology

changes. For the Ni/LCF-91 catalytic porous layer on the same membrane, high performances were maintained for 54 h at 950 and 990^{o}C and the porous layer didn't show any morphology or elemental distribution changes after the long term test [60].

Phase transition or separation is another source of instability in oxygen permeable membranes, especially for mixed phase materials. SFC2 membrane experiences phase transition around 825–850^{o}C and the hydrogen production dropped greatly when temperature decreased below 850^{o}C [73]. Another mixed phase membrane GDC/Cu suffers from coper agglomeration on the membrane surface after hydrogen sweep experiments [74]. But for the 0.3 mm thick layered LNO/CGO membrane, no degradation was found during one week operation of CO sweep [50]. This showed layering design could be another approach to achieve stable mixed phase membranes.

Table 1.5 Water splitting on ITM literature

Ref	Materials	Geometry	Membrane fabrication	Thickness [mm] *	Catalyst	p_{H2O} [atm]	p_{Sweep}† [atm]	T [^oC]	Max H_2 production [μmol/cm^2•s]	Operation period
1. Fluorites										
[37]	$0.9ZrO_2$-0.1CaO	COE tube	/	/	/	0.2	CO-CO_2 0.5-0.5	1400-1800	/	/
[32]	$0.9ZrO_2$-0.1CaO	COE tube	/	/	/	0.2	(i) CO-CO_2, (ii) Ar 1.0	1500-1800	~2.2 [μmol/s]	/
[47]	$(ZrO_2)_{0.8}$-$(TiO_2)_{0.1}$ -$(Y2O_3)_{0.1}$	COE tube	Press + sinter	2	/	0.17	H_2-CO_2	1600, 1683	0.4	/
2. Perovskites										
[52]	$BaCo_xFe_yZr_{1-x-y}O_{3-\delta}$	Microtube	Phase inversion spinning + sinter	0.05-0.1 (~ 0.1)	Ni/Al_2O_3 (sweep)	0.05 - 0.75	CH_4 0.01-0.10	800-950	3.4	/
[56]				0.17 (0.04)	i. / ii.Pd-BCoFZ	0.75	CH_4 0.20	800-950	(i) 0.47 (ii) 1.4	/
[65]				0.17	/	0.75	C_2H_6 0.06 – 0.59	700-800	0.6	100 h @ 800 ^oC
[66]				0.17	Ni/Al_2O_3	0.75	CH_4 0.04	850-950	2.2	/
[54]	$BaFe_{0.9}Zr_{0.1}O_{3-\delta}$	Disk	Press+ sinter	1.6	/	0.03 – 0.49	CO 0.8	600 - 900	0.2	/
[53]	$La_{0.3}Sr_{0.7}FeO_3$	Disk	Press + sinter	3	/	/	CO	860	0.01	20 h @ 860 ^oC
[69]				1-3	/	0.025	CO	900	0.04	8 h @ 900 ^oC
[57]	$La_{0.7}Sr_{0.3}Cu_{0.2}$ $Fe_{0.8}O_{3-\delta}$	Disk	Press + sinter	0.33 - 1.75	Pt	0.03 – 0.79	H_2 0.8	600 - 900	~ 1.4	/

Table 1.5 Water splitting on ITM literature

Ref	Materials	Geometry	Membrane fabrication	Thickness [mm] *	Catalyst	p_{H2O} [atm]	p_{Sweep}† [atm]	T [^oC]	Max H_2 production [μmol/cm^2•s]	Operation period
[57]	$La_{0.7}Sr_{0.3}Cu_{0.2}Fe_{0.8}O_{3-\delta}$	Thin film	Paint + sinter	0.05	Pt	0.03 – 0.79	H_2 0.8	600 - 900	7.8	/
[48]				0.022	/	0.03 – 0.49	(i) CO+CO_2 (CO 0.5-0.99) (ii) H_2 0.8	600 - 900	(i) 3.2 (ii) ~6.8	/
[54]				0.03	/	0.49	CO–CO_2 (CO 0.25 - 0.995)	500 - 900	0.95	80 h
[68]	$La_{0.6}Sr_{0.4}Co_{0.2}Fe_{0.8}O_{3-\delta}$	Microtube	phase-inversion + sinter	0.25	/	0.07	CH_4 0.05	900	0.21 (based on A_{inner})	400 h @ 900 ^{o}C
[70]	$La_{0.7}Sr_{0.3}Cu_{0.2}Fe_{0.8}O_{3-\delta}$	Disk	Press + sinter	0.36	/	0.49	CO+CO_2 (CO 0.1–0.8)	600 – 900	0.09	/
[62]	$SrCo_{0.4}Fe_{0.5}Zr_{0.1}O_{3-\delta}$	Tube	Plastic extrusion	0.3	Ni/Al_2O_3 (sweep)	0.69	EtOH 0.06	700 - 900	2.53	60 h @ 750 ^{o}C
[72]	$La_{0.9}Ca_{0.1}FeO_{3-\delta}$	Disk	/	0.9	/	0.507 – 0.835	H_2 0.01 – 0.05	990	0.1	60 h @ 990^{o}C
[60]				0.5 – 0.9 (0.4)	Ni/LCF-91 (sweep)	0.5	CH_4 0.01 – 0.05	990	0.5	54 h @ 950 – 990^{o}C
[87]	$Ba_{0.98}Ce_{0.05}Fe_{0.95}O_{3-\delta}$	Disk	Press + sinter	0.5	Ru/ $Sm_{0.15}Ce_{0.85}O_{1.925}$	0.9	H_2 0.1 – 1	700 - 950	10.0	100 @ 900^{o}C
3. Mixed phase										
[59]	CeO_2-Gd (-Ni)**	Disk	Press + sinter	0.1-1.5	/	0.03-0.49	(i) H_2 0.04-0.8; (ii) CH_4 0.05	700-900	4.1	/

Table 1.5 Water splitting on ITM literature

Ref	Materials	Geometry	Membrane fabrication	Thickness [mm] *	Catalyst	p_{H2O} [atm]	p_{Sweep}† [atm]	T [^oC]	Max H_2 production [μmol/cm^2•s]	Operation period
[73]	CeO_2-Gd-Ni CeO_2-Gd-NiO	Disk	Press + sinter	0.09 - 0.97	/	0.49	H_2 0.04-0.8	500-900	6.3 on porous CGO/NiO)	/
[74]	Cu-$Ce_{0.8}Gd_{0.2}O_{1.9-\delta}$	Disk	Press +sinter	0.48, 0.7	/	0.03 - 0.49	H_2 0.025-0.9	600 - 900	1.71	/
[73]	$SrFeCo_{0.5}O_x$	Disk	Press + sinter	0.95	/	0.49	H_2 0.04-0.8	750 - 900	3.1	1000 h @ 900 ^oC
[55]		(i) Disk (ii) Thin Film	i. Press + sinter ii. Casting	(i) 0.23 – 1.76 (ii) 0.02	/	0.49	H_2 0.8	900	(i) 4 (ii) 11.9	/
[50]	$La_2NiO_{4+\delta}$ /$Gd_{0.1}Ce_{0.9}O_{1.95}$	Disk (bilayer)	Press + sinter (GDC layer is spin-coated)	0.3	/	0.03	CO 0.016 – 0.1	900	0.09	168 h @ 900 ^oC
[75]	$Gd_{0.2}Ce_{0.8}O_{1.9-\delta}$ – $Gd_{0.08}Sr_{0.88}Ti_{0.95}Al_{0.05}O_{3\pm\delta}$	Disk	i. Press + sinter ii. Spin-coating	(i) 1.2 (ii) 0.025 (2 mm)	/	0.03 – 0.25	H_2	900	7.3	/
[88]	$Ce_{0.85}Sm_{0.15}O_{1.925}$ (75 wt.%) – $Sm_{0.6}Sr_{0.4}Al_{0.3}Fe_{0.7}O_{3-\delta}$ (25 wt.%)	Disk	Co-lamination (layers of porous + dense)	0.03 mm (0.5 mm both)	Ni	0.5	(i) CO 1 (ii) CH_4 0.45 - 1	900 - 950	8.56	90 h @ 900^{o}C
[89]				0.04 mm (0.6 mm feed)	Ru/SDC (sweep), and Ru (feed)	0.9	H_2 0.5	600 - 950	12.1	100 h with 200 ppm H_2S on sweep side

*Numbers in the brackets are the thickness of the porous support on one side

**From [73], this membrane contains Ni. But this paper didn't state that.

†Numbers followed the gas species show the mole fractions of the fuels

Table 1.6 Membrane materials

	Ref	Materials	Powder synthesis	Stability
1. Mixed phase materials				
	[59] [73]	CeO_2-Gd (-Ni)	Mix & sinter	H_2 leakage through the membrane was detected
	[74]	Cu-$Ce_{0.8}Gd_{0.2}O_{1.9-\delta}$	Mix & sinter	Copper agglomeration on surface
	[50]	$La_2NiO_{4+\delta}$/ $Gd_{0.1}Ce_{0.9}O_{1.95}$	Co-precipitation	No degradation during 1 week operation in CO/CO_2/He environment [50].
	[75]	$Gd_{0.2}Ce_{0.8}O_{1.9-\delta}$/ $Gd_{0.08}Sr_{0.88}Ti_{0.95}Al_{0.05}O_{3\pm\delta}$	Solid state reaction	/
	[73] [55]	$SrFeCo_{0.5}O_x$	Solid state reaction	Phase transition at 600 ^oC. The phase at T> 600 ^oC shows better oxygen flux
	[88]	$Ce_{0.85}Sm_{0.15}O_{1.925}$/ $Sm_{0.6}Sr_{0.4}Al_{0.3}Fe_{0.7}O_{3-\delta}$	Solid state reaction	Performance drop due to coke formation, but the degradation is reversible by purging H_2O on the coked side.
2. Single phase materials				
Fluorite	[37] [32]	$0.9ZrO_2$-0.1CaO	/	/
	[47]	$(ZrO_2)_{0.8}$-$(TiO_2)_{0.1}$ -$(Y_2O_3)_{0.1}$	Solid state reaction	No leakage was found
Perovskite	[62]	$SrCo_{0.4}Fe_{0.5}Zr_{0.1}O_{3-\delta}$	Solid state reaction	/
	[52] [56] [65] [66] [54]	$BaCo_xFe_yZr_{1-x-y}O_{3-\delta}$	Sol-gel	For BFZ[54]: Helium leakage through the membrane was detected; and isolated pores and carbon deposition were found after experiments. For BCFZ [65]: Gas tight after 100 h operation; surface eroded (10 μm) by C_2H_6, but no cracks; cobalt reduced and segregate from the membrane.
	[53] [69]	$La_{0.3}Sr_{0.7}FeO_3$	Sol-gel	No leakage was found
	[57] [48] [54] [70]	$La_{0.7}Sr_{0.3}Cu_{0.2}Fe_{0.8}O_{3-\delta}$	Solid state reaction	Helium leak through the membrane was detected; and isolated pores were found following experiments.
	[68]	$La_{0.6}Sr_{0.4}Co_{0.2}Fe_{0.8}O_{3-\delta}$	Combustion spray-pyrolysis	CH_4 was detected on water side. Segregation of SrO and La_2O_3 was found on water side surface, while segregation of Co at cold zone and cracks from hot zone were found on methane side.

Table 1.6 Membrane materials

	Ref	Materials	Powder synthesis	Stability
	[72] [60]	$La_{0.9}Ca_{0.1}FeO_{3-\delta}$	/	Membrane surface morphology changed after water splitting [72]; performance stable for 54 hours[60].
	[87]	$Ba_{0.98}Ce_{0.05}Fe_{0.95}O_{3-\delta}$	Solid state reaction	No obvious change in elemental composition. Catalytic layer on the feed side exfoliated, but that on the sweep side was intact. Ba enrichment on the sweep side was found.

Table 1.7 Co-production in an oxygen permeable membrane

Ref	Membrane materials	Catalysts (Sweep side)	T [oC]	Sweep gas	Co-production
[52]	$BaCo_xFe_yZr_{1-x-y}O_{3-\delta}$	Ni/Al_2O_3	950	1 -10 % CH_4 +He+Ne	When CH_4 increased from 1 to 10%, methane conversion ratio dropped from ~100% to ~60%; but CO selectivity increased from 3% to 45%; coke was found
[59]	Gd-doped CeO_2 (+ Ni [73])	Ni?	900	5% CH_4 +N_2+He	/
[68]	$La_{0.6}Sr_{0.4}Co_{0.2}Fe_{0.8}O_{3-\delta}$	/	900	5% CH_4 +Ar	~0.15% H_2, ~0.1% CO and ~zero CO_2 were produced from methane oxidation
[56]	$BaCo_xFe_yZr_{1-x-y}O_{3-\delta}$	BCoFZPd	800 - 950	20% CH_4 +He+Ne	/
[66]	$BaCo_xFe_yZr_{1-x-y}O_{3-\delta}$	Ni/Al_2O_3	800 - 950	4% CH_4 +He + Ne	/
[60]	$La_{0.9}Ca_{0.1}FeO_{3-\delta}$	Ni/LCF-91	990	1 – 5% CH_4 + He	H_2/CO = 2:1 was observed on the sweep side, and hardly any carbon deposition was found
[65]	$BaCo_xFe_yZr_{1-x-y}O_{3-\delta}$	/	700 - 800	6-59% C_2H_6 +He+Ne	Increasing temperature and C_2H_6 concentration together led to the rise of C_2H_4 selectivity from 67 – 89%. Segregation of Co to surface was detected
[62]	$SrCo_{0.4}Fe_{0.5}Zr_{0.1}O_{3-\delta}$	Ni/Al_2O_3	700 - 900	EtOH 0.06 + H_2O 0.288 + N_2 0.652	Selectivity to H_2 was around 150% and it didn't depend much on the temperature. At higher temperatures, the selectivity to CO increased from ~64% to ~ 76%, the selectivity to CO_2 decreased from ~34% to ~23%, and the selectivity to CH_4 dropped from ~3.1% to 0.

1.4 Current status of membrane-supported CO_2 splitting

Membrane-supported CO_2 splitting has been investigated since 1986 [90], but little progress has been made since then. CO_2 acts as the oxygen source for oxygen permeation across the membrane. As was the case for water splitting membranes, either single phase (fluorite or perovskite) or mixed phase membranes are studied. A non-exhaustive literature review is summarized in Table 1.8. The highest CO production rate reported has been 2.72 μmol/cm^2•s on a 1.5 mm thick $SrCo_{0.4}Fe_{0.5}Zr_{0.1}O_{3-\delta}$ (SCoFZ-451) perovskite membrane (catalyst: Pd/SCoFZ (feed); Ni/Al_2O_3 (sweep)) with methane sweeping at 950^{o}C [91]. In the following sections, three categories of membranes are summarized based on the active phases.

1.4.1 Fluorite-based single phase membranes

Two of the earliest attempts with oxygen permeable membranes for CO_2 splitting were on fluorite-based single phase membranes. As discussed before, fluorite exhibits mixed ionic electronic conductivity at high temperatures, but the electronic conductivity is generally lower than the ionic conductivity. Therefore, the performance of CO_2 splitting on these fluorite membranes is very low and is limited by the low electronic conductivity.

Nigara and Cales [90] tested the 2 mm thick tubular stabilized zirconia ($0.9ZrO_2$–$0.1CaO_2$) membranes at 1427–1727^{o}C with CO as the sweep gas. They found that the CO production rate increased with respect to both the temperature and fuel concentration on the sweep side. The highest rate on this particular membrane was 0.62 μmol/cm^2•s at 1727^{o}C with 99% CO in the sweep gas. And the ceria-doped stabilized zirconia membrane was found to have higher CO production rate than the calcium-doped stabilized zirconia membrane (CO sweep), which may be due to the fact that the former has better electronic conductivity.

Later, Itoh et al. [92] achieved a 0.488 μmol/cm^2•s CO production rate with Ar sweep in a 2 mm thick YSZ tube ($0.06Y_2O_3$-$0.94ZrO_2$) at 1509^{o}C. They found that with increasing CO_2 flow rates on the feed side, the CO_2 conversion ratio first increased and then decreased.

As the oxygen permeation rate through the single phase fluorite membranes is limited by the electronic conductivity of the membrane, researchers generally pursued mixed ionic electronic materials (e.g., perovskite or mixed phase materials) since these two earliest attempts.

1.4.2 Perovskite-based single phase membranes

So far, mainly Sr-based perovskite membranes, (i.e., $SrCo_{0.4}Fe_{0.5}Zr_{0.1}O_{3-\delta}$ (SCoFZ-451) [91, 93, 94], $SrCo_{0.8}Fe_{0.2}O_3$ (SCoF-82) [95, 96] and $La_{0.6}Sr_{0.4}Co_{0.2}Fe_{0.8}O_{3-\delta}$ (LSCoF-4628) [97]) have been explored for CO_2 splitting in the literature. Although Ba-based perovskite membranes perform well with water splitting as shown in Table 1.5, its tendency to form barium carbonate in CO_2 environments prevents them from being applied to CO_2 splitting [98].

Jin et al. [93] studied 1.5 mm thick SCoFZ-451 perovskite membranes with methane as the sweep gas and measured a 2.68 $\mu mol/cm^2 \bullet s$ CO production rate with 4.77wt% Ni/Al_2O_3 catalysts on the sweep side. The highest CO production rate decreased to around 1.56 $\mu mol/cm^2 \bullet s$ when catalysts were absent [94]. It was found that the oxygen fluxes, methane and CO_2 conversion ratios, and CO selectivity from methane oxidation all increased with respect to the temperature [93]. Besides, higher methane concentration at the inlet leads to lower CH_4 conversion ratio but higher CO selectivity. Yet with increasing CO_2 concentrations on the feed side, oxygen fluxes and methane conversion were both raised, but thermolysis ratio and CO selectivity from POM dropped. Moreover, long-term stability studies showed that the oxygen flux increased over the first 3 hours, and then stabilized until the membrane broke after 33 hours of operating with 20% CO_2 feed and 5% CH_4 sweep at 900^oC.

Several methods have been tried to increase the stability of the SCoFZ-451 membrane. Zhang et al. [94] applied porous SCoFZ-451 layers onto the dense membrane and found that the porous layer on either the sweep or feed side slightly enhanced the CO_2 splitting rate, especially at low temperatures. They also found that adding the porous layer onto the feed side had a bigger impact on the performances than adding the porous layer onto the sweep side. Additionally, the porous layer increased the stability of the membrane, especially when the porous layer was added to the sweep side which made the

membrane last three times longer than the unmodified membrane under the same operating conditions (20% CO_2 feed and 5% CH_4 sweep at 900^oC).

Catalysts (e.g., Pd/SCoFZ on the feed side and Ni/Al_2O_3 on the sweep side) also enhanced CO_2 splitting and partial oxidation of methane, respectively, on a 1.5 mm thick SCoFZ-451 membrane [91]. These catalysts enhanced the CO production rate by a factor of 4 – 7 at 850-950^oC, and the highest CO production rate achieved was 2.72 μmol/cm^2•s. Higher temperatures led to higher oxygen fluxes, CH_4 conversion and CO selectivity.

Furthermore, dopants such as Al and Nb were added to SCoF-82 membranes to improve its performances and stability. The Al-doped SCoF-82 membrane lasted 62 hours before it broke [95], while the 0.5 wt% Nb_2O_5 doped SCoF-82 membrane maintained high performances for 500 hours [96]. With $Sr_{0.7}Ba_{0.3}Fe_{0.9}Mo_{0.1}O_{3-\delta}$ (SBFM-7391)+Ni on the sweep side and $La_{0.8}Sr_{0.2}MnO_{3-\delta}$ (LSM-82)/YSZ+Pd on the CO_2 side as catalysts, the CO production rate was 1.6 μmol/cm^2•s on the 1.0 mm thick Nb doped SCoF-82 membrane (25% CO_2 feed and 12.5% CH_4 sweep at 900^oC) [96].

Lanthanum dopants can decrease strontium carbonate formation, but the performance is significantly decreased as a result. A 0.6 mm thick doped LSCoF-6428 membranes has reached a maximum CO production rate of 0.28 μmol/cm^2•s at 1030^oC [97]. Higher temperature led to the increase of both the CO_2 splitting rate on the feed side and the CH_4 conversion ratio on the sweep side. Yet amorphous graphite is detected by XRD after experiments, as a result of methane cracking.

1.4.3 Mixed-phase membranes

Two different types of mixed-phase membranes have been explored in the literature. One is the $SrFeCo_{0.5}O_{3-\delta}$ (SFC2 membrane), which is a mixture of intergrowth ($Sr_4Fe_{6-x}Co_xO_{13\pm\delta}$), perovskite ($SrFe_{1-x}Co_xO_{3-\delta}$) and spinel ($Co_{3-x}Fe_xO_4$) phases [76]. The other is the samarium-doped ceria (SDC) membrane with Ag or Pt circuits at the edge to enhance the electronic conductivity. Both achieved high CO production with methane as the sweep gas.

Fan et al. [99] studied a 2 mm thick SFC2 disk membrane and achieved CO production rate as high as 0.25 μmol/cm^2•s at 940^oC. They also found that increasing the

temperature and CO_2 concentration on the feed side raised the higher oxygen flux, and hence higher CO_2 splitting rate.

For the SDC membrane with Ag or Pt circuits at the edge, Zhang et al. [100] tested it with two different types of catalyst on each side of the membrane: Ag or Pt catalysts for the CO_2 splitting reaction on the feed side and $GdNi/Al_2O_3$ for the partial oxidation of methane on the sweep side. Two different thicknesses were tested, and they found that at low temperatures (750–850^oC), the 20 μm thin film membrane performed slightly better than the 1 mm thick dense membrane, and the former showed the highest CO production rate of 1.819 $\mu mol/cm^2 \cdot s$ at 900 ^oC. In addition, both the Pt and Ag metal circuits enhanced the CO_2 splitting rate by an order of magnitude, and Pt circuits had the superior performance. Higher temperature increased the CO_2 splitting rate on the feed side, the oxygen flux across and the CO selectivity and CH_4 conversion on the sweep side. And higher CO_2 flow rates on the feed side raised the oxygen flux and methane conversion but dropped the CO selectivity from POM. Moreover, higher CH_4 flow rates increased the oxygen flux, CO selectivity on the sweep side and CO_2 conversion on the feed side, but significantly decreased the methane conversion.

Table 1.8 CO_2 thermolysis on oxygen permeable membranes

Ref	Materials	Geometry	Thickness* [mm]	Catalyst	pCO_2 [atm]	pSweep† [atm]	T [^oC]	Max CO production [μmol/cm^2•s]	Stability
1. Fluorites									
[92]	6 mol% Y_2O_3 - 94 mol% ZrO_2	Tubular	2	/	1	Ar	1311 – 1509	0.488	/
[90]	10 mol% CaO – 90 mol% ZrO_2	Tubular	2	/	1	CO +CO_2	1427 – 1727	0.62	/
2. Perovskites									
[93]	$SrCo_{0.4}Fe_{0.5}Zr_{0.1}O_{3-\delta}$	Disk	1.5	NiO/Al_2O_3 (sweep)	0.2 – 0.5	CH_4: 0.05 – 0.15	850 – 950	2.68	Membrane broke at 33 h; $SrCO_3$, Co_2O_3 and Fe_2O_3 were found after experiments on surface
[94]			1.5 (10 μm)	/	0.2	CH_4: 0.05	800 – 950	1.64	Membrane broke at 68 h
[91]			1.5	Pd/SCoFZ (feed); Ni/Al2O3 (sweep)	0.2	Inert or CH_4: 0.1	850 – 950	2.72	Membrane broke at 40 h
[95]	3 wt% Al_2O_3-doped $SrCo_{0.8}Fe_{0.2}O_{3-\delta}$	Tubular	0.6	Ni/Al2O3 (sweep)	0.2	CH_4 : 0.05 – 0.15	850 – 950	1.64	Membrane broke at 62 h
[96]	5 wt% Nb_2O_5-doped $SrCo_{0.8}Fe_{0.2}O_{3-\delta}$	Disk	1.0 (20 μm)	$La_{0.8}Sr_{0.2}MnO_3$/ YSZ+Pd (feed); $Sr_{0.7}Ba_{0.3}Fe_{0.9}Mo_{0.1}O_{3-\delta}$ + Ni (sweep)	0.05 - 0.5	CH_4: 0.05 – 0.125	750 – 900	1.60	Membrane was stable for 500 h
[97]	$La_{0.6}Sr_{0.4}Co_{0.2}Fe_{0.8}O_{3-\delta}$	Tubular	0.6**	/	1	CH_4: 1	840 – 1030	0.28	Amorphous graphite was detected by XRD

Table 1.8 CO_2 thermolysis on oxygen permeable membranes

Ref	**Materials**	**Geometry**	**Thickness* [mm]**	**Catalyst**	**pCO_2 [atm]**	**pSweep† [atm]**	**T [^oC]**	**Max CO production [μmol/cm^2•s]**	**Stability**
3. Mixed phase materials									
[100]	samarium-doped CeO_2 (+Ag)	Disk, with Ag circuit	(a) 1 mm (b) ~20 μm	Pt or Ag (feed), $GdNi/Al_2O_3$ (sweep)	0.125 – 0.5	CH_4: 0.027 – 0.135	750 – 900	1.819	Constant performance was observed with coke resistance (GdNi catalysts) for 100h.
[99]	$SrCo_{0.5}FeO_3$	Disk	2	/	0.2	CH_4: 0.444	760 – 940	0.25	Not stable. Pinhole and crack were found after 30 h hours operation under reactive flow

* Numbers in the brackets are the porous layer thickness

** Total thickness and the porous layer thickness isn't reported

†Numbers followed the gas species show the mole fractions of the fuels

1.5 Flux models: Bulk diffusion and surface reactions

1.5.1 Charged species and conductivities in MIEC materials

1.5.1.1 Charged species concentration

The oxygen permeable membranes (either single phase or mixed phase) exhibit both ionic and electronic conductivities, so no extra electric circuit is required to maintain the charge neutrality inside the bulk of the membranes. The oxygen ion permeation across the membrane is driven by the chemical potential gradient.

The lattice oxygen ions, electrons and/or holes are the charged species in a MIEC membrane. For a single-phase membrane, unless the material is in the intrinsic region, there is usually one dominant electronic charged species either electrons or holes. Hence, in most of the oxygen separation applications, the membrane is considered either an n-type or p-type conductor [101, 102].

However, when the membrane experiences a huge difference in oxygen partial pressure (e.g., fuel processing on the sweep side or when the oxygen source is H_2O/CO_2 rather than air), there may be a transition between the dominant electronic charged species on the feed and sweep surfaces [82]. In order to figure out the concentrations of the charged species inside a MIEC material, thermodynamic values of the defect reactions are required. For example, for the Ca-doped $LaFeO_3$, the non-stoichiometric defect reactions are

$$\frac{1}{2}O_2(g) + V_O^{\bullet\bullet} + 2Fe_{Fe}^{x} \leftrightarrow O_O^{x} + 2Fe_{Fe}^{\bullet} \tag{1-13}$$

$$2Fe_{Fe}^{x} \leftrightarrow Fe_{Fe}^{'} + Fe_{Fe}^{\bullet} \tag{1-14}$$

Together with the site conservation and electro-neutrality,

$$\left[Fe_{Fe}^{x}\right] + \left[Fe_{Fe}^{'}\right] + \left[Fe_{Fe}^{\bullet}\right] = 1 \tag{1-15}$$

$$\left[Ca_{La}^{'}\right] + \left[Fe_{Fe}^{'}\right] = 2\left[V_O^{\bullet\bullet}\right] + \left[Fe_{Fe}^{\bullet}\right] \tag{1-16}$$

the charge species concentration under various temperatures and pressures can be calculated [103]. Figure 1.13 shows the charged species concentrations at equilibrium for $La_{0.9}Ca_{0.1}FeO_{3-\delta}$ (LCF-91) under different oxygen partial pressures at 990^{o}C. Electron holes dominate the electronic conduction at high oxygen partial pressure, while electrons

dominate at low oxygen partial pressures. In other words, the membrane is a p-type conductor on the high oxygen partial pressure side, and an n-type conductor on the low oxygen partial pressure side; the intrinsic region is located where $n = p$ when the partial pressure of oxygen is around 10^{-9} atm.

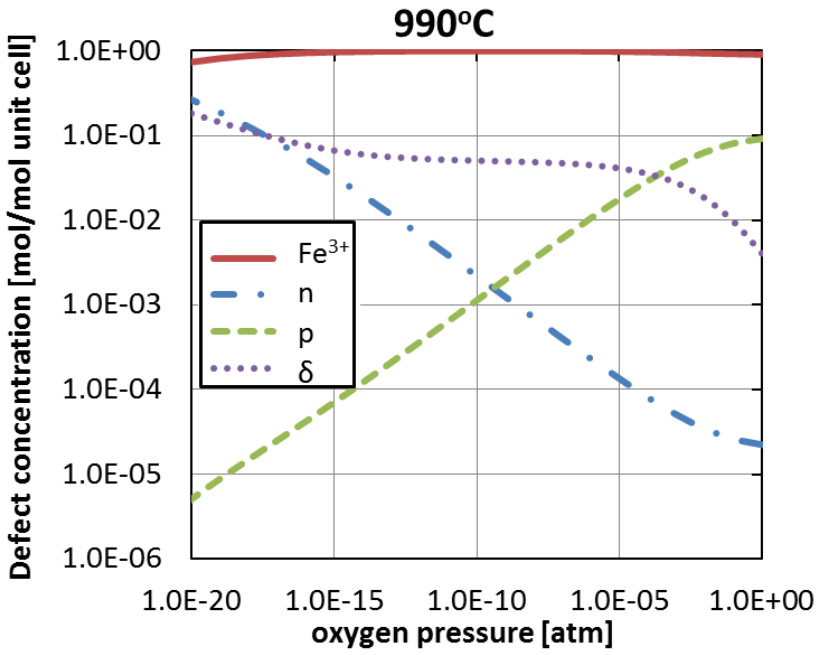

Figure 1.13 Charge species in LCF-91 materials under the equilibrium case at 990°C with oxygen partial pressure increased from 10^{-20} to 1 atm (calculated using the parameters from [103]) $n = Fe'_{Fe}, p = Fe^{\bullet}_{Fe}$

1.5.1.2 Conductivity

As discussed above, there are several different types of charge carriers in the membrane under various operating conditions. Now we summarize the conductivities of species *i* as

$$\sigma_i = n_i q \mu_i , \tag{1-17}$$

where σ_i is the conductivity of species *I* [S/cm], n_i is the carrier *i* density [#/cm^3], *q* is charge of species *i* [C], and μ_i is its mobility [cm^2/(V•s)]. The total conductivity of a mixed ionic and electronic conductor is the sum of the conductivities of all the charge species *j*,

$$\sigma_{tot} = \sum_j \sigma_j = \sum_j n_j q \mu_j \qquad (1\text{-}18).$$

The conductivities of the charged species depend on temperature and oxygen partial pressure. For example, the ionic conductivity can be described using the Nernst-Einstein relation according to [63]

$$\sigma_i = \frac{4F^2 \left[V_O^{\bullet\bullet}\right] D_V}{RTV_m}, \qquad (1\text{-}19)$$

where D_V is the diffusivity of oxygen vacancies [m^2/s], and $\left[V_O^{\bullet\bullet}\right] = \delta$ is nonstoichiometry of oxygen vacancy [-], R is the gas constant [J/(mol•K)], F is the Faraday constant [96485 s•A/mol] and T is temperature [K]. As both $\left[V_O^{\bullet\bullet}\right]$ and D_V depend on the temperature and oxygen partial pressures, the ionic conductivities can be simplified according to

$$\sigma_i(T) = \sigma_i^o(T)\, p_{O_2}^{-n}, \qquad (1\text{-}20)$$

where $\sigma_i^o(T)$ is the ionic conductivity at 1 atm oxygen partial pressure and temperature T, which can be written in the Arrhenius form.

Similarly, the electronic conductivity can be written in the same form

$$\sigma_e(T) = \sigma_e^o(T)\, p_{O_2}^{-n} \ . \qquad (1\text{-}21)$$

where $\sigma_e^o(T)$ is the electronic conductivity at 1 atm oxygen partial pressure and temperature T, which can also be written in the Arrhenius form. More complex models for the electronic and ionic conductivities can be found in [39] and references therein.

The total conductivity and ionic conductivity of typical membranes for water thermolysis are shown in Figure 1.14. Most of these conductivity values were measured in air (P_{O2} = 0.21 atm). As seen in Figure 1.14, the conductivity values range by orders of magnitude between the different mixed ionic-electronic conductors. Yet generally, ionic conductivity is much lower than electronic conductivity in perovskite materials, while the gadolinium doped ceria (CGO) and mixed phase SFC2 exhibit mainly ionic conductivity.

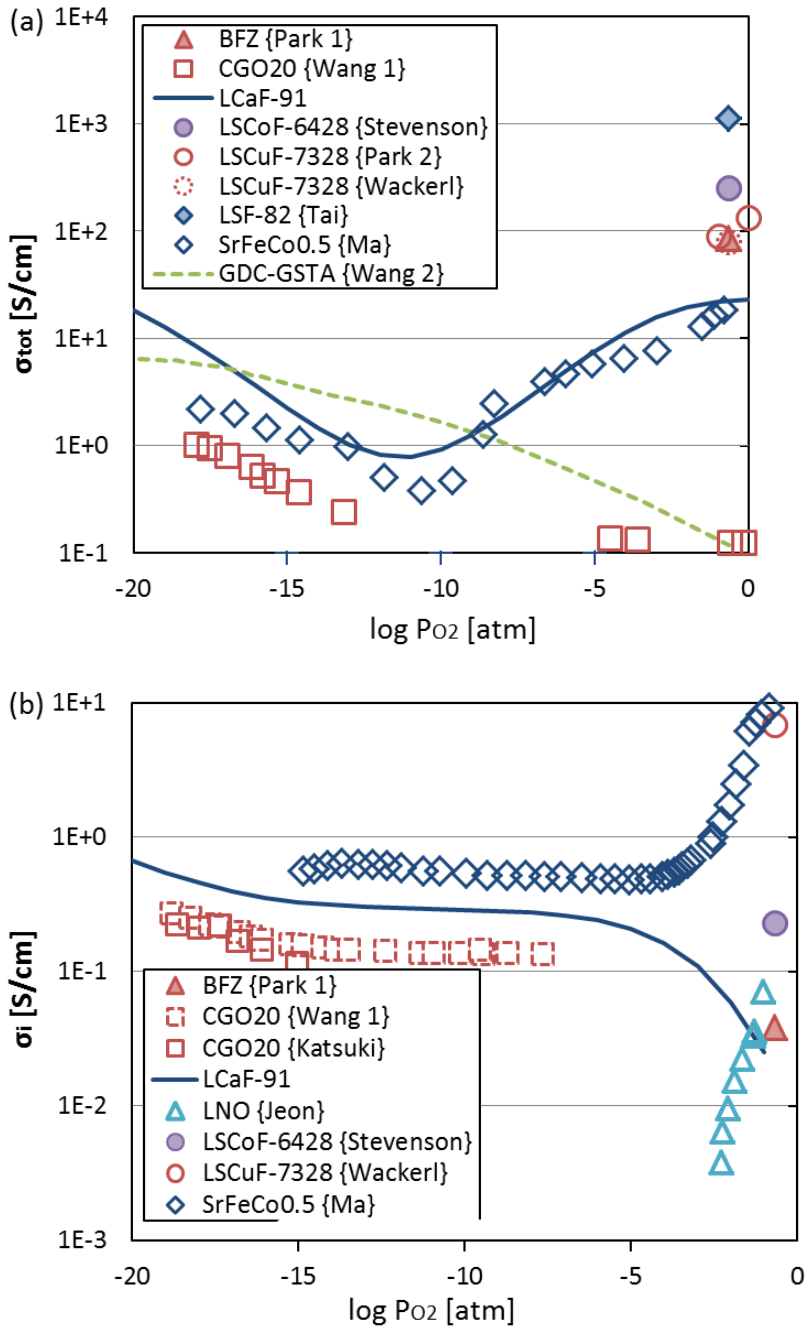

Figure 1.14 (a) Electronic conductivities and (b) ionic conductivities of different membrane materials at 900°C under different oxygen partial pressures (Ref: Wang 1 [104]; Wang 2 [75]; Katsuki [105]; Jeon [51]; Ma [106]; Park 1 [54]; Park 2 [107]; Wackerl [108]; Stevenson [109]; Tai [110])

Various approaches are adopted to enhance the mixed ionic-electronic conductivities of the materials. For fluorites, (e.g., $(ZrO_2)_{0.8}$-$(TiO_2)_{0.1}$-$(Y_2O_3)_{0.1}$), the Y_2O_3

dopant is added up to 10 mol% to keep the high ionic conductivity, while 10% mole TiO_2 is doped to achieve high electronic conductivity [47]. For perovskites, the B site transition metal affects the electronic conductivity while the A site acceptor dopants affects the lattice oxygen ion conduction. For mixed phase materials, metals such as Ni [73] and Ag [100] are added to boost the electronic conductivity of the membranes.

1.5.2 Flux model

The diffusion of the charged species transport is described by the Nernst-Planck equation according to:

$$J_i = -\frac{\sigma_i}{(Z_i F)^2}\nabla\tilde{\mu}_i + c_i v \tag{1-22}$$

where J is the diffusion flux [mol/(cm^2•s)], σ is the conductivity [A/m], Z is the charge [#], $\tilde{\mu}$ is the electrochemical potential [J/mol], c is the concentration [mol/cm^3], v is the velocity of the system [cm/s], and the subscript i denotes the charged species i.

For a 1D stationary system, equation (1-22) becomes

$$\begin{aligned} J_i &= -\frac{\sigma_i}{(Z_i F)^2}\nabla\tilde{\mu}_i \\ &= -\frac{\sigma_i}{(Z_i F)^2}\left(T\frac{d}{dx}\left(\frac{\mu_i}{T}\right) + Z_i F\frac{d\varphi}{dx} + \frac{\mu_j^*}{T}\frac{dT}{dx}\right) \end{aligned} \tag{1-23}$$

where the electrochemical potential $\tilde{\mu}_i$ is broken down into three terms associated with the chemical potential, electro-potential and temperature gradient. φ is electric field and μ* is related with non-isothermal potential. For an isothermal system, equation (1-23) is further simplified to:

$$J_i = -\frac{\sigma_i}{(Z_i F)^2}\left(\frac{d\mu_i}{dx} + Z_i F\frac{d\varphi}{dx}\right) \tag{1-24}$$

The flux density of species i is

$$i_i = Z_i F J_i = -\frac{\sigma_i}{Z_i F}\left(\frac{d\mu_i}{dx} + Z_i F\frac{d\varphi}{dx}\right) \tag{1-25}$$

The net current density in the bulk of a membrane is the sum of flux densities of all charge species,

$$i_{tot} = \sum_j Z_j F J_j = -\sum_j \frac{\sigma_j}{Z_j F}\left(\frac{d\mu_j}{dx} + Z_j F \frac{d\varphi}{dx}\right). \quad (1\text{-}26)$$

We define the transference number of species *j* to be the conductivity of species *j* over the total conductivity of the system,

$$t_j = \frac{\sigma_j}{\sigma_{tot}} = \frac{\sigma_j}{\sum_k \sigma_k} \quad (1\text{-}27)$$

Plugging (1-27) into (1-26) and setting the net current density inside the membrane to zero (as there is no electric circuit applied to the membrane), we obtain,

$$i_{tot} = -\sum_j \frac{\sigma_{tot} \cdot t_j}{Z_j F}\left(\frac{d\mu_j}{dx} + Z_j F \frac{d\varphi}{dx}\right) = 0 \quad (1\text{-}28)$$

Therefore, the electric potential gradient is

$$\frac{d\varphi}{dx} = -\sum_j \left(\frac{t_j}{Z_j F}\frac{d\mu_j}{dx}\right) \quad (1\text{-}29)$$

Plugging (1-29) into (1-25) yields,

$$J_i = -\frac{\sigma_{tot} \cdot t_i}{\left(Z_i F\right)^2}\left(\frac{d\mu_i}{dx} - Z_i \sum_j \left(\frac{t_j}{Z_j} \cdot \frac{d\mu_j}{dx}\right)\right) \quad (1\text{-}30)$$

There are several scenarios discussed below that allow further reduction of this charge species diffusion equation.

1.5.2.1 Bulk-diffusion limiting

The Wagner theory is used to describe the bulk-diffusion limiting case, which assumes quasi-equilibrium reactions on the surface:

$$\frac{1}{2}O_2 = O^{2-} - 2e^- . \quad (1\text{-}31)$$

Assuming that the membrane conducts only electrons and oxygen ions (similar results can be derived for electron hole conductors), the equilibrium of reaction (1-31) gives

$$\frac{1}{2}\nabla\mu_{O_2} = \nabla\mu_{O^{2-}} - 2\nabla\mu_{e^-} \quad (1\text{-}32)$$

Therefore, (1-30) for ionic flux becomes

$$J_i = -\frac{\sigma_{tot} t_i t_e}{2\left(Z_i F\right)^2} \frac{d\mu_{O_2}}{dx} = \frac{1}{2\left(2F\right)^2 L} \int_{\mu''_{O_2}}^{\mu'_{O_2}} \sigma_{tot} t_i t_e d\mu_{O_2} \tag{1-33}$$

For an ideal gas system, the chemical potential is

$$\mu_i = \mu_i^0 + RT \ln\left(P_i / P_o\right) \tag{1-34}$$

where μ_i^0 is the reference chemical potential, and P is the total pressure. Hence, (1-33) can be written as

$$J_{O_2} = \frac{1}{2} J_i = \frac{RT}{\left(4F\right)^2 L} \int_{P''_{O_2}}^{P'_{O_2}} \sigma_{tot} t_i t_e d \ln P_{O_2} \tag{1-35}$$

By assuming that the electronic conductivity of the membrane materials is much higher than the ionic conductivity and that the ionic conductivity is a constant value ($\bar{\sigma}_i$) across the membrane, (1-35) is simplified to:

$$J_{O_2} = \frac{\bar{\sigma}_i RT}{\left(4F\right)^2} \ln \frac{P'_{O_2}}{P''_{O_2}} \tag{1-36}$$

Similarly, for the case of water splitting with hydrogen sweep, the heterogeneous reaction of water is

$$H_2O = O^{2-} - 2e^- + H_2 \tag{1-37}$$

Therefore, assuming the surface reaction is at equilibrium, we get:

$$\nabla\mu_{H_2O} - \nabla\mu_{H_2} = \nabla\mu_{O^{2-}} - 2\nabla\mu_{e^-} \tag{1-38}$$

Plugging (1-38) into (1-30) yields:

$$\begin{aligned} J_i &= -\frac{\sigma_{tot} t_i t_e}{\left(Z_i F\right)^2} \left(\nabla\mu_{H_2O} - \nabla\mu_{H_2}\right) \\ &= \frac{1}{\left(Z_i F\right)^2 L} \left(\int_{\mu'_{H_2O}}^{\mu'_{H_2O}} \sigma_{tot} t_i t_e d\mu_{H_2O} - \int_{\mu'_{H_2}}^{\mu'_{H_2}} \sigma_{tot} t_i t_e d\mu_{H_2} \right) \end{aligned} \tag{1-39}$$

For an ideal gas system, (1-39) can then be written as

$$J_i = \frac{RT}{\left(Z_i F\right)^2 L} \left(\int_{\mu'_{H_2O}}^{\mu'_{H_2O}} \sigma_{tot} t_i t_e d \ln P_{H_2O} - \int_{\mu'_{H_2}}^{\mu'_{H_2}} \sigma_{tot} t_i t_e d \ln P_{H_2} \right) \tag{1-40}$$

Again, by assuming that the electronic conductivity of the membrane materials is much higher than the ionic conductivity and that the ionic conductivity is a constant ($\bar{\sigma}_i$) across the membrane, this equation reduces to:

$$J_i = \frac{RT}{\left(Z_i F\right)^2 L} \sigma_{tot} t_i \left(\ln \frac{P'_{H_2O}}{P''_{H_2O}} - \ln \frac{P'_{H_2}}{P''_{H_2}} \right) \tag{1-41}$$

Similar to the case with water splitting, the case with CO_2 thermolysis with CO as the sweep gas can be evaluated as

$$J_i = \frac{RT}{\left(Z_i F\right)^2 L} \sigma_{tot} t_i \left(\ln \frac{P'_{CO_2}}{P''_{CO_2}} - \ln \frac{P'_{CO}}{P''_{CO}} \right) \tag{1-42}$$

For fluorite membranes, electron diffusion is usually the limiting charged species; similar to the ionic diffusion limiting membranes, the oxygen flux can be calculated as [32]

$$J_{O_2} = \frac{kT}{4qFL} \sigma_e^0 \exp\left(-\frac{\Delta E_e}{kT} \right) \left(P''^{-1/4}_{O_2} - P'^{-1/4}_{O_2} \right) \tag{1-43}$$

where *k* is the Boltzmann constant, *T* is the cell temperature, *q* the electron charge, *F* the Faraday constant, *L* the thickness of the membrane, and σ_e^0 and ΔE_e are the pre-exponential constant and activation energy for electron conductivity, respectively.

1.5.2.2 Generalized transport model

The flux equations above are for the bulk diffusion limiting cases where the surface reactions are assumed to be at equilibrium. For other cases where the surface reaction rates can't be neglected, Xu and Thomson [101] developed a generalized oxygen transport model for air separation considering two gas/solid reactions on both membrane surfaces and one oxygen ion bulk diffusion across the membrane. Later, Wu and Ghoniem expanded this model to other oxygen sources such as H_2O [60, 72].

Several assumptions are made for this transport model:

(1) For oxygen separation, both the forward and backward reactions are considered. But in the H_2O/CO_2 splitting cases, the backward reactions are neglected due to the low hydrogen production rate and hence its low concentration compared to the species

concentrations in the bulk. Similar assumptions have been made and verified in the literature for heterogeneous reactions with MIEC membranes [111];

(2) Electron hole concentrations across the membrane are assumed to be constant as the electronic transference number is much higher than the ionic transference number [112, 113];

(3) The oxygen site concentration inside the stoichiometric perovskite lattice is equal to the sum of the lattice oxygen and oxygen vacancy concentrations

$$C_O = C_{O_O^x} + C_V , \tag{1-44}$$

where C_O , $C_{O_O^x}$ and C_V are the concentrations of oxygen sites, lattice oxygen and oxygen vacancies, respectively. These concentrations are all functions of temperature and the oxygen partial pressure. For example, the total oxygen site concentration of LCF-91 perovskite is assumed to be a constant value of 0.0825 mol/cm^3, estimated from XRD measurements of stoichiometric LCF-91 lattice size in air [114].

(4) The oxygen vacancy diffusion across a dense mixed ionic-electronic material follows Fick's law [39].

Based on these assumptions, the oxygen flux can be expressed in the form as

$$J_V = \frac{\Delta P}{R_\mathrm{f} + R_\mathrm{b} + R_\mathrm{s}} or \frac{C_O}{R_\mathrm{f} + R_\mathrm{b} + R_\mathrm{s}} , \tag{1-45}$$

where ΔP is the potential difference, and R_f, R_b and R_s are the resistances of the feed-side surface reaction, the bulk diffusion and the sweep-side surface reaction, respectively. The potential difference and resistance for water splitting are summarized in Table 1.9 as an example.

However, if the membrane is subject to a large oxygen partial pressure difference across the membrane, then the electronic conductivity could be on the same order of magnitude with the ionic conductivity, especially near the intrinsic region. Therefore, all the charge species must be considered in this case and the full equation for bulk diffusion (1-30) must be modelled using numerical methods as in [115].

Table 1.9 Resistance network for water splitting with various sweep-side mechanisms on an MIEC oxygen permeable membrane [60, 72]

Oxygen source	Water vapor	Water vapor	Water vapor	Water vapor
Sweep side mechanism	Inert sweep	H_2	CO	CH_4
ΔP or C_O	$\frac{\tilde{k}_{r,O}C_O}{\tilde{k}_{r,O}+k_{f,O}C''^{0.5}_{O_2}}$	C_O		
Surface reaction resistance (feed side), R_f	$\frac{1}{k_{r,H}C'_{H_2O}}$			
Bulk resistance, R_b	$\frac{t}{D_V}$			
Surface reaction resistance (sweep side), R_s	$\frac{1}{\tilde{k}_{r,O}+k_{f,O}C''^{0.5}_{O_2}}$	$\frac{1}{\tilde{k}_{f,H}C''_{H_2}}$	$\frac{1}{\tilde{k}_{f,C}C''_{CO}}$	$\frac{1}{\tilde{k}_{f,M}C''_{CH_4}}$

Similarly, in cases where the membrane is tubular, the local oxygen flux is calculated with respect to log-mean membrane area, $dA_m = 2\pi R_m dl$, and the log-mean radius is

$$R_m = \left(R_o - R_i\right) / \ln\left(R_o - R_i\right) \tag{1-46}$$

where R_i and R_o are the inner and outer radius of the tubular membrane [116].

1.6 Adsorption/reaction of H_2O and CO_2 on perovskites

Although many studies have been carried out for membrane-supported H_2O/CO_2 splitting, the surface reaction mechanism and kinetics have yet to be characterized. For air separation applications, H_2O and CO_2 are both regarded as poisonous gases on the sweep side of many oxygen permeable membranes [39], as both water and carbon dioxide react with the oxygen vacancies on oxide membrane surfaces [98, 117, 118]. In this chapter, the adsorption/reaction mechanisms of H_2O and CO_2 on perovskites are summarized. Perovskite membranes have good performances in facilitating H_2O/CO_2 splitting and are found to be one of the most promising oxygen permeable materials in the literature.

1.6.1 H_2O adsorption/reaction

For water splitting on the feed side, the overall reaction is

$$H_2O + V_O^{\bullet\bullet} \leftrightarrow O_O^x + 2h^{\bullet} + H_2 \tag{1-47}$$

But as the first step, water vapor can be incorporated into lattice as protons (as in $SrTiO_3$ [117] and CeO_2 [119]):

$$H_2O + V_O^{\bullet\bullet} + O_O^x \leftrightarrow 2OH_O^{\bullet} \tag{1-48}$$

The reaction between water and oxygen vacancies is thought to explain the low oxygen fluxes observed when water is introduced on the sweep side. Benson et al. [118] investigated the degradation of $La_{0.6}Sr_{0.4}Co_{0.2}Fe_{0.8}O_{3-\delta}$ (LSCF-6428) membrane in a humid environment, and found that bulk degradation was not obvious even after 3 days of annealing in water; but surface changes were observed, which led to degradation of the oxygen flux. Additionally, more O_2 was incorporated into the lattice in the presence of H_2O than in a dry atmosphere.

Zhang et al. [120] found that the catalytic activity of $LaCu_{0.2}Fe_{0.8}O_{3-\delta}$ (LCuF-28) decreased with exposure to 10% water vapor and proposed that the reaction between water and the perovskite was as follows:

$$\begin{array}{l} \quad\quad\quad\quad H_2O^- \\ \quad\quad\quad\quad\ \ | \\ Fe^{2+}\square + H_2O \leftrightarrow Fe^{3+} \end{array} \tag{1-49}$$

$$\begin{array}{l} \quad\quad\quad\quad O^- \\ \quad\quad\quad\quad\ \ | \\ Fe^{2+}\square + H_2O \leftrightarrow Fe^{3+} + H_2 \end{array} \tag{1-50}$$

$$\begin{array}{l} O^- \quad\ O_2^- \quad\quad\quad\quad OH^- \quad OH^- \\ \ \ | \quad\quad\ | \quad\quad\quad\quad\ \ | \quad\quad | \\ Fe^{3+} + Fe^{3+} + H_2O \rightarrow Fe^{3+} + Fe^{3+} + O_2 \end{array} \tag{1-51}$$

where □ is an oxygen vacancy. And the lattice structure and morphology were not affected by H_2O on the sweep side [120].

Similarly, the formation of hydroxides on the membrane surface led to the degradation of oxygen permeability of $Ba_{0.5}Sr_{0.5}Co_{0.8}Fe_{0.2}O_{3-\delta}$ (BSCoF-5582) membranes with H_2O sweep [121]. While water can occupy all the oxygen vacancies on the perovskite surface, the occupation can be reversed by heating and releasing the water. However, in these studies above, water vapor was introduced as an impurity at low concentration. In the water splitting reactions, the water concentrations on the membrane surface are usually very high to enhance the water splitting reaction [72]. In this case, the effects with continuous oxygen incorporation from H_2O can be different from the experiments with exposure to low water concentrations. Further studies are needed to reveal the mechanism of water splitting on a perovskite membrane.

1.6.2 CO_2 adsorption/reaction

There are two pathways for the interactions between the membrane surface and CO_2: 1) CO_2 reacts with the membrane to form a thin carbonate layer, 2) the oxygen atoms in CO_2 molecules incorporate into the membrane as lattice oxygen [39].

For the first pathway, the carbonate formation will stop further surface reaction between the surface and the gas. Depending on the thermodynamics of the carbonates, the reaction can be either reversible or irreversible. From the Ellingham diagram [98], we can see that $CaCO_3$ is less stable than $SrCO_3$ or $BaCO_3$ in a pure CO_2 environment. When exposed to 1 atm CO_2, $CaCO_3$ decomposes spontaneously at above 850^{o}C, while $SrCO_3$ and $BaCO_3$ are stable even at 1000^{o}C. As a result, for Sr-based perovskites, ten Elshof et al. [63] found $SrCO_3$ on the $La_{0.6}Sr_{0.4}Co_{0.8}Fe_{0.2}O_{3-\delta}$ (LSCoF-6482) membrane surfaces exposed to CH_4 due to the reaction between the membrane and CO/CO_2/C as the methane oxidation products. Ravkina et al. [122] found that higher Sr content in $La_xSr_{1-x}Co_yFe_{1-y}O_{3-\delta}$ leads to more carbonate formation. Carbonate formation was also found on SCoF-82 [123] and LSFC-6482 [118] in CO_2 atmospheres. Besides, carbonates CO_3^{2-} were found on a sputtered Fe-doped $SrTiO_3$ single crystal surface, but it decomposed at temperatures higher than 700^{o}C [124]. The authors hypothesized the reactions as [124]

$$2CO_2 + V_O^{\bullet\bullet} + Ti''_{Ti} \rightarrow \left(CO_3\right)_O^X + Ti_{Ti}^X + CO \qquad (1\text{-}52)$$

or

$$CO_2 + Ti''_{Ti} + O_O^X + 2h^\bullet \rightarrow (CO_3)_O^X + Ti_{Ti}^X \quad (1\text{-}53)$$

Here Kröger–Vink notation is used. $V_O^{\bullet\bullet}$ is the lattice oxygen vacancy, O_O^x is the lattice oxygen, Ti''_{Ti} and Ti_{Ti}^X are titanium with +2 and +4 valences, respectively. $(CO_3)_O^X$ is the carbonate occupying an oxygen site.

For Ba-based membranes, similar results were found with CO_2 as the sweep gas. Tong et al. [125] found that carbonates formed on the BCoFZ membrane surfaces exposed to pure CO_2 environment, but the carbonate decomposed when the membrane was exposed to 1%O_2+99%Ar for an hour at 800^{o}C. Similarly, Kovalevsky et al [121] found that when the sweep gas was switched from inert gases to CO_2, the oxygen flux through BSCoF membrane decreased, which was due to the formation of carbonates on the membrane surface. $BaCo_{1-x-y}Fe_xNb_yO_{3-\delta}$ also suffered from carbonate formation that led to lower oxygen flux with CO_2 sweep [126, 127].

On the other hand, the direct incorporation pathway means that CO_2 reacts with the oxygen vacancies in the perovskite to generate CO and lattice oxygen. Benson et al. [118] used isotope methods to study LSCoF-6428 in $H_2O/CO_2/O_2$ environments at 750^{o}C and found that more oxygen dissolved into LSCoF-6428 in $O_2/H_2O/CO_2$ containing environment than that in pure O_2 environment, and that CO_2 dissociated and incorporated into the lattices in the similar manner with O_2. After experiments, impurities phases such as $SrCO_3$, $Fe_2O_3/(Co,Fe)_3O_4$, CoO, $La_2O_2CO_3$ were found on the surface [118].

Argirusis et al [128] proposed the following CO_2 decomposition reaction on a clean Fe-doped $SrTiO_3$ single crystal surface:

$$CO_2(g) \leftrightarrow CO(g) + O_{ads}^- + h^\bullet \quad (1\text{-}54)$$

$$O_{ads}^- + V_O^{\bullet\bullet} \Leftrightarrow O_O^x + h^\bullet \quad (1\text{-}55)$$

Here $h^\bullet$ is the electron hole (or more precisely the net charge in the lattice iron) and O_{ads}^- is the adsorbed oxygen species on the perovskite surface.

However, more studies are required to identify the thermodynamics as well as the kinetics for the carbonate formation and oxygen incorporation mechanisms in CO_2 splitting.

1.7 Thesis objective and outline

Oxygen permeable membrane-supported water splitting was proposed 40 years ago, but it is only in the past decade that a significant research has focused on this field, thanks to the improvement of oxygen permeability and the decrease of operating temperatures. The "solar-fuel" or "thermal-fuel" pathways as alternative energy storage techniques also make fuel production from water and carbon dioxide splitting more appealing. Therefore, understanding the kinetics of the oxygen transport processes in membrane-supported H_2O/CO_2 splitting is of great importance to develop this technology, optimize the reactor and system design and reduce the cost of CO_2 reuse and energy storage.

1.7.1 Research objectives and contributions

This thesis focuses on the kinetic studies of the heterogeneous reactions between H_2O/CO_2 and the LCF-91 perovskite during the splitting process. The fundamentals of the oxygen process are examined carefully using experiments, and the interactions between the gas and solid phases are thoroughly explored. In this thesis, experiments were carried out to understand the kinetics of these reactions under different temperatures and flow rates for a range of gas species, catalysts and porous supports. A resistance-network transport model was then developed based on the oxygen transport process, and this model was expanded to H_2O/CO_2 splitting processes and experimentally verified.

The following questions are addressed in this thesis:

1) What is the limiting step in the membrane-supported H_2O/CO_2 splitting process, and how can we identify it?
2) How will enhancing the surface kinetics affect the overall performance of the membrane reactor?
3) How will the LCF-91 membrane change due to the splitting experiments, and how will these changes affect the reactor performance?
4) How can we apply the kinetic model and parameters from this thesis to guide the design of a membrane reactor for H_2O/CO_2 splitting?

More specifically, my thesis makes the following novel contributions to this field:

1) Quantified H_2O/CO_2 splitting on oxygen permeable $La_{0.9}Ca_{0.1}FeO_{3-\delta}$ membranes experimentally

H_2O/CO_2 splitting is enhanced on LCF-91 membranes at elevated temperatures. This thesis reported the oxygen fluxes, H_2O/CO_2 splitting rates and fuel utilization ratios, and syngas production on both flat and surface-modified membranes under different operating conditions. Surface morphology, elemental distribution and crystal structure of LCF-91 membranes are characterized before and after H_2O/CO_2 splitting experiments and the long-term operational stability of these membranes is reported.

2) Developed an oxygen permeation model using one-step reaction mechanisms and Nernst-Planck diffusion for H_2O/CO_2 splitting on oxygen permeable membranes

This resistance-network permeation model provides information on the oxygen transport process with a good accuracy. The kinetic parameters are derived from the experimental results for oxygen direct-incorporation kinetics for H_2O/CO_2 splitting on the feed side and the Mars-van Krevelen (MvK) mechanism for fuel (H_2, CO or CH_4) oxidation reactions on the sweep side. The limiting step(s) of the oxygen permeation process are identified based on the resistance comparisons for H_2O/CO_2 splitting on LCF oxygen permeable membranes under different operating conditions.

3) Further enhanced H_2O/CO_2 splitting on oxygen permeable LCF-91 membranes under fuel-sweep conditions

By adding a Ni/LCF-91 catalytic layer on the methane side, the hydrogen production from H_2O splitting is enhanced by two orders of magnitude. Reaction mechanisms for CH_4 partial oxidation in this Ni/LCF-91 porous layer are also identified based on experimental measurements taken near and away from the membrane surface.

4) Analyzed an monolith-type oxygen permeation membrane reactor for water splitting and methane partial oxidation

The resistance network permeation model is applied to a 1D plug flow membrane reactor model with coupled gas-phase mass transfer and heterogeneous reactions. This

model, along with the experimental results from this thesis guides the design of a water-splitting membrane reactor with methane partial oxidation. The most critical reactor parameters (e.g., the channel height, operating temperature and methane oxidation kinetics) are identified from the sensitivity analysis and their impacts are quantified.

1.7.2 Thesis outline

This thesis contains a total of nine chapters. Chapter 2 describes the experimental setup and deduction procedures. Chapter 3 details the resistance-network transport model for H_2O/CO_2 splitting on an oxygen permeable membrane. Chapter 4 examines the water-splitting process under both inert and fuel sweep conditions on a flat LCF-91 membrane. Chapter 5 focuses on the enhancement of the limiting step (i.e., the methane oxidation on the sweep side) by using a Ni/LCF-91 porous layer, and examines the products of methane partial oxidation on that side. Chapters 6 and 7 study the CO_2 splitting process in the LCF-91 membrane reactor under different operating conditions and membrane configurations, and quantify the resistances of the oxygen transport steps. Chapter 8 shows the potential of efficiency improvement for membrane-assisted water splitting reactor and implements the kinetic model to guide the design of an oxygen permeable membrane reactor for water splitting integrated with methane partial oxidation. Chapter 9 compares H_2O and CO_2 splitting in an oxygen permeable membrane reactor, summarizes the thesis findings and recommends future work for optimizing an oxygen permeable membrane reactor to enhance H_2O/CO_2 splitting for CO_2 reuse and energy storage.

This page is intentionally left blank

Chapter 2

Experiments

2.1 Introduction

The oxygen fluxes presented in this thesis were obtained in a button-cell membrane reactor in the Reacting Gas Dynamics Laboratory (RGD Lab) at MIT. The membrane characterizations were carried out in the shared instruments in the MIT Center for Materials Science and Engineering (CMSE). In this section, I will first introduce the experimental setup and the $La_{0.9}Ca_{0.1}FeO_{3-\delta}$ membranes examined in this thesis. Then, the data deduction procedures for the oxygen fluxes associated with H_2O/CO_2 splitting are summarized.

2.2 Experimental setup

2.2.1 Introduction

A button-cell membrane reactor with the axis-symmetric stagnation flow field is designed for the oxygen permeation experiments with various oxygen sources (i.e., air, H_2O and CO_2). The reactor is shown in Figure 2.1. It is constructed of alumina and can operate at temperatures up to 1050 ^oC at atmospheric pressure. The reactor is divided into a feed chamber (high p_{O2}) and a sweep chamber (low p_{O2}). Inside the reactor, a flat circular perovskite membrane with an effective diameter of 12.7 mm is installed between the two alumina tubes outside. Two gold rings are used to seal the gap between the membrane edges and the tubes, and a spring is installed at the top to enforce the sealing by a downward force. Different carrier gases are used on the two chambers, so that the leakage around the membrane can be monitored in real time during the experiments. Leakage into the reactor is typically less than 0.05% and that around the membrane is less than 0.03%, which confirms that the leak is kept to a minimum value.

The reactor is installed inside a furnace, which has an electric heater with a PID controller and a K-type thermocouple feedback to control the temperature ramp rate of

3°C/min for both heating and cooling during all the experiments. The small temperature ramp rate ensures low thermal stresses within the membrane, the gold sealant and the reactor. Additionally, each chamber has a K-type thermocouple in a position as close as possible to the surface to measure the temperature on both sides. The distance from the thermocouple tip to the membrane is measured, and the membrane temperature is calculated by linear interpolation between the two temperatures. The furnace temperature is controlled to maintain the set temperature.

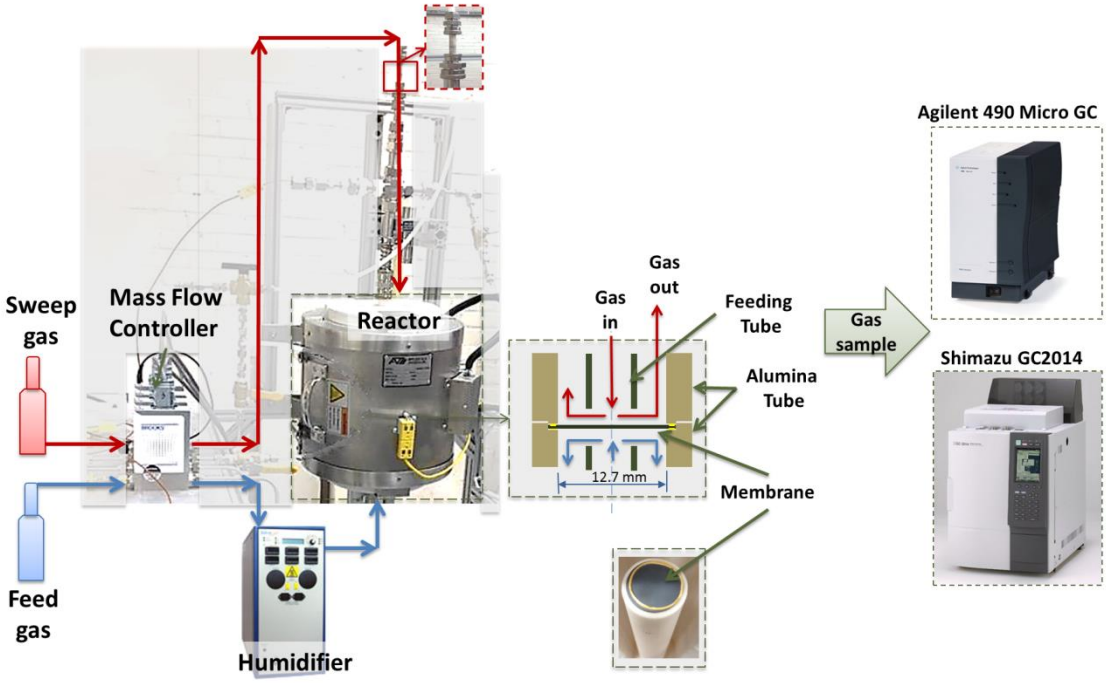

Figure 2.1 Schematic flow chart shows a button-cell reactor. The effective diameter of the membrane is 12.7 mm. For water splitting experiments, inert gas flows through the humidifier to carry desired amount of water vapor into reactor. For CO_2 splitting experiments, the humidifier is by-passed; dry air is fed into the reactor

Gases are supplied into the feed and sweep chambers from high-pressure gas cylinders, and the flow rates are controlled by MFCs (mass flow controller) from Brooks Instrument®. In order to precisely control the flow rate, only one type of gas flows through an MFC at one time; therefore, multiple MFCs are installed at both the feed and

sweep inlets to obtain desired gas mixtures. During the water splitting experiments, argon is used as the carrier gas, which goes through a humidifier (Fideris® Bubble Humidifier) to carry desired amount of water vapor into the feed side chamber; both the water bath and the dew point temperatures of the humidifier can be controlled to maintain the desired water partial pressures. For the experiments with air or CO_2 as the oxygen source, the humidifier is by-passed and dry gases are fed into the reactor. Alumina feeding tubes were inserted into both chambers in the reactor to lead the gases towards the membrane surfaces; the feeding tubes with 4.75 mm ID and 6.35 mm OD were used.

Gas samples, both at the inlet and outlet of feed and sweep chambers, are examined by the GCs (gas chromatograph, Agilent 490 Micro GC and Shimadzu GC2014), where the concentrations of different gases are measured and printed. The Micro GC has a 10 m 5 Å molecular sieve column (helium carrier gas) with thermal conductivity detectors (TCD) to measure H_2, O_2, N_2, CO and CH_4 concentrations. The Shimadzu GC2014 has a pulsed discharge helium ionization detector (PDHID) to detect hydrogen concentration at ppm levels, a TCD to measure H_2, O_2, N_2, CO, CO_2, CH_4, C_2H_2, C_2H_4 and C_2H_6, and a flame ionization detector (FID) to measure CH_4, C_2H_2, C_2H_4 and C_2H_6. FID has higher sensitivity to trace amounts of hydrocarbons than TCD; therefore, the former can reveal the higher hydrocarbon formation precisely on the sweep side when methane is used as the sweep gas.

Careful calibrations were made to the GCs, and the two-point interpolation method was used for the measurements. These well-mixed bulk values at the inlets and outlets of the membrane reactor describe the overall reaction and performances inside the reactor.

2.2.2 Local measurements

Experiments and simulations have showed that the measurements of species concentrations close to the membrane surface describe the oxygen transport process better [79-81]. Especially in the case with hydrocarbons on the sweep side, the products that leave the membrane surface continue to react in the gas phase until they are quenched near the outlet. Therefore, in order to examine the reactions near the membrane surface and identify the possible reaction pathways in the vicinity of the membrane

surface, capillary probes are inserted into the membrane reactor to measure the gas species very close to the membrane surface. By comparing the measurements near the membrane surfaces and at the outlet of the membrane reactor, we can identify the important steps in the heterogeneous and homogeneous reactions. Results will be presented in the cases with methane partial oxidation on the sweep side to illustrate the perks of the local measurements (in Chapter 5).

The capillary probes are inert fused silica capillary tubes from RESTEK with outer diameter of 0.53 mm. As is shown in Figure 2.2, the capillary probes are touching the membrane surfaces. With the pump in the Agilent Micro GC, gas samples are sucked out from the membrane reactor and analyzed. Due to the small sample volume of the capillary probes, we assumed that the samples taken out from the probes are quenched and can represent the gas species at the vicinity of the membrane surface.

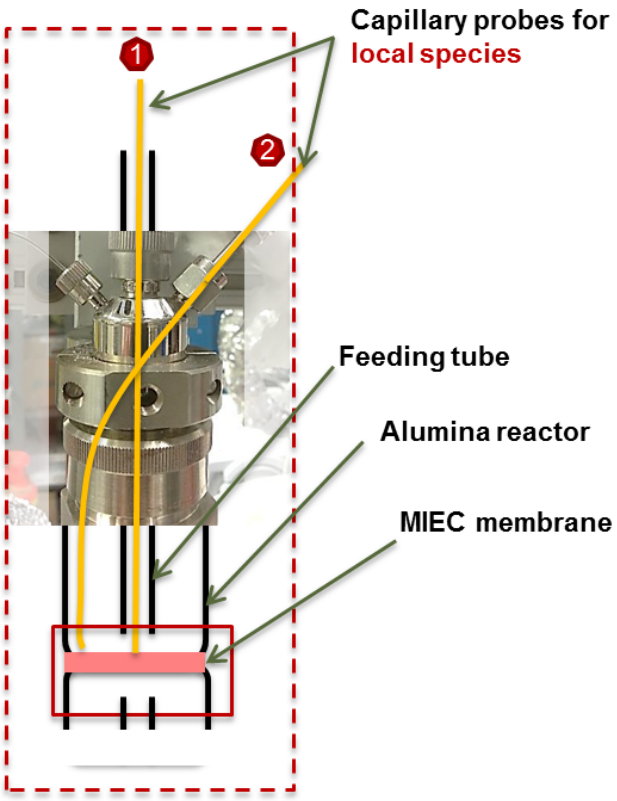

Figure 2.2 Capillary probles are inserted into the reactor to measure gas species near the membrane surface. This allows us examine the reactions close to the membrane surface

2.2.3 Non-uniformity of flow field

A zoom-in schematic figure of the button cell reactor is shown in Figure 2.3 (a). We can see that the flow from the center feeding tube impinges onto the membrane, and then changes its direction and flows out. The non-uniform flow field is shown in the computational fluid dynamic (CFD) simulations of a similar reactor design [129]. As a result, gas species concentration varies along the radius of the membrane, and this non-uniformity depends on the gap height between the feeding tube and the membrane, the flow rates, the temperature and the oxygen fluxes [129].

Larger gap heights or smaller gas flow rates decrease the non-uniformity, but both also lead to lower oxygen fluxes [129]. When air is the oxygen source, the oxygen fluxes versus the gap heights are shown in Figure 2.4 (a). We can notice that, the effect of the gap height is more profound at higher flow rate. For example, when the helium flow rate on the sweep side is 250 sccm, the oxygen fluxes increase from 0.06 to 0.085 $\mu mol/cm^2 \bullet s$ when the gap height decreases from 5 mm to 1 mm at 990^{o}C.

In Figure 2.4 (b), we can see the oxygen concentration non-uniformity from the local measurements near the center and the edge of the membrane on the sweep side (labelled as “center” and “out” in the figure, respectively). When the gap height is 1 mm, the difference of these two values is higher than that at a 3 mm-gap. Besides, when the gap is 3 mm, the variation along the radius is negligible especially when the flow rate is higher than 100 sccm. In our experiments, we keep the gap height around 2 mm to have reasonable uniformity of species concentration along the radius of the membrane surface as well as high oxygen fluxes.

2.2.4 Mass transfer in the gas phase

The surface reaction rates depend on the rate constant and the gas/solid species concentrations. The gases in the vicinity of the membrane are directly involved in the reactions and can better describe the oxygen permeation process [79, 80]. Yet in the literature, the gas species at the outlet of the membrane reactor are usually used to describe the surface kinetics.

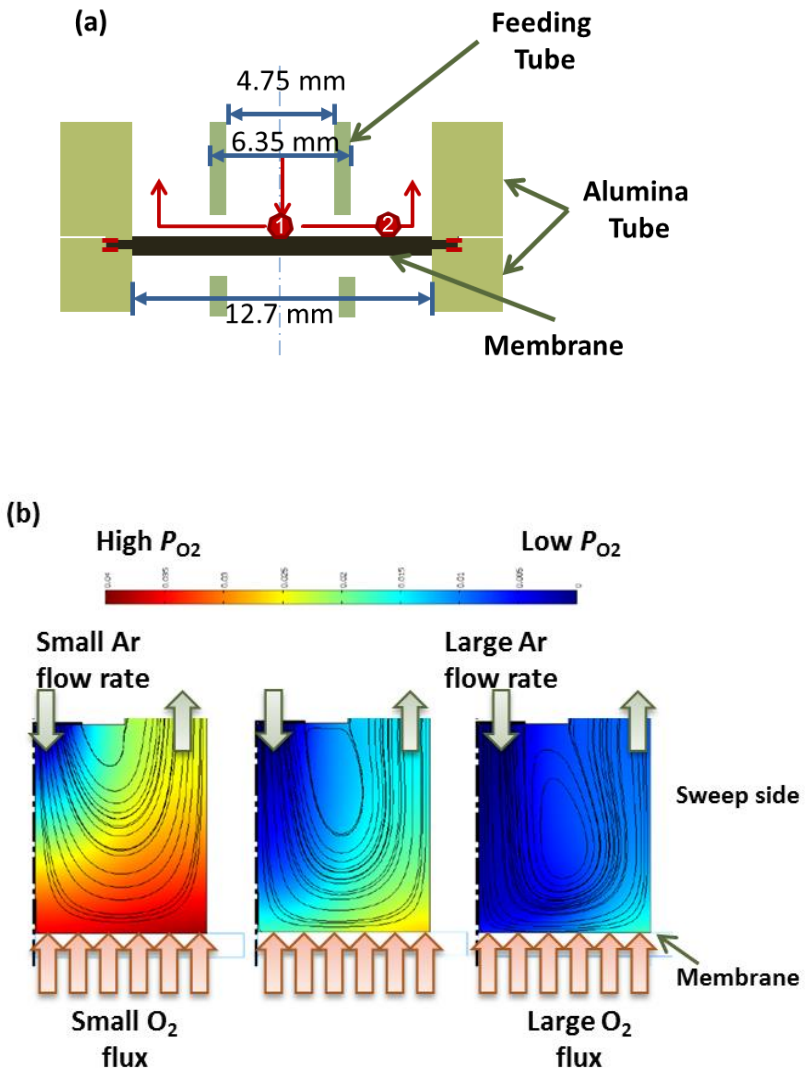

Figure 2.3 (a) A zoom-in schematic figure shows the dimensions of the reactor (in the graph, label 1 and 2 are the center and out measurements in Figure 2.4(a), respectively), (b) CFD simulations show the non-uniformity of the oxygen concentration along the radius of the membrane[129]

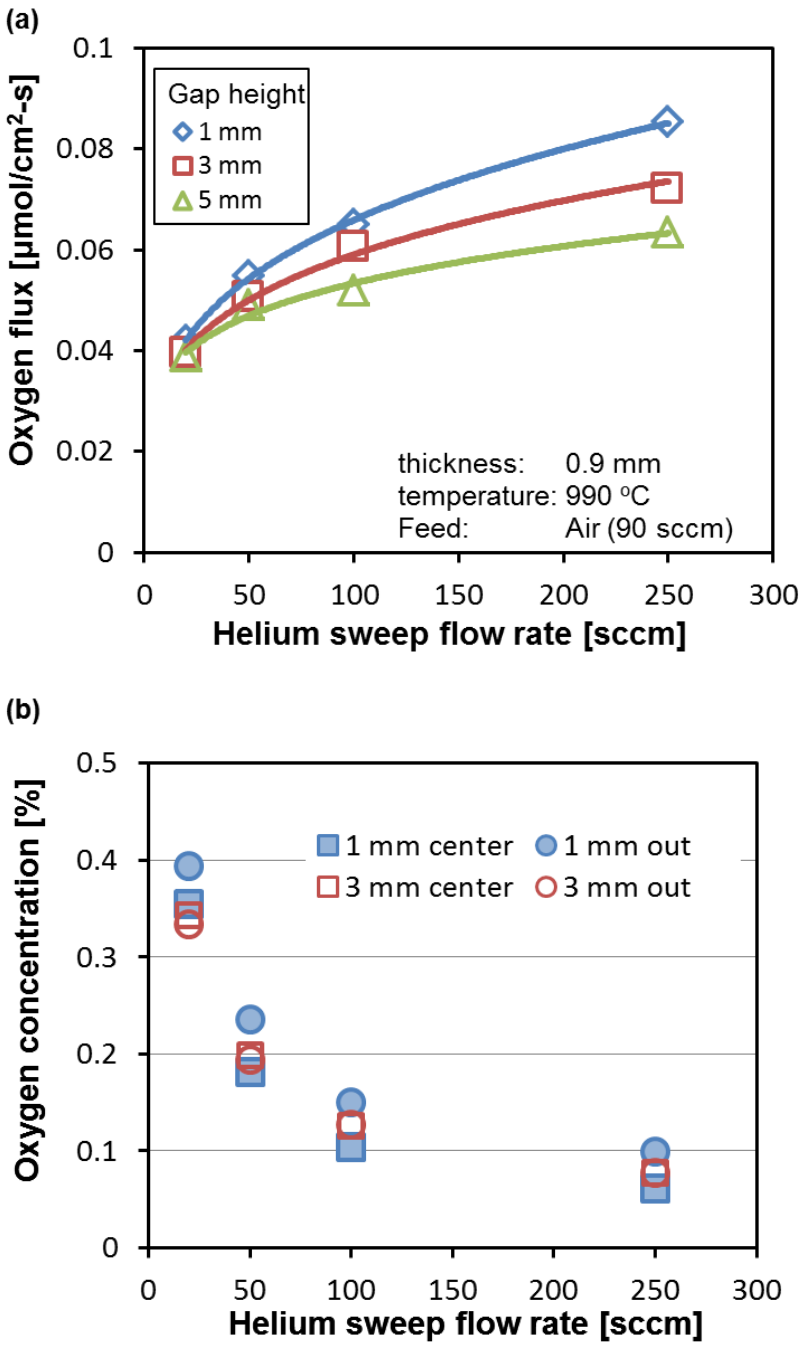

Figure 2.4 (a) Experiments show that when the gap between the feeding tube and the membrane increases, the associated oxygen fluxes decreases; (b) the oxygen concentration at the center and outside of the membrane as shown in Figure 2.3 (a)

As is described in the previous section, two capillary probes are inserted into the membrane reactor to measure the gas species in the vicinity of the membrane surface. A parametric study is carried out to quantify how the gas flow rates and the gap distance between the feeding tube and the membrane surface will affect the mass transfer in the gas phase.

The results are shown in Figure 2.5. From it we can see that when the gas flow rate is higher than 50 sccm, the oxygen concentration measured near the membrane surface is close to that measured at the outlet of the membrane. Therefore, in the experiments present in this thesis, the mass flow rate is set to be higher than 50 sccm, in which case, the mass transfer in the gas phase can be neglected, and the species measured at the outlet of the reactor can be used to estimate the gas species concentration in the vicinity of the membrane to describe the kinetics.

However, the reactions in the gas phase from the membrane surface to the reactor outlet can't be neglected, as they play an important role in the products coming out of the reactor. The impact of gas phase reactions will be discussed later in Section 5.4.2.

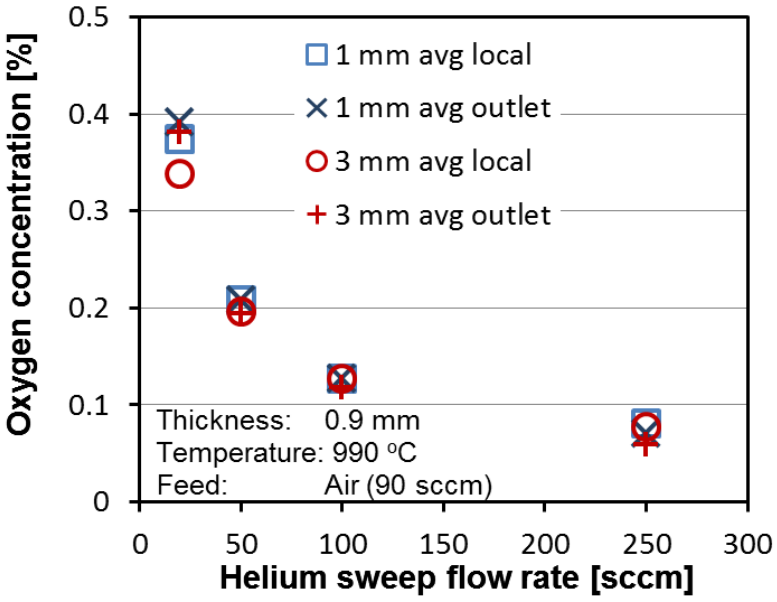

Figure 2.5 The effects of sweep gas flow rate and the gap distance between the feeding tube and the membrane surface on the oxygen concentration near the membrane and at the outlet of the reactor

Table 2.1 Quantitative EDX results show the stoichiometry of the LCF-91 membrane materials

	Elements	**La**	**Ca**	**Fe**
New membrane	**Atomic concentration* (%)**	42.41 ±1.16	5.53 ±0.56	52.06 ±1.24
	Calculated stoichiometry	0.885 ±0.023	0.115 ±0.011	1.09 ±0.025
* Only cations are counted: $X_{La} + X_{Ca} + X_{Fe} = 1$				

2.2.5 Membrane characterization

Under operating conditions such as high temperatures and reducing gases, new phase formations or element segregations may occur on the perovskite surface. Hence, the membranes were characterized both before and after the experiments to identify the changes due to the splitting experiments. Scanning electron microscopy (SEM) and energy-dispersive X-ray spectroscopy (EDX) were carried out on a JEOL 5910 General Purpose SEM and a Zeiss Merlin High-resolution SEM. X-ray powder diffraction (XRD) patterns were obtained from PANalytical X'Pert Pro Multipurpose Diffractometer with nickel filtered copper source with X'Celerator detector. EDX results for the membranes before experiments are shown in Table 2.1, from which we can see that the concentration of cations matches the ideal LCF-91 stoichiometry. The XRD data of LCF-91 membrane before the experiments shows only the LCF-91 perovskite peak as in Figure 2.6.

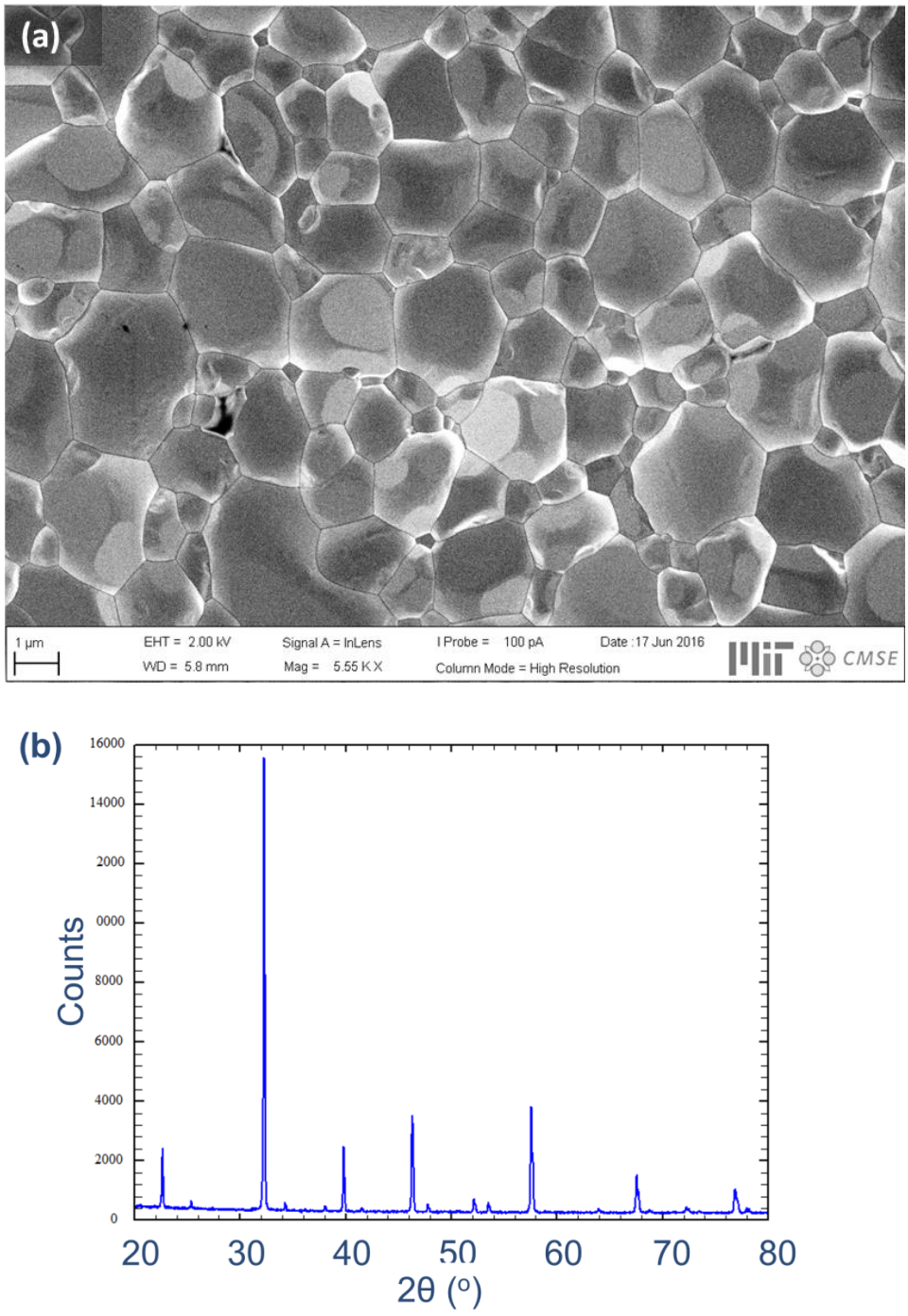

Figure 2.6 (a) The SEM image, and (b) XRD patterns of a new membrane

2.3 LCF membrane

The perovskite membrane tested in this thesis is various $La_{0.9}Ca_{0.1}FeO_{3-\delta}$ (LCF-91) dense membranes provided by Ceramatec. Ca-substitution in the La site of $LaFeO_3$ (LFO) lattice leads to charge compensation by either forming oxygen vacancies or oxidizing Fe^{3+} to Fe^{4+}, hence, decreasing oxygen permeation barriers [130]. However, as Ca is substituted, phase separation might occur, which leads to a mixture of perovskite ($La_{1-x}Ca_xFeO_3$), Grenier ($LaCa_2Fe_3O_8$) and brownmillerite ($Ca_2Fe_2O_5$) phases [131]. The Goldschmidt tolerance factor, T_G, is often used to identify whether the chemical compound can form a stable perovskite lattice, and the tolerance factor for $La_xCa_{1-x}FeO_{3-\delta}$ can be calculated as

$$T_G = \frac{xr_{La} + (1-x)r_{Ca} + r_O}{\sqrt{2}\left(r_{Fe} + r_O\right)} \tag{2-1}$$

in which, r_i is the radius of the *i* ion. For LCF, radii of the ions are [132]: La^{3+}: 1.36 Å, Ca^{2+}: 1.34 Å, Fe^{3+}: 0.55 Å (low spin) & 0.645 Å (high spin), Fe^{4+}: 0.585 Å, O^{2+}: 1.40 Å. As the concentrations of Fe^{3+} and Fe^{4+} vary at different oxygen vacancy concentrations, the tolerance factor T_G reaches the maximum when all iron ions are at Fe^{3+} low spin state and it reaches the minimum when all iron ions are at Fe^{3+} high spin state. Therefore, LCF-91 has a tolerance factor in the range of $0.954 < T_G < 1.00$, indicating that at least the material LCF-91 is in a stable perovskite structure.

LCF-91 is a mixed ionic and electronic conductor. Depending on the temperatures and the environments, the charge species and the conductivity of LCF-91 vary. Geary et al. [103] studied the charged species of LCF-91, and showed that at high oxygen partial pressures, such as in air, LCF-91 is mainly a p-type (electron hole) conductor, while at low oxygen partial pressures, it becomes an n-type (electron) conductor, as is shown in Figure 2.7. In both cases, the electron conductivity is much higher than the ionic conductivity. And the effective oxygen vacancy diffusivity for LCF-91 was derived from separate transient dilatometry studies [80]. The values are shown in Table 2.2.

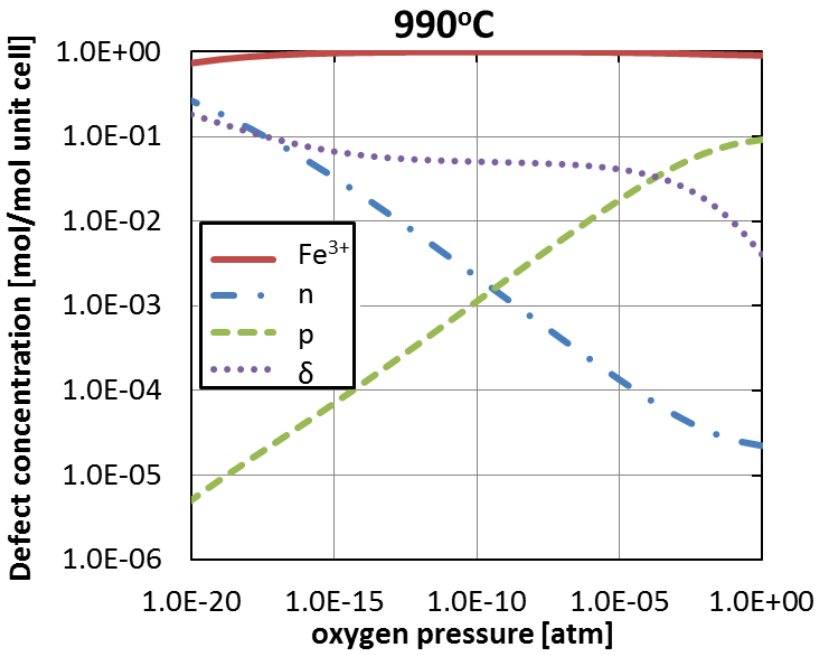

Figure 2.7 Charge species in LCF-91 materials under equilibrium case at 990°C with oxygen partial pressure increases from 10^{-20} to 1 atm (calculated using the parameters from [103]) $n = Fe'_{Fe}, p = Fe^{\bullet}_{Fe}$

Table 2.2 Effective oxygen vacancy diffusivity of LCF-91 membrane [80]

Parameter	*A*		*E*a	
	Value	Unit	Value	Unit
Vacancy diffusivity, D_v	4.98E-3	[cm^2/s]	5.96E4	[J/mol]

2.4 Data deduction

2.4.1 Splitting experiments

During the H_2O or CO_2 splitting experiments, H_2/CO concentrations at the outlet of the feed side is measured by the gas chromatograph. The homogeneous reaction of H_2O or CO_2 splitting is slow even at elevated temperature around 990°C, so in the analysis, the homogeneous splitting reactions are ignored and only heterogeneous splitting reactions on membrane surfaces are considered. Therefore, the H_2/CO production rates (yields) are calculated as

$$Y_{H_2} = X'_{H_2,\text{out}} \times n' \tag{2-2}$$

$$Y_{CO} = X'_{CO,\text{out}} \times n' \tag{2-3}$$

where $X'_{H_2O,out}$ and $X'_{CO_2,out}$ are the H_2 and CO mole fractions at the outlet of the feed side, respectively [dimensionless] and n' is total molar flow rate [mol/s]. The splitting reactions (2-4) and (2-5) show that the total molar flow rate of the feed gas mixture does not change,

$$H_2O + V_O^{\bullet\bullet} \rightarrow O_O^x + 2h^{\bullet} + H_2 \tag{2-4}$$

$$CO_2 + V_O^{\bullet\bullet} \rightarrow O_O^x + 2h^{\bullet} + CO \tag{2-5}$$

Therefore, the total molar flow rates on the feed side are

$$n' = n'_{Ar} + n'_{H_2O} = \frac{n'_{Ar}}{1 - X'_{H_2O,in}} \tag{2-6}$$

$$n' = n'_{Ar} + n'_{CO_2} = \frac{n'_{Ar}}{1 - X'_{CO_2,in}} \tag{2-7}$$

where $X'_{H_2O,in}$ and $X'_{CO_2,in}$ are the mole fractions of H_2O and CO_2 at the inlet on the feed side, respectively.

During the water splitting experiments, the hydrogen mole fraction $X'_{H_2,\text{meas}}$ is measured in the dry gas after passing the drier, which is not the same with that at the outlet of the reactor, $X'_{H_2,out}$. They are related as

$$\begin{aligned} X'_{H_2,out} &= \frac{X'_{H_2,\text{meas}} \cdot n'_{Ar}}{n'} \\ &= X'_{H_2,\text{meas}} \cdot (1 - X'_{H_2O,in}) \end{aligned} \quad . \tag{2-8}$$

Combining Equations (2-2), (2-6) and (2-8), we have

$$Y_{H_2} = X'_{H_2,\text{meas}} \times n'_{Ar} \, . \tag{2-9}$$

Then the splitting ratios are defined as

$$R'_{H_2O} = \frac{Y_{H_2}}{n'_{H_2O}} = \frac{Y_{H_2}}{n'_{Ar} \cdot \frac{X'_{H_2O,in}}{1 - X'_{H_2O,in}}} \quad (2\text{-}10)$$

$$R'_{CO_2} = \frac{Y_{CO}}{n'_{CO_2}} \quad (2\text{-}11)$$

Besides, as the H_2O/CO_2 splitting rates are low, we assume that all the oxygen produced from diffuses through the membrane. Hence, the oxygen flux is related to the H_2 yield or CO yield, as

$$J_{O_2} = \frac{Y_{O_O^x} / 2}{A_{memb}} = \frac{Y_{H_2}}{2A_{memb}} \quad (2\text{-}12)$$

$$J_{O_2} = \frac{Y_{O_O^x} / 2}{A_{memb}} = \frac{Y_{CO}}{2A_{memb}} \quad (2\text{-}13)$$

where $Y_{O_O^x}$ is the lattice oxygen yield from Equations (2-4) or (2-5).

2.4.2 Air separation experiments

We also measured the oxygen fluxes when air was used as the feed gas for comparison. For the air feed-inert sweep case, the absolute amount of oxygen that diffuses through the membrane is calculated by excluding the air leakage into the sweep side. The air leakage is tracked from the nitrogen concentration by assuming that oxygen and nitrogen molar ratio in air leakage is 21:79. Nitrogen and oxygen atom balance as well as the overall molar balance (no reaction between gases) are as

Oxygen balance: $\dot{n}''_{t,\text{in}} X''_{O_2,in} + \dot{n}_{O_2} + 0.21\dot{n}_{leak} = \dot{n}''_{t,out} X''_{O_2,out}$ (2-14)

Nitrogen balance: $0.79\dot{n}_{leak} = \dot{n}''_{t,out} X''_{N_2,out}$ (2-15)

Overall balance: $\dot{n}''_{t,in} + \dot{n}_{O_2} + \dot{n}_{leak} = \dot{n}''_{t,out}$ (2-16)

where $\dot{n}''_{\text{t,in}}$ and $\dot{n}''_{\text{t,out}}$ are the molar flux at the inlet and outlet of the sweep chamber, respectively, [mol/s]; $\dot{n}_{O_2}$ is the oxygen molar flux through the membrane, [mol/s]; $\dot{n}_{leak}$

is the molar flux of the air leakage, [mol/s]; $X''_{\mathrm{i,in}}$ and $X''_{\mathrm{i,out}}$ are the mole fractions of species *i* at inlet and outlet of the sweep chamber, respectively, [dimensionless].

At the inlet, as high-purity helium gas flows into the reactor, the oxygen concentration is zero, (i.e., $X''_{O_2,in} = 0$). From Equations (2-14), (2-15) and (2-16), we can calculate the oxygen flux and leak flux as:

$$\dot{n}_{O_2} = \frac{\left(X''_{O_2,out} - \frac{0.21}{0.79} X''_{N_2,out} \right)}{1 - X''_{O_2,out} - X''_{N_2,out}} \dot{n}''_{t,in} \tag{2-17}$$

$$\dot{n}_{leak} = \frac{X''_{N_2,out} / 0.79}{1 - X''_{O_2,out} - X''_{N_2,out}} \dot{n}''_{t,in} \tag{2-18}$$

Then the oxygen flux is

$$J_{O_2} = \dot{n}_{O_2} / A_{memb} \tag{2-19}$$

where A_{memb} is the effective area of membrane surface, [m^2].

For the air feed-fuel sweep case, the oxygen fluxes can be calculated from either oxygen permeation on the feed side or hydrogen consumption on sweep side. From oxygen permeation (the feed side), we have

Oxygen balance: $\dot{n}'_{t,\mathrm{in}} X'_{O_2,in} - \dot{n}'_{t,\mathrm{out}} X'_{O_2,out} = \dot{n}_{O_2}$ (2-20)

Overall balance: $\dot{n}'_{t,\mathrm{in}} - \dot{n}'_{t,\mathrm{out}} = \dot{n}_{O_2}$ (2-21)

Therefore, from the above balance equations, the oxygen flux is

$$\dot{J}_{O_2} = \frac{\dot{n}_{O_2}}{A_{memb}} = \frac{\dot{n}'_{t,\mathrm{in}} \left(X'_{O_2,in} - X'_{O_2,out} \right)}{A_{memb} \left(1 - X'_{O_2,out} \right)} \tag{2-22}$$

On the other hand, as hardly any oxygen was detected in the sweep side when hydrogen is used as a sweep gas, we assume that all the oxygen permeated through the membrane reacts with the hydrogen. The permeated oxygen won't change the total molar flux of the gas mixture ($O_O^x + 2h^\bullet + H_2(g) \rightarrow H_2O(g) + V_O^{\bullet\bullet}$), which leads to

$$\dot{n}''_{t,\mathrm{in}} = \dot{n}''_{t,\mathrm{out}} = \dot{n}''_{t} \tag{2-23}$$

Therefore, the oxygen flux equals half of the hydrogen consumption rate in the sweep side, which is

$$J_{O_2} = \frac{\left(X''_{H_2,in} - X''_{H_2,out}\right) \times \dot{n}''_t}{2A_{memb}} \tag{2-24}$$

The oxygen fluxes calculated from Equations (2-22) and (2-24) are compared to verify the mass balance in the reactor.

And for all the cases, the residence time inside the reactor is estimated as

$$\tau = \frac{V}{Q} = \frac{\pi d_r^{\,2} L}{4} \frac{T_s}{Q_s T_r} \tag{2-25}$$

where V is the volume of the reactor, [m^3], Q is the volumetric flow rate, [m^3/s], d_r is the inner diameter of the reactor, [m], L is the length of the reactor inside the furnace, [m], T_s is the standard temperature, [K], Q_s is the standard volumetric flow rate, [m^3/s] and T_r is the temperature in the reactor, [K].

2.5 Summaries

In this chapter, the experimental setup to quantify the membrane performance is introduced in details. The properties of the LCF-91 membranes are also discussed. Finally, the data deduction procedures are summarized for both splitting and air separation experiments.

Chapter 3

Resistance-Network Kinetics Model for Oxygen Permeation

3.1 Introduction

As discussed in Chapter 1, one of the questions that this thesis answers is "What is the limiting step in the membrane-supported H_2O/CO_2 splitting process, and how can we identify it?" In order to quantify the kinetics of the oxygen permeation processes, I developed a resistance-network kinetics model to analyze the oxygen transport barriers. Analogous to the Ohm's law, this resistance-network model treats each step as a 'resistance' for oxygen permeation. A series of resistances is then identified to summarize the barriers for the oxygen permeation from the oxygen source on the feed side to the oxygen sink on the sweep side.

As oxygen diffuses across the perovskite membrane in the form of oxygen ions or oxygen vacancies [39], the oxygen flux J_{O2} is half of the vacancy flux, J_v. Hence, the hydrogen or carbon monoxide production rates from the splitting process are,

$$J_{H_2} = J_V = 2J_{O_2} \tag{3-1}$$

or

$$J_{CO} = J_V = 2J_{O_2} \tag{3-2}$$

Kinetics are parameterized with experiments with different oxygen sources (i.e., air, H_2O and CO_2) and sweep gases (i.e., inert gas, H_2, CO and CH_4). In this section, I first introduce the kinetic model for the oxygen permeation process. Next the kinetic parameters for the associated surface reactions are presented.

3.2 Resistance-network model

The oxygen permeation process across an oxygen permeable membrane can be divided into five steps: two mass transfer steps in the gas phase from the bulk-gas to the

membrane surfaces, two surface reaction steps on the membrane surfaces and a bulk diffusion step across the membrane. The steps are shown in Figure 3.1. Depending on the reactor configuration, temperature and membrane thickness, any of these five steps could be rate-limiting. The two mass transfer processes in the gas phase depend on the flow rate and the mass diffusion coefficients. The other three processes involve the gas/solid reactions and depend on the characteristics of the membrane material. These five processes are modelled as a resistance network, as shown in Figure 3.1. The resistance-network permeation model has been successfully used in the literature to describe the oxygen permeation with air as the oxygen source [79, 101, 133, 134]. In my thesis, the use of this model is expanded to H_2O/CO_2 splitting processes.

As discussed in Section 2.2.4, the mass transfer can be neglected when the gas flow rate is higher than 50 sccm in our experimental setup. Hence, the gas species measured at the outlet of the membrane reactor can represent the gas species at the vicinity of the membrane when the gas phase reaction can also be neglected. When the gas phase reactions play an important role, the concentrations measured from the capillary probes (described in section 2.2.2) or estimated by mass balances near the membrane surface are used to model the surface reactions. In all these cases, the gas diffusion resistances are not considered in the resistance-network model shown in Figure 3.1.

One-step reaction is used to describe the surface reactions. Later I will show that this simplified model can predict the oxygen flux accurately. On the feed side, oxygen direct-incorporation mechanism gives:

Oxygen feed: $$\frac{1}{2}O_2 + V_O^{\bullet\bullet} \underset{}{\overset{k_{f,O_2}/k_{r,O_2}}{\rightleftharpoons}} O_O^x + 2h^{\bullet} \quad (3\text{-}3)$$

Water feed: $$H_2O + V_O^{\bullet\bullet} \underset{}{\overset{k_{f,H_2O}/k_{r,H_2O}}{\rightleftharpoons}} O_O^x + 2h^{\bullet} + H_2 \quad (3\text{-}4)$$

CO_2 feed: $$CO_2 + V_O^{\bullet\bullet} \underset{}{\overset{k_{f,CO_2}/k_{r,CO_2}}{\rightleftharpoons}} O_O^x + 2h^{\bullet} + CO \quad (3\text{-}5)$$

On the sweep side, the oxygen evolution or Mars-van Krevelen (MvK) mechanism for fuel oxidation gives:

Inert sweep: $$O_O^x + 2h^{\bullet} \underset{}{\overset{k_{r,O_2}/k_{f,O_2}}{\rightleftharpoons}} \frac{1}{2}O_2 + V_O^{\bullet\bullet} \quad (3\text{-}6)$$

H_2 sweep: $$O_O^x + 2h^\bullet + H_2 \underset{}{\overset{k_{r,H_2O}/k_{f,H_2O}}{\rightleftharpoons}} H_2O + V_O^{\bullet\bullet} \quad (3\text{-}7)$$

CO sweep: $$O_O^x + 2h^\bullet + CO \underset{}{\overset{k_{r,CO_2}/k_{f,CO_2}}{\rightleftharpoons}} CO_2 + V_O^{\bullet\bullet} \quad (3\text{-}8)$$

CH_4 sweep: $$O_O^x + 2h^\bullet + CH_4 \underset{}{\overset{k_{f,CH_4}/k_{r,CH_4}}{\rightleftharpoons}} CO + 2H_2 + V_O^{\bullet\bullet} \quad (3\text{-}9)$$

Here, $V_O^{\bullet\bullet}$ is oxygen vacancy in membrane, $h^\bullet$ is the electron holes. k_f and k_r are the forward and reverse reaction rate constants for corresponding reactions, respectively. Note that reactions (3-3), (3-4) and (3-5) are the backward reactions of (3-6), (3-7) and (3-8), respectively.

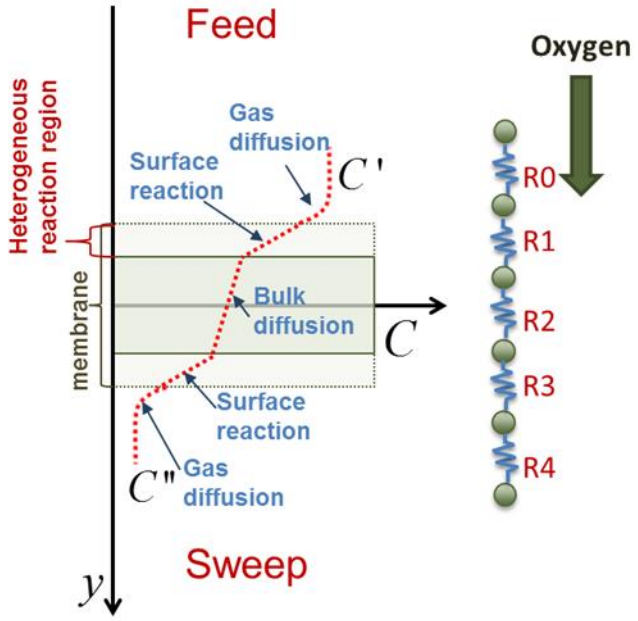

Figure 3.1 The three-resistance model for oxygen permeation through an inorganic membrane is illustrated. Feed and sweep sides are with high and low potential, respectively

From the above surface reactions, we have the absolute oxygen vacancy fluxes at the surface under various conditions:

Feed side:

Oxygen: $$J'_V = k_{f,O_2} C'^{0.5}_{O_2} C'_V - k_{r,O_2} C'_{O_O^x} C'^{2}_{h^\bullet} \quad (3\text{-}10)$$

H_2O: $$J'_V = k_{f,H_2O} C'_{H_2O} C'_V - k_{r,H_2O} C'_{O_O^x} C'^2_{h\bullet} C'_{H_2} \quad (3\text{-}11)$$

CO_2: $$J'_V = k_{f,CO_2} C'_{CO_2} C'_V - k_{r,CO_2} C'_{O_O^x} C'^2_{h\bullet} C'_{CO} \quad (3\text{-}12)$$

Sweep side:

Inert: $$J''_V = k_{r,O} C''_{O_O^x} C''^2_{h\bullet} - k_{f,O} C''^{0.5}_{O_2} C''_V \quad (3\text{-}13)$$

H_2: $$J''_V = k_{r,H_2O} C''_{O_O^x} C''^2_{h\bullet} C''_{H_2} - k_{f,H_2O} C''_{H_2O} C''_V \quad (3\text{-}14)$$

CO: $$J''_V = k_{r,CO_2} C''_{O_O^x} C''^2_{h\bullet} C''_{CO} - k_{f,CO_2} C''_{CO_2} C''_V \quad (3\text{-}15)$$

CH_4: $$J''_V = k_{f,CH_4} C''_{O_O^x} C''^2_{h\bullet} C''_{CH_4} - k_{r,CH_4} C''_{CO} C''^2_{H_2} C''_V \quad (3\text{-}16)$$

Here, J'_V and J''_V are the absolute values of oxygen vacancy fluxes on the feed and sweep side surfaces, respectively; C'_i and C''_i are the concentrations of species i on the feed side and sweep side, respectively.

Several assumptions are made to simplify the permeation model:

(1) The backwards reactions are neglected due to the low oxygen flux compared to the total flow rate and hence the low product concentrations compared to the reactants. Similar assumptions have been made and verified in the literature for heterogeneous reactions with MIEC membranes [111];

(2) Electron hole concentration across the membrane is assumed to be constant as the electronic transference number is much higher than ionic transference number [112, 113]. Therefore, the vacancy flux is viewed as zero-order in electron hole concentrations, $C'^2_{h\bullet}$ and $C''^2_{h\bullet}$ [79, 101, 135]. [1]

(3) The total site concentration for oxygen species C_o is

$$C_O = C_{O_O^x} + C_V \quad (3\text{-}17)$$

[1] However, when the mixed ionic and electronic conductor is around the intrinsic region where the electron and electron hole concentrations are the same (i.e., $n = p$), the electronic conductivity could be in similar order of magnitude with the ionic conductivities. In this intrinsic regime, all the charge species are need to be considered, the full equation for bulk diffusion (1-30) can be modelled using high fidelity numerical methods as in 115. Dimitrakopoulos, G. and Ghoniem, A.F., *A two-step surface exchange mechanism and detailed defect transport to model oxygen permeation through the $La_{0.9}Ca_{0.1}FeO_{3-\delta}$ mixed-conductor*. Journal of Membrane Science, 2016. **510**: 209-219.. Yet this is not in the case of either water or CO_2 splitting, as both surfaces are in very reducing environments due to low partial pressure of oxygen

where $C_{O_O^x}$ and C_V are the concentrations of lattice oxygen and oxygen vacancies, respectively. C_o is assumed to be a constant value (0.0825 mol/cm^3) estimated from the XRD measurements of the stoichiometric LCF-91 lattice size in air [114].

With the above assumptions, the vacancy fluxes are simplified:

Feed side:

Oxygen: $$J'_V = k_{f,O_2} C'^{0.5}_{O_2} C'_V - \tilde{k}_{r,O_2}\left(C_O - C'_V\right) \quad (3\text{-}18)$$

H_2O: $$J'_V = k_{f,H_2O} C'_{H_2O} C'_V \quad (3\text{-}19)$$

CO_2: $$J'_V = k_{f,CO_2} C'_{CO_2} C'_V \quad (3\text{-}20)$$

Sweep side:

Inert: $$J''_V = \tilde{k}_{r,O_2}\left(C_O - C''_V\right) - k_{f,O_2} C''^{0.5}_{O_2} C''_V \quad (3\text{-}21)$$

H_2: $$J''_V = \tilde{k}_{r,H_2O} C''_{H_2}\left(C_O - C''_V\right) \quad (3\text{-}22)$$

CO: $$J''_V = \tilde{k}_{r,CO_2} C''_{CO}\left(C''_O - C''_V\right) \quad (3\text{-}23)$$

CH_4: $$J''_V = \tilde{k}_{f,CH_4} C''_{CH_4}\left(C''_O - C''_V\right) \quad (3\text{-}24)$$

Here, $\tilde{k}$ are the new reaction constants after lumping the electron hole concentration.

The oxygen vacancy diffusion flux is modelled in (1-30)

$$J_i = -\frac{\sigma_{tot}\cdot t_i}{\left(Z_i F\right)^2}\left(\frac{d\mu_i}{dy} - Z_i \sum_j \left(\frac{t_j}{Z_j}\cdot\frac{d\mu_j}{dy}\right)\right) \quad (3\text{-}25)$$

When the ionic conductivity is the limiting step for the bulk diffusion, the flux can be rewritten as

$$J_V = -\frac{\sigma_V}{\left(z_V F\right)^2}\frac{\partial \mu_V}{\partial y} \quad (3\text{-}26)$$

The conductivity of oxygen vacancy is

$$\sigma_V = \frac{\left(z_V F\right)^2}{RT} C_V D_V \ , \quad (3\text{-}27)$$

where C_V is the oxygen vacancy concentration, D_V is the diffusivity of oxygen vacancy, R is the universal gas constant and T is the temperature.

The chemical potential gradient of oxygen vacancy across of the membrane is

$$\frac{\partial \mu_V}{\partial y} = \frac{\partial \left(RT \ln \left(C_V \right) \right)}{\partial y} = \frac{RT}{C_V} \frac{\partial \left(C_V \right)}{\partial y} \quad . \tag{3-28}$$

Combining (3-26), (3-27) and (3-28), we obtain the oxygen vacancy diffusion rate in the bulk:

$$J_V = -D_V \frac{\partial C_V}{\partial y} = D_V \frac{C''_V - C'_V}{t}, \tag{3-29}$$

where t is the thickness of the membrane.

By equating the oxygen vacancy flux on the feed side surface, through the bulk and on the sweep side surface, the flux equation is expressed in the form of the potential difference over the sum of three resistances as

$$J_V = \frac{\Delta P}{R_f + R_b + R_s} or \frac{C_O}{R_f + R_b + R_s}, \tag{3-30}$$

where ΔP is the potential difference, R_f, R_b and R_s are the resistances of the feed-side surface reaction, the bulk diffusion and the sweep-side surface reaction, respectively. In the case when H_2O or CO_2 is the oxygen source, the numerator is the oxygen species concentration in a perovskite lattice, C_O, in Equation (3-17), which corresponds to the maximum oxygen vacancy concentration difference across the membrane. The resistances under various feed and sweep conditions are summarized in Table 3.1.

Table 3.1 Resistance network for various oxygen sources and sweep side mechanisms on an MIEC oxygen permeable membrane

Oxygen source	**Sweep side**	**ΔP or C_O**	**Surface reaction resistance (feed side), R_f**	**Bulk resistance, R_b**	**Surface reaction resistance (sweep side), R_s**
Air	Inert	$\left(\frac{\tilde{k}_{r,O}C_O}{\tilde{k}_{r,O}+k_{f,O}C''^{0.5}_{O_2}}-\frac{\tilde{k}_{r,O}C_O}{\tilde{k}_{r,O}+k_{f,O}C''^{0.5}_{O_2}}\right)$	$1\Big/\left(\tilde{k}_{r,O}+k_{f,O}C'^{0.5}_{O_2}\right)$	$\frac{t}{D_V}$	$1\Big/\left(\tilde{k}_{r,O}+k_{f,O}C''^{0.5}_{O_2}\right)$
	H_2	$C_O-\frac{\tilde{k}_{r,O}C_O}{\tilde{k}_{r,O}+k_{f,O}C'^{0.5}_{O_2}}$	$1\Big/\left(\tilde{k}_{r,O}+k_{f,O}C'^{0.5}_{O_2}\right)$		$1\Big/\left(\tilde{k}_{r,H_2O}C''_{H_2}\right)$
H_2O	Inert	$\left(\tilde{k}_{r,O}C_O\right)\Big/\left(\tilde{k}_{r,O}+k_{f,O}C''^{0.5}_{O_2}\right)$	$1\Big/\left(k_{f,H_2O}C'_{H_2O}\right)$		$1\Big/\left(\tilde{k}_{r,O}+k_{f,O}C''^{0.5}_{O_2}\right)$
	H_2	C_O			$1\Big/\left(\tilde{k}_{r,H_2O}C''_{H_2}\right)$
	CH_4				$1\Big/\left(\tilde{k}_{f,CH_4}C''_{CH_4}\right)$
CO_2	Inert	$\left(\tilde{k}_{r,O}C_O\right)\Big/\left(\tilde{k}_{r,O}+k_{f,O}C''^{0.5}_{O_2}\right)$	$1\Big/\left(k_{f,CO_2}C'_{CO_2}\right)$		$1\Big/\left(\tilde{k}_{r,O}+k_{f,O}C''^{0.5}_{O_2}\right)$
	H_2	C_O			$1\Big/\left(\tilde{k}_{r,H_2O}C''_{H_2}\right)$
	CO				$1\Big/\left(\tilde{k}_{r,CO_2}C''_{CO_2}\right)$
	CH_4				$1\Big/\left(\tilde{k}_{f,CH_4}C''_{CH_4}\right)$

3.3 Reaction kinetics

In order to parameterize the kinetics, experiments with different oxygen sources and sweep conditions were conducted at various operating conditions. Table 3.2 summarizes the experimental conditions. In this section, I will present the results with air as the oxygen source. Other results with H_2O or CO_2 as the oxygen source will be reported and discussed in the following corresponding chapters.

Table 3.2 Experiment list to parameterize the kinetic data

Oxygen source	**Sweep side**	**Temperature [^oC]**	**Membrane thickness [mm]**
Air	He	800 – 1010	0.5, 0.9
	H_2 (1-8%)		0.9
H_2O	He	950 – 1030	0.5, 0.9
	H_2 (1-5%)		0.9
	CH_4 (1-5%)		0.9
CO_2	H_2 (1-10%)	850 – 1010	1.3
	CO (1-10%)		1.3

3.3.1 Air as the oxygen source

Air separation has been studied using LCF-91 membranes in the literature [80, 81]. Here, we present the oxygen fluxes through 0.9-mm thick LCF-91 membranes at the 990 ^oC in the experimental setup to verify the results. Hunt et al. [81] has measured the oxygen flux on a 1.5 mm thick LCF-91 membrane with CO_2 as the sweep gas at 950 – 1050 ^oC, and reported the oxygen flux from 0.02 to 0.05 μmol/cm^2•s. In my experiments, I used a 0.9 mm thick LCF-91 membrane with helium as the sweep gas. The results in Figure 3.2 shows that the oxygen fluxes increase with increasing helium flow rate from 0.05 to 0.13 μmol/cm^2•s. Similar results that oxygen fluxes increasing at higher sweep flow rate were also found for other perovskite membranes [101, 136].

The values reported in Figure 3.2 are in the same order of magnitude with Hunt et al.'s experiments [81]. The reasons for the higher values reported here is that the membrane tested in this thesis was thinner and helium was used as the sweep gas. Helium as the sweep gas leads to higher oxygen fluxes than CO_2 [125, 137, 138].

Figure 3.2 also shows that when the helium sweep gas flow rate increases from 20 to 500 sccm, the oxygen partial pressure at the outlet of the sweep chamber drops by an order of magnitude (i.e., from 0.4 to 0.077 kPa).

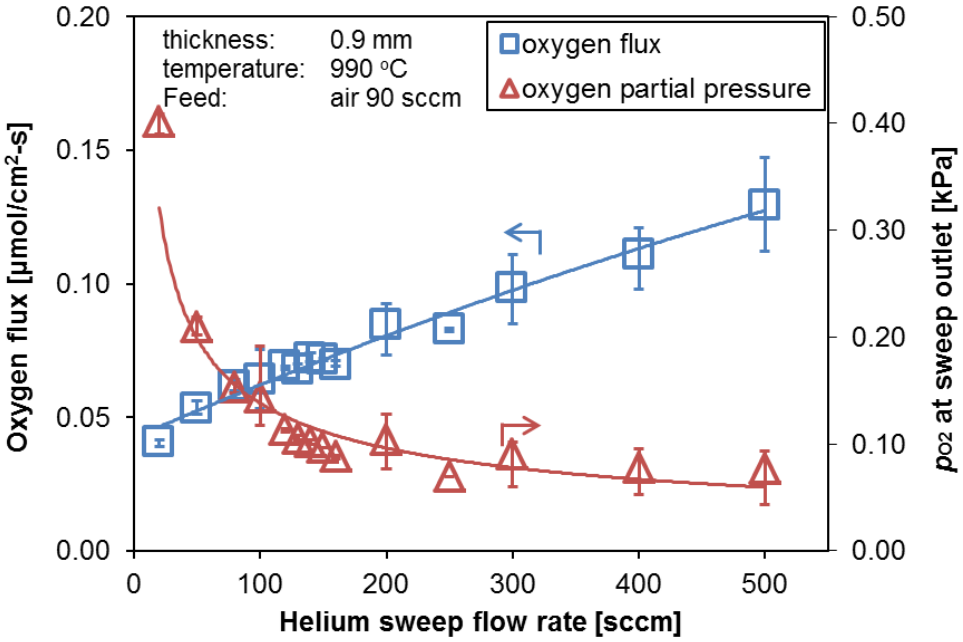

Figure 3.2 For the 0.9 mm LCF-91 membrane at 990°C, oxygen flux increases but the values of oxygen partial pressure on the sweep side drops at higher sweep flow rate

When hydrogen and helium mixture acts as the sweep gas, the oxygen fluxes are shown in Figure 3.3. The total flow rate of the sweep mixture is fixed at 500 sccm while the hydrogen concentration changes. The oxygen fluxes calculated from the feed side (Equation(2-22))

$$\dot{J}_{O_2} = \frac{\dot{n}_{O_2}}{A_{memb}} = \frac{\dot{n}'_{t,\text{in}}\left(X'_{O_2,in} - X'_{O_2,out}\right)}{A_{memb}\left(1 - X'_{O_2,out}\right)} \tag{3-31}$$

or from the sweep side (Equation(2-24))

$$J_{O_2} = \frac{\left(X''_{H_2,in} - X''_{H_2,out}\right) \times \dot{n}''_t}{2A_{memb}} \tag{3-32}$$

are the same. Thus, material balance inside the reactor is satisfied, which also means that all oxygen permeated through the membrane reacts with the hydrogen in the sweep chamber.

Figure 3.3 (a) shows that the oxygen fluxes increase with hydrogen concentrations in the sweep stream. The oxygen flux with 15 vol% hydrogen in the sweep side is 5 times higher than that in the inert sweep case. The consumption ratio of hydrogen in the sweep gas is shown in Figure 3.3 (b). The consumption ratio is as low as 2-6%, and it decreases at higher hydrogen concentrations on the sweep side. Beyond 3% hydrogen concentration, the consumption ratio stays constant around 2%. The short residence time of the sweep mixture and the limited availability of oxygen may be the reasons for the low hydrogen consumption ratio.

3.3.2 Kinetic parameters

Based on the data, the reaction rate constants of k_{f,O_2} and $\tilde{k}_{r,O_2}$ for the oxygen incorporation/dissociation

$$\frac{1}{2}O_2 + V_O^{\bullet\bullet} \underset{}{\overset{k_{f,O_2}/k_{r,O_2}}{\rightleftharpoons}} O_O^x + 2h^{\bullet} \qquad (3\text{-}33)$$

are fitted using the Arrhenius form $k_i = A_i \bullet \exp(-E_{a,i}/RT)$ by a least squares fitting using air feed-inert sweep data. The values of k_{f,H_2O} and $\tilde{k}_{r,H_2O}$ for the hydrogen reaction will be fitted with water splitting data and be reported in the following chapter.

Figure 3.4 shows the fitting data agrees very well the experimental measurements, which confirms that the simplified resistance-network permeation model can describe the oxygen flux for air separation well. The discrepancy may come from the fact that bulk measurements are used in this study to estimate the local conditions at membrane surface. As shown by Hong et al. [79], the difference between the bulk and local values, especially on the sweep side, may lead to different kinetic parameter fittings. And when the oxygen fluxes are low, the local values differ from the bulk to a larger extend. Additionally, the one-step heterogeneous mechanism may not be able to capture the limiting sub-steps under various operating conditions, which may also result in the difference between the calculated and experimental values.

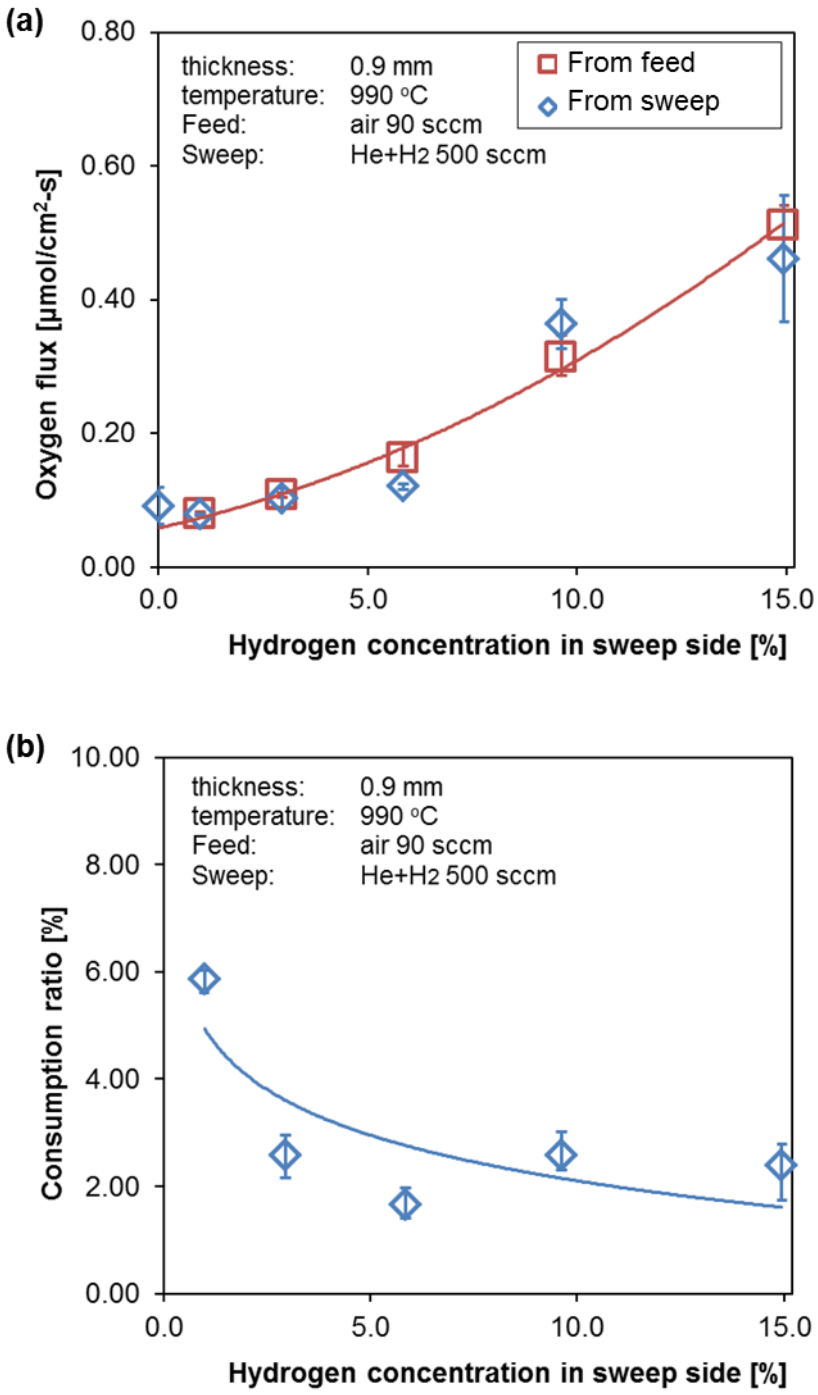

Figure 3.3 Oxygen flux through a 0.9 mm LCF-91 membrane at 990°C increases with hydrogen concentration in the sweep chamber. Air flows on the feed side at 90 sccm, and helium and hydrogen mixture flows on the sweep side at a total flow rate of 500 sccm. (a) Oxygen fluxes and (b) hydrogen consumption ratio dependence are shown

The values of the fitted rate constants are shown in Table 3.3. These rate constants are in the same orders of magnitude with those values in the literature under similar conditions [80]. Using these reaction rate constants obtained, the resistances for the oxygen permeation processes can be compared, and the limiting step(s) can be identified. Later in this thesis, I will identify and discuss the limiting step(s) in the membrane-supported H_2O/CO_2 splitting process under various operating conditions using this resistance-network model.

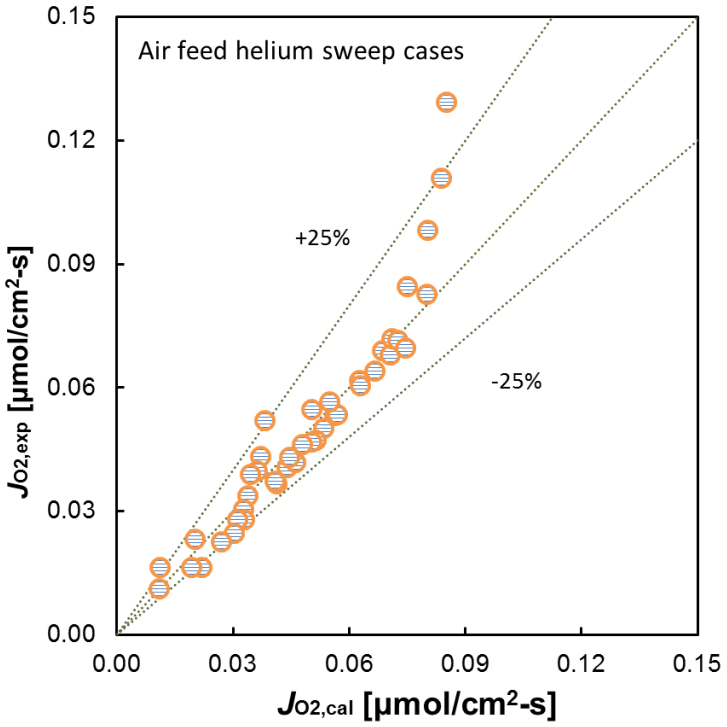

Figure 3.4 Kinetic data fitting shows good agreement with the experimental values within ±25% in most of the cases

Table 3.3 Reaction kinetic parameters for oxygen surface reactions for LCF-91 membranes

Oxygen surface reaction		A		E_a		
		Value	Unit	Value	Ref [80] *	Unit
$\frac{1}{2}O_2 + V_O^{\bullet\bullet} \leftrightarrow O_O^x + 2h^{\bullet}$	k_{f,O_2}	5.66	[$cm^{2.5}/mol^{0.5}$•s]	1.06E+4	7.810E+4	[J/mol]
	$\tilde{k}_{r,O_2}$	0.145	[cm/s]	1.11E+5	1.106E+5	[J/mol]
	D_v **	4.98E-3	[cm^2/s]	5.96E+4		[J/mol]

* Ref [80] shows oxygen incorporation/dissociation with air feed-CO_2 sweep through LCF-91 membranes

** Effective oxygen vacancy diffusivity was derived from separate transient dilatometry studies [80]

3.4 Summaries

In this chapter, the resistance-network model is introduced, and the reaction kinetic parameters for oxygen surface reactions are derived. This model incorporates one-step surface reaction mechanisms and the Nernst-Planck diffusion. It successfully predicts the limiting step(s) and guides the improvement of the membrane configuration, which will be discussed in the following chapters.

Acknowledgement:

Parts of the contents in this chapter have been firstly published in

Wu XY, Chang L, Uddi M, Kirchen P, Ghoniem AF. Toward enhanced hydrogen generation from water using oxygen permeating LCF membranes. *Physical Chemistry Chemical Physics.* 2015, 17(15): 10093 - 10107.

This page is intentionally left blank

Chapter 4

Hydrogen Production from Water Splitting Supported on a Flat LCF membrane

4.1 Introduction

Molecules that contain oxygen atoms may theoretically serves as the oxygen source for the permeation process through an MIEC membrane. When water serves as the oxygen source, a water splitting reaction takes place on the feed side (high p_{O_2}), while the permeated oxygen is carried away by an inert gas or consumed by fuel mixtures on the sweep side (low p_{O_2}).

Both homogeneous and heterogeneous water splitting may take place. However, homogeneous water dissociation in the gas phase is a very slow process with low thermodynamic equilibrium constants even at temperatures as high as 990^{o}C. We calculated the thermodynamic equilibrium and the kinetic process using Cantera [35] and GRI-Mech 3.0 mechanism [36] was implemented to resolve the gas phase reactions. Results are shown in Figure 4.1. At 990^{o}C, the equilibrium hydrogen mole fraction varies from 1 to 16 ppm as water concentration in the initial H_2O+Ar mixture increases from 1 vol% to 100 vol%. When the initial water concentration is higher than 50 vol%, the increase of equilibrium hydrogen mole fraction slows down. Therefore, initial water concentration at 50 vol% is chosen as the base case in this chapter to compare with the experimental data, with hydrogen concentration being 10.1 ppm at equilibrium. Furthermore, Figure 4.1 (b) shows the evolution of mole fractions in a well stirred reactor for homogeneous water thermolysis at 990^{o}C with initial water concentration to be 50 vol%. Homogeneous thermolysis is very slow even at 990^{o}C: it takes about 1100 s for the gas mixture to reach 90% of the equilibrium values, and 512 s to reach 50%.

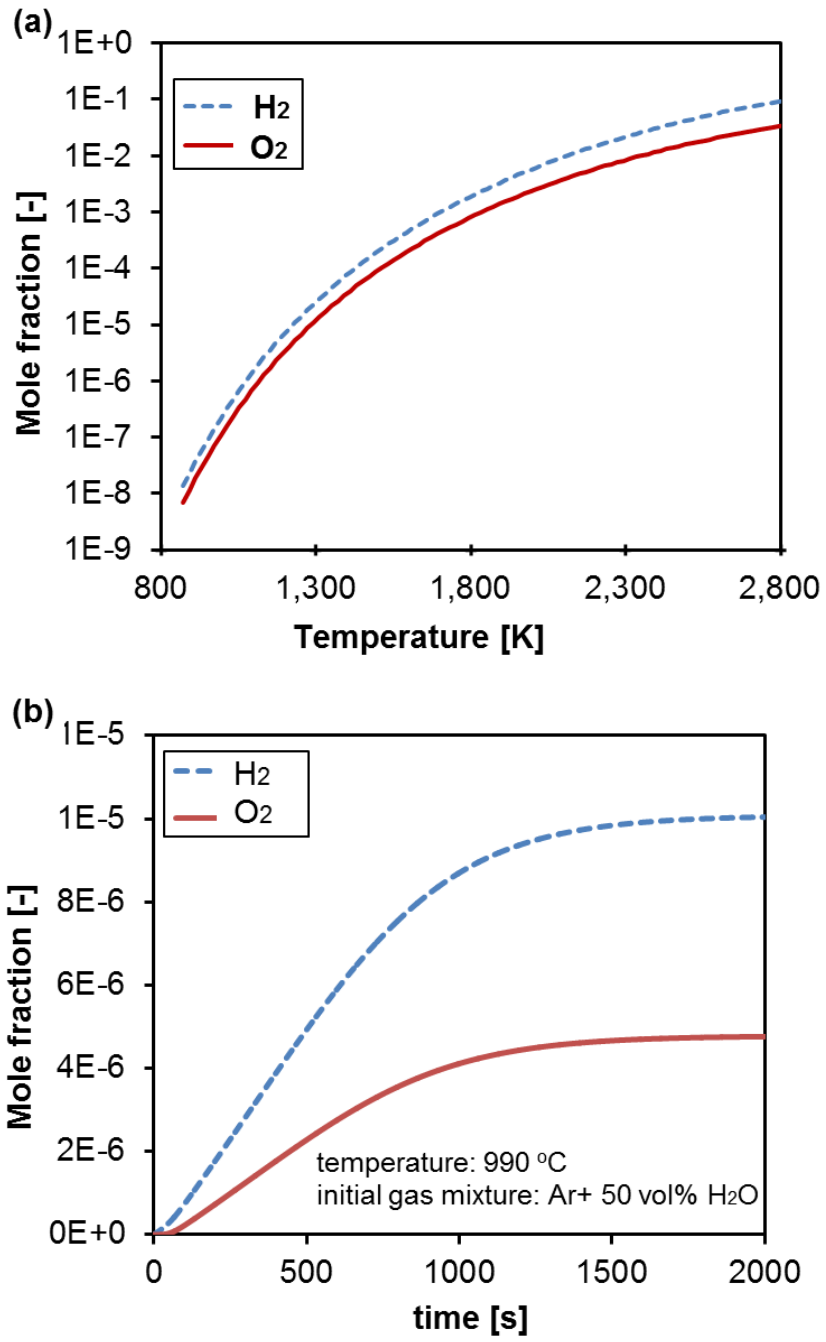

Figure 4.1 Homogeneous water thermolysis (a) Water concentration in the mixture affects the equilibrium hydrogen and oxygen mole fractions in the mixtures at 990°C; (b) the species mole fractions, i.e., X_{H_2} and X_{O_2} evolve with time under the initial condition of Ar and 50 vol% water mixture at 990°C

In this chapter, I am going to show that water splitting can be enhanced by the oxygen permeating LCF-91 membranes. Experiments were carried out to demonstrate the effect of different parameters such as feed and sweep side flow rates, feed side water concentration and fuel concentration on the sweep side. For each operating condition, we waited for the equilibrium of the reactor and then recorded the temperatures and species concentrations from successive measurements (at least five).

Besides, LCF-91 membranes with the same thickness but from different batches were examined. Most of the measured values were averaged over data sets from at least two different 0.9 mm thick LCF-91 membranes in order to eliminate the effects of membrane preparations. The mean values of each dataset are presented with error bars representing the range of values due to experimental uncertainties and different LCF-91 membranes.

Hydrogen and methane are used as the fuel on sweep side to enhance water splitting rate on the feed side. As discussed before, hydrogen is chosen in part in order to model the reverse water splitting using the resistant-network model as discussed in Chapter 3. In order to exclude the leakages of hydrogen from sweep to feed chambers around the membrane, we measured the leakage under the conditions where feed and sweep flow rates were the same but the feed gas was a dry inert gas. In this way, the hydrogen leakage into the feed side could be quantified and the absolute amount of hydrogen produced from water splitting derived.

Table 4.1 Experiment conditions in this chapter

Oxygen source	**Sweep gas**	***T*** **[^{o}C]**	**Membrane dimension [mm]**	
			Thickness	**Effective Diameter**
H_2O + Ar	He	950 – 1030	0.9	12.7
	H_2 (1-5%) + He			
	CH_4 (1-5%) + He			

4.2 Hydrogen production from water splitting

Different operating conditions are tested to quantify the kinetic parameters for membrane-supported water splitting on a perovskite LCF-91 membrane. The conditions

are summarized in Table 4.1. In this chapter, effects of these conditions on the hydrogen production from water splitting are reported. Then the fitted parameters are reported and the resistances for oxygen permeation are compared.

4.2.1 Mixture flow rate on feed side

For water splitting on the feed side, the hydrogen-oxygen bond first breaks either on the membrane surface (heterogeneously) or in the gas phase (homogeneously). Then, the hydrogen radicals recombine into hydrogen molecules that are carried away by the feed gas. Meanwhile, oxygen radicals occupy the vacancies and incorporate to form lattice oxygen. Similar reaction pathways have been proposed in thermochemical reduction of water on ceria-based materials [119].

In order to study how the mixture flow rates on feed side affect the hydrogen yield, we examined the water splitting rate and hydrogen yield by varying the argon carrier gas flow rate while fixing the water concentration at 50.7 vol% (the corresponding dew point temperature is 82^{o}C in the humidifier) and membrane temperature at 990^{o}C. Results are shown in Figure 4.2(a); higher feed rate leads to higher oxygen flux. However, the water splitting ratio at the outlet on the feed side increases first and then reaches a plateau at higher flow rate. The same trend is observed with the hydrogen concentration on the feed side. As shown in Figure 4.2 (b), the hydrogen concentration on the feed side increases as the feed flow rate increases from 100 to 200 sccm; after that, the hydrogen concentration saturates.

Increasing the gas flow rate on the feed side increases the mass transfer rate in the gas phase. Moreover, the recirculation zone size at the membrane corner is reduced as the flow rate increases, leading to smaller mass transfer resistance. As a result, at higher flow rate the hydrogen produced from water splitting can be convected away from the feed side membrane surface more effectively, and the hydrogen concentration at the membrane surface decreases. Additionally, the residence time in the reactor is in the order of magnitude around 0.01s, and yet the hydrogen concentration measured at the exit of the reactor is about half of the homogeneous equilibrium case which could be achieved in 512 s in homogeneous water dissociation reaction. Due to mass transfer in gas phase, the hydrogen concentration at the membrane surface where heterogeneous reaction takes

place can be higher than the concentration at the exit. Therefore, we can conclude that water splitting rate is enhanced on the LCF-91 membrane.

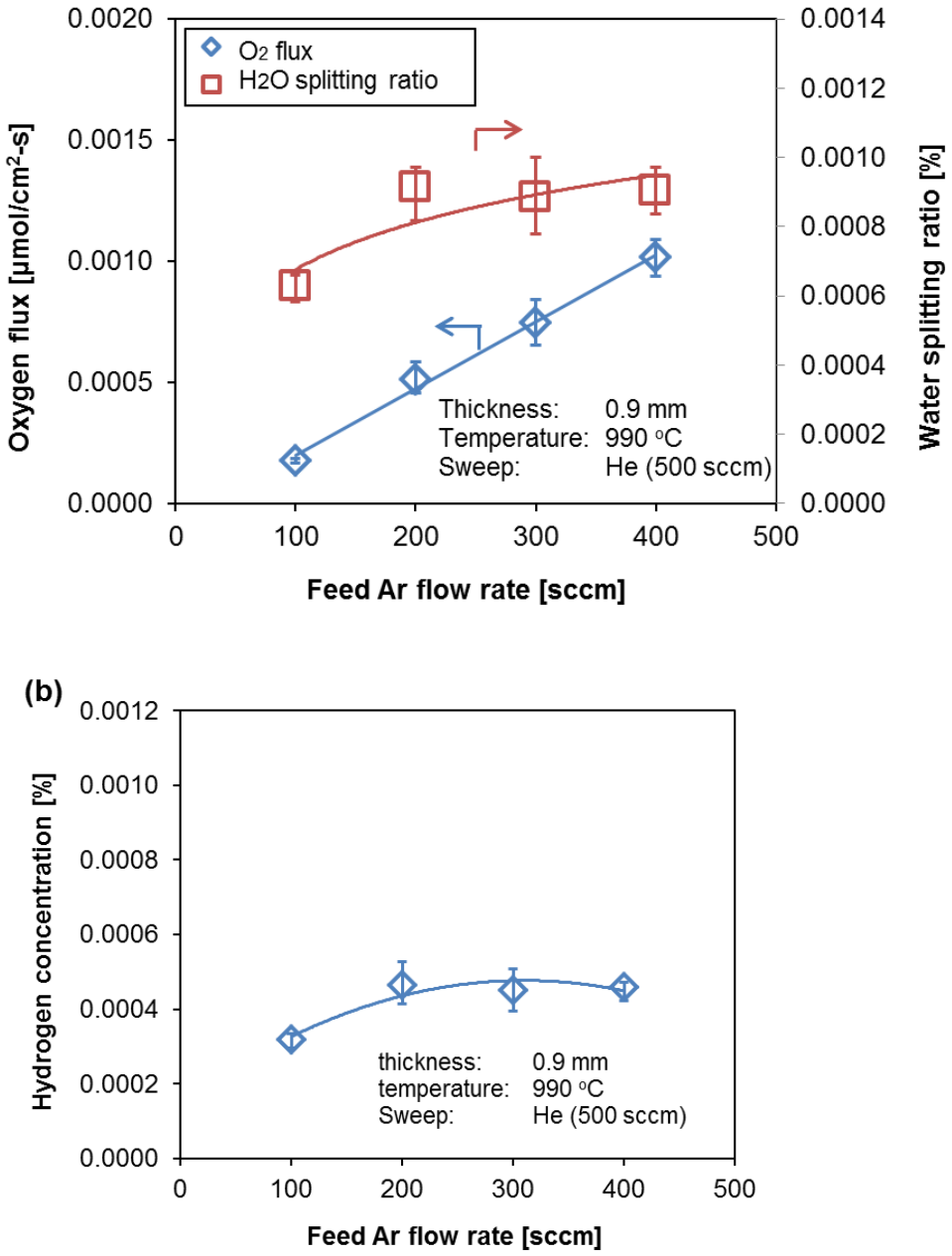

Figure 4.2 Water splitting rate on feed side increases with the carrier gas, i.e., argon flow rate. Yet the water splitting ratio (a) and hydrogen concentration (b) reaches a plateau at argon flow rate higher than 200 sccm. Feed side water concentration is fixed at 50 vol.%

4.2.2 Feed water concentration

The water concentration on the feed side also affects the oxygen permeation rate and the water splitting rate. During the experiments, we fixed the argon carrier gas flow rate at 400 sccm while changing the water concentration in the gas mixture from 50.7 to 83.5 vol% by varying the dew point temperature of the humidifier from 82 to 95^{o}C. At higher water concentration, the total flow rate of the feed gas mixture increases because the argon carrier gas has a constant flow rate of 400 sccm.

Figure 4.3 (a) shows that the oxygen flux has a three-fold increase when water partial pressure increases from 0.507 atm to 0.835 atm. As increasing the water concentration drives the forward reaction of water splitting further, the hydrogen production rate or oxygen permeation rate increases. However, the water splitting ratio decreases by 30% percent with increasing water concentration from 50.7 to 83.5 vol%. On the other hand, the hydrogen concentration on the feed side doesn't change much with increasing water concentration, as shown in Figure 4.3 (b). When water concentration increases, the hydrogen concentration at the exit of the reactor remains around 0.0005%. As the water splitting ratio is defined as

$$R'_{H_2O} = \frac{Y_{H_2}}{n'_{H_2O}} = \frac{Y_{H_2}}{n'_{Ar} \cdot \dfrac{X'_{H_2O,in}}{1 - X'_{H_2O,in}}}, \qquad (4\text{-}1)$$

the water splitting ratio decreases at higher water concentrations.

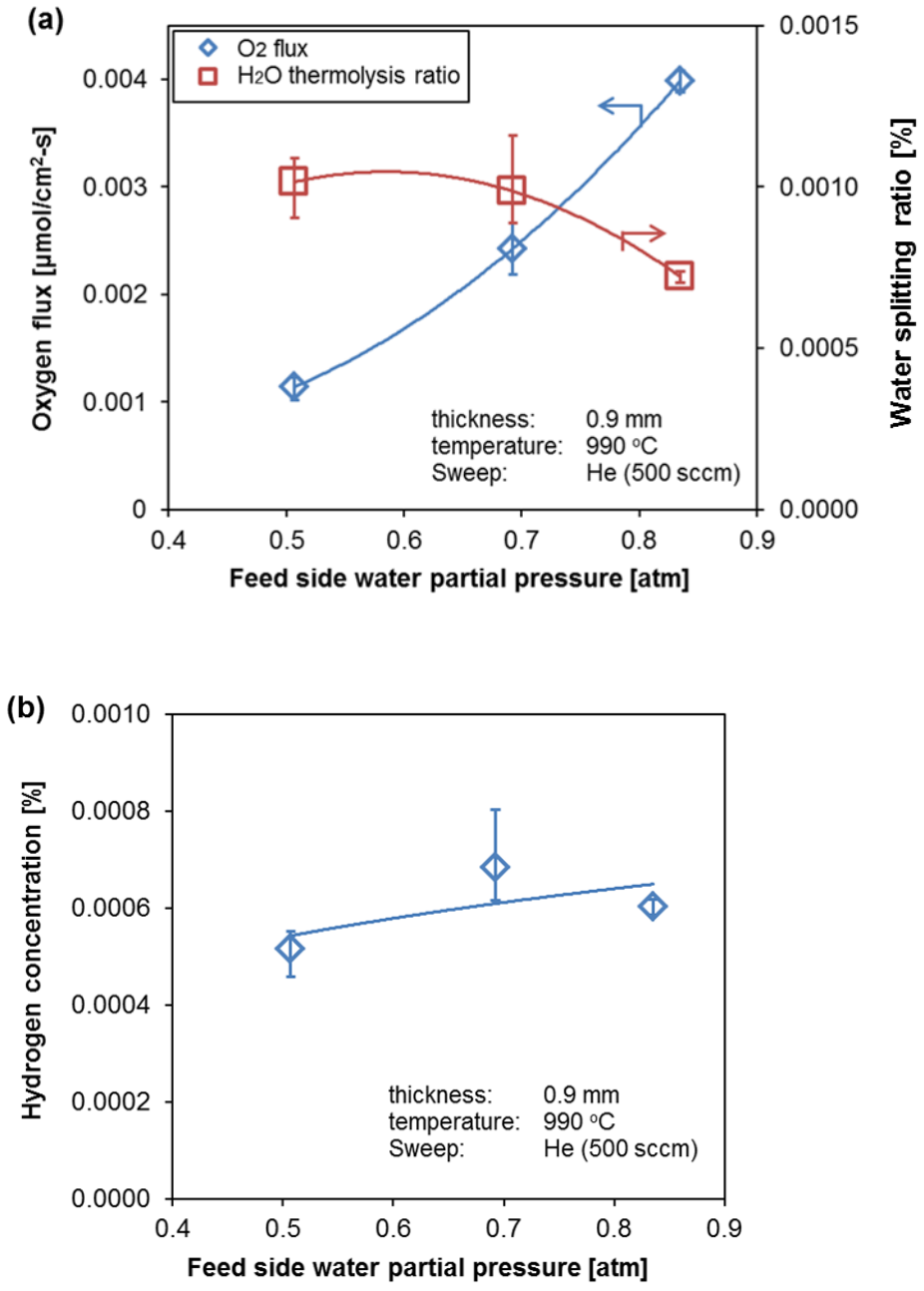

Figure 4.3 With increasing water concentration, (a) the oxygen fluxes increases, but the water splitting ratio decreases; and (b) the hydrogen concentration at feed side keeps constant

4.2.3 Helium sweep gas flow rate

In order to examine the impact of the inert gas flow rate on the sweep side on the overall oxygen permeation, helium sweep gas flow rates varying in the range of 130 – 3000 sccm were tested on a 0.9 mm thick membrane at 990°C. The feed side condition was fixed: the argon carrier gas flows at 400 sccm and the water partial pressure is 0.507 atm. Results shown in Figure 4.4 indicate that the oxygen flux has no obvious dependence on the helium sweep rate, and the flux is around 1.0×10^{-3} μmol/cm^2•s. The same trend is observed for the water splitting ratio, which remains at around 0.001% in all the cases.

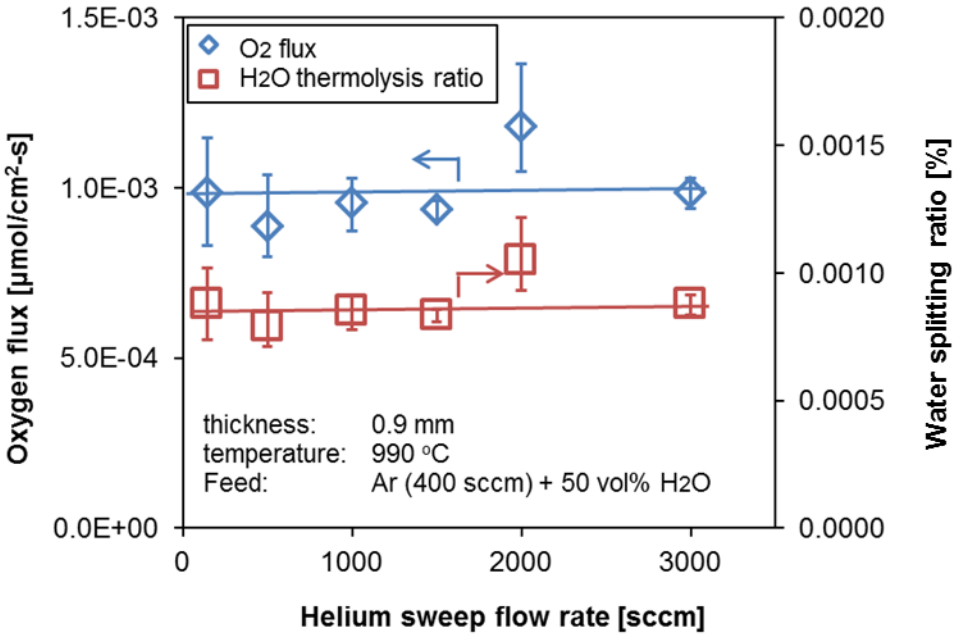

Figure 4.4 The oxygen fluxes and water splitting ratio don't change with increasing helium sweep gas flow rate

Sweep gas carries away the oxygen desorbed from the membrane surface. Higher flow rate leads to higher convective mass transport away from the membrane. This also increases the oxygen desorption rate on the sweep side as the local oxygen concentration decreases. The very weak dependence of the oxygen flux on the sweep flow rate means that the oxygen permeation process depends very weakly on the oxygen desorption

process on the sweep side for this 0.9 mm LCF-91 membrane. The limiting step(s) on this case will be further discussed later in this chapter.

4.2.4 H_2 concentration in sweep gas mixture

Because the helium sweep flow rate has hardly any effects on the water splitting rate, we tried another way to maintain low oxygen chemical potential in the sweep chamber, which is to add reactive gases to the sweep gas. In this case, the sweep flow not only carries away the oxygen permeated through the membrane but also reacts with it to further enhance the oxygen chemical potential gradient across the membrane. In this section, I will discuss hydrogen as the sweep gas. Then methane sweep is discussed in the following section.

Hydrogen addition into the sweep gas is found to enhance the oxygen fluxes, as shown in Figure 4.5. The use of hydrogen is by construction in order to derive the kinetic parameters for water splitting reaction shown later in this chapter. As discussed above, the hydrogen leakage into the feed side is quantified at the operating conditions and the absolute hydrogen production rate is calculated by excluding the leakage into the feed side. The argon carrier gas flows at 200 sccm on the feed side, and 50.7 vol% H_2O exists in the feed gas mixtures. The sweep side total flow rate is set to be either 400 or 500 sccm, and the experimental values are averaged and reported. As shown in Figure 4.5 (a), the oxygen flux and hydrogen concentration on the feed side increase with the fuel concentration in the sweep gas. When 5 vol% hydrogen is added, the oxygen flux reaches 0.15 μmol/cm^2•s at 990^{o}C and 0.19 μmol/cm^2•s at 1030^{o}C, which are around 2 orders of magnitude higher than the pure helium sweep case.

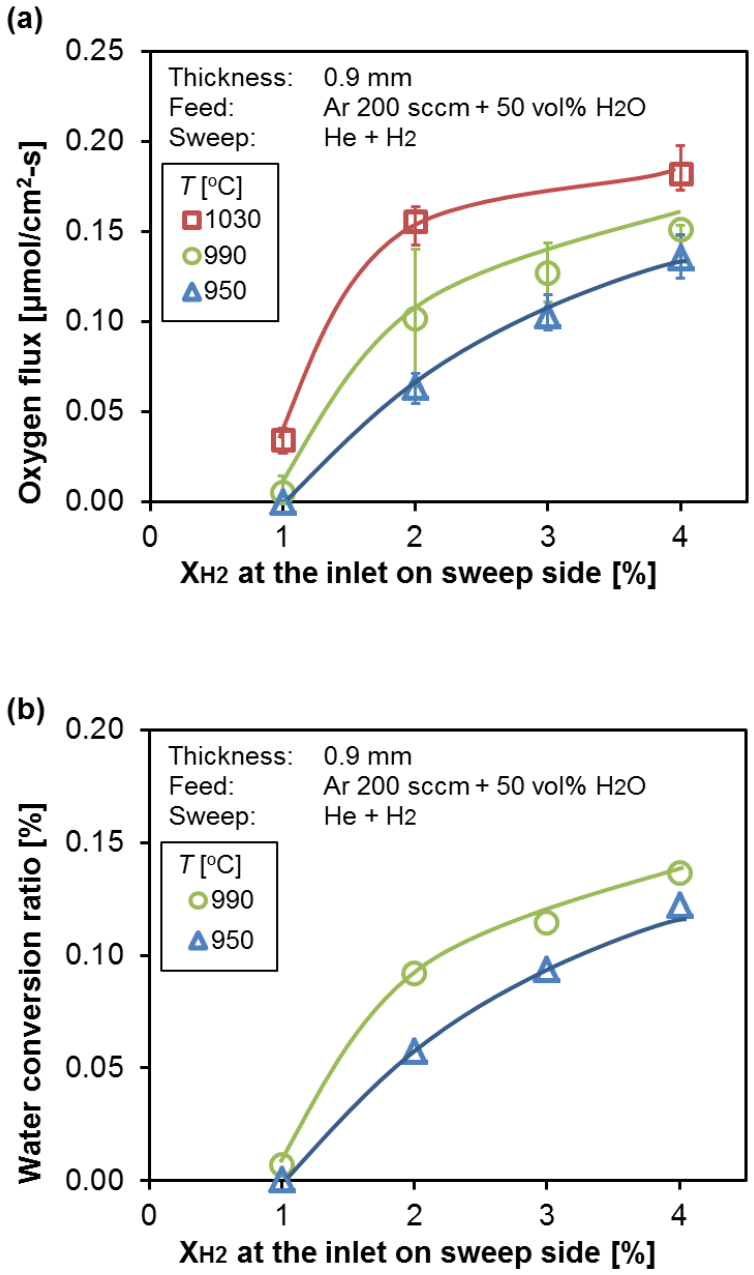

Figure 4.5 With increasing hydrogen concentration at the inlet on the sweep side, both (a) oxygen fluxes and (b) water splitting ratio rise

Additionally, the water splitting ratio (defined in Equation(4-1)) also increases with the hydrogen concentration at the inlet on the sweep side, as shown in Figure 4.5 (b). Thus, the addition of a fuel in the sweep gas mixture is very important for increasing the

water splitting rate and the effectiveness of the overall process. However, highly reducing could decompose the perovskite, which leads to failures of the membrane reactor [39]. Therefore, the stability of the membrane material in a highly reducing environment should be considered and studied. Besides, it is undesirable to use hydrogen as a fuel to enhance water splitting, unless ultrahigh-purity hydrogen is produced [87, 89].

4.2.5 CH_4 as the sweep gas

The previous sections show that water splitting rates, compared to the homogeneous gas phase water thermolysis, were enhanced when using a 0.9-mm thick flat symmetric LCF-91 membrane with inert gas sweep. This is due to the heterogeneous reactions on the perovskite surface and the continuous separation of oxygen. Further enhancement of the water splitting rate requires a larger driving potential for oxygen transport and faster surface kinetics, which can be achieved by adding fuel to the sweep gas. In this section, I will introduce co-produce hydrogen and syngas in a perovskite membrane reactor, and hence CH_4 is added to the sweep gas. The experiments were carried out on the same 0.9 mm thick symmetric membrane as described before at 990 and 1030^{o}C.

Figure 4.6 shows the results with 1 - 5 vol% methane on the sweep side. As the inlet methane concentration is raised, the hydrogen production rate on the feed side increases slowly. Yet we note that the hydrogen production rate with methane on the sweep side is two orders of magnitude lower than that observed in the case with hydrogen sweep under the same fuel concentrations which was shown in Figure 4.5 (a). Clearly, hydrogen is more reactive on the sweep side surface than methane. Additionally, when the total sweep flow rate is raised from 100 to 500 sccm at 990^{o}C, the membrane performance doesn't change, as is shown in Figure 4.6.

At 1030^{o}C, hydrogen production rates from water splitting decrease slightly at higher methane concentrations, but remains within the error bar. This can be a result of coking as reported in the literature [97]. Given the low oxygen flux, carbon formed by methane decomposition on the membrane surface may not be oxidized and instead accumulates on the surface. Solid carbon covers the active membrane surface and decreases the surface reaction rate and hence, the oxygen flux. Further evidence and

discussion on coking and carbon balance from methane partial oxidation will be presented in Chapter 5.

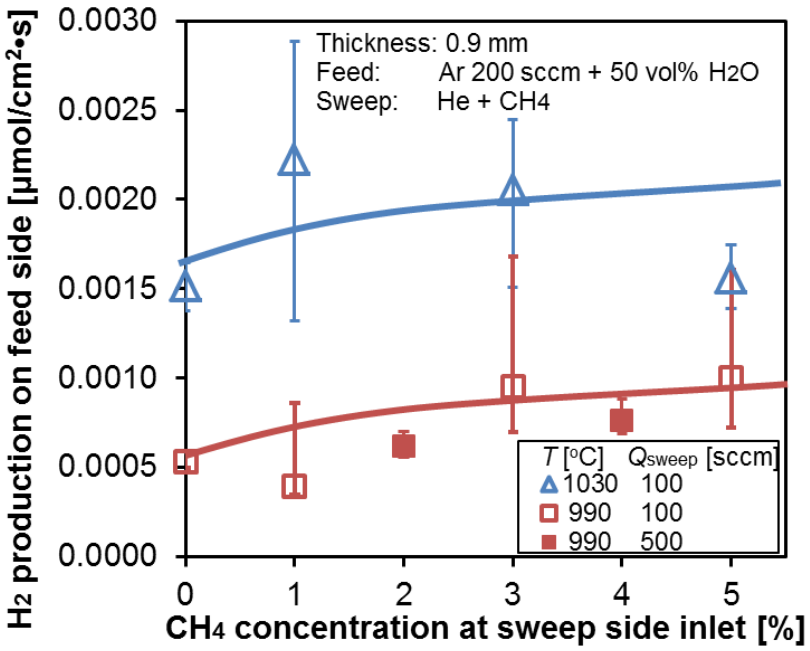

Figure 4.6 For a 0.9 mm thick flat LCF-91 membrane, the methane (1-5 vol%) on sweep side has small enhancement effects on the hydrogen production rate from water splitting at elevated temperatures of 990 and 1030°C

4.3 Kinetic parameters and limiting step(s) identification

In this section, I first present the kinetic parameters for water splitting and compare the resistances for oxygen permeation through an MIEC perovskite membrane with water or air being the oxygen sources and inert or reactive gases being the sweep gas. Limiting steps can be then identified under various operating conditions. A summary of the comparison between resistances of feed side surface reaction R_f, oxygen ion bulk diffusion R_b and sweep side surface reaction R_s is listed in Table 4.3.

4.3.1 Kinetic parameters

Based on the experimental data, the reaction rate constants of k_{f,H_2O} and $\tilde{k}_{r,H_2O}$ for the water splitting/hydrogen oxidation reaction

$$H_2O + V_O^{\bullet\bullet} \underset{}{\overset{k_{f,H_2O}/k_{r,H_2O}}{\rightleftharpoons}} O_O^x + 2h^{\bullet} + H_2 \qquad (4\text{-}2)$$

are fitted using the Arrhenius form $k_i = A_i \bullet \exp(-E_{a,i}/RT)$ by a least squares fitting using air feed-hydrogen sweep and water-feed-hydrogen sweep data. Due to the coke formation, the methane oxidation reaction constant for the flat membrane is only fitted for the data at 990°C, and partial oxidation of methane is assumed to be the sweep reaction due to the limited amount of oxygen available on that side,

$$O_O^x + 2h^\bullet + CH_4 \xrightarrow{k_{f,CH_4}} CO + 2H_2 + V_O^{\bullet\bullet} \quad (4\text{-}3)$$

Although reaction (4-3) cannot describe the complex reactions pathways when methane is on the sweep side of the membrane, the kinetic data is fitted to qualitatively compare the relative significance of the resistances of oxygen permeation. And this fitted value is lower than the rate constant (~0.175) for catalytic methane combustion in packed $La_{0.99}Fe_{1.01}O_{3-\delta}$ catalysts [139], as partial oxidation of methane is less energy favorable than full oxidation [140, 141]. The kinetic parameters on a flat membrane as well as those on a porous support reported later in Chapter 5 are all summarized in Table 4.2.

Figure 4.7 shows that the fitting data agrees very well with the experimental data, which again confirms that the simplified resistance-network permeation model can describe the oxygen flux for water splitting accurately. The discrepancy may come from the simplification of the surface reaction steps and the bulk diffusion dynamics.

Table 4.2 Reaction kinetic parameters for oxygen surface reactions for LCF-91 membranes

Oxygen surface reaction		***A***		***E_a***	
		Value	**Unit**	**Value**	**Unit**
$H_2O + V_O^{\bullet\bullet} \leftrightarrow O_O^x + 2h^\bullet + H_2$	k_{f,H_2O}	193	[cm^4/mol•s]	7.88E+3	[J/mol]
	$\tilde{k}_{r,H_2O}$	5.39E+4	[cm^4/mol•s]	9.10E+4	[J/mol]
$CH_4 + O_O^x + 2h^\bullet \rightarrow 2H_2 + CO + V_O^{\bullet\bullet}$	$\tilde{k}_{f,CH_4}(990^oC)$	0.029	[cm^4/mol•s]	/	/
	$\tilde{k}_{f,CH_4}$ (porous)	1.68E+8**	[cm^4/mol•s]	1.726E+5	[J/mol]
**: This value is fitted from stable performances of Ni/LCF-91 porous layer after the initial degradation as shown in [60], as the initial degradation is due to the close of pores in the porous layer which decreases the effective surface area					

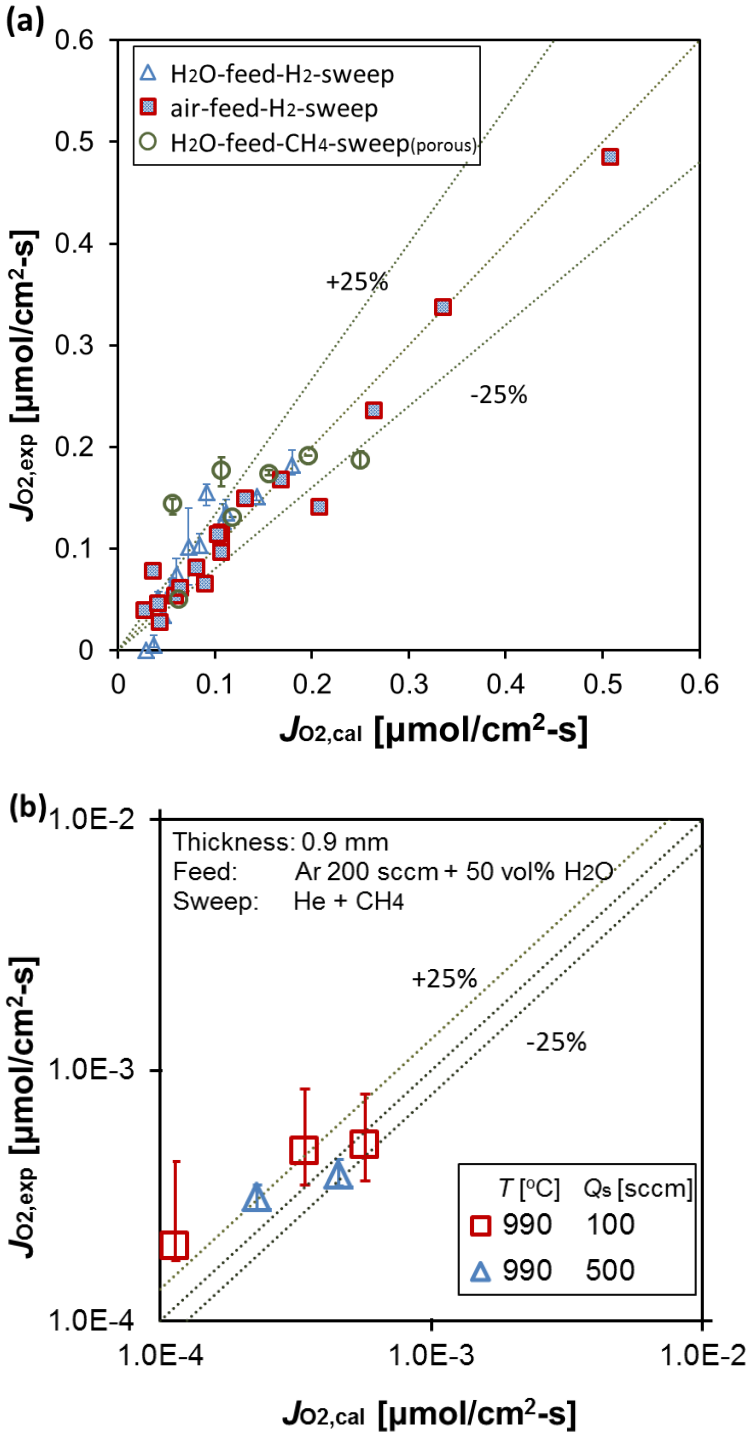

Figure 4.7 Kinetic data fitting shows good agreement with the experimental values within ±25% in most of the cases (a) either H_2O or air feed with H_2/CH_4 sweep, (b) H_2O feed with CH_4 sweep on a flat membrane

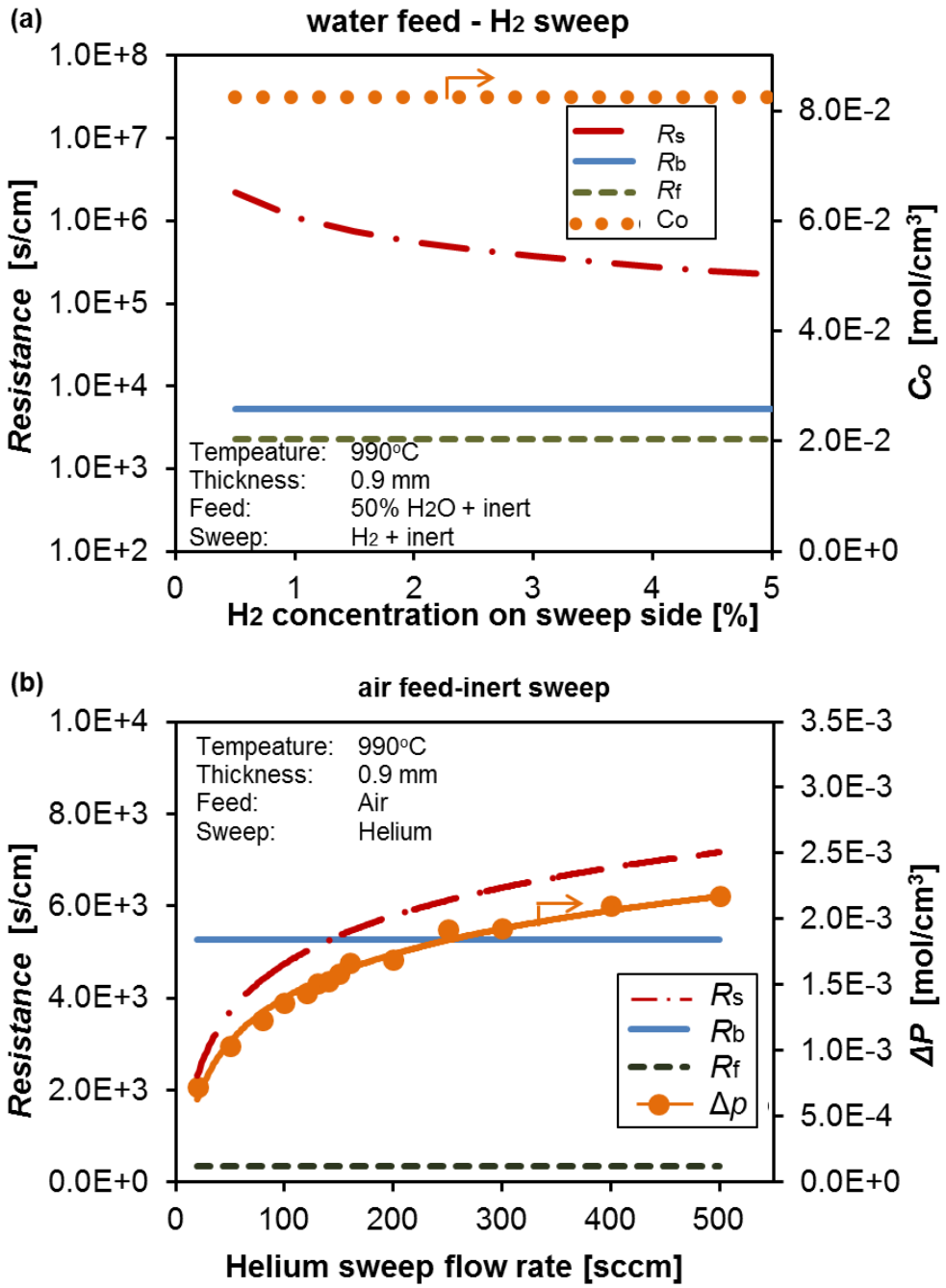

Figure 4.8 Resistances and potential difference in the five cases at 990°C reported in section 4.2: (a) water feed-H_2 sweep, (b) air feed-inert sweep, (c) air feed-fuel sweep, (d) water feed-inert sweep and (e) water feed-CH_4 sweep

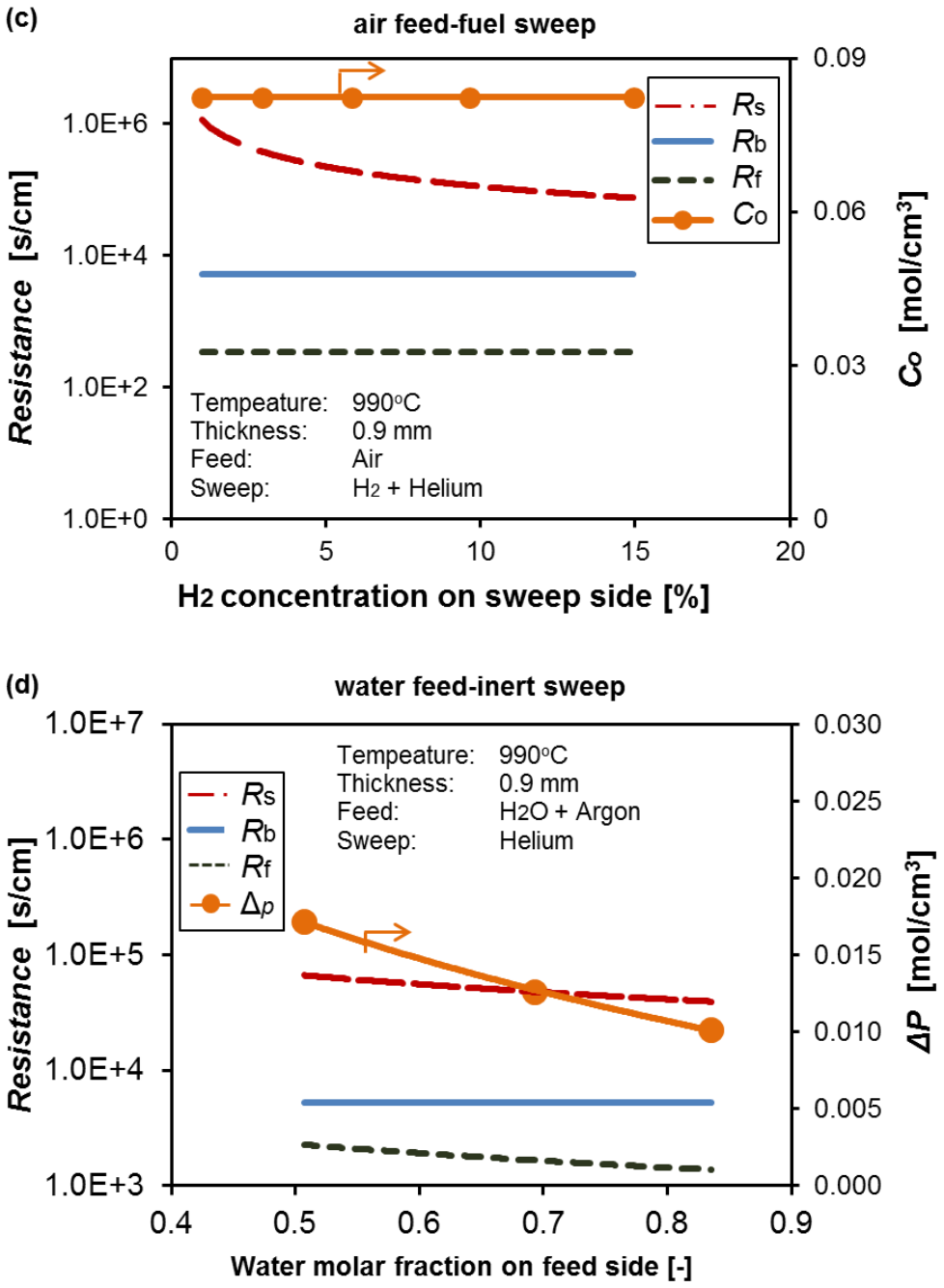

Figure 4.8 Resistances and potential difference in the five cases at 990°C reported in section 4.2: (a) water feed-H_2 sweep, (b) air feed-inert sweep, (c) air feed-fuel sweep, (d) water feed-inert sweep and (e) water feed-CH_4 sweep (continued)

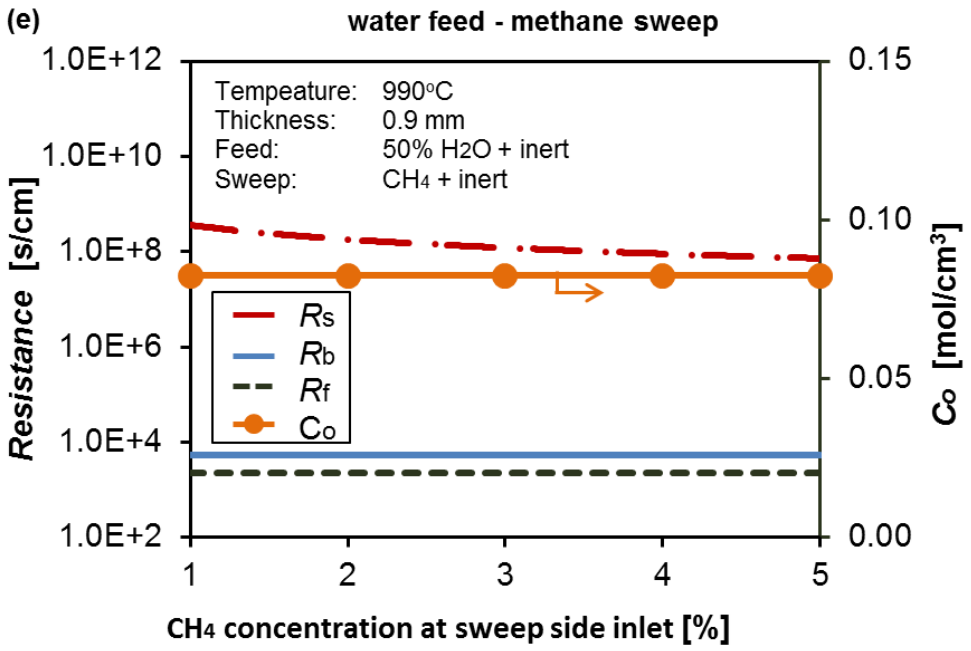

Figure 4.8 Resistances and potential difference in the five cases at 990°C reported in section 4.2: (a) water feed-H_2 sweep, (b) air feed-inert sweep, (c) air feed-fuel sweep, (d) water feed-inert sweep and (e) water feed-CH_4 sweep (continued)

4.3.2 Water feed-H_2 sweep

First, we discuss the case when the oxygen source is water vapor and the sweep gas is hydrogen. In this case, the feed side surface reaction is the forward water splitting

$$H_2O + V_O^{\bullet\bullet} \rightarrow O_O^x + 2h^{\bullet} + H_2 \tag{4-4}$$

and the sweep side surface reaction is hydrogen oxidation (reverse water splitting)

$$O_O^x + 2h^{\bullet} + H_2 \rightarrow H_2O + V_O^{\bullet\bullet} \tag{4-5}$$

Referring to Table 3.1, the oxygen flux is

$$J_{O_2} = \frac{1}{2} J_V = \frac{1}{2} \cdot \frac{C_O}{\frac{1}{k_{f,H_2O} C'_{H_2O}} + \frac{t}{D_v} + \frac{1}{\tilde{k}_{r,H_2O} C''_{H_2}}} . \tag{4-6}$$

The resistances are shown in Figure 4.8 (a). The bulk resistance and the feed side surface reaction resistance remain constant by construction. As the hydrogen concentration on the sweep side increases, the sweep side surface reaction resistance drops. The sweep side surface reaction resistance is the largest among the three, and it is

the limiting steps for this 0.9-mm thick membrane, when 50 vol% water is the oxygen source and hydrogen-helium mixture (1 – 5 vol% H_2) the sweep gas.

4.3.3 Air feed-inert sweep

In the case where oxygen source is air and the sweep gas is inert, only the oxygen surface incorporation/dissociation,

$$\frac{1}{2}O_2 + V_O^{\bullet\bullet} \underset{}{\overset{k_{f,O_2}/k_{r,O_2}}{\rightleftharpoons}} O_O^x + 2h^{\bullet} \tag{4-7}$$

is involved. In this case, the oxygen flux is:

$$J_{O_2} = \frac{1}{2}J_V = \frac{1}{2}\cdot\frac{\left(\frac{\tilde{k}_{r,O_2}C_O}{\tilde{k}_{r,O_2}+k_{f,O_2}C''^{0.5}_{O_2}} - \frac{\tilde{k}_{r,O_2}C_O}{\tilde{k}_{r,O_2}+k_{f,O_2}C'^{0.5}_{O_2}}\right)}{\frac{1}{\tilde{k}_{r,O_2}+k_{f,O_2}C'^{0.5}_{O_2}} + \frac{t}{D_v} + \frac{1}{\tilde{k}_{r,O_2}+k_{f,O_2}C''^{0.5}_{O_2}}}\cdot \tag{4-8}$$

As in Figure 4.8 (b), the bulk resistance and the feed side surface reaction resistance remain constant by construction. Both the potential difference ΔP and the sweep side surface reaction resistance R_s increase with helium sweep flow rate. The growth of ΔP and R_s are associated with the drop in oxygen concentration on the sweep side when helium sweep rate increases (see Figure 3.2). However, as ΔP grows faster than R_s, the overall oxygen flux in this case increases at higher helium flow rate.

Additionally, as shown in Figure 4.8 (b), the feed side surface reaction resistance is the lowest among the three resistances. Yet there are two regimes that can be identified by comparing the bulk resistance and sweep side surface reaction resistance for this 0.9 mm thick LCF-91 membrane at 990 ^oC. At low flow rate with the helium sweep rate lower than 150 sccm, the bulk resistance dominates; but at high flow rate regime, the sweep side surface reaction resistance dominates.

4.3.4 Air feed-fuel sweep

The two cases discussed above involve one type of surface reactions only, either oxygen incorporation/dissociation or forward/reverse water splitting. Yet in the air feed-fuel sweep case, oxygen incorporation/dissociation (4-7) occurs on the feed side while reverse water splitting (or hydrogen oxidation, (4-5)) takes place on the sweep side.

From Table 3.1, the overall oxygen flux is,

$$J_{O_2} = \frac{1}{2} J_V = \frac{1}{2} \cdot \frac{\left(C_O - \frac{\tilde{k}_{r,O_2} C_O}{\tilde{k}_{r,O_2} + k_{f,O_2} C'^{0.5}_{O_2}} \right)}{\frac{1}{\tilde{k}_{r,O_2} + k_{f,O_2} C'^{0.5}_{O_2}} + \frac{t}{D_v} + \frac{1}{\tilde{k}_{r,H_2O} C''_{H_2}}} \cdot \qquad (4\text{-}9)$$

As shown in Figure 4.8 (c), the potential difference, the feed side surface reaction resistance and the bulk diffusion resistance remain constant by construction. And feed side surface reaction resistance R_f is the lowest among the three resistances which is the same with that in air feed-inert sweep case. Yet sweep side surface reaction resistance R_s drops at higher hydrogen concentration. Therefore, the enhancement of oxygen flux by adding hydrogen on the sweep side is mainly due to the decrease of sweep side surface reaction resistance.

4.3.5 Water feed-inert sweep

Another case that involves both oxygen incorporation/dissociation (4-7) and forward water splitting (4-4) is the one with water as the feed gas and helium as the sweep gas. Results in previous section show that the oxygen flux is dependent on the mixture flow rate and water concentration on the feed side, but independent on the helium sweep flow rate.

From Table 3.1, the oxygen flux in this case is

$$J_{O_2} = \frac{1}{2} J_V = \frac{1}{2} \cdot \frac{\left(\frac{\tilde{k}_{r,O_2} C_O}{\tilde{k}_{r,O_2} + k_{f,O_2} C''^{0.5}_{O_2}} \right)}{\frac{1}{k_{f,H_2O} C'_{H_2O}} + \frac{t}{D_v} + \frac{1}{\tilde{k}_{r,O_2} + k_{f,O_2} C''^{0.5}_{O_2}}} \cdot \qquad (4\text{-}10)$$

Figure 4.8 (d) shows the three resistances and potential difference corresponding to the case where the feed side water concentration changes. For this 0.9-mm thick membrane, R_f is the lowest among the three resistances and R_s is the highest. The oxygen permeation process is limited by the sweep side surface reaction rate. Besides, with increasing water concentration on the feed side, the feed and sweep side surface reaction resistances as well as the potential difference drops.

4.3.6 Water feed–CH_4 sweep

In the case when methane is the sweep gas, partial oxidation of methane is assumed to be the reaction on the sweep side due to the limited amount of oxygen available for the reaction.

From Table 3.1, the oxygen flux is

$$J_{O_2} = \frac{1}{2} J_V = \frac{1}{2} \cdot \frac{C_O}{\frac{1}{k_{f,H_2O} C'_{H_2O}} + \frac{t}{D_v} + \frac{1}{\tilde{k}_{f,CH_4} C''_{CH_4}}} . \qquad (4\text{-}11)$$

Figure 4.8 (e) shows that the limiting step for the oxygen flux is the surface reaction on the sweep side, when methane concentration is 1 – 5 vol%. At higher methane concentration, the sweep surface reaction resistance decreases a bit, but remains the highest among the three resistances. At 990^{o}C, the sweep surface reaction resistance is in the range of 0.7 – 3.5 $\times 10^8$ S/cm when methane concentrations change from 1 to 5 vol%, while the values are 0.28 – 1.11 $\times 10^6$ S/cm for the same concentration of hydrogen on the sweep side.

4.3.7 Comparisons between different conditions

The resistances to the oxygen permeation through the 0.9-mm thick LCF-91 membrane with various oxygen sources and sweep gases are summarized in Table 4.3. For the 0.9 mm thick membrane, the bulk diffusion is the limiting step in the air feed-helium sweep case; in other cases, the bulk resistance, R_b, is orders-of-magnitude lower than the highest resistance.

In the air feed cases, the feed side surface reaction resistance, R_f, can be neglected with either inert or reactive sweep gas; yet the sweep side surface reaction resistance R_s plays the important role. In the air feed-inert sweep case, R_s is in the same order of magnitude with R_b; in the air feed-fuel sweep case, R_s becomes the highest but drops and approaches the values of R_b at higher fuel concentration. Therefore, apart from utilizing thinner LCF-91 membranes, improvements should be applied on the sweep side such as increasing surface area and applying catalysts to enhance oxygen dissociation or fuel oxidation rates, and hence, to increase the overall oxygen flux.

In the water feed cases, R_s dominates no matter when the sweep gas is inert or reactive, and R_f is the smallest similar to the air feed cases. Therefore, for the water splitting reactor with LCF-91 membrane, improvements on the sweep sides are also necessary.

Table 4.3 Summary of the importance of the resistances for oxygen permeation through a 0.9-mm thick LCF-91 membrane at 990 ^{o}C

Oxygen source		**Air**		**Water vapor**		
Sweep gas		Helium	1-15 vol% H_2 + helium	Helium	1-5 vol% H_2 + helium	1-5 vol% CH_4 + helium
Resistance comparison	$\boldsymbol{R_f}$	3	3	3	3	3
	$\boldsymbol{R_b}$	1	2	2	2	2
	$\boldsymbol{R_s}$	1	1	1	1	1
1 is the largest, and 3 is the smallest.						

4.4 Membrane stability under water splitting conditions

4.4.1 Long term stability test

A long term stability test was carried out for the water vapor as oxygen source in order to verify that this LCF-91 oxygen permeable perovskite membrane is stable in the experimental environments in this study. Results are shown in Figure 4.9 (a), which shows stable oxygen fluxes through the membrane were maintained over a 30-hour period. After 60 hours of exposure to water vapor at the feed side, the oxygen source was switched to air and oxygen permeation rate was measured. As shown in Figure 4.9 (b), the oxygen fluxes from air are within the error bar, which means that exposing to high concentration of water vapor (50.7 to 83.5 vol%) on the feed side didn't deteriorate the oxygen permeation performances of the membrane.

4.4.2 Membrane morphology and lattice structure

The characteristics of the membrane bulk and surface were examined by the SEM and XRD to study the surface morphology and lattice structures. Figure 4.10 (a) – (c)

shows the SEM images of the LCF-91 membrane before and after oxygen permeation experiments with air or water vapor as the oxygen source. The membrane before experiments shows very fine grains with sizes ranging from 0.5 -5 μm. Yet after the experiments, the surface morphologies change on both feed and sweep sides. On the sweep side where surface reduction reaction occurs, the grains became coarse with smaller sizes. On the feed side where oxygen incorporates into the membrane surface, smaller particles appear on the surfaces and the grain boundaries are obscure.

Figure 4.10 (d) compares the XRD patterns of the new membranes and the used membrane surfaces. The sweep side shows very good LCF-91 peaks, while the feed side shows lanthanum silicate impurity peaks. The source of the silicon on the surface is likely to be the silica gel desiccant on the downstream of the reactor outlet used to dry the gas samples before entering the gas chromatographer. Despite the changes on the morphologies as well as the silica impurities, the oxygen permeation performances of the membrane didn't change during the experiments.

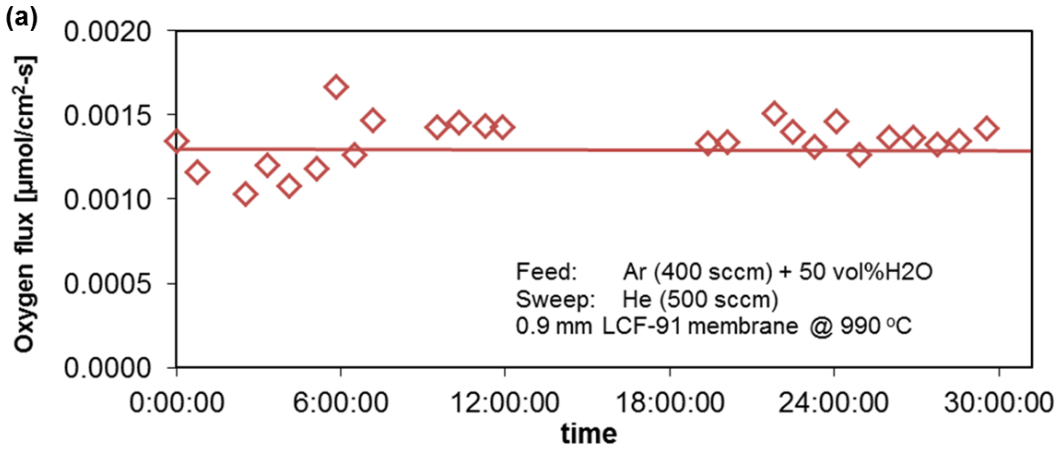

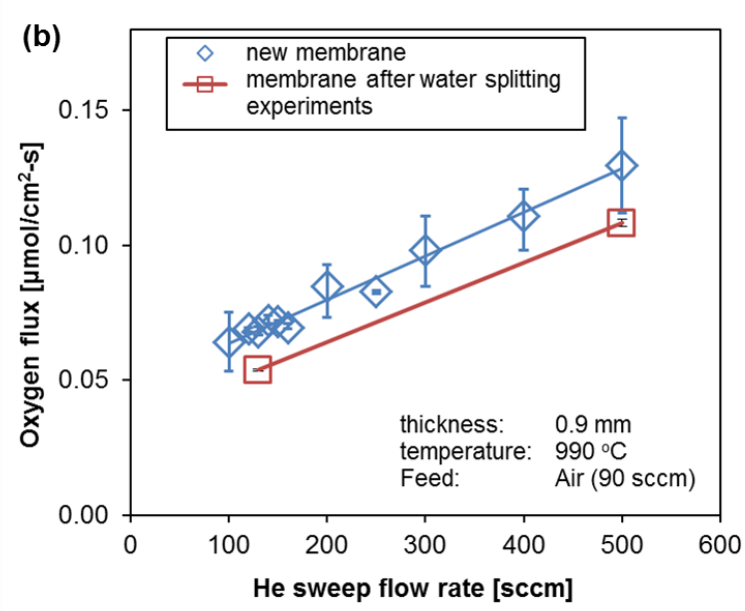

Figure 4.9 Long term stability studies of membrane using water as oxygen source. (a) Oxygen flux (water thermolysis rate) keeps constant for 30 hours of experiments. (b) After 60 hours of exposure to water vapor on the feed side, the oxygen flux of air separation for this 0.9 mm LCF-91 membrane didn't degrade

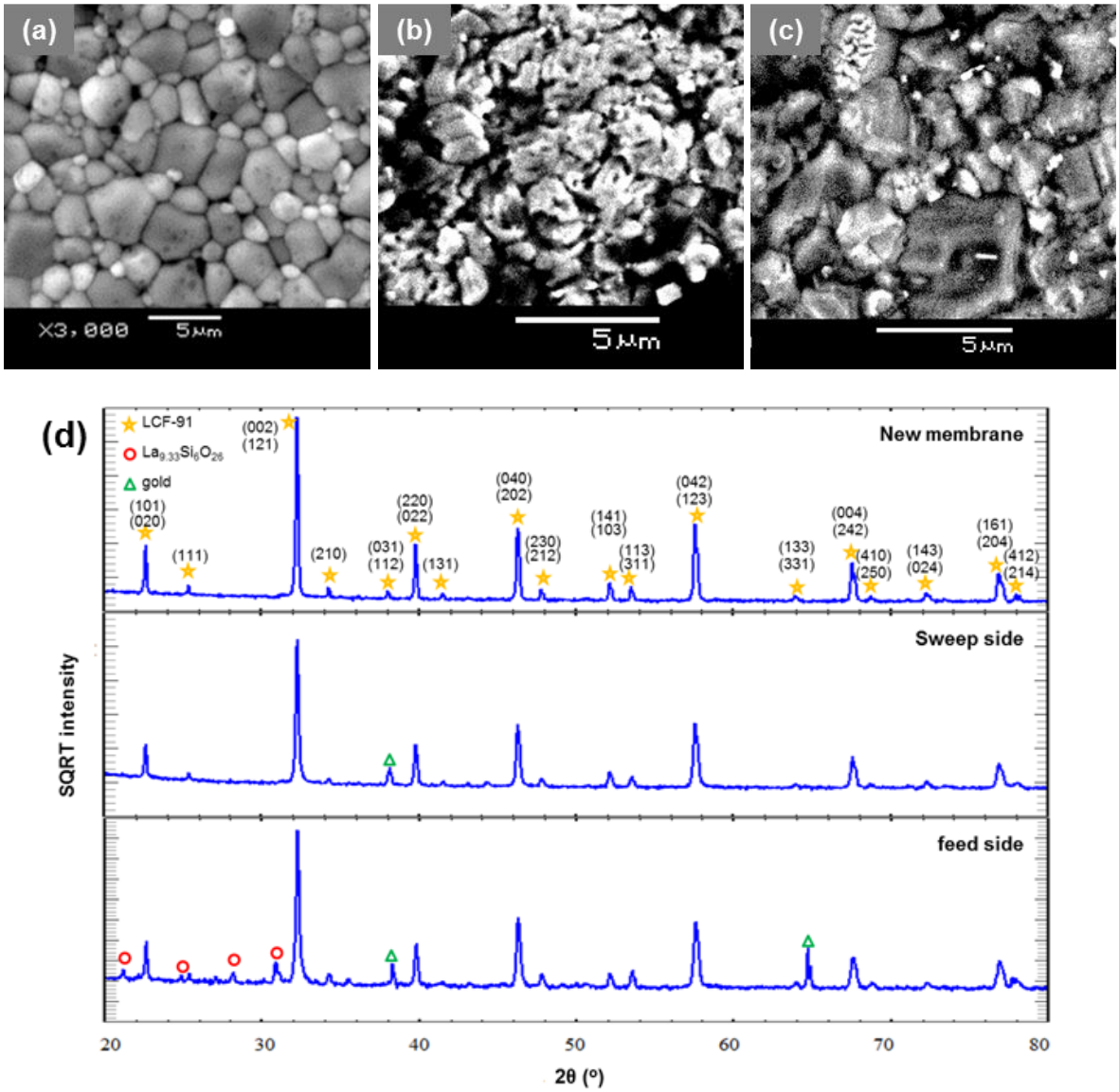

Figure 4.10 Characterization of LCF-91 membranes before and after experiments: SEM images of (a) a new membrane, (b) sweep side and (c) feed side of a used membrane and (d) XRD profiles (diffraction plane numbers of LCF-91 are listed by the XRD peaks.)

4.5 Conclusions

Mixed ionic and electronic conducting membranes have the capabilities of permeating oxygen selectively. Oxygen separation from air by MIEC membranes has been studied extensively in the literature, but only a few studies present enhanced water splitting supported by an MIEC membrane reactor. In this work, we present the LCF-91

membrane-supported water splitting in a lab-scale button-cell reactor with inert or reactive sweep gas. As oxygen flux is a good illustrator for water thermolysis rate, we study the oxygen fluxes under various operating conditions such as the gas flow rates and species concentrations on feed or sweep sides. Oxygen flux from air separation is also studied, and three-resistance models for water thermolysis and air separation are compared. Results show the following:

(1) The limiting step of oxygen permeation process is different depending on both the oxygen source and the sweep gas. A summary is shown in Table 4.3, comparing the resistances of the five cases studied in this chapter.

(2) Water splitting rate is enhanced by the LCF-91 membranes compared to the homogeneous water thermolysis case. With inert or reactive sweep gas, the limiting step is oxygen reaction on the sweep side. The water splitting rate is enhanced with increasing hydrogen concentration, as the sweep side surface reaction resistance drops.

(3) Methane is less reactive than hydrogen as the sweep gas, with reaction rate two orders of magnitude lower than that of hydrogen oxidation. Therefore, further enhancement for methane partial oxidation is required to utilize methane as the sweep gas to enhance water splitting on the feed side.

(4) Long term stability tests were carried out and there is no degradation of oxygen flux with either air or water vapor as the oxygen sources. Yet surface morphologies changes as well as impurities were identified by SEM and XRD results

Acknowledgement:

Contents in this chapter have been firstly published in

[1] Wu XY, Chang L, Uddi M, Kirchen P, Ghoniem AF. Toward enhanced hydrogen generation from water using oxygen permeating LCF membranes. *Physical Chemistry Chemical Physics.* 2015, 17(15): 10093 - 10107.

[2] Wu XY, Ghoniem AF, Uddi M. Enhancing co-production of H_2 and syngas via water splitting and POM on surface-modified oxygen permeable membranes. *AlChE Journal.* 2016 62(12): 4427 - 4435.

This page is intentionally left blank

Chapter 5

Enhanced Co-Production of H_2 and Syngas on LCF Membranes with Catalytic Porous Layers

5.1 Introduction

Syngas, a mixture of H_2 and CO, is an important feedstock for the production of synthetic fuels and chemicals, such as methanol and ammonia which are among the top ten chemicals produced annually in the world [9, 14]. Each chemical requires an optimum syngas composition in terms of the H_2/CO ratio [83]. Four approaches have been used to produce syngas from methane; each results in a unique H_2/CO ratio:

(1) Dry reforming (H_2/CO ratio = 1)

$$CH_4 + CO_2 \leftrightarrow 2CO + 2H_2 \qquad \Delta H_{298}^0 = 247 kJ/mol \qquad (5\text{-}1)$$

(2) Partial oxidation (H_2/CO ratio = 2)

$$CH_4 + \frac{1}{2}O_2 \leftrightarrow CO + 2H_2 \qquad \Delta H_{298}^0 = -36 kJ/mol \qquad (5\text{-}2)$$

(3) Steam reforming (H_2/CO ratio = 3)

$$CH_4 + H_2O \leftrightarrow CO + 3H_2 \qquad \Delta H_{298}^0 = 206 kJ/mol \qquad (5\text{-}3)$$

(4) Autothermal reforming (H_2/CO ~ 2.15)

$$CH_4 + 0.425O_2 + 0.15H_2O \leftrightarrow CO + 2.15H_2 \quad \Delta H_{298}^0 \approx 0 \ kJ/mol \qquad (5\text{-}4)$$

Among these, partial oxidation of methane (POM) produces syngas with a stoichiometric H_2/CO ratio of 2.0, making it an optimum reaction for gas-to-liquids (GTL) process.

As cited by the IEA [142], global consumption of hydrogen is approximately 7.2 exajoules (EJ) annually. Hydrogen can be produced from syngas by water-gas-shift (WGS) reaction with CO_2 separation, but the downstream reactors increase the cost and complexity. Besides, the impurities from syngas, i.e., sulfur and CO are poisonous for applications such as proton-exchange membrane (PEM) fuel cell.

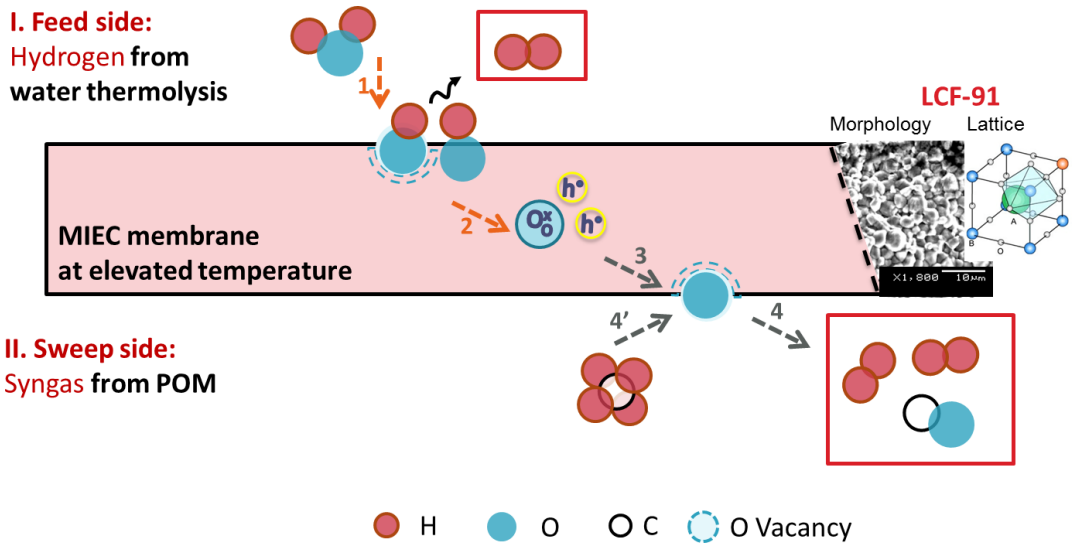

Figure 5.1 A schematic diagram showing the oxygen transport process with water splitting on the feed side and partial oxidation of methane (POM) on the sweep side. LCF-91 perovskite membrane is used to illustrate the process in a dense mixed ionic-electronic conductive (MIEC) membrane

In this chapter, water splitting is integrated with partial oxidation of methane to co-produce separated streams of H_2 and syngas (H_2/CO = 2) simultaneously in a single oxygen permeable membrane reactor. A schematic graph is shown in Figure 5.1. On the feed side, water reacts with oxygen vacancies to produce hydrogen while oxygen incorporates into the lattice. Lattice oxygen diffuses to the sweep side where it reacts with fuels or is swept away as oxygen molecules. Thus, water dissociation on the feed side is no longer limited by thermodynamic equilibrium as O_2 is removed. Besides, the permeation of oxygen ions (lattice oxygen) to the sweep side can be optimized to suppress carbon formation during hydrocarbon fuel reforming. As methanol is among the top five large-volume products that dominate the global energy use in the chemical industry [14], the optimum H_2/CO ratio from the sweep side can benefit the GTL process. Additionally, when the heat source is solar energy, this co-production technology can be used as an energy storage technology.

This membrane approach is different from chemical looping or redox cycles for hydrogen/syngas production. In redox cycles, water and methane react with an oxygen carrier (i.e., Fe_2O_3 [143, 144], CeO_2 [145, 146] and $La_{0.8}Sr_{0.2}FeO_{3-\delta}$ [147]) cyclically to produce hydrogen and syngas separately in a fluidized bed [144] or a rotary reactor [148]. An oxygen permeable membrane reactor combines the cyclical oxidization and reduction processes into one single unit. Both technologies are still under development.

Several high performance oxygen permeable materials have been proposed to support water splitting, such as single phase perovskites, $BaCo_xFe_yZr_{1-x-y}O_{3-\delta}$ (BCFZ) [52, 65], $La_{0.3}Sr_{0.7}FeO_3$ [69], $La_{0.6}Sr_{0.4}Co_{0.2}Fe_{0.8}O_{3-\delta}$ [68] and $La_{0.7}Sr_{0.3}Cu_{0.2}Fe_{0.8}O_{3-\delta}$ [48], mixed fluorites-metal, CeO_2-Gd [73] and $Ce_{0.8}Gd_{0.2}O_{1.9-\delta}$-Cu [74] and other oxides, $SrFeCo_{0.5}O_x$ [55]. At intermediate and higher temperatures, these are all mixed ionic-electronic conductive materials. When methane is used as a sweep gas, the highest reported hydrogen production rate from water splitting is 3.4 μmol/cm^2•s on a BCFZ membrane with 75 vol% water-feed and 10 vol% methane-sweep at 950^{o}C [52]. A summary of the literature on co-production in an oxygen permeable membrane reactor has been shown in Table 1.7. However, high performance Ba and Co containing perovskites often suffers from degradation such as carbonate formation or cobalt segregation, respectively [39]. Phase segregation [68], pores [54] as well as surface morphology changes [72] have also been observed during water splitting.

Much is yet to be learned regarding the oxygen transport process and the rate limiting steps, especially in case of co-production of H_2 and syngas. Therefore, in this chapter, I will present the study using $La_{0.9}Ca_{0.1}FeO_{3-\delta}$ (LCF-91) membranes to examine this co-production process. Results show that LCF-91 membranes can be applied to co-produce H_2 and syngas (H_2/CO = 2) from water splitting and POM, respectively, at temperatures around 990^{o}C. As Chapter 4 identifies the rate limiting step to be the POM reaction, surface modification such as adding a porous layer and nickel catalysts are applied to overcome this barrier as well as to increase the selectivity of syngas produced from methane oxidation. Experimental results show that surface modification on the sweep side can enhance water splitting on the feed side by two orders of magnitude, and syngas with H_2/CO = 2 is produced with negligible solid carbon leaving the reactor.

5.2 Experimental

The oxygen permeable material studied is $La_{0.9}Ca_{0.1}FeO_{3-\delta}$ (LCF-91). The flat dense membranes and the LCF-91 powders are provided by Ceramatec. The stoichiometry is verified by EDX (Table 2.1). The properties of LCF such as charged species diffusivity [103, 112, 149] and catalytic activities for hydrocarbon oxidations [150] can be found in the literature. The oxygen permeability of dense LCF-91 membranes at elevated temperatures with air source has also been reported [80, 81].

The porous layers on the flat dense membranes are fabricated according to a two-step method. LCF-91 powders were mixed with graphite powders (<20μm, Sigma-Aldrich®) at 50 vol% in mortar and pestle for twenty minutes. The perovskite particles before sintering have surface area of 1.8 m^2/g. The mixed powders were compressed into a flat circular plate at 10 metric ton-force for 1 minute. After that, the green plate was attached to a flat dense membrane and together they were sintered at 1450^oC for half an hour in air (including slow heat-up and cool down at ramp rates around 10^oC, the entire process takes around 24 hours). The diameter of the porous layer is by design smaller than the dense membrane so that the gold sealant can keep the membrane reactor air-tight. Yet since the porous layer shrinks after sintering, the actual thickness and diameter of the porous layer are measured and reported in Table 5.1. Following sintering, the porous layer and the original membrane were well attached (i.e., they couldn't be separated simply by hand).

Table 5.1 Summary on membrane configurations in this study

		Original Membrane	**Modified Membrane 1**	**Modified Membrane 2**
thickness	**Dense [mm]**	0.9	0.5	0.9
	Porous [mm]	/	0.4	0.4
Effective diameter	**Dense [mm]**	12.70	12.70	12.70
	Porous [mm]	/	12.37	11.53
Catalysts		/	/	Nickel

The membranes were inspected using SEM and EDX on JEOL 5910 General Purpose SEM to identify the surface morphology and the element distribution. SEM images in Figure 5.2 shows the surface morphologies of (a) the dense and (b) the porous surfaces as well as (c) the cross-section of the porous layer after sintering. The grain sizes are in the order of magnitude of several micrometers on both the dense and porous membrane surfaces. Pores with large sizes in the order of magnitude of ten micrometers were formed on the porous membrane after the graphite was burnt off. These pores can also be identified in the cross-section of the porous layer as in Figure 5.2 (c).

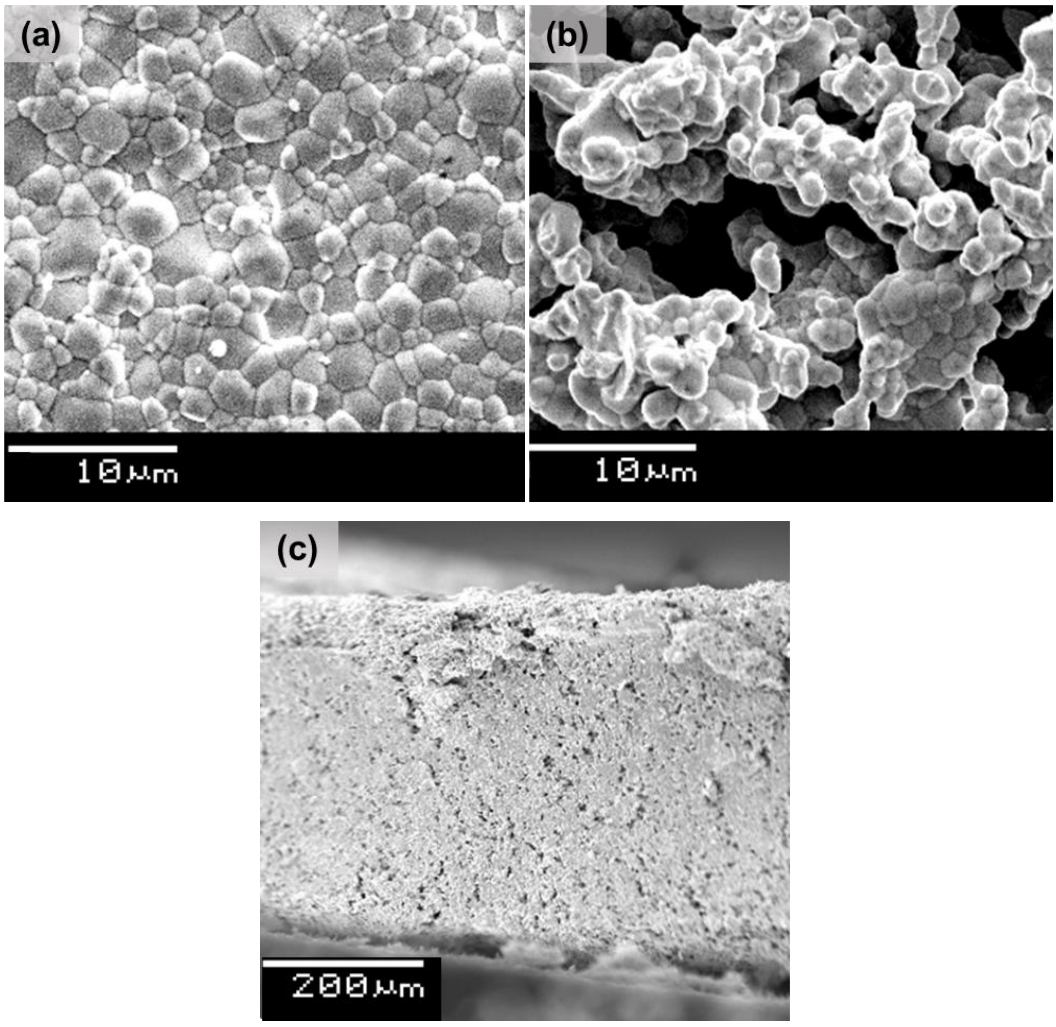

Figure 5.2 The SEM images of the membrane (a) Dense membrane surface has grain sizes in the order magnitude of micrometers; (b) Porous membrane surface shows the large pores in sizes of several micrometers; (c) The cross-section of the porous membrane shows the pores along the thickness of the membrane

Nickel catalyst particles were applied to the porous layer by wet impregnation method. The asymmetric membrane is soaked in 1M $Ni(NO_3)_2$ solution (prepared from $Ni(NO_3)_2$ $6H_2O$, Sigma-Aldrich®) for 24 h. Then the liquid on the flat membrane surface was wiped out by tissue paper. The membrane was dried in air at room temperature for 24 h, heated up to 400^{o}C and kept for 30 minutes, and then up to 900^{o}C and kept for 30 minutes.

The nickel catalyst in the porous layer was examined in SEM and EDX after the wet impregnation. In the EDX signals in Figure 5.3 (a), we can clearly identify the peak corresponding to nickel. The SEM image in Figure 5.3 (b) shows that after wet impregnation the morphology of the porous layer doesn't change and the grain sizes are in the order of magnitudes of one micrometer. The weight of the membrane is measured before and after wet impregnation, and the concentration of nickel particles in porous layer was 0.4 wt% in the porous layer. The diameter of the porous layer is 11.53 mm, and the thicknesses of the porous layer and the dense membrane are 0.4 and 0.9 mm, respectively.

We also examined the porous layer after splitting experiments. The EDX analysis shows that the element distribution of the porous layer doesn't change obviously after the experiments, as is shown in Figure 5.3 (a). Besides, the SEM images in Figure 5.3 (c) show that the porous layer still maintain the high porosity and the size of the grains and the pores are still in the order of magnitude of several micrometers. As the grain clusters are ~10 μm in diameter, assuming a sphere structure, the sintered porous layer has an estimated surface area of 938 cm^2/g. As 0.135 g of LCF-91 powder was used to fabricate the porous layer, the estimated surface area on the sweep porous layer is more than 126 cm^2, which is about two orders of magnitude higher than the flat surface area.

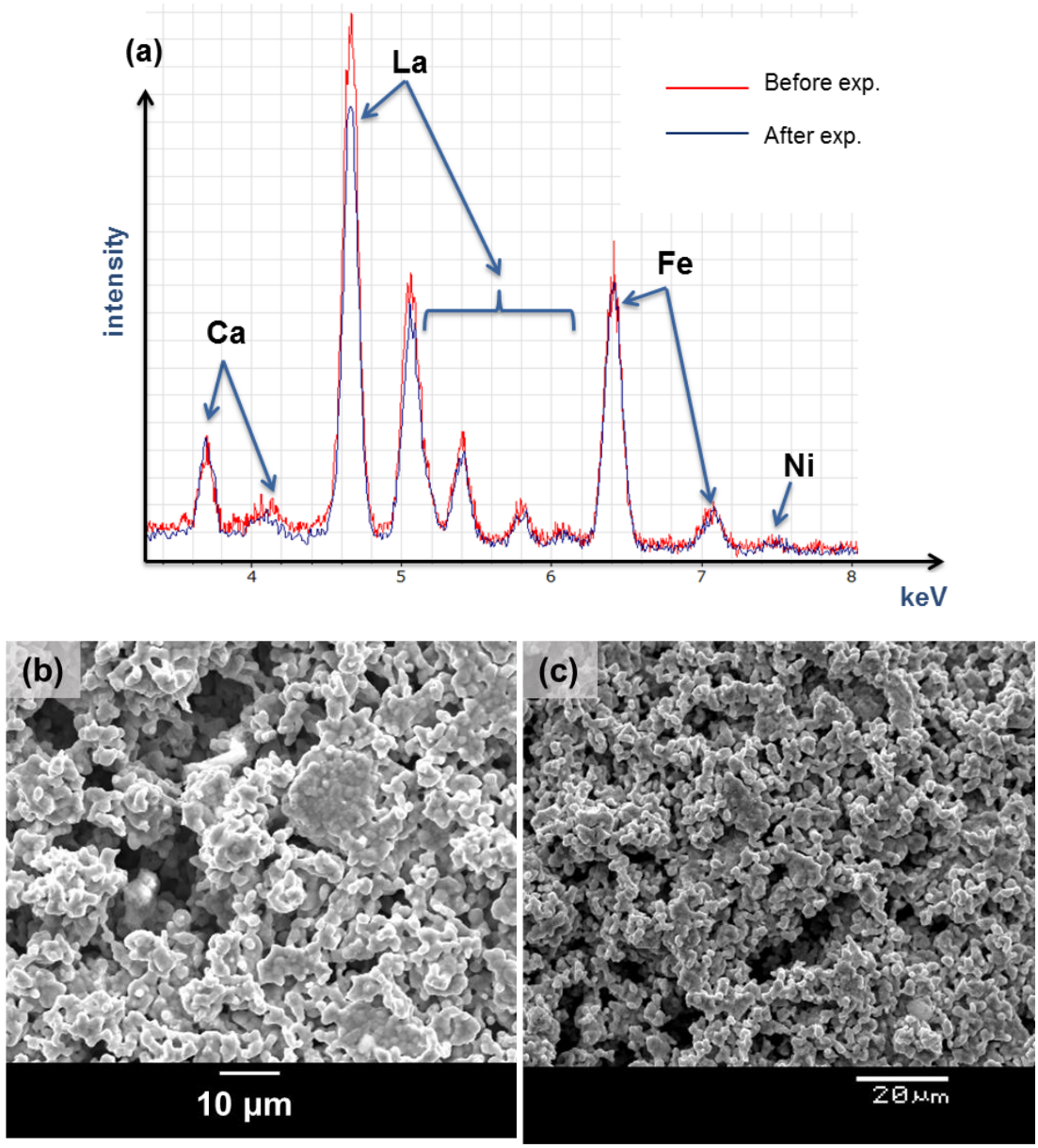

Figure 5.3 (a) The EDX analysis shows the existence of nickel on the porous layer after wet impregnation (before and after splitting experiments); (b) The SEM image shows the morphology of the porous layer after the wet impregnation of the nickel catalysts; (c) SEM images show that the porous layer maintains the same high porosity after the splitting experiments

5.3 Adding a porous layer for performance enhancement

5.3.1 Hydrogen production from water splitting

Methods to improve fuel-surface reactivity such as adding a porous layer and catalysts, i.e., Pt and/or CeO_2 on the sweep side, and oxygen reduction reactive layer on the feed side such as $La_{0.8}Sr_{0.2}FeO_3$ (LSF) (when air is used to oxidize the surface) have been found to enhance the oxygen flux through an LCF-91 membrane when CO is used as the sweep gas [150]. In this study, we focus on the sweep side given that the reaction on that side is the limiting step as discussed in section 4.3.6. First, we increase the effective sweep side surface area by attaching a porous LCF-91 layer onto that side. The dimensions of this membrane are shown in Table 5.1 as "modified membrane 1".

Results for this new configuration are shown in Figure 5.4. The zoom-in figure at the top left shows the hydrogen production rate from water splitting in the corresponding inert sweep case is 6.3×10^{-4} μmol/cm^2•s, which is in the same order of magnitude as that for the 0.9-mm symmetric membrane under the same operating conditions. With the addition of 1 vol% methane, the hydrogen production rate from water splitting increases by two orders of magnitude to 0.077 μmol/cm^2•s. Further increase of the inlet methane concentration leads to higher hydrogen production until a plateau of 0.15 μmol/cm^2•s is reached at around 2 - 3 vol%.

The significant enhancement gained by attaching the porous layer is due to the increase of the surface area available for the POM reactions. Since LCF-91 is a mixed ionic-electronic conductive material, the porous layer provides an extended surface for the reaction between methane and lattice oxygen, and hence reduces the corresponding resistance. This is similar to what is observed in the triple phase boundary in the electrodes of a solid oxide fuel cell [151].

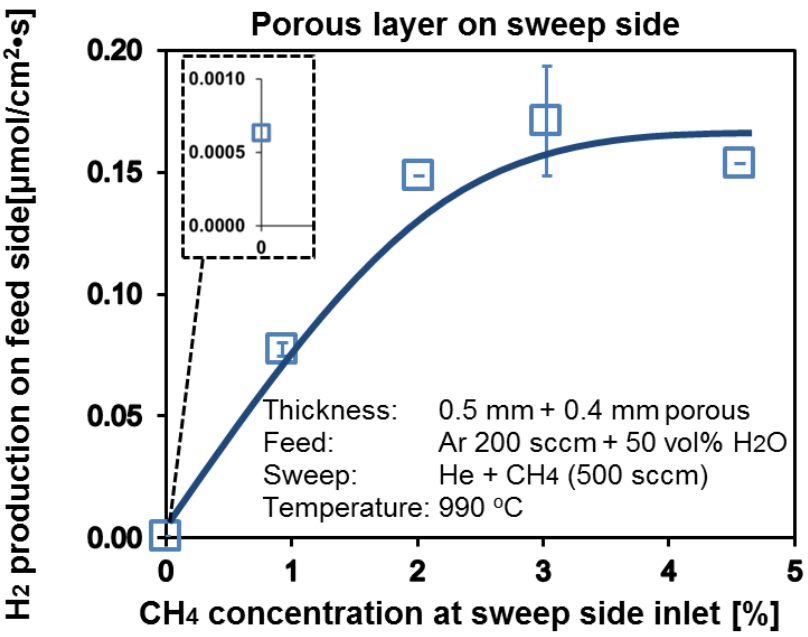

Figure 5.4 By adding a porous layer on the sweep side, the hydrogen production rate from water splitting increases by two orders of magnitude compared to the original membrane (in Figure 4.6). However, with increasing methane concentration on the sweep side, the hydrogen production rate reaches a plateau. The zoom-in figure shows the hydrogen production rate in helium sweep case

As shown in Figure 5.4, the performance reaches a plateau at methane concentrations of 2 – 3 vol%. This could be due to carbon formation and deposition on the surface at higher methane concentration, which covers the active surface of the porous layer. This hypothesis is supported by the carbon balance depicted in Figure 5.5. The carbon balance is defined as the ratio of the carbon content of the gaseous species at the reactor outlet over that at the inlet. It is less than unity especially at methane concentration greater than 3 vol%, which indicates the existence of solid carbon species. Following the experiments, carbon black was also found inside the reactor.

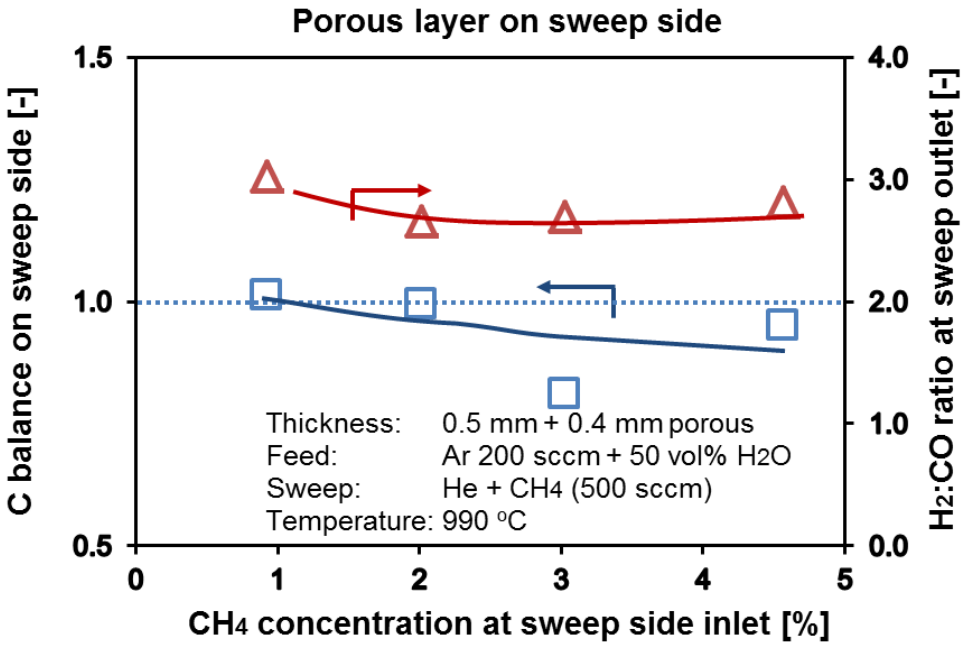

Figure 5.5 Carbon balance in the gas phase is around unity at low CH_4 concentration, but less than unity at higher CH_4 concentrations. The H_2/CO ratios at the outlet are around 2.7, which is higher than the stoichiometric value of POM reaction

Thermodynamic equilibrium calculation using Cantera[35] with GRI-Mech 3.0 mechanism[36] shows that homogeneous methane pyrolysis in the gas phase at 990°C produces primarily H_2, C_2H_2 and C_2H_4, with carbon mole fraction as low as 3.5×10^{-19}. Therefore, we suggest that carbon on the membrane surface is formed via heterogeneous methane decomposition, while the oxidation of carbon is slow because of the small amount of lattice oxygen available on the sweep side. Similar carbon formation has been reported on reduced metal catalysts such as Co, Ni and Fe during catalytic methane decomposition at elevated temperatures[152].

The H_2/CO ratio at the outlet on the sweep side is shown in Figure 5.5. For all concentrations, the H_2/CO ratio is around 2.7, which is higher than the ratio expected in the stoichiometric POM reactions. Meanwhile, very low CO_2 concentrations, around 0.001%, are detected at the outlet of the sweep side. These indicate that excessive amount of hydrogen was produced via heterogeneous methane decomposition, with only a fraction of the carbon getting oxidized to CO and CO_2 and the rest remaining in the solid carbon form, supporting again the lack of suffice oxygen on the sweep side.

5.3.2 Methane decomposition and carbon oxidation

In our experiments, coke, CO and CO_2 are all observed near the membrane surface at finite concentrations, indicating that the three end states of methane surface reaction shown in Figure 5.6 could occur simultaneously: (a) decomposition into carbon and hydrogen; (b) partial oxidation of carbon; or (c) full oxidation of carbon. Decomposition on a reduced surface results in coking, which has been observed on $LaNi_{1-x}M_xO_{3-\delta}$ (M = Co and Fe) catalysts [153] and on a LCF-91 membrane [154]. If not oxidized, carbon remains attached to an otherwise active site and slows down the surface reaction in a manner similar to catalyst poisoning [155]. On the other hand, carbon oxidation can follow either partial oxidation or combustion depending on catalysts and reactant flow rates [156]. As lattice oxygen is more active than gas-phase oxygen species in oxidizing carbon species [157], the oxygen flux from water splitting on the feed side can affect the relative concentrations of these carbon species.

As discussed in the previous section, the surface reaction on the sweep side is the limiting step. Carbon covering the surface active sites (pathway (a)) is related to the drop of the oxygen flux at high methane concentrations at higher temperature (i.e., 1030 ^oC in Figure 4.6) and the leveling off in hydrogen production rate from water beyond 3 vol% of methane (Figure 5.4). Similar results have been reported for catalytic decomposition of methane, that higher operating temperature and methane concentration lead to faster catalysts deactivation due to encapsulation of active catalytic sites by deposited carbon [158]. Therefore, in order to further enhance the flux, we need to provide more active sites on the sweep side, or enhance carbon oxidation rates and thus prevent it from blocking these sites.

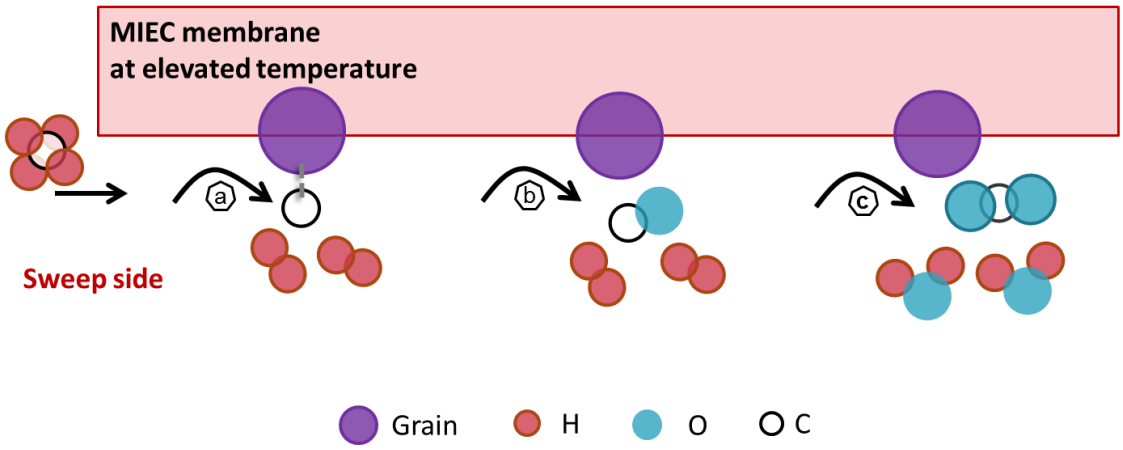

Figure 5.6 Schematic diagram illustrates three possible products of methane decomposition and carbon oxidation on the sweep surface: (a) decomposition into carbon and hydrogen; (b) partial oxidation of carbon; or (c) full oxidation of carbon

5.4 Further enhancements using a nickel catalyst

5.4.1 Hydrogen production from water splitting

In order to increase the oxygen flux further, we added a catalyst to the porous layer on the sweep side to accelerate the surface reaction. Nickel catalysts are reported to be one of the most effective base metal catalysts for POM in both packed bed or membrane reactors [141, 156, 159]. While solid carbon is prone to form on nickel from methane decomposition, it is found that the active lattice oxygen from the catalysts or the support can facilitate the oxidation of surface carbon [141] or soot [160, 161]. As is described earlier in this chapter, the nickel catalysts were applied onto the porous LCF-91 layer by wet impregnation. Because LCF-91 is a good oxygen conductor, the synergic effect between the porous LCF-91 support and the nickel catalysts is expected to improve the performance. The dimension of this membrane is shown in Table 5.1 under "modified membrane 2".

The hydrogen production rate from water splitting is shown in Figure 5.7. It continues to rise with increasing methane concentration, reaching more than double the value without a catalyst ("modified membrane 1" in Figure 5.4). Given that the LCF-91 porous layer for both membranes are the same and that the bulk diffusion is not the

limiting step with 1-5 vol% methane sweep, the thickness of the dense membrane is not expected to affect the results significantly and the enhancement of the oxygen flux is attributed to the increase of reaction rate on the sweep surface by the nickel catalysts. Besides, the hydrogen production rate from water splitting to increase slowly with increasing methane concentration, as adding nickel reduces the fraction of carbon attached to the surface by raising the oxygen flux. However, further studies are needed to examine the details of the suggested enhancement mechanism.

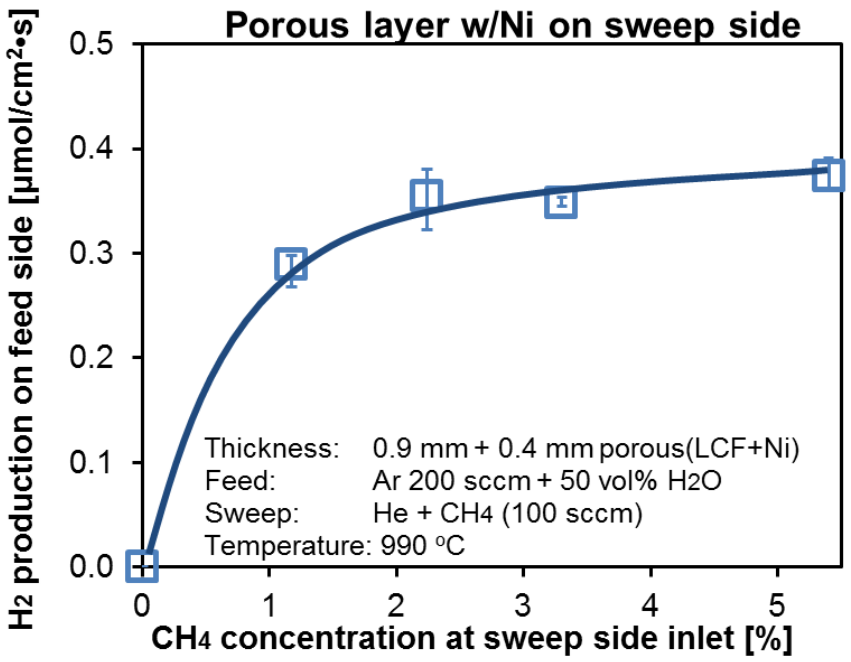

Figure 5.7 The nickel catalysts on the porous layer further enhances the hydrogen production rates from water splitting to double of those values without nickel catalysts in Figure 5.4. Further increase of the inlet methane concentration leads to slow rise of hydrogen production rate

5.4.2 Syngas production

As is shown in Figure 5.8, the CH_4/O_2 ratio increases from 3.3 to 11.0 when the inlet methane concentration is raised from 1 to 5 vol%; this shows a slower rise in the oxygen flux as methane concentration increases. This also leads to lower methane conversions at higher inlet methane concentrations: conversion rate is almost 80% when the inlet methane concentration is 1 vol%, but it drops to around 20% at 5 vol% methane.

The products at the reactor outlet are shown in Figure 5.9. Syngas with H_2/CO ratio of 2 is measured in all cases with 1-5 vol% inlet methane concentrations. This matches well with the stoichiometric ratio in POM reaction. Besides, the H_2/CO ratio stays constant when CH_4 inlet concentration increases. Thus, CH_4/O_2 ratio doesn't affect the syngas selectivity on this surface modified oxygen permeable membrane. Furthermore, in Figure 5.9 (b), plots of hydrogen productions versus methane consumptions fall well on the 2:1 line in all cases. These indicate that syngas is produced by a combined effect of surface and gas phase reactions on the sweep side.

However, the syngas near the surface has a H_2/CO ratio higher than the stoichiometric value 2. This has been found on LCF-91 membranes with air feed and methane sweep [154]. This can be due to two reasons: 1) steam reforming is favored on LCF-91 that produces more H_2 [162] and 2) water gas shift is also favored on LCF-91 [154]. As a result, more H_2 is observed near the membrane surface than stoichiometric methane partial oxidation.

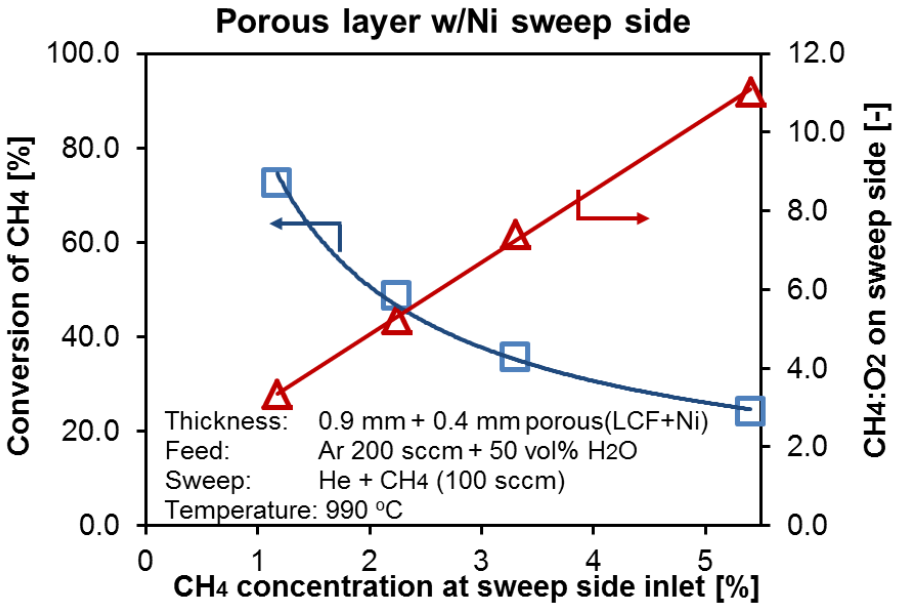

Figure 5.8 When the inlet methane concentration changes from 1 to 5 vol%, the CH_4/O_2 ratio rises due to the slower increase of oxygen flux at higher inlet methane concentration. The conversion ratio of methane decreases at higher inlet methane concentration

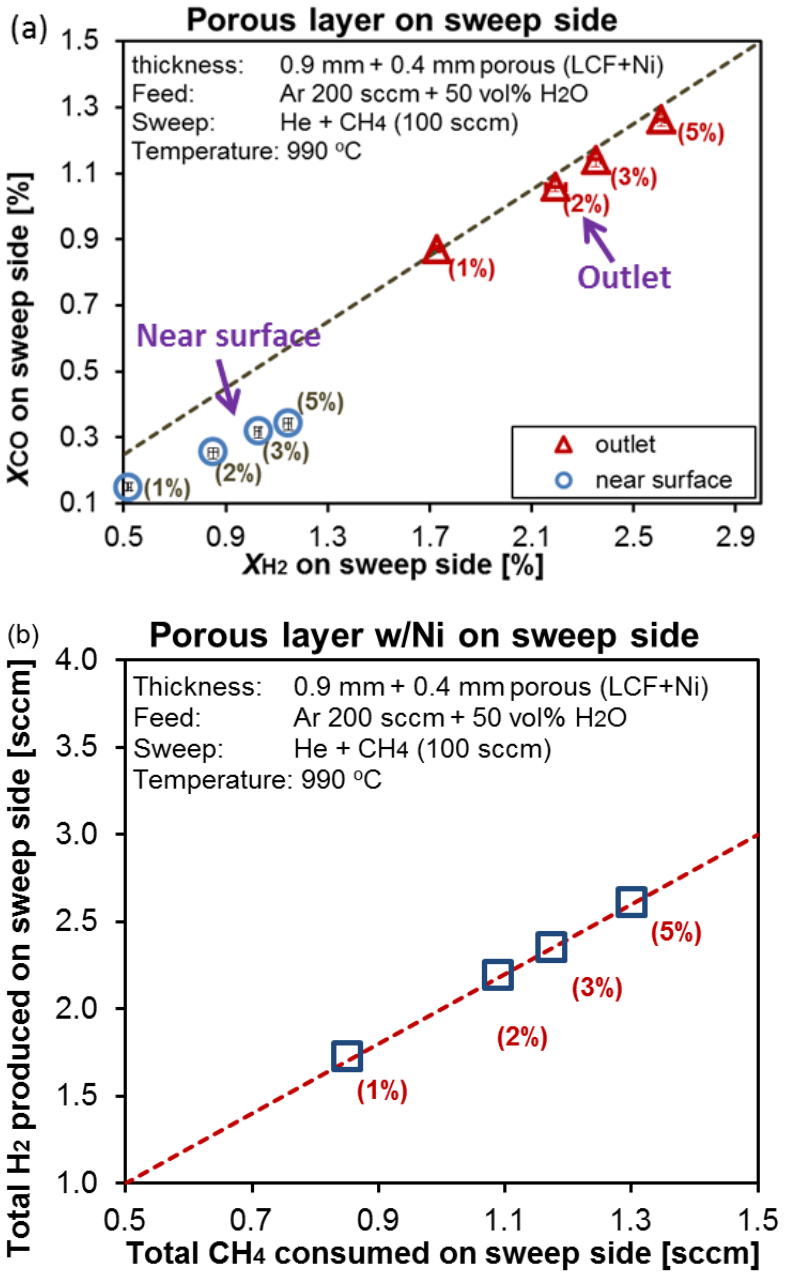

Figure 5.9 (a) The syngas at the outlet of the reactor has a H_2/CO ratio of 2 while the syngas near the membrane surface shows a ratio higher than 2 (The dotted line shows a ratio of 2) (b) Hydrogen atoms in methane are converted to hydrogen molecules at the outlet of the reactor (The dotted line shows a $n_{H_2}/\Delta n_{CH_4}$ ratio of 2). On both figures, the numbers in the brackets near the symbols represent the inlet methane concentration at that specific data point, and Q''_i is the flow rate of species i on sweep side under standard condition

There are three different end states for methane reaction as illustrated before in Figure 5.6. The carbon balance in the gas phase in Figure 5.10 shows that the gaseous carbon species near the membrane surface and at the outlet of the sweep side match very well with those at the inlet. As almost all the carbon species are in the gas phase, this means that the solid carbon deposition pathway is very unlikely in this LCF-91 porous layer with nickel catalysts under the operating conditions in our experiments. Compared with the observed carbon formation without nickel catalysts (in Figure 5.5), the higher oxygen fluxes and the enhancement of surface reaction by nickel are attributed to less solid carbon, as is observed in Figure 5.10.

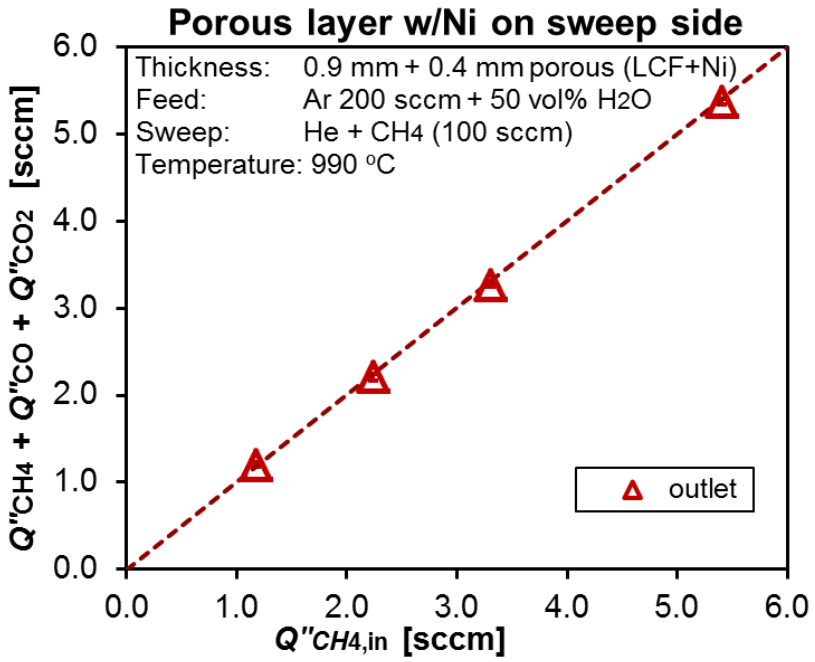

Figure 5.10 On the sweep side, the gaseous carbon species at the outlet both match well with the inlet carbon species, showing that hardly any solid carbon was formed. $Q"_i$ is the flow rate of species *i* on sweep side under standard condition

The selectivity to CO_2 is defined as

$$S_{CO_2} = \frac{n"_{CO_2,out}}{n"_{CO,out} + n"_{CO_2,out}} \qquad (5\text{-}5)$$

where $n"$ is the molar flow rate of the species on the sweep side, mol/s. This value illustrates the relative importance of the full oxidation pathway. Figure 5.11 shows that S_{CO_2} close to the membrane surface is around 8% when the inlet methane concentration is 1 vol%, and decreases to 0.55% at 5 vol% methane. Full oxidation is less favorable at higher CH_4:O_2 ratio, as less oxygen is available to fully oxidize the carbon species. Yet S_{CO_2} at the outlet is always lower than its value near the surface, showing that CO_2 generated by full oxidation on the membrane surface reforms methane to produce CO when the products travel from the surface to the reactor exit.

Previous studies on packed catalytic bed reactors showed that methane tends to be oxidized into CO_2 and H_2O on nickel surface; therefore, it is proposed that syngas is formed in the gas phase by dry or steam reforming [140]. However, in our case, the available oxygen depends on the water splitting reaction on the feed side. Therefore, whether the adsorbed carbon species are oxidized into CO or CO_2 depends on the oxygen flux or the water splitting rate.

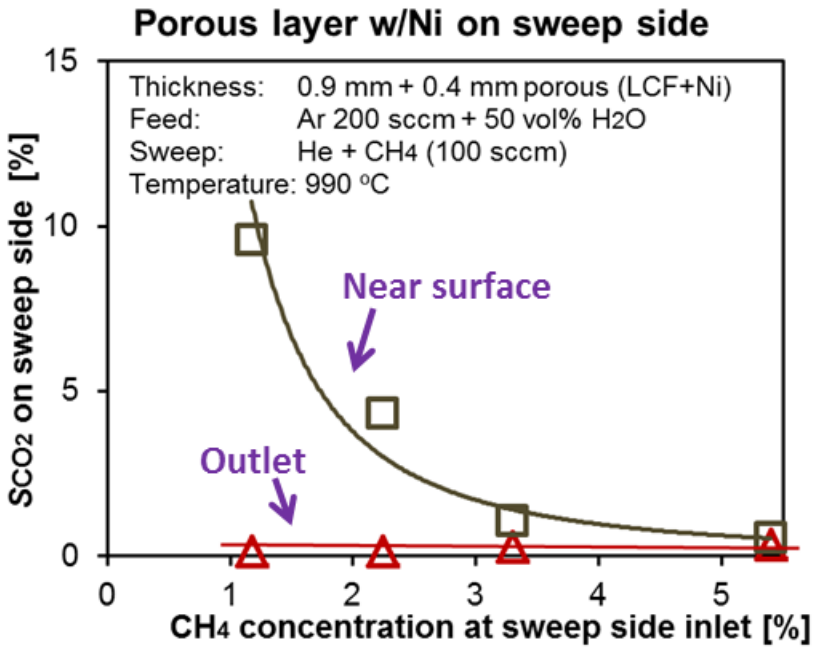

Figure 5.11 The selectivity to CO_2 is higher near the local membrane surface than that at the outlet. At inlet higher methane concentration, the local CO_2 selectivity decreases

5.5 Long term study

The long term performance of the Ni/LCF-91 catalytic porous layer was studied for 54 hours. Results are shown in Figure 5.12 for 1 vol% methane sweep at 950 and 990^{o}C. There is an obvious degradation of performance at the first few hours. After that the stable performance was maintained for 50 hours at 950 ^{o}C. The stable performance is attributed to the low carbon deposition from the POM with continuous supply of oxygen from water splitting. However, parts of the porous layer detaches from the dense part easily followed the splitting experiments. The detachment between the porous layer (delamination) as well as the sintering of the porous structure and hence, the decrease of the surface area have been found as the degradation reasons for SOFC or SOEC electrodes [163-165]. These can also be the reason for the initial degradation observed in our experiments. Further studies on the porosity, lattice structure as well sintering effect will be carried out to investigate the degradation in the first few hours. And the dependence of the performances on the surface area of the porous layer should also be studied with well-structured porous layer to identify the enhancement mechanism.

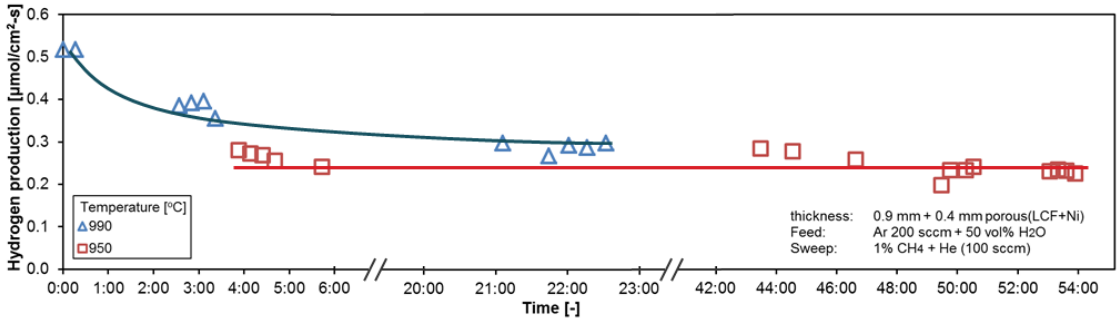

Figure 5.12 Long term stability studies show that the flat LCF-91 membrane with a porous layer undergoes a deterioration in the first few hours, but then high performance maintains for the next 50 hours

5.6 Conclusions

LCF-91 exhibits good ionic and electronic conductivities at elevated temperatures. Studies have shown the application of LCF-91 membrane for oxygen production, oxy-

fuel combustion and syngas production. In this chapter, we investigate the co-production of H_2 and syngas on LCF-91 membranes and demonstrate that the understanding of the transport phenomenon guides better membrane and reactor designs. Two surface modified asymmetric membranes were tested by adding a porous layer and nickel catalysts to improve performance. Results show the following:

(1) Performance is improved by applying a 0.4-mm thick porous LCF-91 layer on a 0.5-mm thick dense LCF-91 membrane. The hydrogen production rate from water splitting increases by two orders of magnitude compared to the original membrane. However, due to the lack of sufficient oxygen on the sweep side, carbon formation from methane decomposition is observed and the H_2/CO ratios of the syngas produced on the sweep side are around 2.7.

(2) Nickel catalyst is applied on the porous LCF-91 layer to further improve the performances. The hydrogen production rate from water splitting is further increases by a factor of 2 with the maximum value reaching 0.37 μmol/cm^2•s at 990^{o}C. Syngas produced on the sweep side has a H_2/CO ratio of 2 when the inlet methane concentration changes from 1 to 5 vol%. This is due to the combined effect of reactions on the surface and in the gas phase. Besides, hardly any solid carbon is found from carbon balance in gas species.

(3) Under different conditions, finite amount of coke, CO and CO_2 are observed near the membrane surface. The oxygen fluxes and CH_4/O_2 ratios affect the relative concentration of these carbon species.

Further studies of the synergic effects between LCF-91 and Ni on POM in a membrane reactor are needed, especially when using thinner membranes and optimum porous support thickness. Besides, further examination of the surface reaction mechanism which affects the oxygen flux through the membrane is also important for designing better membranes and catalysts. The complexity of the combined effects of the reactions on the solid surface and in the gas phase as well as the flow fields in the porous layer and membrane reactor also requires more investigations from both experimental and numerical aspects to understand the co-production process.

Acknowledgement:

Parts of the contents in this chapter have been firstly published in

Wu XY, Ghoniem AF, Uddi M. Enhancing co-production of H_2 and syngas via water splitting and POM on surface-modified oxygen permeable membranes. *AlChE Journal* 2016 62(12): 4427 - 4435.

Chapter 6

CO_2 Splitting Supported on a Flat LCF Membrane

6.1 Introduction

The accumulation of greenhouse gases CO_2 in the atmosphere has reached a global average concentration above 400 ppm [4]. Capturing and utilizing CO_2 have both environmental and economic benefits [12, 166, 167]. As CO_2 is a very abundant and cheap C1 feedstock for industry application [8, 166], upgrading CO_2 to value-added chemicals such as CO [168-170], CH_3OH [171] and CH_4 [172, 173] have been attractive in both industry and academia. In this chapter, I will focus on splitting of CO_2 to CO, which can be enhanced by an oxygen permeable membrane (OPM) at elevated temperatures. This thermochemical reduction method is also an energy storage technology, as it can utilize clean heat sources such as solar or nuclear heat to upgrade CO_2 to CO as a fuel or a chemical feedstock [174].

Many attempts have been tried to use thermochemical cycles to reduce CO_2 with oxygen carriers such as CeO_2 [145], Zn/ZnO [175, 176], FeO/Fe_3O_4 [176] and doped $LaMnO_3$ [177]. The cycle usually operates at different oxidation and reduction temperatures [145]. However, these temperature-swing cycles have lower efficiency and are harder to be implemented than the isothermal thermochemical cycles [178, 179]. Meanwhile, CO_2 splitting in an isothermal oxygen permeable membrane reactor that operates at temperatures as high as 1500^oC has been proposed in 1980s [92]. Compared with the thermochemical cycles, this membrane reactor has the advantages of isothermal oxidation and reduction processes and process intensification into one single reactor unit. Besides, in a membrane reactor, the thermal dissociation rate is facilitated by the heterogeneous catalytic surface reactions and the thermodynamic equilibrium is shifted to further dissociate the reactants. No electricity is consumed in this thermal dissociation

process on an oxygen permeable membrane; only carbon-free heat sources from solar or nuclear power is utilized to upgrade CO_2.

Several types (i.e., single-phase perovskite or fluorite and mixed phase membranes) have been studied [91, 97, 99]. Table 1.8 summaries the materials and performances for different membrane materials. The highest CO_2 reduction rate reported was 2.72 μmol/cm^2-s on a 1.5 mm thick $SrCo_{0.4}Fe_{0.5}Zr_{0.1}O_{3-\delta}$ (SCFZ) perovskite membrane at 950^{o}C with Pd/SCFZ and Ni/Al_2O_3 catalysts on the feed CO_2 and sweep CH_4 sides, respectively [91]. However, the membrane had unstable performances and broke after 40 hours due to the corrosion of SCFZ by CO_2 and CO and the deactivation of the Ni/Al_2O_3 catalysts [91]. Nb_2O_5 dopant was found to be able to stabilize the SCFZ membrane in CO_2 atmosphere but decrease its performance [96]. Another perovskite $La_{0.6}Sr_{0.4}Co_{0.2}Fe_{0.8}O_{3-\delta}$ (LSCF) membrane was studied to decrease strontium carbonate formation by substituting part of the strontium by lanthanum and the highest CO_2 splitting rate on this 0.6 mm thick tubular membrane was 0.28 μmol/cm^2-s at 1030^{o}C with CH_4 sweep [97]. While both SCFZ and LSCF perovskites are single-phase mixed ionic and electronic conductive materials, mixed-phase materials have also been tested. An example is the short-circuit samarium-doped ceria (SDC) membrane with Ag or Pt pastes at the membrane edge [100]. For this mixed-phase membrane with a dense layer thickness of 20 μm and with SDC/Ag porous support on the Ar sweep side, the highest CO_2 splitting rate achieved was 1.819 μmol/cm^2-s at 900 ^{o}C with methane sweep and $GdNi/Al_2O_3$ catalysts on the sweep side [100].

However, there are still several questions that are needed to be answered in order to develop this CO_2 reduction technology on an oxygen permeable membrane, such as ‘what are the limiting step(s) in the oxygen transport process?’ ‘How can we improve the performance of this membrane reactor?’ In order to answer these questions and guide the design of better membrane configurations for CO_2 splitting processes, reactions kinetics studies are required for the surface reactions and an oxygen transport model should be developed. Therefore, experimental study is carried out to quantify the reaction kinetics of CO_2 splitting to CO in a $La_{0.9}Ca_{0.1}FeO_{3-\delta}$ (LCF-91) OPM reactor at temperatures between 850 and 1030^{o}C. Based on the experimental results, a resistance-network model is developed to describe the oxygen transport process. LCF-91 perovskite is chosen as it

has been tested for air separation and water splitting with stable performances [60, 72, 80], and calcium carbonate is less stable than strontium and barium carbonates and will decompose into calcium oxide and carbon dioxide in pure CO_2 environment above 850^oC [98]. Both CO and H_2 as the sweep gas are tested to maintain the oxygen partial pressure gradient across the membrane. CO is used by construction to derive the kinetic parameters for CO_2 splitting, while other fuels such as H_2 and hydrocarbons can be used in practice on the sweep side to reduce the corresponding chemical potential on that side. The effects of feed and sweep gas species and concentration are also investigated and the dependence of oxygen fluxes on these factors is reported and discussed. The resistance-network model developed based on the experimental data shows that the surface kinetics of both sides can be the rate limiting steps depending on the gas species concentrations and operating temperature.

6.2 CO_2 splitting on an OPM

6.2.1 Schematic

A schematic of the CO_2 splitting on an oxygen permeable membrane is shown in Figure 6.1. There are three processes involved in the vicinity of and inside the membrane: (1) Carbon dioxide is thermochemically reduced by the oxygen vacancy on the feed side surface into oxygen and carbon monoxide, (2) Oxygen diffuses across the bulk of the membrane, together with the electrons/holes to maintain electron neutrality in the bulk of the membrane [180], (3) On the sweep side, oxygen leaves the surface as gas or it is consumed by fuel oxidation. Elevated temperatures are required for these process and the overall reaction is endothermic, so heat sources such as concentrated solar or nuclear heat can be utilized and be stored in chemical bonds for further applications.

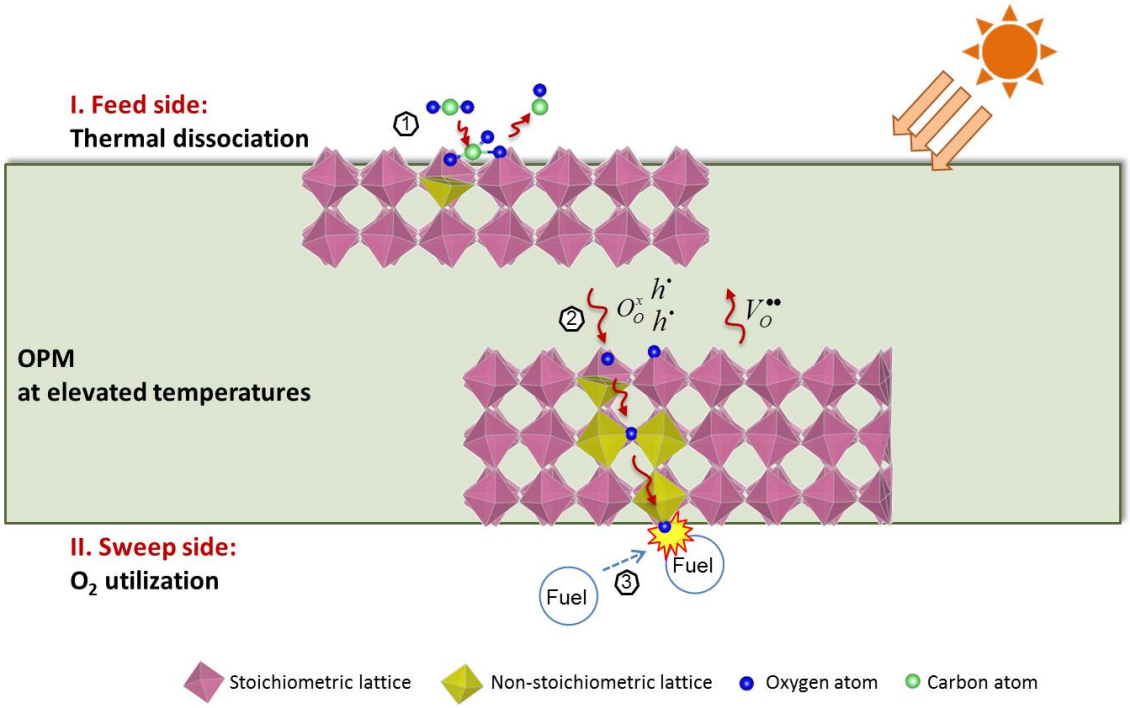

Figure 6.1 This shows a schematic of CO_2 splitting on a perovskite OPM with partial oxidation of fuels and solar heat utilization as an example

Homogeneous CO_2 thermal dissociation in gas phase has very low kinetics parameters and low thermodynamic equilibrium constant. Simulation on the Cantera software [35] using GRI-Mech 3.0 mechanism [36] shows the equilibrium CO concentration is 5.49 ppm at 900^{o}C and the value increases to 24.9 ppm at 1000^{o}C and 3620 ppm at 1500^{o}C. Although solar thermal utilization can achieve temperatures as high as 1500^{o}C [181], high-temperature operation makes the technology expensive to carry out. Radiation heat loss to the environment also makes high temperature operations above 1000^{o}C unfavorable. Therefore, medium temperature in the range of 800 – 1000^{o}C applications are desirable for this OPM reactor. At such temperatures, CO_2 splitting can be enhanced by the use of OPM reactor to shift the thermodynamic equilibrium and catalyzing the dissociation by heterogeneous reaction.

6.2.2 Reaction mechanism

The detail mechanism of heterogeneous CO_2 reaction on different perovskite is still unclear. Yet there are two possible mechanisms that were proposed, either that one of the oxygen atoms in CO_2 molecules incorporate into the membrane as lattice oxygen, or that CO_2 reacts with the membrane to form carbonate [39]. On the one hand, the isotope experiments on a Fe-doped $SrTiO_3$ single crystal surface at 850 – 1000^{o}C reveal the oxygen incorporation mechanism [128]:

$$CO_2(g) + V_O^{\bullet\bullet} \rightarrow CO(g) + O_O^X + 2h^{\bullet} \quad (6\text{-}1)$$

Here Kröger–Vink notation is used. $V_O^{\bullet\bullet}$ is the lattice oxygen vacancy, O_O^x is the lattice oxygen, $h^{\bullet}$ is the electron hole, or more precisely the net charge in the lattice iron. Similar mechanism is also expected for CO_2 splitting on Ca-doped $LaFeO_3$ at high temperatures, as both are acceptor-doped perovskites. On the other hand, for the carbonate mechanism, experiments shows that CO_3^{2-} is formed on various perovskites, such as Fe-doped [124] or Rh-doped [182] $SrTiO_3$ surfaces, $SrCo_{0.8}Fe_{0.2}O_{3-\delta}$ [123] and $BaCo_{0.4}Fe_{0.6-x}Zr_xO_{3-\delta}$ [125] when the surface is exposed to CO_2. Yet the stability of the carbonate formation depends on temperature and CO_2 partial pressure, and these carbonates decompose into oxides and CO_2 at higher temperatures [123, 124].

In the experiments of CO_2 splitting present in this chapter, the membrane operates at a temperature range of 850-1000^{o}C. From the Ellingham diagram [98], $CaCO_3$ decomposes spontaneously when exposed to 1 atm CO_2 at temperatures higher than 850^{o}C. And following 106 hours of CO_2 splitting experiments, carbonates are found sparsely on the membrane surface by EDX and XRD. Therefore, in high-temperature applications like membrane-supported CO_2 splitting in this chapter, the oxygen incorporation reaction is regarded as the more important pathway and the oxygen incorporation reaction (6-1) is used to model the thermal dissociation reaction on the feed side. This oxygen incorporation reaction is similar with those for O_2 [80-82, 115, 154] or H_2O [60, 72] incorporation in LCF-91.

On the sweep side, the Mars-van Krevelen (MvK) mechanism is used to model the fuel (i.e., CO and H_2) oxidation on the perovskite membrane, as:

CO sweep case: $CO(g) + O_O^X + 2h^{\bullet} \rightarrow CO_2(g) + V_O^{\bullet\bullet}$ (6-2)

H_2 sweep case: $H_2(g) + O_O^X + 2h^\bullet \rightarrow H_2O(g) + V_O^{\bullet\bullet}$ (6-3)

The MvK mechanism has been proposed for oxidation on most of the doped or undoped oxides at elevated temperatures [183].

6.2.3 Resistance-network transport model

From Chapter 3 and Table 3.1, the oxygen fluxes on the feed and sweep sides as well as across the membrane are

CO_2 feed side: $J'_V = k_{f,CO_2} C'_{CO_2} C'_V$ (6-4)

CO sweep side: $J''_V = \tilde{k}_{r,CO_2} \left(C_O - C''_V\right) C''_{CO}$ (6-5)

Bulk diffusion: $J_V = -D_V \frac{\partial C_V}{\partial y} = D_V \frac{C''_V - C'_V}{t}$ (6-6)

At steady state, the fluxes are equal, and they give

$$J_V = \frac{C_O}{\frac{1}{k_{f,CO_2} C'_{CO_2}} + \frac{t}{D_V} + \frac{1}{k_{r,CO_2} C''_{CO}}} = \frac{C_O}{R_f + R_b + R_s}, \quad (6\text{-}7)$$

where R_f, R_b and R_s are the resistances of the feed side surface reaction, the bulk diffusion and the sweep side surface reaction, respectively. And C_o is the oxygen site concentration including lattice oxygen and oxygen vacancies.

Table 6.1 Operating conditions in our experiments

Temperature [^{o}C]	Feed side (dilute with He)		Sweep side (dilute with Argon)	
	CO_2 concentration	flow rate [sccm]	fuel concentration	flow rate [sccm]
850 – 1030	2 – 100 %	100	1 – 12%	100

Experiments at various operating conditions such as gas species concentrations and temperatures (shown in Table 6.1) have been carried out to parameterize the surface reaction kinetics. Effective oxygen vacancy diffusivity was derived from separate transient dilatometry studies as shown in Table 3.3 [80]. The surface reaction kinetics for reactions (6-1) and (6-2) are fitted with the CO_2 feed-CO sweep data presented later in

this chapter. The parameters are summarized in Table 6.2. As is shown in Figure 6.2, the resistance network model predicts the experimental data within ±25% error. In the following sections, we show that this resistance network model can be used to analyze the dependence of oxygen fluxes on various factors.

Table 6.2 Reaction kinetic parameters for CO_2/CO surface reactions on LCF-91

		A		*E*a	
		Value	Unit	Value	Unit
$CO_2 + V_O^{\bullet\bullet} \rightarrow O_O^x + 2h^\bullet + CO$	k_{f,CO_2}	1.28E15	[cm^4/mol•s]	3.64E5	[J/mol]
$CO + O_O^x + 2h^\bullet \rightarrow CO_2 + V_O^{\bullet\bullet}$	k_{r,CO_2}	1.64E7	[cm^4/mol•s]	1.57E5	[J/mol]

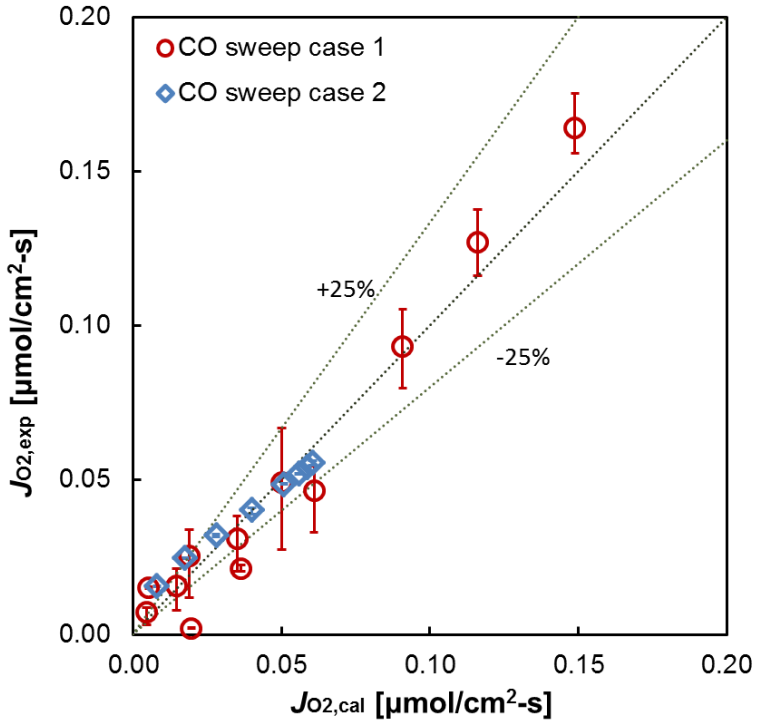

Figure 6.2 Kinetic data fitting (CO sweep case 1 is experimental data shown in Figure 6.3 and Figure 6.5 at various temperatures and sweep side CO concentrations, while CO sweep case 2 shows the feed side CO_2 concentration dependent data in Figure 6.4)

6.3 CO_2 splitting rate study

As is shown in Figure 6.1, different reducing agents such as CO, H_2 and hydrocarbons can be used as the sweep gas to maintain the oxygen chemical potential gradient across the membrane and enable oxygen ion diffusion. In Chapter 5, I discussed the intensification of water splitting and partial oxidation of methane in a LCF-91 membrane reactor and show that the dissociation process can be enhanced by the methane partial oxidation reaction and syngas with $H_2/CO = 2$ is produced on the sweep side [60]. In this chapter, carbon monoxide is firstly used as the sweep gas by construction to understand the oxygen diffusion characteristics with CO_2 as the oxygen source and the kinetics of the surface reactions on the LCF-91 membrane are parameterized. Then I will compare CO_2 splitting with CO and H_2 sweep and discuss the limiting steps in the oxygen transport processes under different sweep conditions.

6.3.1 Effects of fuel concentration on the sweep side

The CO_2 reduction rate and CO yield are examined with introduction of fuel on the sweep side. When there is only argon on the sweep side, hardly any CO_2 dissociation on the feed side can be detected from gas chromatograph. With an introduction of 1% of CO on the sweep side, the oxygen fluxes increases to 0.002 μmol/cm^2•s as is shown in the zoom-in figure in Figure 6.3 (a); and leakage tests show there is no cross-membrane CO leak during the experiments. Further increase of fuel concentration on the sweep side to 11.7% leads to a rise of J_{O2} to 0.164 μmol/cm^2•s. Similar trends are observed for the CO concentration measured at the outlet on the feed side with increasing fuel concentration.

From Figure 6.3 (a), we notice that the slope of J_{O2} decreases at higher fuel concentrations. This is due to that the limiting step changes from the sweep side surface kinetics to both the feed and sweep side surface kinetics, as shown in Figure 6.3 (b). When the fuel concentration is as low as 1%, the surface reaction resistance on the sweep side is 2×10^6 s/cm, which is one order of magnitude higher than the value on the feed side (i.e., 8.8×10^4 s/cm).

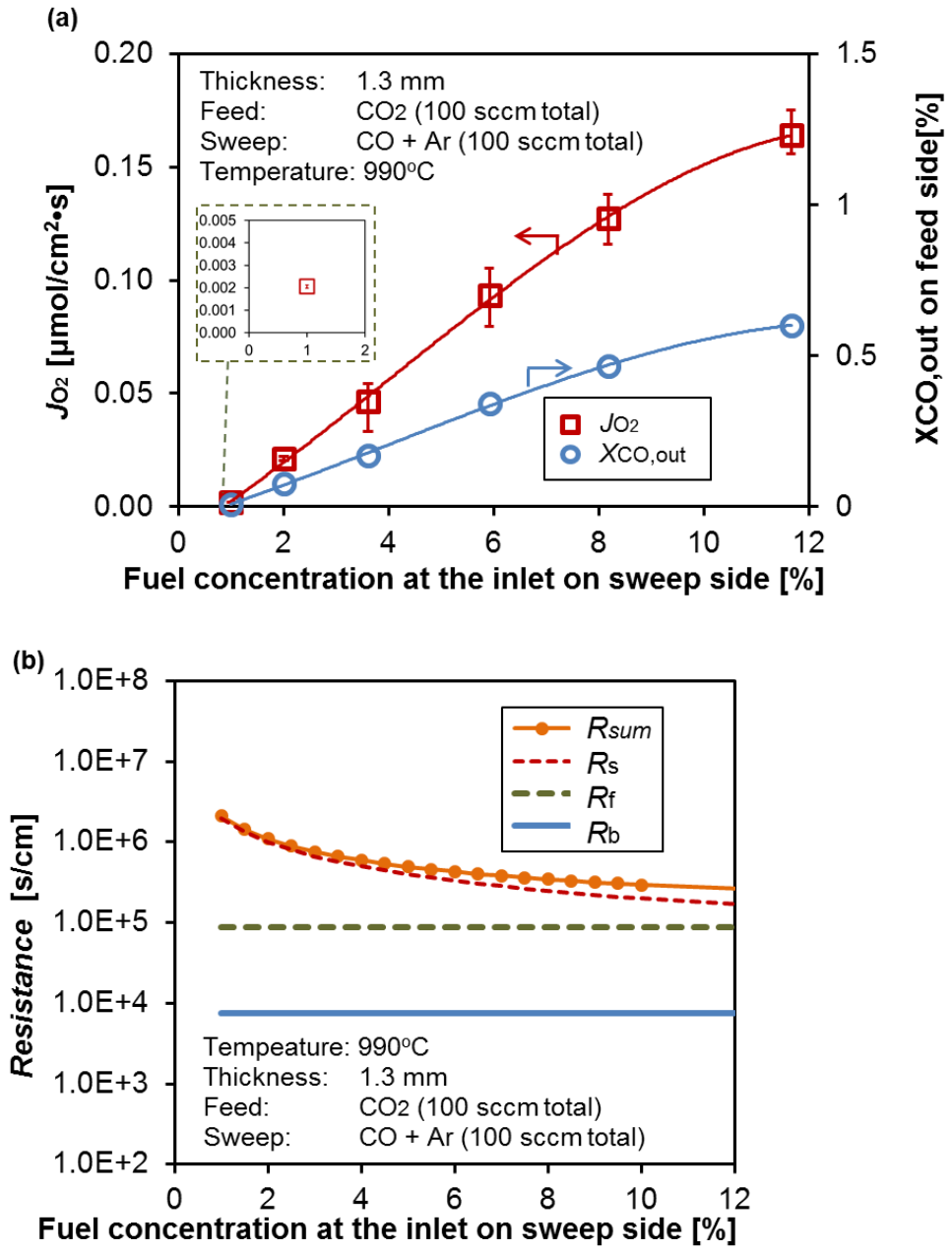

Figure 6.3 (a) At 990°C, CO_2 dissociation rate and CO concentration on the outlet of the feed side increase at larger fuel concentrations on the sweep side. The zoom-in figure shows the oxygen flux at 1% CO on the sweep side. (b) Resistance values are plotted under the same operating conditions on (a), which shows the feed and sweep side kinetics can be both rate-limiting at high fuel concentration

Yet with increasing fuel concentration, the resistance on the sweep side approaches to that on the feed side and hence, both reactions on the feed and sweep sides become the rate limiting steps. The total resistance in Figure 6.3 (b) also shows that at CO concentrations less than 3% on the sweep side, the total resistance drops rapidly with the fuel concentration, following the trend of the sweep side reaction resistance. Yet at higher fuel concentrations, the total resistance flattens out and deviates from the sweep side resistance, which shows the contribution of feed side resistance. As a result, the increase of oxygen flux due to higher fuel concentration becomes less profound at higher fuel concentrations, and the slope of J_{O2} decreases. Similar trends that oxygen fluxes flatten out at higher fuel concentration have also been observed when water is the oxygen source [48, 60].

6.3.2 Effects of CO_2 concentration on the feed side

As is discussed in the previous section, the surface kinetic resistance of 100% CO_2 on the feed side is lower than that on the sweep side; but the values have similar orders of magnitude, especially at high fuel concentration on the sweep side. Therefore, changing CO_2 concentration on the feed side will affect the magnitude of the sum of the resistances and hence the oxygen fluxes across the membrane. The results of oxygen fluxes versus CO_2 concentrations on the feed side on a 1.3-mm thick LCF-91 membrane at 990^{o}C are in Figure 6.4 (a). On the sweep side there is the 3.6% CO and argon mixture.

With rising CO_2 concentrations on the feed side, we can notice there are two regimes for the increase of oxygen fluxes. When CO_2 concentration increases from 2% to 40%, there is a rapid oxygen flux increase from 0.015 to 0.049 μmol/cm^2•s. Yet when CO_2 concentration is above 60%, the oxygen flux approaches constant, with a 7% increase of J_{O2} when CO_2 concentration changes from 60% to 100%.

These two regimes can be explained by plotting the three transport resistances in Figure 6.4 (b). As fuel concentration is constant on the sweep side, the resistance on that side remains constant as 6.65×10^5 s/cm. When CO_2 concentration on the feed side is lower than 10%, the feed side resistance is the highest among the three. Therefore, oxygen flux J_{O2} rises rapidly with CO_2 concentration increasing from 2 to 10%. After that, the sweep side resistance is the highest, while the feed side resistance keeps

decreasing with increasing CO_2 concentration on the feed side. As a result, the total resistance decreases and the oxygen flux increases at higher CO_2 concentration on the feed side. When CO_2 concentration is higher than 60%, the sweep side resistance is more than 5 times higher than the feed side resistance. This leads to the flattening out of the total resistances (Figure 6.4 (b)) and hence, the oxygen fluxes (Figure 6.4 (a)).

Figure 6.4 (a) also shows the CO_2 dissociation ratio, which is defined as

$$R_{CO_2,diss} = \frac{\dot{Q}_{CO,outlet,feed}}{\dot{Q}_{CO_2,inlet,feed}}. \quad (6\text{-}8)$$

The maximum CO_2 dissociation ratio of 3% is achieved when CO_2 concentration is as low as 2% and the associated oxygen flux is 0.015 μmol/cm^2•s. This ratio drops continuously with increasing CO_2 concentration and it reaches 0.2% when there is pure CO_2 on the feed side. The low values of CO_2 dissociation ratio is due to the low oxygen flux compared to the high CO_2 feed flow rate. Optimization is required to achieve high CO_2 dissociation ratio such as increasing membrane surface area, applying active catalysts for CO_2 dissociation and optimizing the flow rate and oxygen flux ratio.

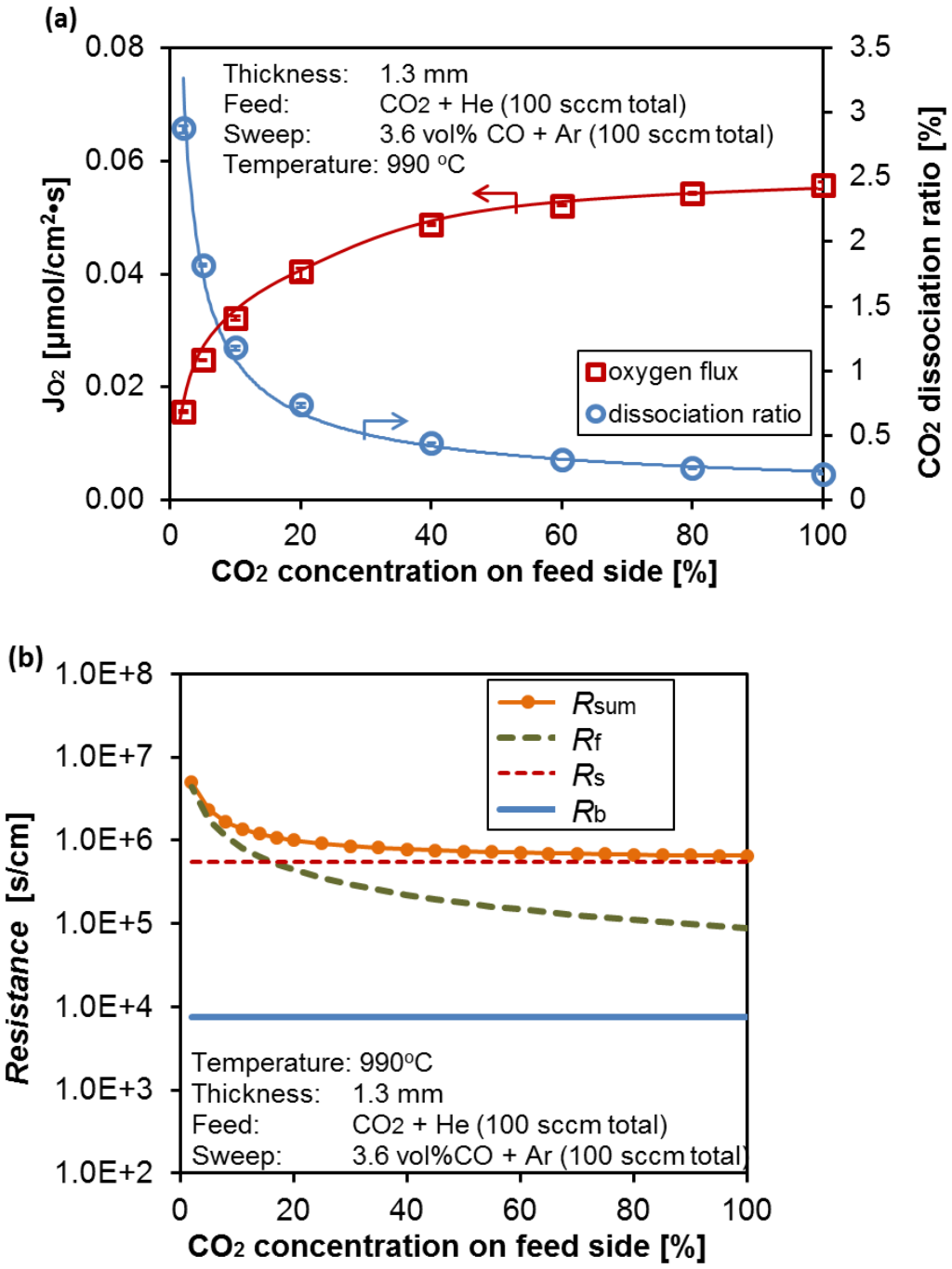

Figure 6.4 (a) Oxygen flux increases but the dissociation ratio drops at higher CO_2 concentration on the feed side. (b) Resistance values are plotted under the same operating conditions on (a), which shows a switch of rate limiting step from the surface reactions on the feed side to the sweep side when CO_2 concentration on the feed side increases

6.3.3 Temperature effect

The dependence of oxygen flux on operating temperatures is shown in the Arrhenius plot in Figure 6.5 (a). In this case, pure CO_2 flows on the feed side and the 3.6% CO and argon mixture on the sweep side. From it, we can see the apparent activation energy for oxygen flux changes with increasing temperature: At temperatures higher than 900^{o}C, the apparent activation energy is smaller than that at lower temperatures.

This change of activation energy is due to the change of limiting steps at rising operating temperatures. As is shown in Figure 6.5 (b), at low temperature, the limiting step is the feed side surface resistance, while at high temperature, sweep side surface resistance dominates. As a result, the total resistance follows two regimes: at low temperature, the barrier for oxygen transport is dominated by the CO_2 thermal reduction on the feed side (i.e., $CO_2 + V_O^{\bullet\bullet} \rightarrow O_O^x + 2h^{\bullet} + CO$), and this reaction has the activation energy of 364 kJ/mol as in Table 6.2. At higher temperature, the activation is dominated by CO oxidation on the sweep side, $CO + O_O^x + 2h^{\bullet} \rightarrow CO_2 + V_O^{\bullet\bullet}$ with the activation energy of 157 kJ/mol. Therefore, the apparent activation energy for oxygen transport process drops at higher temperatures.

As the limiting step changes from the feed side to sweep side surface reactions when operating temperatures increases, different enhancement techniques have to be applied to both sides in order to improve the performances of the membrane reactor. Further studies on facilitating the heterogeneous reactions on different surfaces will be discussed in Chapter 7 to enhance CO_2 splitting on the LCF-91 membrane.

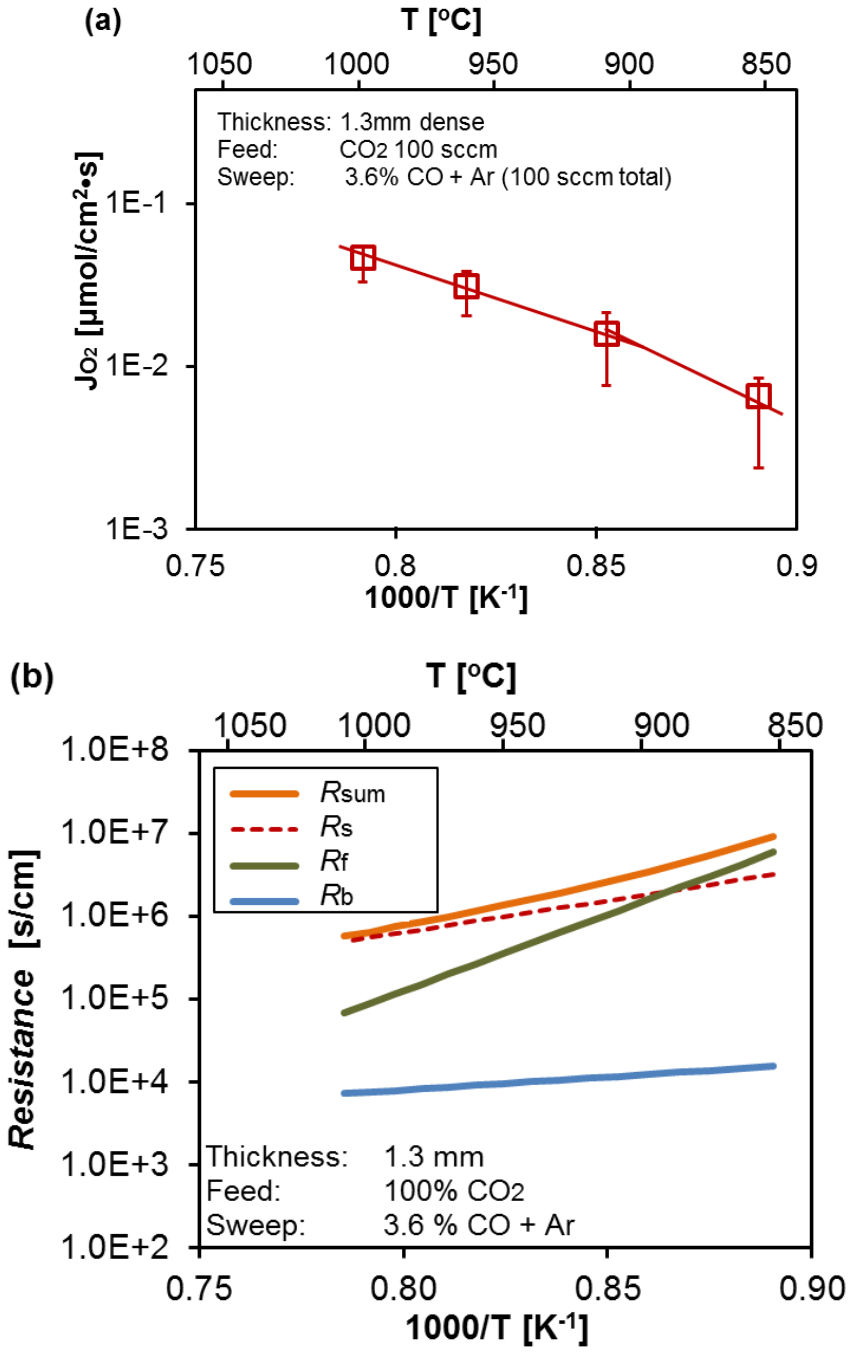

Figure 6.5 (a) Arrhenius plot shows two activation regimes for oxygen flux of CO_2 dissociation on the 1.3 mm thick LCF-91 membrane with 3.6% CO on the sweep side; (b) Resistance values are plotted under the same operating conditions on (a) showing the dominating resistances for oxygen transport changes from feed side to sweep side surface reactions at higher temperatures

6.3.4 H_2 as sweep gas to enhance CO_2 reduction

H_2 oxidation has been found to be faster than CO oxidation on many oxide surface, such as $BaCo_{0.7}Fe_{0.2}Nb_{0.1}O_{3-\delta}$ [184], $La_{0.9}Ca_{0.1}FeO_{3-\delta}$ [82] and Ni/YSZ [185]. As the sweep side surface kinetics is the limiting step at 990^{o}C when the CO_2 concentration is higher than 50%, adding more reactive fuels on that side are expected to improve the splitting of CO_2. Therefore, in this section, we investigate the effects of H_2 as a sweep gas on enhancing the sweep side surface kinetics and hence, the oxygen fluxes.

Results are shown in Figure 6.6 (a) that when H_2 is used on the sweep gas, the oxygen flux is higher than the CO sweep case, and the value rises to 0.19 μmol/cm^2•s at 9.5% of H_2 on the sweep side. Similar to the CO sweep case, the flattening out of oxygen flux at higher H_2 concentrations is also observed. This is again due to that the resistance on the hydrogen sweep side decreases and approaches the value on the CO_2 feed side when fuel concentration increases, which are plotted in Figure 6.6 (b). As H_2 reacts faster than CO on $La_{0.9}Ca_{0.1}FeO_{3-\delta}$ [82], the sweep side resistance becomes of the same order of magnitude with the feed side resistance at a lower H_2 concentration than CO concentration. Therefore, in the H_2 sweep case, the oxygen flux starts to flatten out at an even lower H_2 concentration (i.e., 4-6%) as is shown in Figure 6.6 (a).

For the H_2 sweep case, the dependence of oxygen flux on the operating temperature is shown in Figure 6.7 (a), together with the CO sweep case under similar operating conditions (Figure 6.5 (a)). From the figure, we can see the apparent activation energy for oxygen flux decreases with increasing temperatures for both the H_2 and CO sweep cases, which is due to the transition of the limiting step at higher temperatures. Additionally, the transition temperature at which the slope changes are different for the two fuels, and the transition occurs at higher temperature when H_2 is on the sweep side. This is due to that the rate limiting step changes from the feed side resistance to the sweep side resistance when temperature increases to around 950^{o}C in the H_2 sweep case, as is shown in Figure 6.7 (b). Yet in the CO sweep case, the limiting step transition between the two surface reaction resistances occurs at lower temperatures around 900^{o}C as in Figure 6.5 (b).

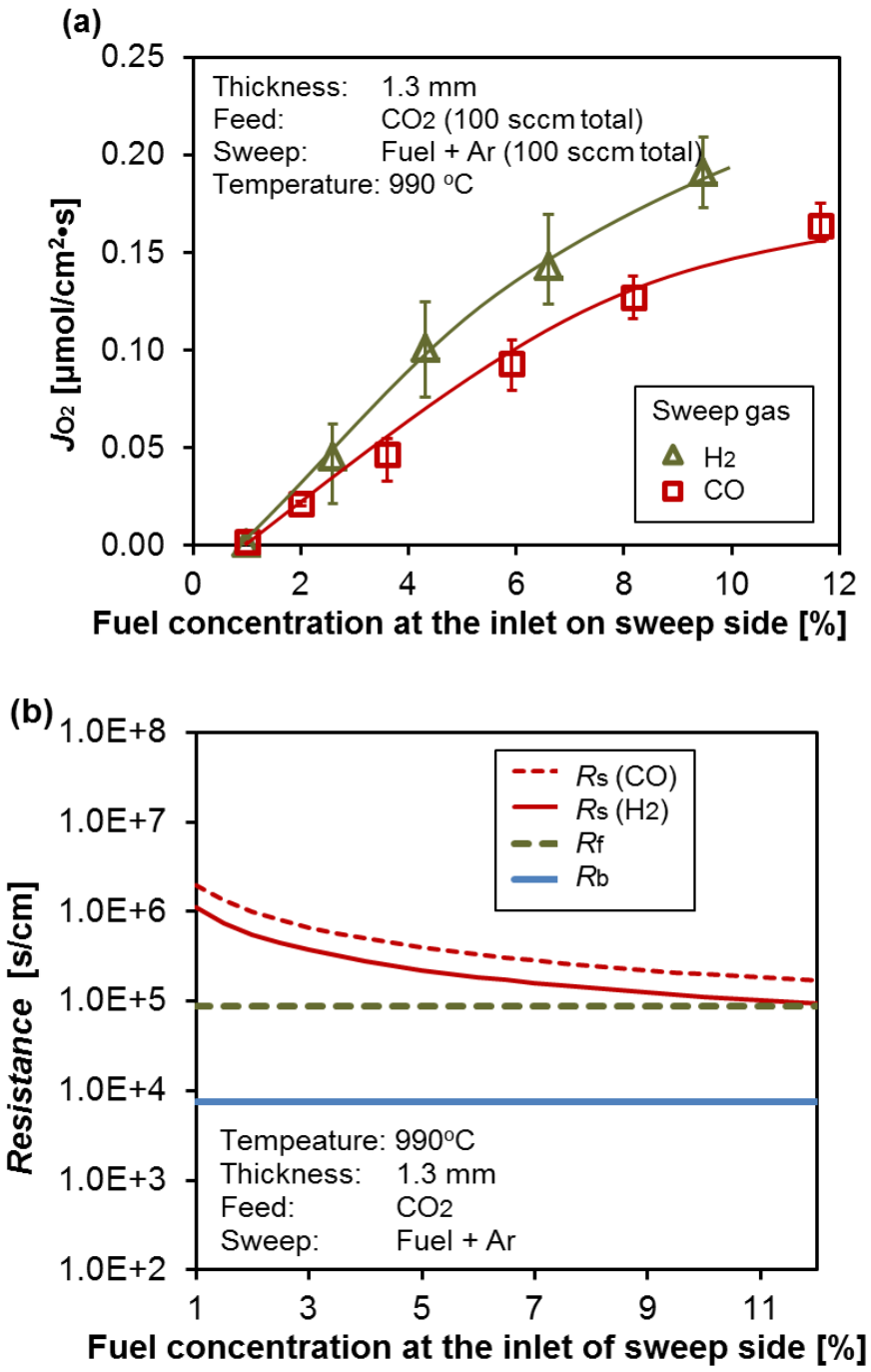

Figure 6.6 (a) By increasing sweep side surface kinetics with hydrogen as a sweep gas, the oxygen flux associated increases compared with the case of CO sweep. (b) Comparison between the resistances show that in the H_2 sweep case, the sweep side resistance value approaches to the same order of magnitude with the feed side resistance value at a lower fuel concentration compared with the CO sweep case.

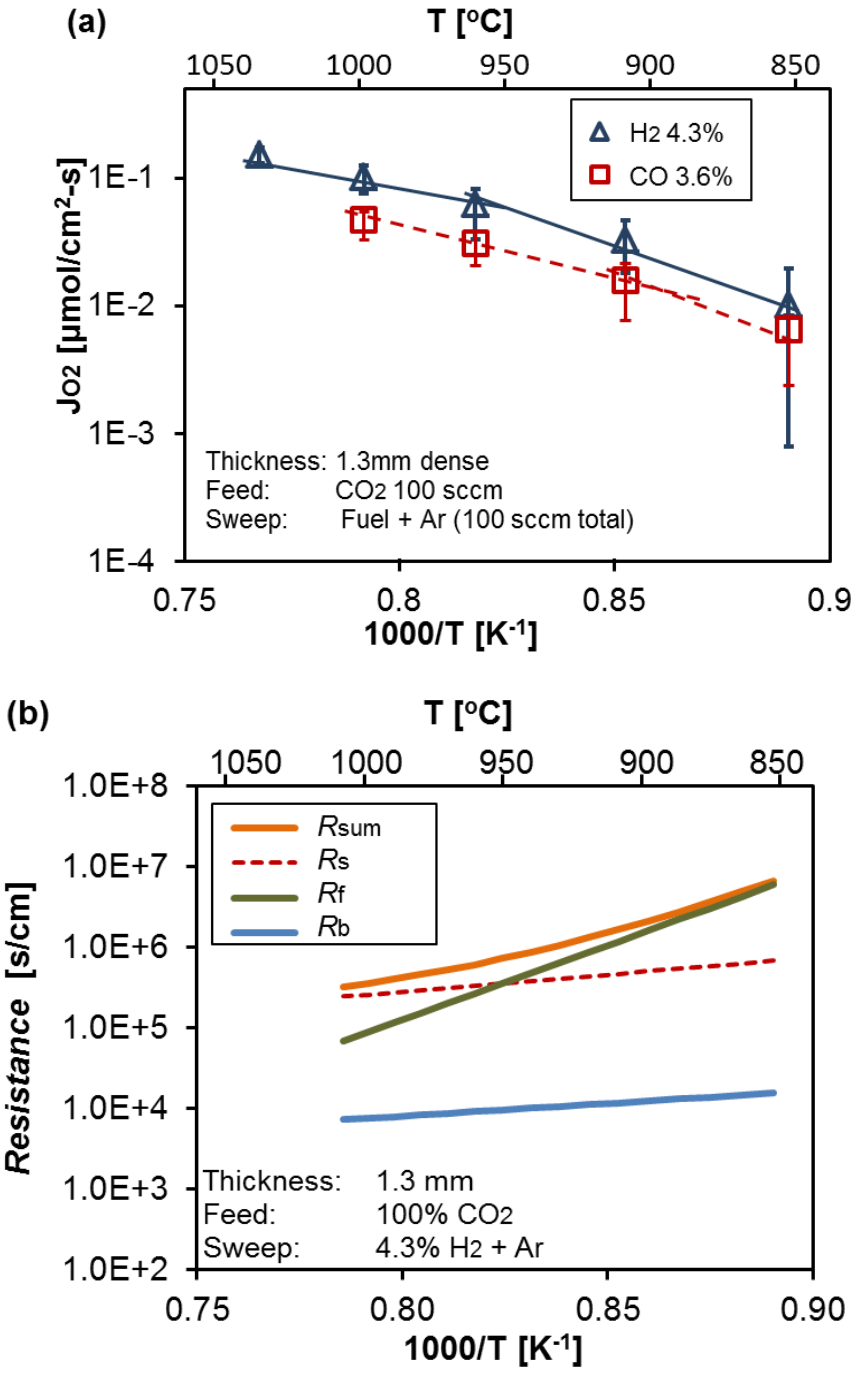

Figure 6.7 (a) Arrhenius plot shows two activation regimes for CO_2 dissociation with 4.3% H_2 on the sweep side on the 1.3 mm thick LCF91 membrane (b) The resistance values are plotted under the same operating conditions on (a), which shows that the rate-limiting step transition between the feed and sweep side reactions occurs around 950°C

6.3.5 Long term stability

After 106 hours of CO_2 splitting experiments with different sweep conditions, the oxygen flux remains about constant, as is shown in Figure 6.8 (a). Yet morphology changes and impurities are found on the membrane surfaces following the experiments, as is shown in the SEM, EDX and XRD analysis in Figure 6.8 (b) and (c).

From the SEM images in Figure 6.8 (b), we can see the morphology on the feed side of the membrane changes after experiments, and irregular particles in sizes of around 1 μm appear on that surface. EDX shows calcium and iron enrichment on these irregular particles and XRD confirms that the appearance of carbonates, oxides and brownmillerite ($Ca_2Fe_2O_5$) phases forming on the feed side of the membrane. On the other hand, the sweep side surface remains clean and shows clear grain boundaries as is seen in Figure 6.8 (b). EDX and XRD analysis reveal that the elemental distribution and the crystal structure remain the same as that before experiments, respectively. These results show that impurities formation occurs when the feed side of the LCF-91 membrane is exposed to CO_2 and under the operating conditions in our experiments as in Table 6.1. Nevertheless, the impurities locate sparsely on the membrane and do not change the membrane performance over the period of 106 hours.

Carbonate formation was found on other alkaline metal containing perovskite membranes especially on barium and strontium containing membranes such as $Ba_xSr_{1-x}Co_yFe_{1-y}O_3$ [45] and $BaCo_{1-x-y}Fe_xNb_yO_{3-\delta}$ [126] when exposed to high concentrations of CO_2. It has been found that for $BaCo_{1-x-y}Fe_xNb_yO_{3-\delta}$ membranes, oxygen flux for air separation decreased to zero immediately when the sweep gas was switched to CO_2, but it restored when sweep gas was switched back to inert, indicating that carbonates formation is reversible and depends on temperature and CO_2 concentration [126]. In the cases reported in this chapter, the calcium carbonates formed on the LCF-91 membrane are less stable than strontium and barium carbonates. As a result, the performance of the LCF-91 membrane didn't degrade from carbonate formation.

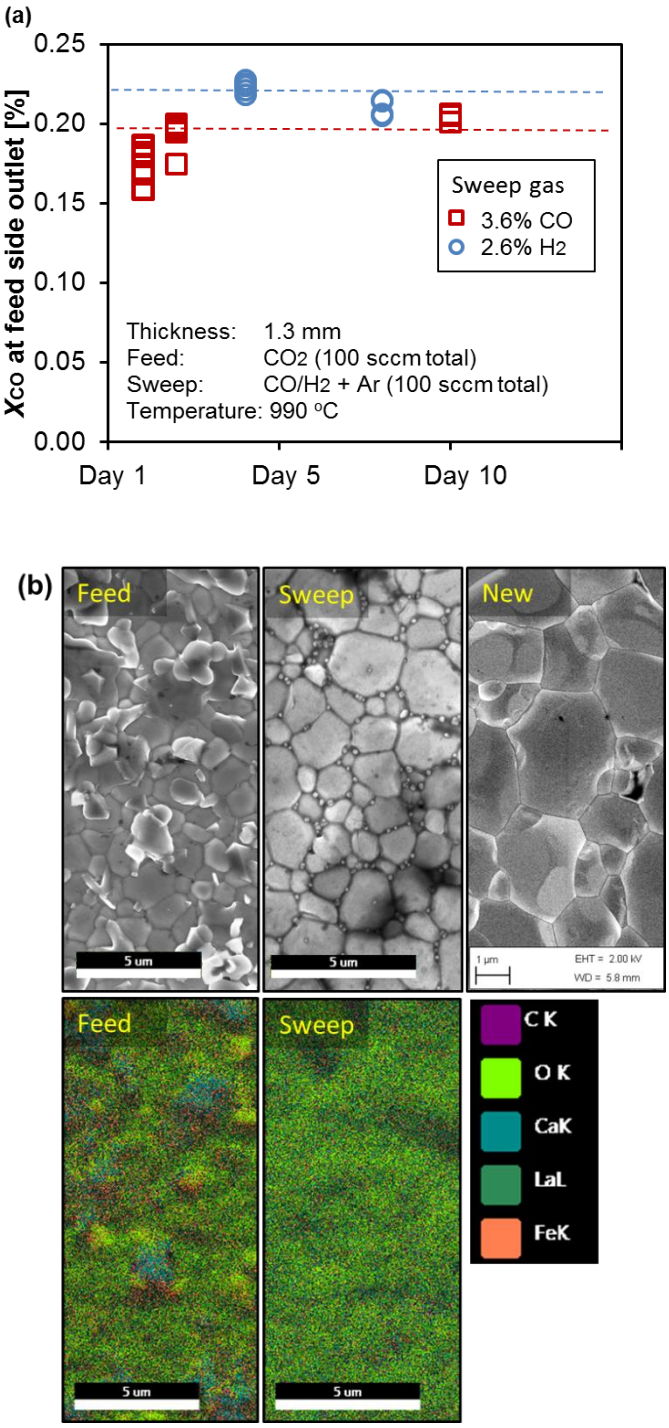

Figure 6.8 (a) Long-term operation shows that the performances remain constant for 10 days (total CO_2 splitting operation hour is 106 hours). (b) SEM images show morphology changes on the CO_2 feed side, and EDX analysis shows calcium and iron enrichment on the particles on that surface. (c) XRD analysis shows the existence of impurities such as carbonates and oxides on the feed side surface

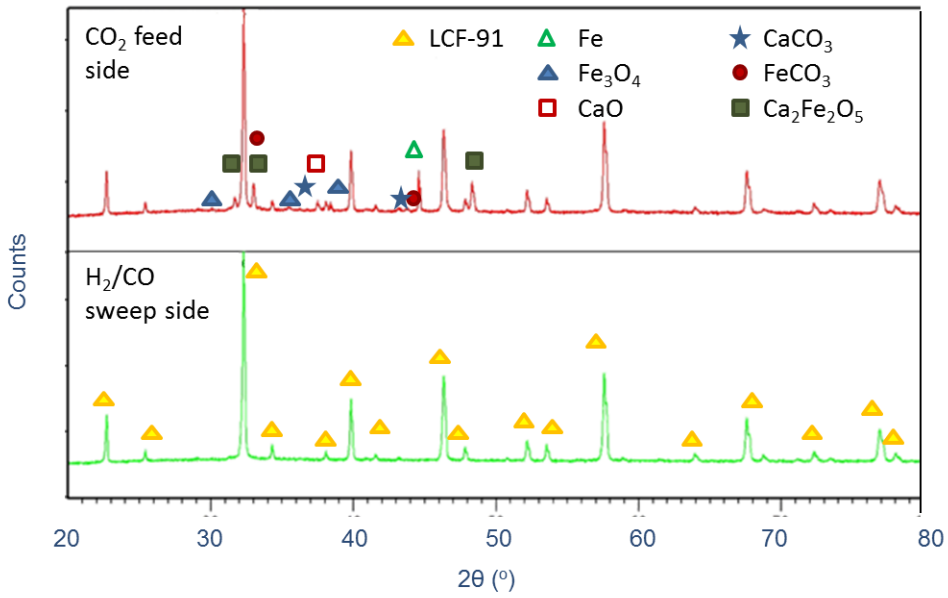

Figure 6.8 (a) Long-term operation shows that the performances remain constant for 10 days (total CO_2 splitting operation hour is 106 hours). (b) SEM images show morphology changes on the CO_2 feed side, and EDX analysis shows calcium and iron enrichment on the particles on that surface. (c) XRD analysis shows the existence of impurities such as carbonates and oxides on the feed side surface (cont.)

6.4 Conclusions

Different oxygen sources such as air and H_2O have been tested for the oxygen transport process on $La_{0.9}Ca_{0.1}FeO_{3-\delta}$ (LCF-91) membranes for oxygen separation, H_2O splitting and syngas production. In this chapter, the choice of oxygen source is extended to carbon dioxide, and the kinetics of CO_2 splitting on this oxygen permeable membrane is characterized.

(1) The dependences of oxygen fluxes on operating conditions such as oxygen source and fuel concentrations and temperatures are quantified. Both H_2 and CO were used as sweep gases; the former showing better performances for enhancing CO_2 reduction. The maximum oxygen flux achieved in this work was 0.19 μmol/cm2•s with 9.5% H_2 on the sweep side on a 1.3 mm thick LCF-91 membrane at 990°C.

(2) A resistance-network model is developed to describe the oxygen transport process during CO_2 splitting on an oxygen permeable membrane. Kinetics data for CO_2/CO surface reactions on LCF-91 membrane are parameterized with experimental data. This model compares the magnitude of different resistances for the oxygen transport process and indicates the limiting steps and trends for oxygen fluxes which are consistent with experimental results.

(3) This kinetic model reveals the rate limiting step transitions between the surface reactions on both feed and sweep sides under different operating conditions. For example, in the cases where either H_2 or CO is the sweep gas, the rate limiting step changes from CO_2 splitting reaction on the feed side to fuel oxidation on the sweep side with increasing operating temperatures. As a result, the Arrhenius plot of oxygen fluxes shows two regimes with different activation energy.

(4) Long term operation shows CO_2 splitting performances remains constant after 106 hours of operation, even though morphology changes, carbonate formation and calcium/iron enrichment are observed on the CO_2 feed side surface following the experiments.

This page is intentionally left blank

Chapter 7

Further Enhanced CO_2 Splitting by LCF Porous Layers

7.1 Introduction

Capturing and utilizing CO_2 have both environmental and economic benefits [12, 166, 167]. Analysis shows that CO_2 utilization by a scaled-up enhanced oil recovery has more economic incentive than the CO_2 to chemical pathway based on current technologies [186]. However, utilizing CO_2 as an abundant and cheap C1 feedstock for chemical production is attractive to close the carbon loop in using fossil fuel [8, 166]. Therefore, more studies have to be carried out to enhance the CO_2 conversion rate at a lower cost.

One factor that hinders the development of the membrane materials to support CO_2 splitting is that most of the oxygen permeable membrane materials with high performances are with Ba or Sr on the A site [39]. These Ba or Sr membranes suffer degradation due to the continuous formation of carbonates under the operation of high concentration of CO_2 [98]. Calcium carbonates are much less stable than barium or strontium carbonates, as is shown in the Ellingham diagram in Figure 7.1. But the Ca-base membrane has lower oxygen flux in air separation cases [39] and H_2O splitting cases [60].

The stability of LCF-91 under CO_2 environment makes it a good candidate for supporting CO_2 splitting. Yet as is discussed in the Chapter 6 and summarized in Table 7.1, the performances of LCF-91 membrane are not the highest among the state-of-the-art membranes. Therefore, modifications of the lattice structure or surfaces based on the LCF-91 materials are to be studied to achieve better performance on this stable oxygen permeable membrane.

Table 7.1 CO_2 thermolysis on oxygen permeable membranes

Ref	Materials	Thickness* [mm]	Catalyst	T [°C]	Max rate* [μmol/cm^2•s]	Stability
[96]	Nb doped $SrCo_{0.4}Fe_{0.5}Zr_{0.1}O_{3-\delta}$	1.5	NiO/Al_2O_3 (sweep)	750 – 900	1.60	Stable operates for ~500 h, flux is about 60% of the undoped membrane
[97]	$La_{0.6}Sr_{0.4}Co_{0.2}Fe_{0.8}O_{3-\delta}$	0.6**	/	840 – 1030	0.28	Amorphous graphite was detected by XRD
[100]	SDC (+Ag)	(a) 1 mm (b) ~20 μm	Pt or Ag (feed), $GdNi/Al_2O_3$ (sweep)	750 – 900	1.819	Constant performance with coke resistance (GdNi catalysts) for 100h.
[99]	$SrCo_{0.5}FeO_3$	2	/	760 – 940	0.25	Not stable. Pinhole and crack after 30 h hours operation under reactive flow
This work	$La_{0.9}Ca_{0.1}FeO_{3-\delta}$	1.3	/	850 - 1030	0.38	Stable for 106 hours of experiments
* CO production rate, which is twice of oxygen flux: $J_{CO} = 2 \times J_{O2}$						

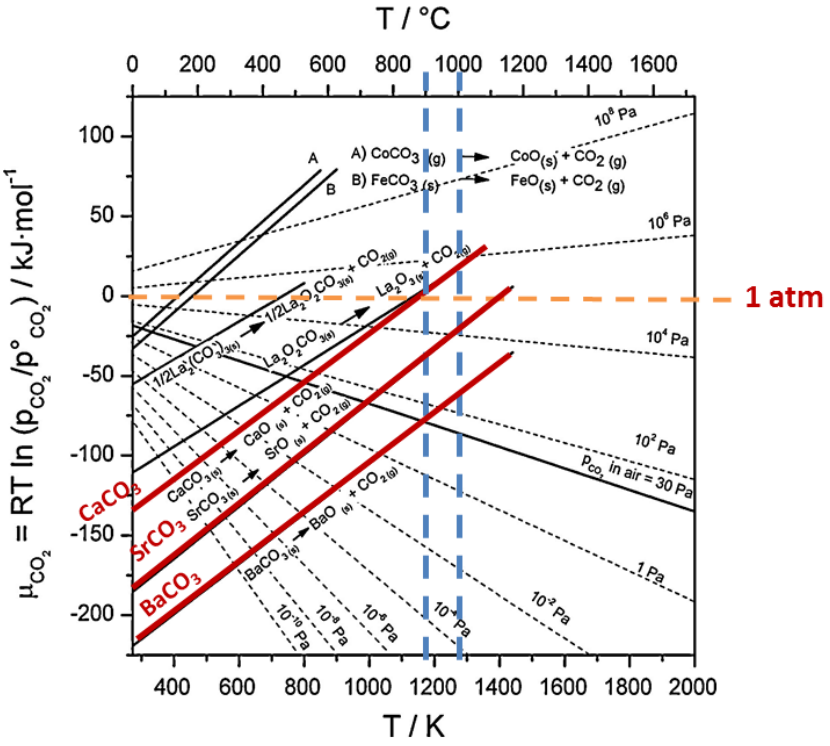

Figure 7.1 Ellingham diagram shows calcium carbonates are less stable than strontium and barium carbonates under the operating conditions for CO_2 splitting [98]

Therefore, in the chapter I will answer the question 'how the performances of CO_2 splitting on the stable LCF membrane are enhanced?' Previous kinetics studies show that there is a limiting step transition from the CO_2 splitting on the feed side to the fuel oxidation on the sweep side at higher temperatures. As a first step to demonstrate the enhancement of CO_2 splitting by facilitating the limiting step, porous layers of LCF-91 are fabricated and sintered on both sides of the flat membrane. As a result, CO_2 splitting rates are further enhanced.

7.2 Experiments

Dense $La_{0.9}Ca_{0.1}FeO_{3-\delta}$ (LCF-91) perovskite membranes with thickness of 1.3 mm and diameter of 16 mm are fabricated by Ceramatec. The effective diameter of the membrane is 12.7 mm as part of the membrane is covered with the gold sealant. The porous layer is added on both side of the membrane by a two-step method. First, LCF-91 powders (specific surface area is 1.8 m^2/g, density is 6.4 g/cm^3) were mixed with graphite powders (<20 μm, 2.16 g/cm^3, Sigma-Aldrich®) at 50 vol% in mortar and pestle for twenty minutes. The mixed powders were then compressed into a flat circular plate at 10 metric ton-force for one minute. Following that, the green plate was attached to a flat dense membrane and together they were sintered at 1450^oC for half an hour in air (including slow heat-up and cool down at ramp rates around 10^oC, the entire process takes around 24 hours). The dimensions of this surface modified membrane are shown in Table 7.2.

Table 7.2 Summary of membrane configuration

Thickness	Dense (mm)	1.3
	Porous (mm)	0.3
Effective diameter	Dense (mm)	12.7
	Porous layer - feed side (mm)	12.69 ± 0.4
	Porous layer - sweep side (mm)	12.42 ± 0.8

The SEM image in Figure 7.2 shows the pore structures in the porous layer. Large pores with diameter in the scales of 10 μm are observed, while the grains in the sizes of ~1 μm are lumped into large clusters in the sizes of ~50 μm after sintering. By estimation using the surface-to-volume ratio of spheres with a 50 μm diameter, the estimated surface area for the porous layer is 34 cm^2.

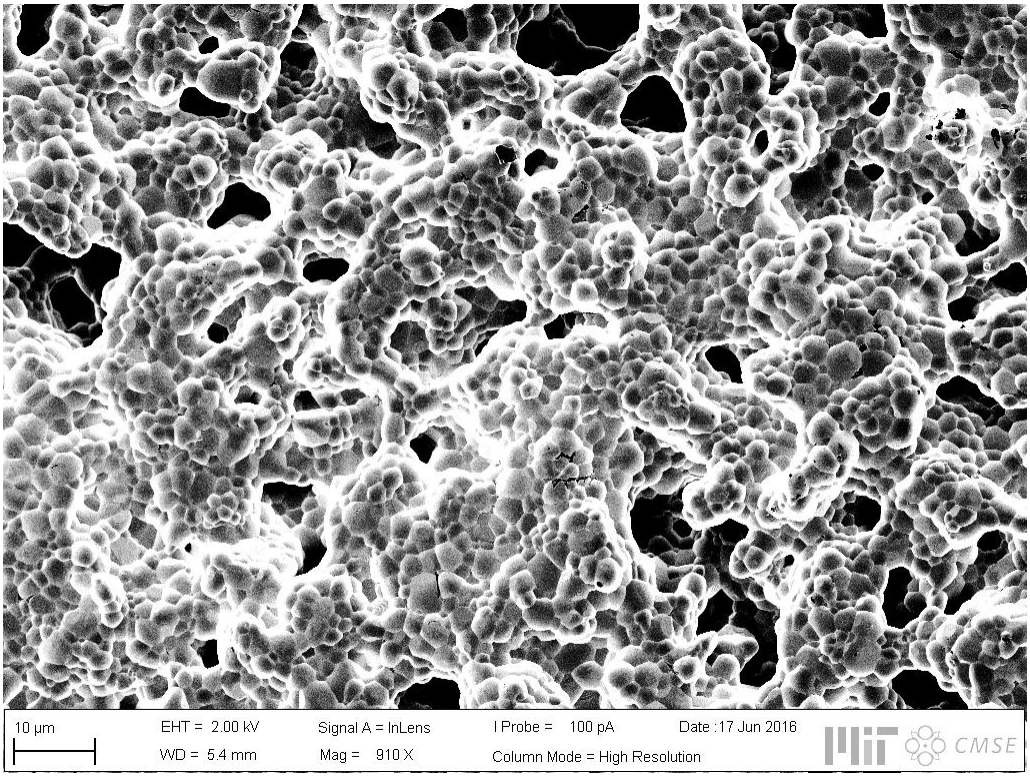

Figure 7.2 The SEM image of the pore structures on the porous layer attached to the membrane after sintering at 1450^oC

7.3 Results and discussion

7.3.1 Performance enhancement

The comparison between the fluxes on the membranes with and without porous layers is shown in Figure 7.3. There is an obvious enhancement when porous layers of LCF-91 material are added onto both sides of the membrane. With rising CO concentration on the sweep side, the oxygen fluxes across the membrane increases and the flux is raised by about 0.02 μmol/cm^2•s due to the porous layers.

Similar with the trend on the unmodified membrane, the oxygen fluxes for the modified membrane also increases rapidly and then flattens out at higher CO concentration on the sweep side. This is attributed to that the surface reaction resistance on the sweep side drops and approaches that on the feed side, and the sum of the resistance for oxygen fluxes flattens out at higher CO concentrations.

7.3.2 Temperature dependence

The dependence of oxygen flux on temperature is also studied on this surface-modified membrane for CO_2 splitting and the results are shown in Figure 7.4. For both cases when CO concentrations on the sweep side are 2% and 3%, we can observe a similar trend of the Arrhenius plot: with increasing temperature, the slope drops at around 900^{o}C for both cases. The same trend is also observed for the unmodified membrane (shown in the dotted lines in Figure 7.4), which is due to the transition of limiting step from CO_2 splitting on the feed side to CO oxidation on the sweep side at temperatures higher than 900 ^{o}C as is shown in Figure 6.5 (b).

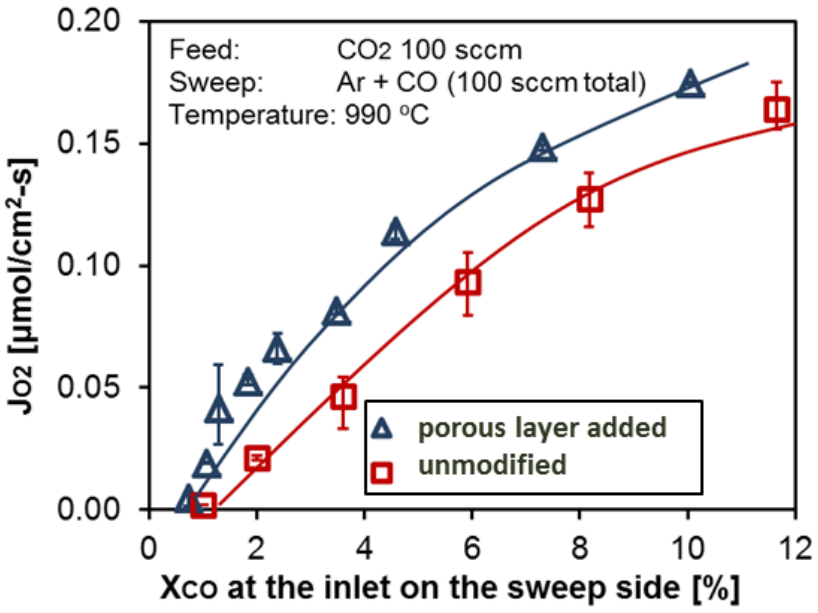

Figure 7.3 After adding the porous layer on both sides of the membrane, the oxygen flux associated with CO_2 splitting is raised by about 0.02 µmol/cm^2•s compared with the unmodified membranes

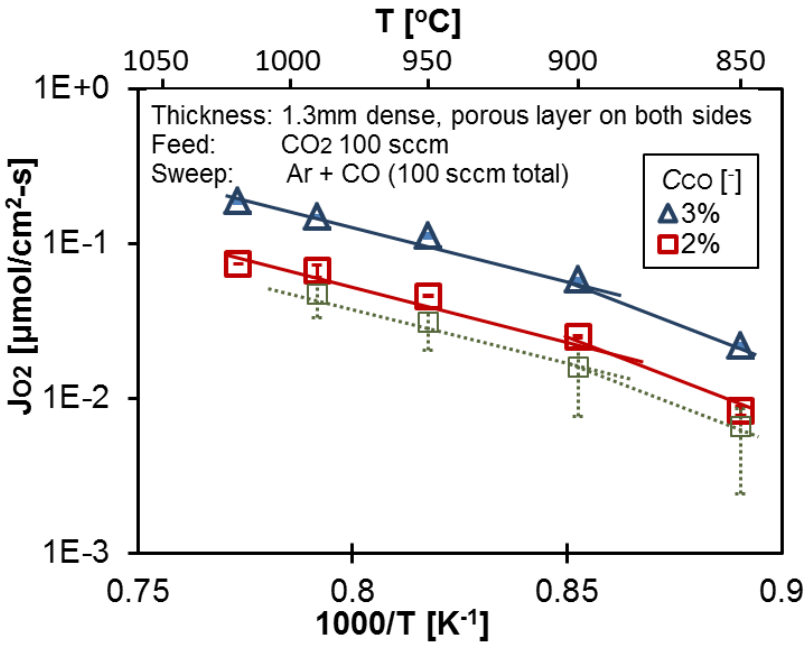

Figure 7.4 Arrhenius plot shows change of the slope at temperature around 900°C, which is similar to the unmodified membrane results (shown in the green dotted line in the figure with CO conentration of 3.6% on the sweep side)

The merit of adding a porous layer on both sides of the membrane is mainly to increase the active reaction sites for the surface reactions: oxygen vacancy sites on the feed side and the lattice oxygen on the sweep side. However, as the CO_2 splitting/CO oxidation reactions have comparably higher activation energy than the H_2O splitting/H_2 oxidation, the effect of porous layer addition (i.e., surface area) increase is not as profound as in H_2O splitting. Catalysts such as CeO_2 [187] that facilitate CO_2 splitting can be added to the porous layer to further enhance the splitting rate.

7.3.3 Surface reaction rate enhanced by the porous layer

As discussed before, the porous layer mainly increases the surface area, which can be translated into the pre-exponential factor in the Arrhenius rate constant expression as,

$$k_i = A_i e^{-\frac{E_a}{RT}} \tag{7-1}$$

where k_i is the rate constant for reaction *i*, A_i is the pre-exponential factor, E_a is the activation energy, *R* is the gas constant and *T* is the temperature. The porous layers on both sides are prepared by the same procedures and are expected to have the same properties such as porosity and surface areas. Therefore, by using the E_a values fitted in Table 6.2, the values of *A* for both the CO_2 splitting and CO oxidation reactions are fitted by multiplying the *A*'s in Table 6.2 with the same constant. The newly fitted values are shown in Table 7.3, and the kinetic parameters predict the experimental data very well as is shown in Figure 7.5. By comparing the new fitted values with the values on an unmodified membrane, we can see that the new pre-exponential constants are 1.41 times higher.

As discussed in section 7.2, the estimated surface area of the porous layer is 34 cm^2 which is 27 times larger than the flat surface of the membrane. However, the increase of the pre-exponential factor *A* is 1.41, which is smaller than expected. One reason can be that the sphere surface-to-volume ratio overestimates the surface areas of the porous layer. The other reason is that the diffusion of gas species into and out of the porous layers also plays an important role in the enhancement effects of the porous layer. Therefore, simulation of the gas diffusion into the porous layer coupled with the surface reactions, similar to those for solid oxide fuel cells [188, 189] or electrolysis cells [190-192] are needed to quantify the enhancement effect of the porous layer on CO_2 splitting rate. Besides, well designed patterned porous layers similar to the patterned electrodes can also be used to quantify the effects of the increase of surface areas.

Table 7.3 Reaction kinetic parameters for CO_2/CO surface reactions on the porous LCF-91 layers

	Parameter	*A*		*E*a*	
		Value	Unit	Value	Unit
$CO_2 + V_O^{\bullet\bullet} \rightarrow O_O^x + 2h^{\bullet} + CO$	k_{f,CO_2}	1.81E15	[cm^4/mol•s]	3.64E5	[J/mol]
$CO + O_O^x + 2h^{\bullet} \rightarrow CO_2 + V_O^{\bullet\bullet}$	k_{r,CO_2}	2.31E7	[cm^4/mol•s]	1.57E5	[J/mol]

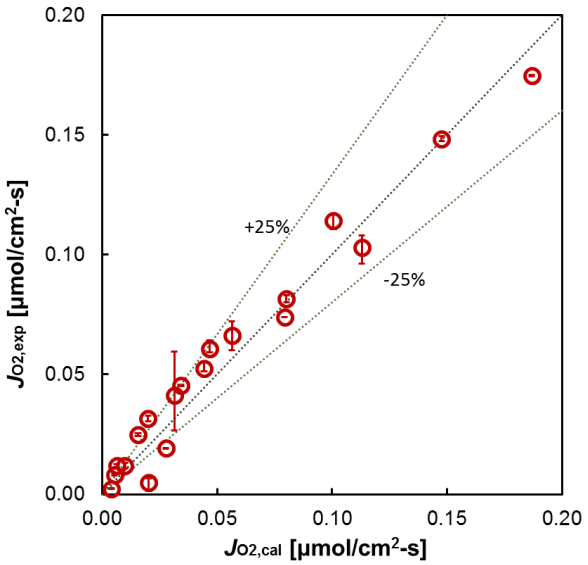

Figure 7.5 The resistanc-network model with new pre-exponential values predits the experimental values well

7.4 Conclusions

In this chapter, CO_2 splitting is further enhanced on a LCF-91 membrane with porous supports on both the feed and sweep sides. A two-step method is adapted to fabricate the porous layers and the oxygen flux is raised by about 0.02 μmol/cm^2•s compared with the unmodified membranes. Arrhenius plots of the oxygen flux with different CO concentration on the sweep side show a change of the slope and the same transition temperature is observed with or without porous layers. This indicates that for the modified membrane, there is also a transition in the limiting step from CO_2 splitting on the feed side to CO oxidation on the sweep side.

New pre-exponential factors are fitted for the surface reactions on both feed and sweep sides. The new value is 1.41 times higher than the unmodified value, which shows the enhancement factor of the porous layer. However, the enhancement is not as high as expected, which is likely due to the overestimation of the surface area by the surface are-to-volume ratio of spheres and the effects of gas transport in the porous layer. Further studies with patterned surfaces can quantify the effects of the increase of the surface area and the gas transport in the porous layer.

Chapter 8

Monolith Membrane Reactor Design for Hydrogen and Syngas Production

8.1 Introduction

Interest has grown in producing hydrogen in an efficient and environment-friendly way. Approximately 7.2 exajoules (EJ) of hydrogen is used every year in global industries as cited by IEA from the *Chemical Economics Handbook* [142]. 96% of the global hydrogen production is from hydrocarbons, among which half is from natural gas reforming; only 4% of the hydrogen is produced from water electrolysis [193]. As a result, 500 megatonnes (Mt) of CO_2 is emitted to atmosphere from hydrogen production [142], which adds to the carbon footprint of the 'carbon-free' hydrogen utilization.

In order to decrease the carbon footprint, renewable energies such as solar, wind and hydropower are proposed for hydrogen production [194]. Thermochemical processes that utilize solar or nuclear heat, such as the chemical looping and the oxygen transport membrane technologies are among the most promising technologies for the clean hydrogen production [29]. In the previous chapters, membrane-supported H_2O/CO_2 splitting for fuel production has been discussed. In this chapter, the co-production of hydrogen and syngas from water splitting and partial oxidation of methane (POM), respectively is investigated. Unlike the chemical looping or redox cycles where the oxygen carriers move between the oxidizing and reducing environments at high temperatures [148, 194, 195], this membrane technology combine the oxidizing and reducing processes into one unit without mechanical movements of the reactor. Easier operation, thus, can be achieved. Additionally, the oxygen permeable membrane can shift thermodynamic equilibrium to further split water to produce hydrogen as well as *in situ* separation of hydrogen from other non-condensable gases (i.e., CO_2 and CO).

A schematic graph of this technology is shown in Figure 8.1. There are five sub-steps in the process: 1) water diffuses to the membrane surface and the products move

away from the surface; 2) water reacts with the oxygen vacancies to produce hydrogen, while the oxygen atom from water incorporates as the lattice oxygen; 3) oxygen diffuse through the membrane due to the chemical potential gradient; 4) methane reacts with the lattice oxygen ions to produce syngas; 5) methane diffuses to and the products away from the surface. The products on different sides of the membrane (i.e., hydrogen and syngas) can be collected for further applications. For example, ultrahigh-purity hydrogen can be separated from the steam-hydrogen mixture on the feed side for fuel cell or semiconductor industries [89]. On the other hand, the syngas from POM on the sweep side has a stoichiometric H_2/CO ratio of 2.0 for methanol production [83].

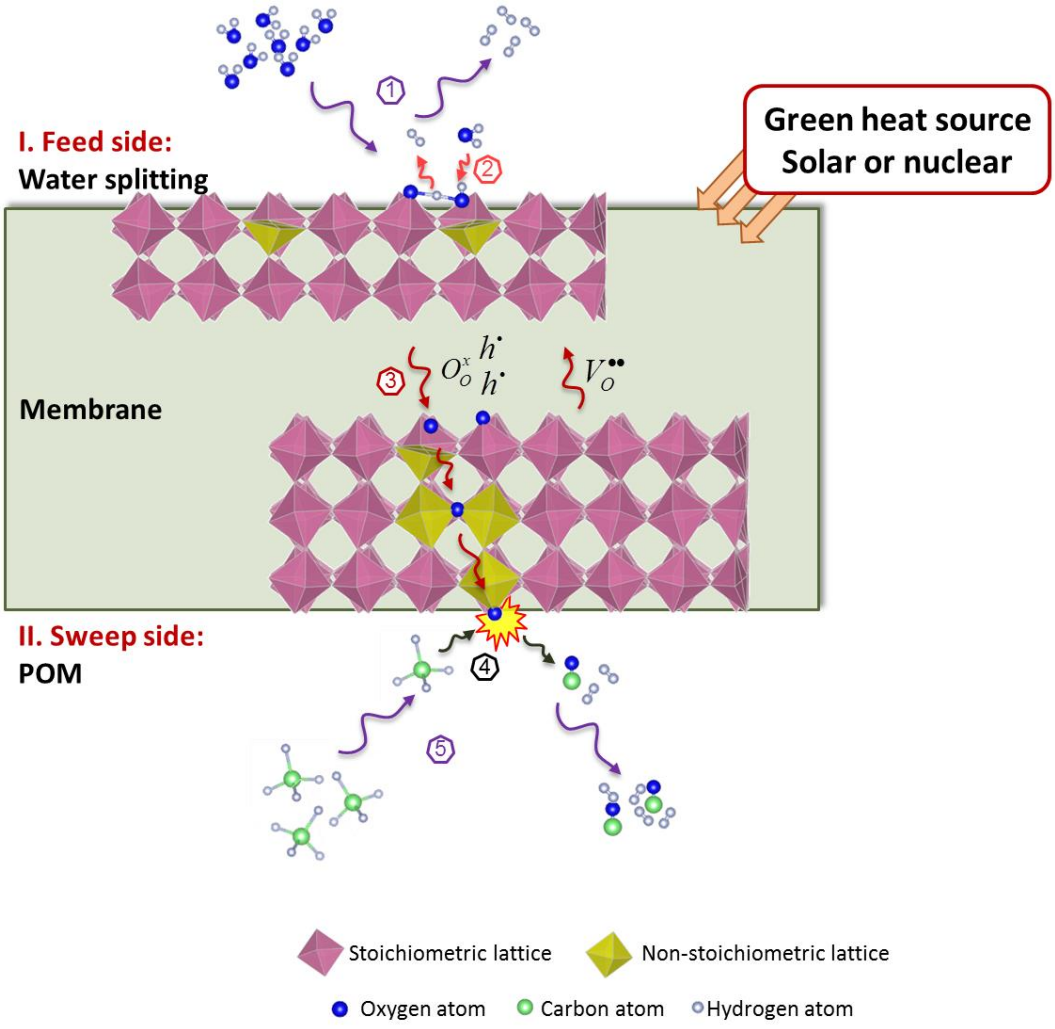

Figure 8.1 Schematic shows co-production of hydrogen and syngas from water splitting on the feed side and methane partial oxidation on the sweep side, respectively

Experimental studies have been carried out on various mixed ionic electronic materials for this application, such as $La_{0.9}Ca_{0.1}FeO_{3-\delta}$ (LCF) [60], $BaCo_xFe_yZr_{1-x-y}O_{3-\delta}$ (BCFZ) [65], $La_{0.6}Sr_{0.4}Co_{0.2}Fe_{0.8}O_{3-\delta}$ (LSCF) [68] and CeO_2-Gd (CGO) [73]. The highest hydrogen production rate was achieved as 3.4 μmol/cm^2•s on a 0.05 mm thick BCFZ membrane with 75% water feed and 10% methane sweep at 950^{o}C. However, the CO selectivity on this membrane was found to be less than 60% and other carbon species, (i.e., CO_2 and coke) were found on the sweep side [52]. For a LCF membrane, Wu et al. [60] identified the limiting step to be the POM reaction on the sweep side, and applied Ni/LCF porous catalysts on that side to enhance the hydrogen production rate from water splitting by two orders of magnitude compared to the values on a unmodified flat membrane, reaching 0.37 μmol/cm^2•s. Besides, by applying the Ni/LCF catalysts, a stoichiometric ratio of H_2/CO ~ 2 was produced at the outlet of the membrane reactor due to the combined effects of reactions on the surface and in the gas phase [60].

In this chapter, the monolith membrane reactor is studied for co-production of hydrogen and syngas. Several membrane reactor designs such as planar [43], tubular [196] and monolith [197, 198] reactors have been proposed. Yet since the monolith reactors can be readily produced in industry scale and they have high surface-area-to-volume ratio, we focus on their application in this chapter. Based on the resistant-network permeation model and the kinetics parameters described in previous chapters, the oxygen flux through the membrane under different operating conditions is modelled [39, 72]. Different from the previous models in the literature that assume the thermodynamic equilibrium in gas phase [199], both surface reactions and ion diffusion kinetics are considered in this reactor model. First, this membrane reactor is compared with the conventional steam methane reforming process for the production of high-purity hydrogen (purity > 99%). Results show the membrane reactor has higher thermal efficiency due to the advantages of *in situ* separation of hydrogen. Then the monolith membrane reactor is studied using a plug-flow reactor model. A base case with operating conditions similar to the solid oxide electrolysis cell (SOEC) is discussed and a sensitivity analysis is performed to identify the important parameters that affect the co-production performances in a membrane reactor.

8.2 Comparison between membrane reactor and steam reformer for high-purity hydrogen production

First, the membrane-supported water splitting with methane-sweep is compared with the conventional catalytic steam methane reforming for the production of high-purity hydrogen (purity>99%). The process modelling platform gPROMS [200] is used to model these two processes. Previous studies have successfully used this platform to model solid oxide electrolysis cells [201, 202]. The schematics for the two processes are shown in Figure 8.2, and the operating conditions are summarized in Table 8.1. More details of the models can be found in the Appendix B in this chapter.

The two processes are compared based on the first law efficiency, which is defined as

$$\eta_{th}^{overall} = \frac{Q_{prod}}{Q_{total}^{in}} = \frac{Q_{prod}}{W_{elec}^{in} / \eta_e + Q_{react}^{in} + Q_{source}^{in}} \tag{8-1}$$

where Q_{total}^{in} is the total thermal energy [W], and Q_{react}^{in}, Q_{source}^{in} and Q_{prod} are the thermal energies of the reactants, the heat source and the products [W], W_{elec}^{in} is the electricity consumed [W], η_e is the averaged thermal power plant efficiency, 38% [203].

The following assumptions are made:

(1) The heat source is available at 100^{o}C (i.e., solar-steam) and the heat required for the high-temperature reactors is from CH_4 combustion;

(2) The membrane reactor is modelled as a well-stirred reactor. Similar to the methane-assisted solid oxide electrolysis, steam is added on the fuel side to reform the methane and facilitate the reactions on that side [204];

(3) In the steam reforming process, both the reformer and the water gas shift reactor are assumed to be adiabatic and at thermodynamic equilibrium;

(4) Pressure drops in the reactors are neglected. Compressors/turbines are used to pressurize/expand the gases for steam reforming processes with isentropic efficiency of 80%. The compression work is partly recovered from the expansion of the exhaust gases;

5) The penalty for the pressure swing adsorption (PSA) process is modelled by H_2 recycle ratio, which gives

$$\dot{n}_{H_2}^{product} = \varphi_{H_2\_recycle}\dot{n}_{H_2}^{input} \quad (8\text{-}2)$$

where $\dot{n}_{H_2}^{input}$ and $\dot{n}_{H_2}^{product}$ are the hydrogen molar flow rates input and output of the PSA, respectively, [mol/s], and $\varphi_{H_2\_recycle}$ is the recycle ratio which has a value of 90% [205].

6) In the condenser, 100% of hydrogen recovery is assumed, and the energy consumption for the condensation separation process is neglected.

Table 8.1 Operating conditions for the two processes

		SMR-PS [205, 206]	**MR**
Operating pressure (bar)		20*	1
Operating temperature (^{o}C)		Steam reformer: 850 WGS reactor: 350	990
Pressure swing adsorption (PSA) [205]	Operating temperature (^{o}C)	25	
	Hydrogen recycle ratio	90%	
X_{H2O}:X_{CH4} at the inlet of reformer and membrane sweep side		3.2:1	2.44:1†
X_{H2O} on the feed side of the MR		/	1
Heat source temperature (^{o}C)		100	
Hydrogen production		**Purity > 99%‡ at 1 bar**	

SMR-PSA: steam methane reformer with pressure swing adsorption

MR: membrane reactor

* The steam reformer operates at high pressures, and the exhaust gases go through turbines to recover part of the compression work required for the input stream

† This value is optimized to achieve 90% methane conversion rate at the outlet of the membrane reactor

‡ Only the hydrogen concentration (>99%) is evaluated and compared between these two processes. The impurities (i.e., CO_2, CO, H_2O) concentrations in the hydrogen streams are not evaluated in this study

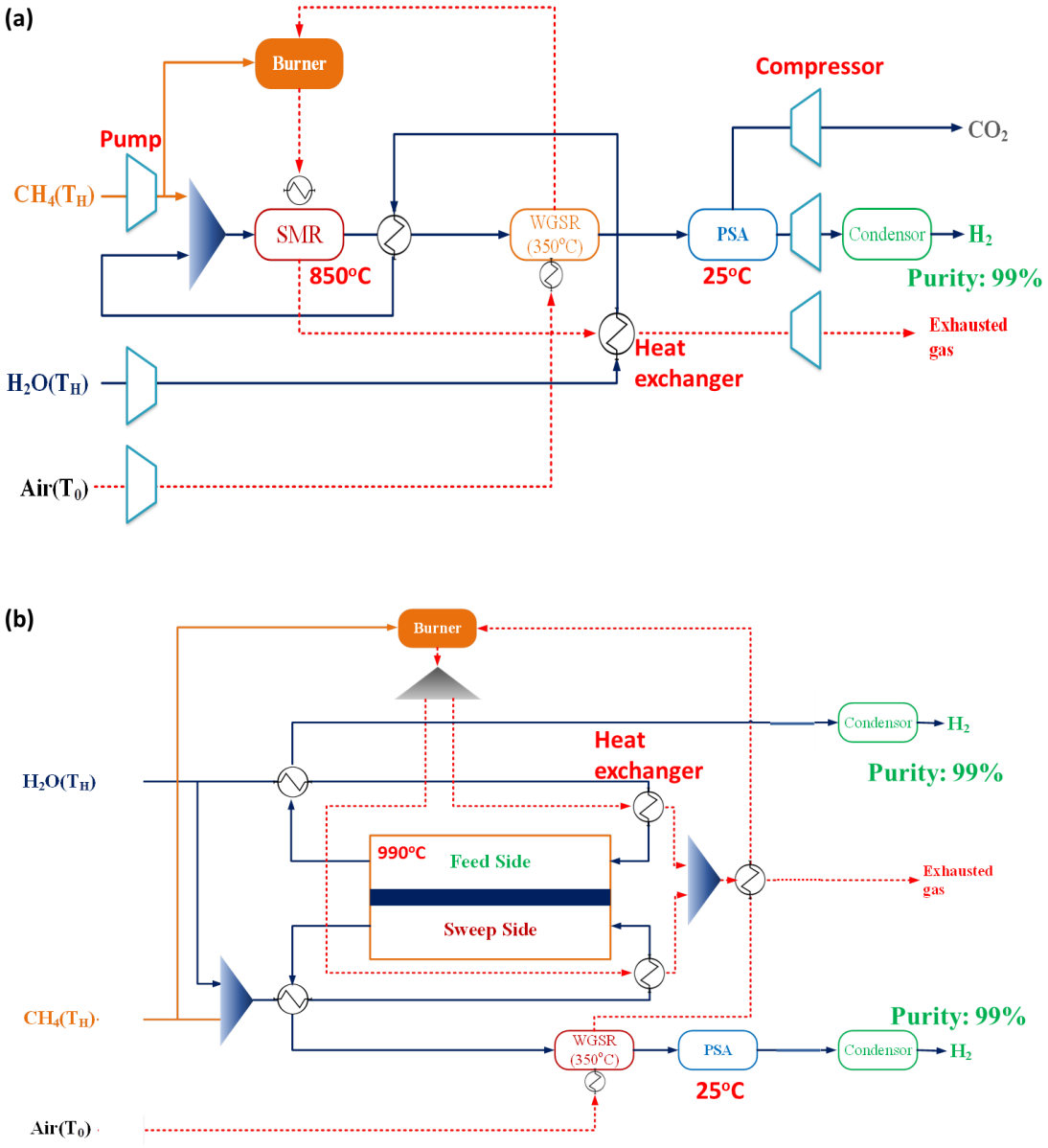

Figure 8.2 Schematic for (a) the conventional catalytic steam methane reformer [205] (b) the membrane-supported water splitting with methane sweep (High-purity hydrogen >99% is produced)

The results for the simulation are shown in Table 8.2. We can see that the major part (over 78%) of the energy supply is from the methane input. As the membrane reactor requires less methane, it has a higher efficiency than the steam reformer. The difference

in the methane input comes from the amount of hydrogen that undergoes the pressure swing adsorption (PSA) purification process, as the PSA process results in a penalty that only 90% of the hydrogen in the input stream is recovered [205]. In the membrane reactor, 79% of the high-purity hydrogen is produced from water splitting on the feed side, which can be easily purified to >99% by condensation. Yet in the reformer, all the hydrogen produced is from the mixture coming out of the water gas shift reactor (i.e., H_2, H_2O, CO, CO_2 and CH_4) that requires PSA purification. As a result, more methane is required in the reformer to compensate for this loss of hydrogen during PSA purification.

Note that the operating pressure of the steam reformer is 20 bar in this study. In order to recover the compression work, the exhaust gases from the reforming process go through the turbines and hence, decrease the electricity required for compression.

Table 8.2 Simulation results for the two processes to produced 1 Nm^3 (15°C, 1 bar) of hydrogen with purity higher than 99%

	SMR-PSA	MR
Reactor temperature (°C)	850	990
CH_4 flow rate (Nm^3/Nm^3 H_2)	0.45	0.38
H_2O flow rate (kg/Nm^3 H_2)	0.75	1.49
Heat sources temperature (°C)	100	
Electricity – compressor/turbine (MJ/Nm^3 H_2)	0.01	-
Ratio of hydrogen from PSA (Purity>99%)	1.00	0.21
Ratio of hydrogen requires no PSA	-	0.79
Summary		
Heat value of CH_4 (MJ/Nm^3 H_2)	**17.32**	**14.66**
Heat from heat sources (MJ/Nm^3 H_2)	**2.00**	**3.95**
Total electricity (MJ/Nm^3 H_2, equiv. therm.)	**0.04**	**0.00**
Heat value of H_2 (MJ/Nm^3 H_2)	**12.74**	
Thermal efficiency η_{th}(%)	**65.80**[†]	**68.45**

[†] A reference value is 61% in a similar SMR-PSA process [206]

As the membrane reactor has a higher efficiency to produce high-purity hydrogen, in the following sections, the monolith membrane reactor is modelled and sensitivity analysis is carried out to identify the important parameters that impact the reactor performance.

8.3 Base case parametric studies of the monolith membrane reactor

8.3.1 Reactor model

A monolith reactor for co-production of hydrogen and syngas is modelled as shown in Figure 8.3. Monolith membrane reactors have been studied in the literature for other applications, such as oxy-fuel combustion [197] and methane reforming [198]. A plug-flow reactor model is used and the assumptions are:

(1) The total pressures of each channel are the same at atmospheric pressure, and the pressure drop in the axial direction is neglected [148];

(2) Isothermal operating is considered, and the temperature of the monolith reactor is constant;

(3) In this study, we consider steady operation, so the reaction rates on the feed and sweep side are correlated with the oxygen flux across the membrane (shown in Equation (8-6)).

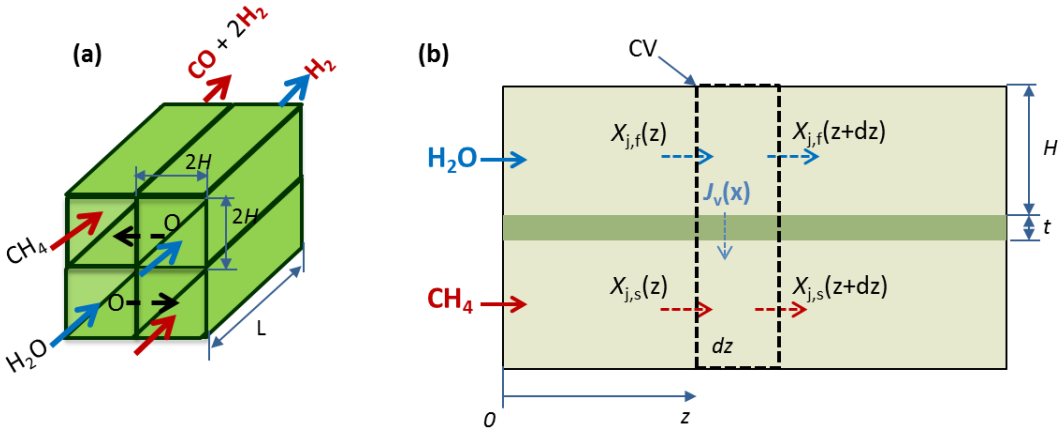

Figure 8.3 A monolith reactor is modelled in this study. (a) The channels are with dimensions: $2H \times 2H \times L$; (b) the control volume of the plug-flow reactor model

Based on the assumptions, a 1D model is shown Figure 8.3 (b), which models half a channel based on the symmetry configuration. The governing equations are

(1) Continuity: $$\frac{d\left(u_i C_i\right)}{dx} = \sum_j \dot{\omega}_{j,i} \tag{8-3}$$

(2) Species: $$\frac{d\left(u_i C_i X_{j,i}\right)}{dx} = \dot{\omega}_{j,i} \tag{8-4}$$

(3) Energy equation: $$\dot{Q} = \sum_i \frac{d\left(u\hat{h}_i C_i\right)}{dx} \tag{8-5}$$

Here, u is the velocity [m/s], C is molar concentration [mol/m^3], $\dot{\omega}$ is net production rate, [mol/m^3/s], X is mole fraction [-], $\hat{h}$ is enthalpy [J/mol], $\dot{Q}$ is heat transfer rate [W]. The subscript i is either f or s for feed or sweep side, respectively; the subscript j stands for species j. The homogeneous reaction in the gas phase is neglected due to the slow kinetics compared to heterogeneous surface reaction. Therefore, the net production of species j is proportional to the oxygen vacancy flux J_V [mol/m^2/s], as

$$\dot{\omega}_{j,i} = a\left(J_v \big/ H\right) \tag{8-6}$$

where a is the stoichiometry coefficient [-], and H is the channel height [m].

Ordinary differential equation solver from Matlab is used to solve equations (8-3) and (8-4), while equation (8-5) is used to calculate the heat input requirement of the reactor to maintained isothermal operation.

Gas phase reaction is neglected [148], and the mass diffusion in the gas phase is modelled as

$$J_j = h_{m,j,i}\left(X_{b,j,i} - X_{s,j,i}\right)C_{b,i} \tag{8-7}$$

where $h_{m,j,i}$ is mass transfer coefficient for species j on the side i [m/s]. It can be calculated from Sherwood number, which is 3.61 for laminar flow in a squared channel [148, 207]. As the feed side has high concentration of water and the sweep side of argon, binary diffusion coefficient is used to model different gas species diffusion on either the feed or sweep side. The binary diffusion coefficients D_{AB} between species A and B are calculated using [208]

$$D_{AB} = \frac{1.00\times10^{-3}T^{1.75}\left(1/M_A + 1/M_B\right)^{1/2}}{p\left[\left(\Sigma_A \upsilon_i\right)^{1/3} + \left(\Sigma_B \upsilon_i\right)^{1/3}\right]^2} \tag{8-8}$$

where T is the temperature [K], M_A and M_B are the atomic mass for species A and B, respectively, [g/mol], and $\Sigma_A \upsilon_i$ and $\Sigma_B \upsilon_i$ are the diffusion volumes of molecules A and B, respectively.

8.3.2 Validation of the numerical approach

Because there are no experimental data available for the monolith membrane reactor for water splitting, the numerical model in this chapter is validated with the analytical results of the internal flow cases with oxygen permeation, similar to [148]. In this case, the sweep side methane concentration is fixed at a certain value, while the feed side water concentration at the inlet is set to be 80%. At every position z along the reactor length, the oxygen flux is,

$$J_V(z) = \frac{C_O}{\frac{1}{k_{f,H_2O}C'_{H_2O}(z)} + \frac{t}{D_v} + \frac{1}{\tilde{k}_{f,CH_4}C''_{CH_4}}}, \tag{8-9}$$

where C_o is the concentration of oxygen species (including lattice oxygen and oxygen vacancies), k_{f,H_2O} and $\tilde{k}_{f,CH_4}$ are the reaction rate constants for water splitting and methane partial oxidation, respectively. C'_{H_2O} and C''_{CH_4} are the concentrations of water and methane on the feed and sweep side, respectively. t is the membrane thickness and D_v the oxygen vacancy diffusivity.

Therefore, correlating the oxygen flux and the water splitting rate, we can get

$$\frac{dX_{f,H_2O}(z)}{dz} = -\frac{C_O}{\frac{1}{k_{f,H_2O}C_f X_{f,H_2O}(z)} + \frac{t}{D_v} + \frac{1}{\tilde{k}_{f,CH_4}C_s X_{s,CH_4}}} \cdot \frac{1}{HU_c}. \tag{8-10}$$

Here, X is the mole fraction, H is the height of the channel and U_c is the total molar flow rate in the channel. By separating the variables and integrating, the analytical solution of H_2O concentrations along the length is from

$$\frac{1}{k_{f,H_2O}C_f}\ln\left[X_{f,H_2O}(z)\right]+\left(\frac{t}{D_v}+\frac{1}{\tilde{k}_{f,CH_4}C_sX_{s,CH_4}}\right)X_{f,H_2O}(z)$$
$$-\frac{1}{k_{f,H_2O}C_f}\ln\left[X_{f,H_2O}(0)\right]+\left(\frac{t}{D_v}+\frac{1}{\tilde{k}_{f,CH_4}C_sX_{s,CH_4}}\right)X_{f,H_2O}(0)\cdot \qquad (8\text{-}11)$$
$$=-\frac{C_O}{HU_c}z$$

The comparison between the values calculated from the model and the analytical solution is shown in Figure 8.4 for a 0.9 mm membrane at 990°C with different fixed concentrations of methane on the sweep side. The model matches very well with the analytic solutions.

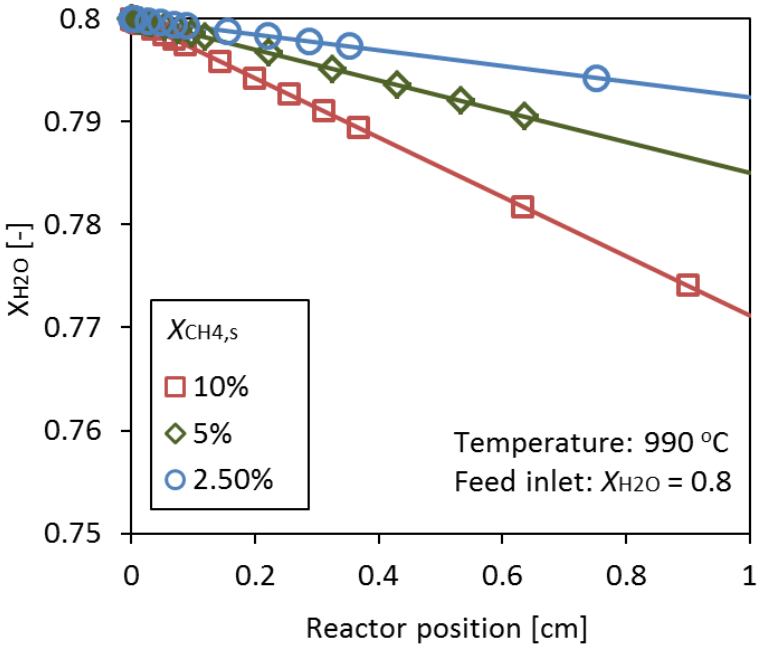

Figure 8.4 Comparison between the values from model calculation (symbols) and analytical solutions (lines) at three different methane concentrations on the sweep side

8.3.3 Base case study

The base case is chosen based on the geometry and the operating conditions of the solid oxide electrolysis cells [201, 209] and the monolith reactors [148, 194]. The parameters are listed in Table 8.3. The water concentration at the inlet on the feed side is 80%, and the methane concentration at the inlet on the sweep side is 5%. The water

concentration is kept high as the unconverted water can be separated from hydrogen by condensation and then recycled. The fuel concentration is kept low to decrease coke formation as well as to prevent the membrane from breaking in the highly reducing environment on the sweep side. The fuel utilization ratio is usually assumed to be 90% for a solid oxide fuel cell [210], and the unconverted fuel is burned to supply heat.

Table 8.3 Geometry and operating conditions of the base case

Channel height 2*H* [mm]	2
Channel length *L* [mm]	100
Membrane thickness [mm]	0.9
Temperature *T* [^{o}C]	990
Fee side flow rate [sccm/cm^2]	2.1
Feed water concentration [-]	80%
Sweep side flow rate [sccm/cm^2]	2.1
Sweep methane concentration [-]	5%

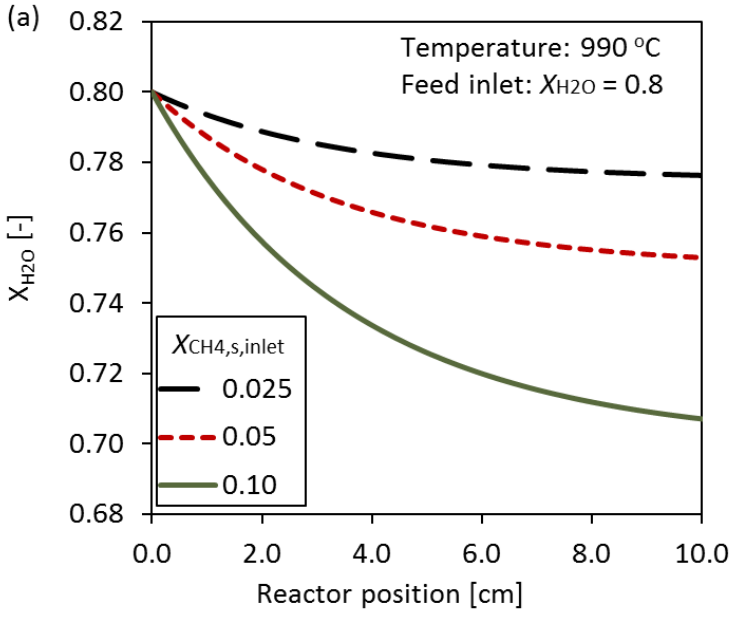

Figure 8.5 (a) Water concentration decreases along the reactor length (b) Methane conversion ratios are above 90% at the exit of the reactor (c) Oxygen vacancy flux drops along the reactor

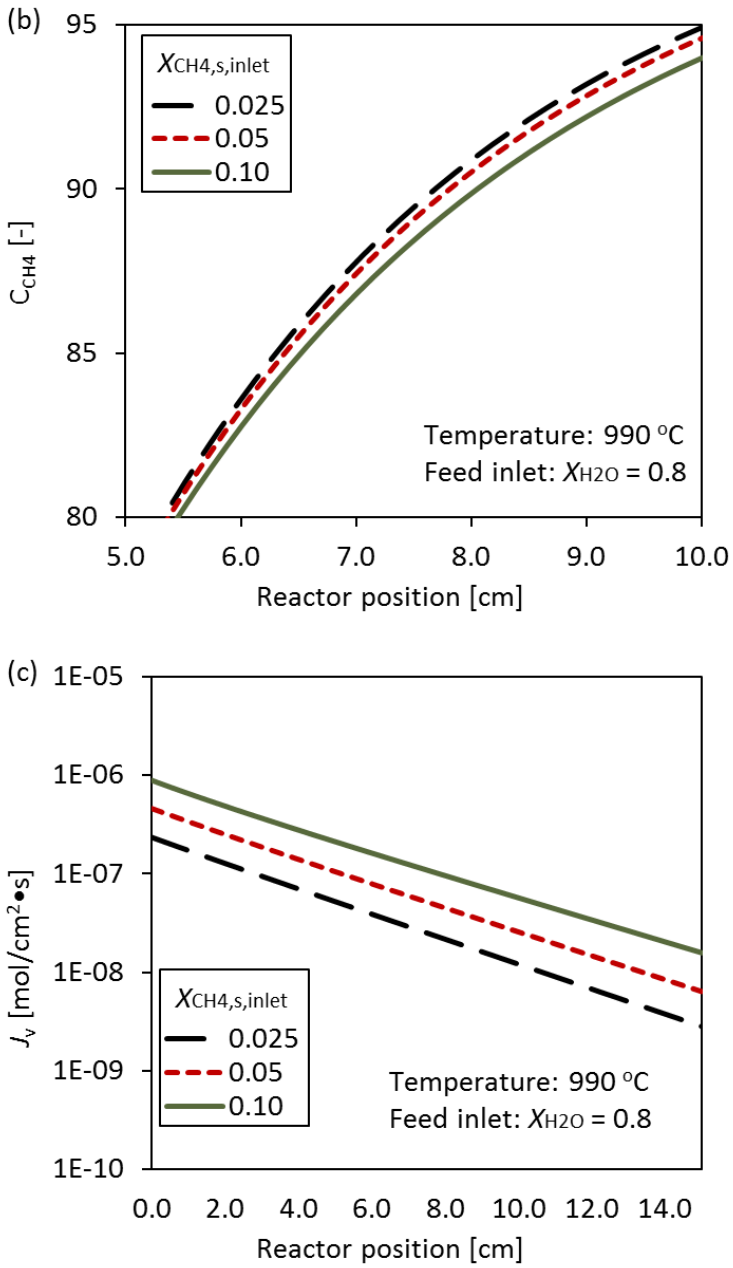

Figure 8.5 (a) Water concentration decreases along the reactor length (b) Methane conversion ratios are above 90% at the exit of the reactor (c) Oxygen vacancy flux drops along the reactor due to the decrease of water and methane concentration on the feed and sweep sides, respectively (cont.)

The results including the water concentration, the methane conversion ratio and the oxygen flux along the reactor for the base case are shown in Figure 8.5. The methane conversion ratio along the length, *z*, is defined as,

$$R_{CH_4}(z) = 1 - \frac{X_{CH_4}(z)}{X_{CH_4}(0)} \tag{8-12}$$

where $X_{CH_4}(0)$ is the methane concentration at the inlet on the sweep side.

First, the water concentration along the channel is shown in Figure 8.5 (a). The water concentration decreases along the channel due to the splitting reaction. Higher methane concentration on the sweep side leads to a further drop of the water concentration. This is attributed to the fact that as more methane is available on the sweep side to react with the oxygen, the water splitting reaction is pushed to a further degree. Figure 8.5 (a) also shows that the water concentration drop rapidly near the inlet of the channel and then flattens at the outlet. This is due to the drop of the oxygen flux along the channel.

Next, the methane conversion ratio along the channel is plotted in Figure 8.5 (b). At the end of the reactor, more than 90% of methane is converted. This means the 10 cm channel is long enough to achieve the desired fuel utilization of 90% under the operating conditions in the base case. Note that when methane concentration on the sweep side increases from 2.5% to 10%, the conversion ratio at the outlet of the reactor drops slightly.

The oxygen flux drops along the channel as shown in Figure 8.5 (c). As both water and methane concentrations drop along the membrane, the chemical potential difference for the oxygen permeation decreases. As a result, the oxygen flux at the outlet of the channel is one or two orders of magnitude lower than the values at the inlet. This makes the membrane surface near the outlet less effective for supporting water splitting.

8.4 Sensitivity analysis

Two metrics are defined to describe the effectiveness of the membrane surface: (1) the channel position L_{90,CH_4} at which 90% of methane conversion ratio is achieved; (2) water conversion ratio R_{H2O} at the outlet of the membrane reactor.

For the base case described in Table 8.3, at the position where 90% of methane conversion is achieved ($L_{90,CH_4} = 7.81\ cm$), the oxygen flux is 0.047 μmol/cm^2•s. And the water conversion ratio at the outlet is $R_{H_2O} = 5.88\%$.

In this section, a sensitivity analysis is performed to evaluate the dependence of these two metrics on different parameters. The parameters are grouped into: design parameters, operation parameters and kinetic parameters. The sensitivity is calculated as:

$$S_{a-b} = \frac{\partial \ln b}{\partial \ln a} \approx \frac{a}{b}\frac{\Delta b}{\Delta a} \tag{8-13}$$

where a is parameter and b is the metric for which the sensitivity is calculated. The sensitivity is calculated over a large range of percent changes ($\pm 10\%$) and averaged.

8.4.1 Design parameters

The sensitivity analysis results with respect to the design parameters are summarized in Table 8.4. We can see that the effectiveness of the membrane reactor is more sensitive to the channel height, which affects the mass transport in the gas phase from the center of the channel to the surface of the membrane. From Figure 8.6 (a) we can see that increasing channel height requires longer channel to achieve 90% methane conversion ratio. This is due to that fact that larger channel height leads to a drop of the mass transfer coefficient $h_{m,j,i}$. As a result, the difference between the gas species in the bulk and on the surface increases. The oxygen flux drops and longer reactor is required to achieve the desired methane conversion ratio. Similarly, increasing the thickness of the membrane also leads to a drop of oxygen flux. However, as the bulk diffusion across the membrane is not the limiting step, the effect of varying membrane thickness is not obvious.

Table 8.4 Sensitivity analysis results for design parameters

Parameter	Base value	$S_{L_{90,CH_4}}$	$S_{R_{H_2O}}$
H	1 mm	1.019	-0.178
t	0.9 mm	1.125×10^{-2}	-1.615×10^{-3}

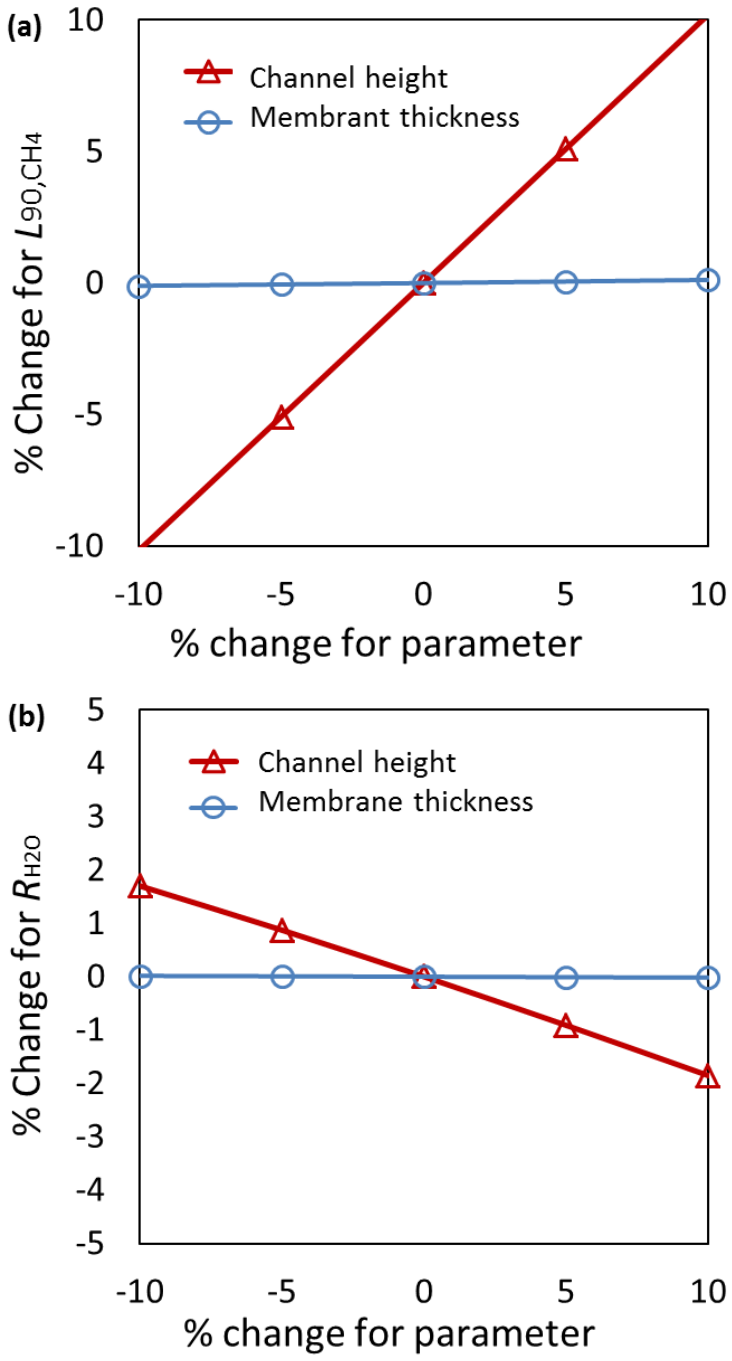

Figure 8.6 Sensitivity of (a) L_{90,CH_4} and (b) R_{H_2O} to the reactor design parameters (i.e., channel height and membrane thickness)

The sensitivity for the water conversion ratio at the outlet is also shown in Table 8.4 and Figure 8.6 (b). We can also see that the channel height has a higher impact on the water conversion ratio at the outlet than the thickness of the membrane. Larger channel

height and thicker membrane both lead to lower oxygen fluxes along the channel and hence, a drop of the water conversion.

Table 8.5 Sensitivity analysis results for operating parameters

Parameter	Base value	$S_{L_{90,CH_4}}$	$S_{R_{H_2O}}$
T	1263 K	-14.602	2.800
X_{CH4}	5%	3.174×10^{-2}	0.9873
X_{H2O}	80%	-3.339×10^{-3}	-1.006

8.4.2 Operating parameters

The sensitivity results for the operating parameters (i.e., temperature, H_2O and CH_4 inlet concentrations on feed and sweep sides, respectively) are summarized in Table 8.5, while the plots are shown in Figure 8.7 and Figure 8.8. The results show that the membrane performance is most sensitive to the operating temperature. In this study, isothermal operating is assumed. Yet since the overall reaction in the membrane reactor is endothermic, it is critical to have effective heat supply and thermal management in industrial application to achieve the best performances.

From Figure 8.7 we can see that increasing operating temperature will decrease the reactor length to have 90% methane conversion ratio and increase the water conversion ratio at the outlet. This is due to the fact that higher operating temperature leads to faster surface kinetics and vacancy diffusivity, and therefore, methane is consumed faster with the increase of oxygen flux.

Figure 8.8 shows the increasing the methane concentration at the inlet on the sweep sides leads to longer reactor length to achieve 90% of methane conversion ratio. This can also be seen from the results of the base case in Figure 8.5 (b). As is shown previously in Figure 5.7, the oxygen flux flattens at higher methane concentration. Therefore, it requires longer channel length to convert 90% of the methane at higher inlet

methane concentrations. Meanwhile, increasing methane concentration also increases the water conversion ratio at the outlet.

On the other hand, higher water inlet concentration decreases both the reactor length for 90% methane conversion ratio and the water conversion ratio at the outlet. This is due to that increasing water concentration slightly increases the oxygen flux and hence, more methane is oxidized on the sweep side. However, the water conversion ratio at the outlet of the channel drops at higher water concentration.

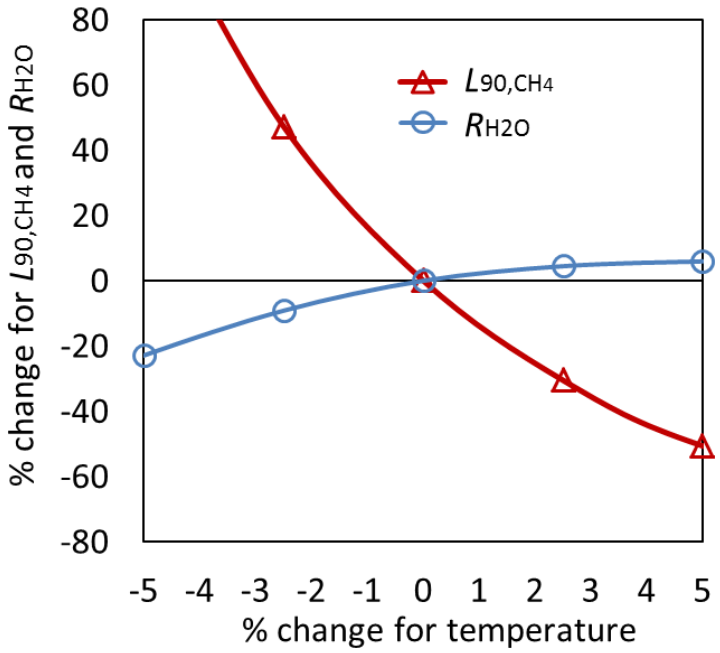

Figure 8.7 Sensitivity of L_{90,CH_4} and R_{H_2O} to operating temperature

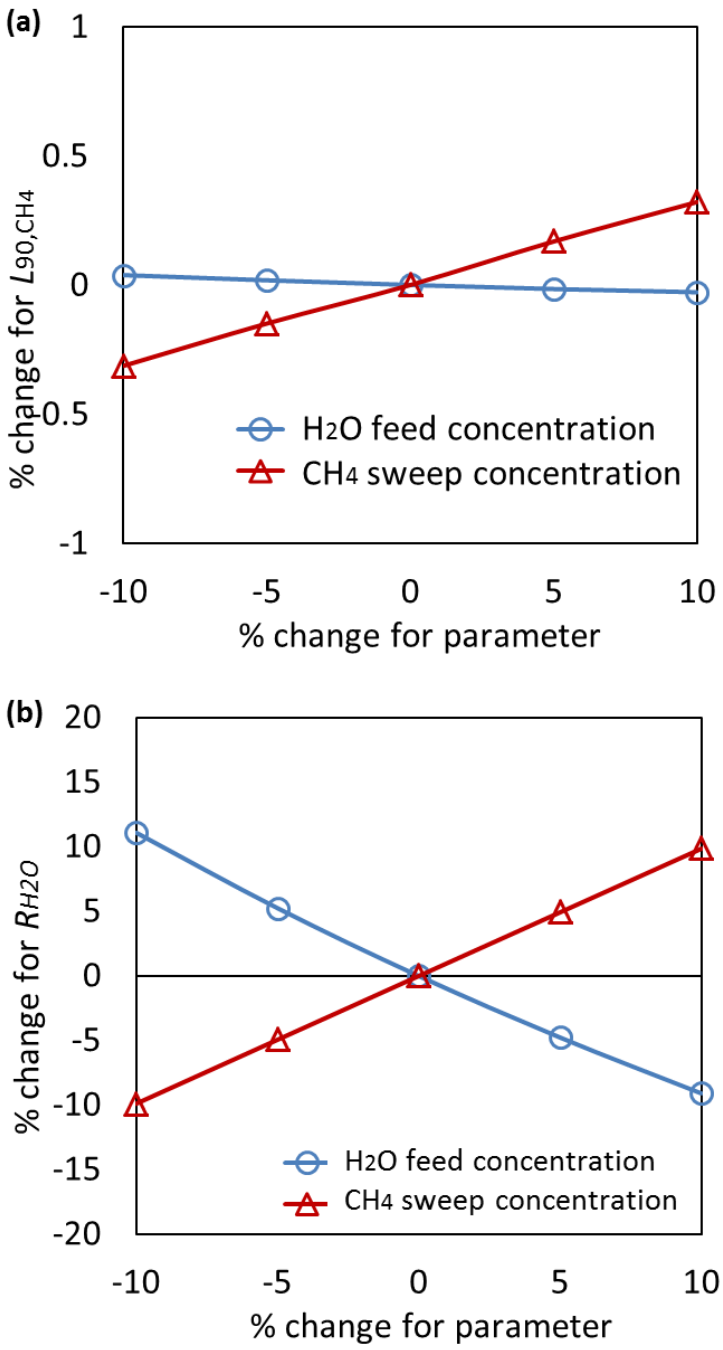

Figure 8.8 Sensitivity of (a) L_{90,CH_4} and (b) R_{H_2O} to the operation parameters (i.e., concentrations of H_2O and CH_4 at the inlets on the feed and sweep sides, respectively)

Table 8.6 Sensitivity analysis results for kinetic parameters

Parameter	Base value	$S_{L_{90,CH_4}}$	$S_{R_{H_2O}}$
D_V	1.707×10^{-5} cm^2/s	-1.137×10^{-2}	1.626×10^{-2}
k_{H2O}	91.17 cm^4/mol•s	-3.240×10^{-3}	4.517×10^{-3}
k_{CH4}	12.21 cm^4/mol•s	-0.973	0.171

8.4.3 Kinetic parameters

Table 8.6 summarizes the sensitivity analysis results for the kinetic parameters, namely water splitting rate, k_{H_2O} , methane partial oxidation rate, k_{CH_4} and the vacancy diffusivity, D_V . From the results, we can see that the reaction kinetics for methane partial oxidation reaction on the sweep side affect the performances the most, while water splitting rate on the feed side and the oxygen vacancy diffusivity have very small impacts.

Improving the kinetics for methane partial oxidation significantly decrease the required length to achieve 90% methane conversion (Figure 8.9 (a)). As the methane partial oxidation reaction is the rate-limiting step with resistances orders of magnitude higher than other resistances (discussed in Chapter 4), decreasing its resistance leads to larger oxygen flux, and hence, more methane can be oxidized. On the other hand, the water splitting rate and the oxygen diffusivity are not the rate-limiting steps under the base case conditions. Improving these two kinetic parameters will result in only very small increase of the oxygen flux.

Additionally, Figure 8.9 (b) shows the effects of the kinetic parameters on the water conversion ratios at the outlet. We can see that similar to the results of the required length for 90% methane conversion, increasing the kinetics for methane partial oxidation increases the water conversion ratio at the outlet significantly. This is, again, due to the improved oxygen flux by enhancing the methane partial oxidation rate. As the oxygen flux is proportional to the water splitting rate, higher flux leads to an increasing water conversion ratio at the outlet.

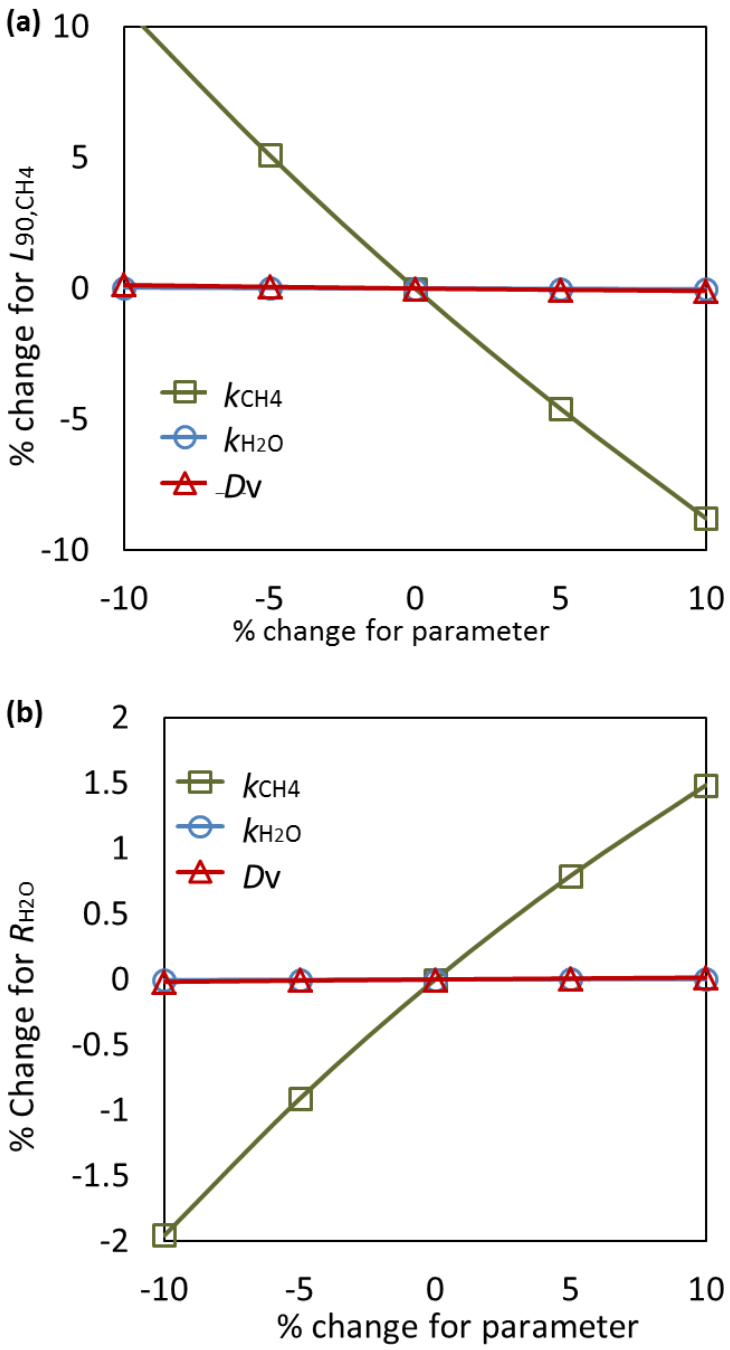

Figure 8.9 Sensitivity of (a) L_{90,CH_4} and (b) R_{H_2O} to the kinetics parameters (i.e., rates of H_2O splitting and CH_4 oxidation at the inlets on the feed and sweep sides, respectively as well as the oxygen vacancy diffusivity)

8.5 Conclusions

In this chapter, the co-production of hydrogen and syngas from water splitting and methane partial oxidation, respectively in a membrane reactor is studied. First, the membrane reactor is compared with the steam reforming process to produce high-purity hydrogen (>99%). Results show that the membrane reactor has a thermal efficiency about ~2.5% point higher thanks to the *in situ* separation of hydrogen from other non-condensable gases in the product stream (i.e., CO_2 and CO).

Then a sensitivity analysis of the monolith membrane reactor performances with respective to various design, operating and kinetic parameters is presented. The results show that the performances of the membrane reactor are very sensitive to the operating temperatures. As a result, the effective heat input and thermal management is crucial to maintain the best performances. Moreover, the methane partial oxidation kinetics on the sweep side is the most important kinetic parameters to be considered to improve the reactor performances. Hence, developing better catalysts (i.e., high reactivity and stability) for methane partial oxidation to enhance the rates and the selectivity to syngas is important for an efficient reactor. Finally, the channel height also has an important impact on the performance by affecting the effectiveness of the mass transfer between the center of the channel and the membrane surface.

Appendix A: Resistance-network permeation model

The resistance-network model described in Chapter 3 is used to model the oxygen permeation process across the membrane. H_2O direct-incorporation mechanism is used on the feed side, and the Mars-van Krevelen (MvK) mechanism for CH_4 partial oxidation reactions on the sweep side:

Water feed: $$H_2O + V_O^{\bullet\bullet} \xrightarrow{k_{f,H_2O}} O_O^x + 2h^{\bullet} + H_2 \quad \text{(A8.1)}$$

CH_4 sweep: $$O_O^x + 2h^{\bullet} + CH_4 \xrightarrow{k_{f,CH_4}} CO + 2H_2 + V_O^{\bullet\bullet} \quad \text{(A8.2)}$$

Here, $V_O^{\bullet\bullet}$ is oxygen vacancy in membrane, $h^{\bullet}$ is the electron holes. k_{f,H_2O} and k_{f,CH_4} are the reaction rate constants for the water splitting and methane partial oxidation reactions, respectively.

The Nernst-Planck equation is used to model the charged species transfer, and with the assumption that the ionic conductivity is the limiting step for the bulk diffusion, we have

$$J_V = -D_V \frac{\partial C_V}{\partial y} = D_V \frac{C''_V - C'_V}{t}, \quad \text{(A8.3)}$$

where *t* is the thickness of the membrane.

In steady state condition, the flux equation can be expressed as

$$J_V = \frac{C_O}{R_f + R_b + R_s}, \quad \text{(A8.4)}$$

where C_O is the concentration of oxygen species (including lattice oxygen and oxygen vacancies), R_f, R_b and R_s are the resistances of the feed side surface reaction, the bulk diffusion and the sweep side surface reaction, respectively. More details of the resistance-network model can be found in Chapter 3 and the reaction kinetic parameters in Chapter 4.

Appendix B: Process model library in gPROM

The steam methane reformer and the membrane reactor are compared using the process modelling software gPROM. The model libraries are summarized in Appendix table 8.1. More information about the software can be found in [201] and [202].

Appendix table 8.1 List of the models for the components modelled in two processes

Components	Modelling approaches
Steam reforming reactor	Thermodynamic equilibrium model
Water-gas shift reactor	
Membranes	Triple-resistance network model
Pipelines	Linear pressure drop
Burner	Mass and energy conservation
Mixer & Condenser	
PSA	Mass and energy conservation considering H_2 recovery ratio
Heat exchanger	ε-NTU method
Compressor/Turbine	Isentropic efficiency model

The membrane reactor is modelled as a well stirred reactor with the governing equations as:

(1) Continuity

$$V_k \frac{dc_{t,k}}{dt} = \dot{n}_{k,in} - \dot{n}_{k,out} - A_k \sum_i \left(N_{i,k}\big|_k - R_i \right) \left(k = feed, \text{sweep} \right) \tag{A8.5}$$

where V_K is the volume of the reactor [m^3], $c_{t,k}$ is the total concentration [mol/m^3], t is the time [s], $\dot{n}$ is the molar flow rate [mol/s], A is the surface area [m^2], N is the flux, [$mol/m^2/s$], R is the reaction rate [$mol/m^2/s$].

Steam methane reforming and water gas shift reactions are modelled in the gas phase. Steam reforming rate is derived from that on nickel catalysts [211]. This rate is dependent on the membrane surface area, which is 0.307 m^2 in this work similar to the size of a solid oxide electrolysis cell:

$$R_{SMR} = 4274 \exp\left(-\frac{8.2\times10^4}{RT} \right) \left(\frac{p_{\mathrm{CH_4}}}{p_0} - \frac{p_{\mathrm{CO}} p_{\mathrm{H_2}}^3}{p_0^2 p_{\mathrm{H_2O}} K_{\mathrm{eq,SMR}}} \right), \mathrm{mol/m^2/s} \tag{A8.6}$$

$$\begin{aligned} K_{\mathrm{eq,SMR}} = 1.0267\times10^{10} \times \exp(&-0.2513Z^4 + 0.3665Z^3 \\ &+0.5810Z^2 - 27.134Z + 3.277) \end{aligned} \tag{A8.7}$$

$$Z = \frac{1000}{T(K)} - 1 \tag{A8.8}$$

Water gas shift reaction is assumed to be in equilibrium, so the kinetic expression is used with k_0 is an arbitrary large value limited by numerical stability in the model [201, 212]

$$R_{WGS} = k_0 \left(p_{\mathrm{CO}} p_{\mathrm{H_2O}} - \frac{p_{\mathrm{H_2}} p_{\mathrm{CO_2}}}{K_{\mathrm{eq,WGS}}} \right), mol/m^3/s \tag{A8.9}$$

$$K_{\mathrm{eq,WGS}} = \exp(-0.2935Z^3 + 0.6351Z^2 + 4.1788Z + 0.3169) \tag{A8.10}$$

Z is from Equation (A8.8)

(2) Species conservation

$$\begin{aligned} V_k c_{t,k} \frac{dx_{i,k}}{dt} = {} & \dot{n}_{k,in} \left(x_{i,k,in} - x_{i,k} \right) + A_k \left(R_i - x_{i,k} \sum_i R_i \right) \\ & - A_k \left(N_{i,k}\big|_{k/ch} - x_{i,k} \sum_i N_{i,k}\big|_{k/ch} \right) (k = feed, sweep) \end{aligned} \tag{A8.11}$$

where x is the mole fraction for the species, [dimensionless].

(3) Energy conservation

$$\rho_s c_{p,s} V_s \frac{dT}{dt} = \sum_k \left(\dot{n}_{k,in} H_{k,in} \right) - \sum_k \left(\dot{n}_{k,out} H_{k,out} \right) - Q_{loss} (k = feed, sweep) \tag{A8.12}$$

where ρ_s, $c_{p,s}$ and V_s are the density [kg/m^3], heat capacity [J/kg/K] and volume [m^3] of the membrane, T is the temperature [K], H is the enthalpy [J/kg], and Q_{loss} is the heat loss (assumed to be zero in this study) [W].

(4) Oxygen flux (from Equation (A8.4))

$$J_V = \frac{C_O}{R_{\mathrm{f}} + R_{\mathrm{b}} + R_{\mathrm{s}}} \tag{A8.13}$$

As discussed in this chapter, the membrane reactor is modelled as similar to the methane assisted solid oxide electrolysis, steam is added on the fuel side to reform the methane and facilitate the reaction [204]. H_2 and CO kinetics from the previous chapters (Chapter 4 and Chapter 6) are used to derive the oxygen flux.

Acknowledgement:
The process comparison in this chapter is carried out with collaboration with Mr. Yu Luo from Tsinghua University. The license for the software gPROM is owned by Tsinghua University.

Chapter 9

Conclusions

9.1 Comparison between H_2O and CO_2 splitting

Overall, membrane-supported H_2O and CO_2 splitting is studied using different configurations of $La_{0.9}Ca_{0.1}FeO_{3-\delta}$ membranes in this thesis. On the feed side of the membrane, the oxygen sources (i.e., H_2O or CO_2) undergo bond breaking processes allowing the oxygen incorporation into the lattice. A cartoon is shown in Figure 9.1 for the feed side splitting processes.

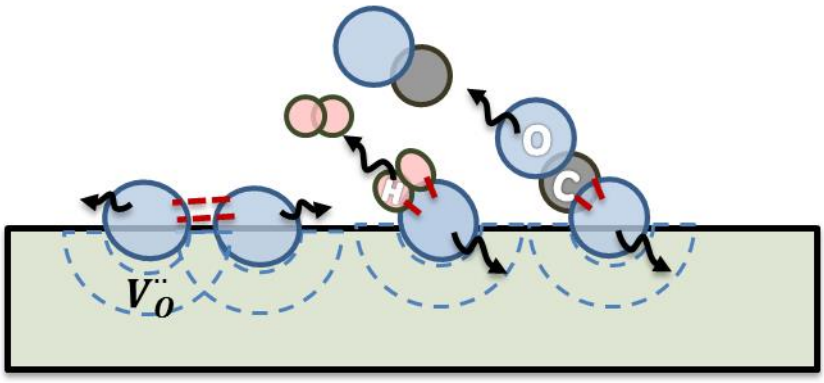

Figure 9.1 A cartoon shows the O_2, H_2O and CO_2 splitting processes on the feed side of the membrane. $V_O^{\cdot\cdot}$ is the oxygen vacancy in the lattice

The bond strength of the oxygen sources are expected to play an important role in the kinetics of the splitting process, and the values are listed in Table 9.1. We can see that the O=O, OH-O and O-H bond dissociation energies are in similar orders of magnitude, while OC=O bond has a value of 100 kJ/mol higher. Besides, C-O bond is very difficult to break unless activated by catalysts.

Table 9.2 summarizes the splitting reaction kinetic parameters in this thesis. We can notice that the oxygen and water splitting reactions have activation energies in the same order of magnitude, while the CO_2 splitting reaction has higher activation energy.

In this chapter, I will compare the difference between H_2O and CO_2 splitting based on the results in the previous chapters, especially the performances and the changes on the membrane surfaces.

Table 9.1 Bond dissociation energies of different molecules [34]

Bond	Bond dissociation energy [kJ/mol]
O=O	498.34
OH-O	498.7
O-H	428.0
OC=O	532.2
C-O	1075

Table 9.2 A summary of the reaction kinetic parameters for different oxygen sources on LCF-91 membrane

Oxygen surface reaction		A		E_a	
		Value	Unit	Value	Unit
$\frac{1}{2}O_2 + V_O^{\bullet\bullet} \leftrightarrow O_O^x + 2h^\bullet$	k_{f,O_2}	5.66	[$cm^{2.5}/mol^{0.5}$•s]	1.06E+4	[J/mol]
	$\tilde{k}_{r,O_2}$	0.145	[cm/s]	1.11E+5	[J/mol]
$H_2O + V_O^{\bullet\bullet} \leftrightarrow O_O^x + 2h^\bullet + H_2$	k_{f,H_2O}	193	[cm^4/mol•s]	7.88E+3	[J/mol]
	$\tilde{k}_{r,H_2O}$	5.39E+4	[cm^4/mol•s]	9.10E+4	[J/mol]
$CO_2 + V_O^{\bullet\bullet} \leftrightarrow O_O^x + 2h^\bullet + CO$	k_{f,CO_2}	1.28E+15	[cm^4/mol•s]	3.64E+5	[J/mol]
	k_{r,CO_2}	1.64E+7	[cm^4/mol•s]	1.57E+5	[J/mol]

9.1.1 Performances comparison

As discussed in the previous section, H_2O molecule has lower bond dissociation energy and its splitting kinetics is faster than CO_2. As a result, the oxygen flux associated

with H_2O splitting is higher than that with CO_2 splitting, as shown in Figure 9.2. For both cases, the hydrogen and argon mixtures are used as the sweep gas.

With increasing H_2 concentrations on the sweep side, oxygen fluxes in both cases rise. The oxygen flux for water splitting at 4% H_2 sweep is about 0.15 μmol/cm^2•s, while the value for CO_2 splitting is about 0.10 μmol/cm^2•s. Note that the membrane thicknesses are different for the two splitting cases: the membrane for water splitting is 0.9 mm, while that for carbon dioxide is 1.3 mm. Yet as discussed in previous chapters, the bulk diffusion is not the limiting step for either case. Hence, the membrane thickness has very small impacts on the difference in the oxygen flux, while the faster splitting kinetics leads to the higher oxygen fluxes in water splitting.

The temperature dependence of the oxygen flux for H_2O and CO_2 splitting are shown in the Arrhenius plot in Figure 9.3. The slope is constant for H_2O splitting, while the slope for CO_2 splitting decreases at higher temperatures. As shown in Figure 9.4 (a), the limiting step is always the hydrogen oxidation on the sweep side for water splitting. Hence, the slope doesn't change with rising temperatures. However, for CO_2 splitting, the limiting step changes from the CO_2 splitting reaction on the feed-side to the H_2 oxidation reaction on the sweep-side at around 950^{o}C, as shown in Figure 9.4 (b). This leads to the decrease of the slope at higher temperatures (see the activation energies for the reactions in Table 9.2).

Figure 9.3 also shows that at high temperatures, the slope of CO_2 splitting approaches that of H_2O splitting, as the limiting steps for both cases are the hydrogen oxidation on the sweep side at high temperatures. And the oxygen fluxes for H_2O and CO_2 splitting at 1030^{o}C are very close.

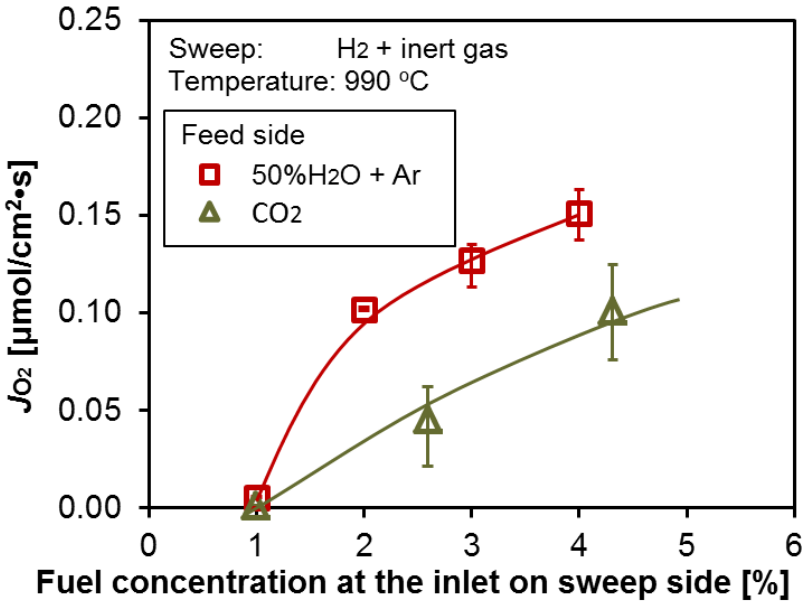

Figure 9.2 Oxygen flux increases at higher fuel concentrations at the sweep side inlet for both H_2O and CO_2 splitting, but the former has high fluxes (the membrane thickness for H_2O splitting is 0.9 mm, and that for CO_2 splitting 1.3 mm)

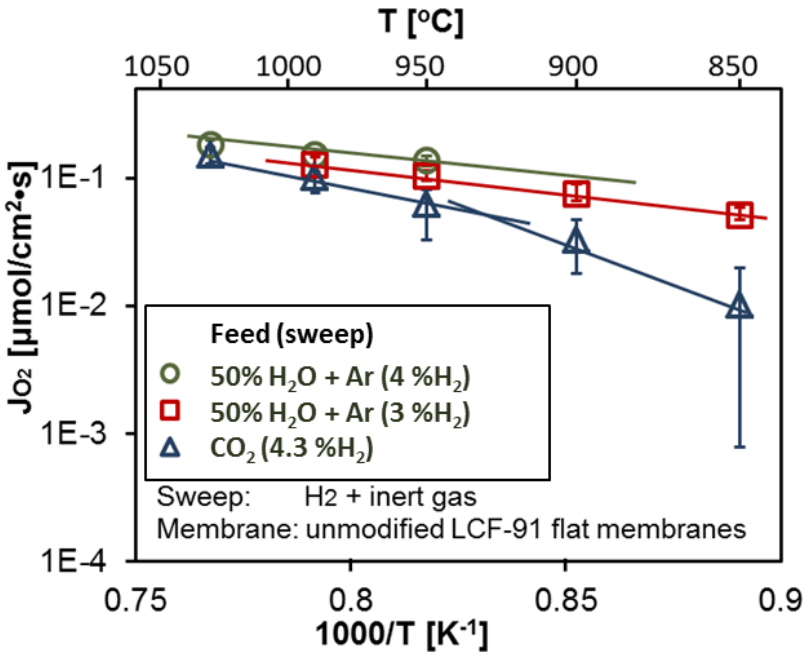

Figure 9.3 Arrhenius plot for H_2O and CO_2 splitting shows that the CO_2 splitting rate is approaching the H_2O splitting rate at higher temperatures

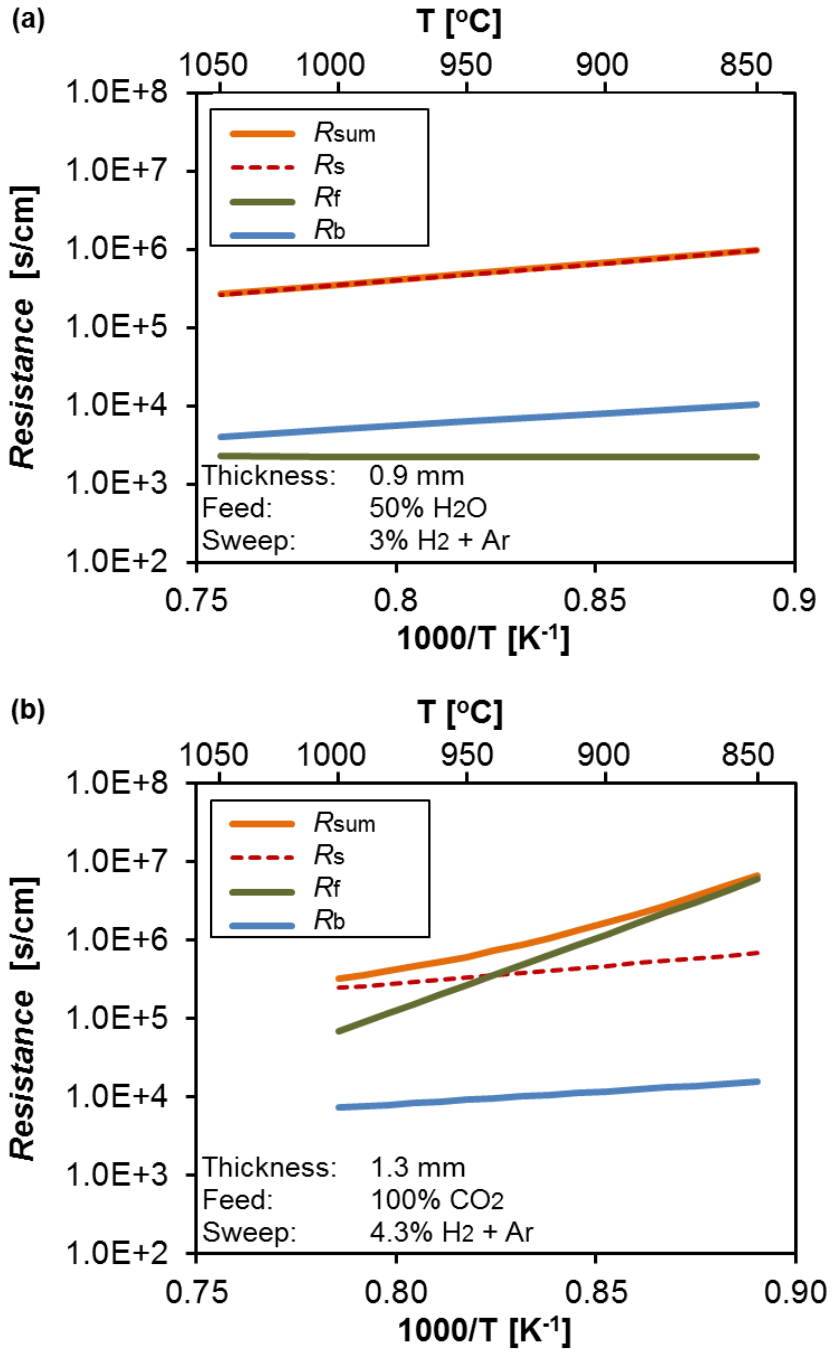

Figure 9.4 The resistances for oxygen transport for (a) H_2O splitting and (b) CO_2 splitting under the same operating conditions shown in Figure 9.3

9.1.2 *Ex situ* characterization

Previous chapters show that the feed side surface undergoes more morphological and elemental changes than the sweep side for both H_2O and CO_2 splitting cases. However, the changes are observably different for H_2O and CO_2 splitting as shown in Figure 9.5 and Figure 9.6.

For CO_2 splitting, there are clusters on the CO_2 feed side surfaces, while clear grain boundaries can still be identified on the surfaces that are not covered by these clusters. The EDX analysis (Figure 9.5) shows that the clusters are rich in calcium and irons, and some show carbon signals. These clusters are identified as carbonates, metal oxides and brownmillerite ($Ca_2Fe_2O_5$) by XRD. On the other hand, for H_2O splitting, the water feed side appears to be heavily corroded by the steam, and hardly any grain boundary can be identified from the SEM (Figure 9.6). EDX also shows some calcium and silicon clusters. The silicon species are likely from the impurities during the membrane fabrication [213].

Yet these morphologies changes on the feed side didn't change the overall performances for around 50 – 100 hours, as discussed previously in this thesis.

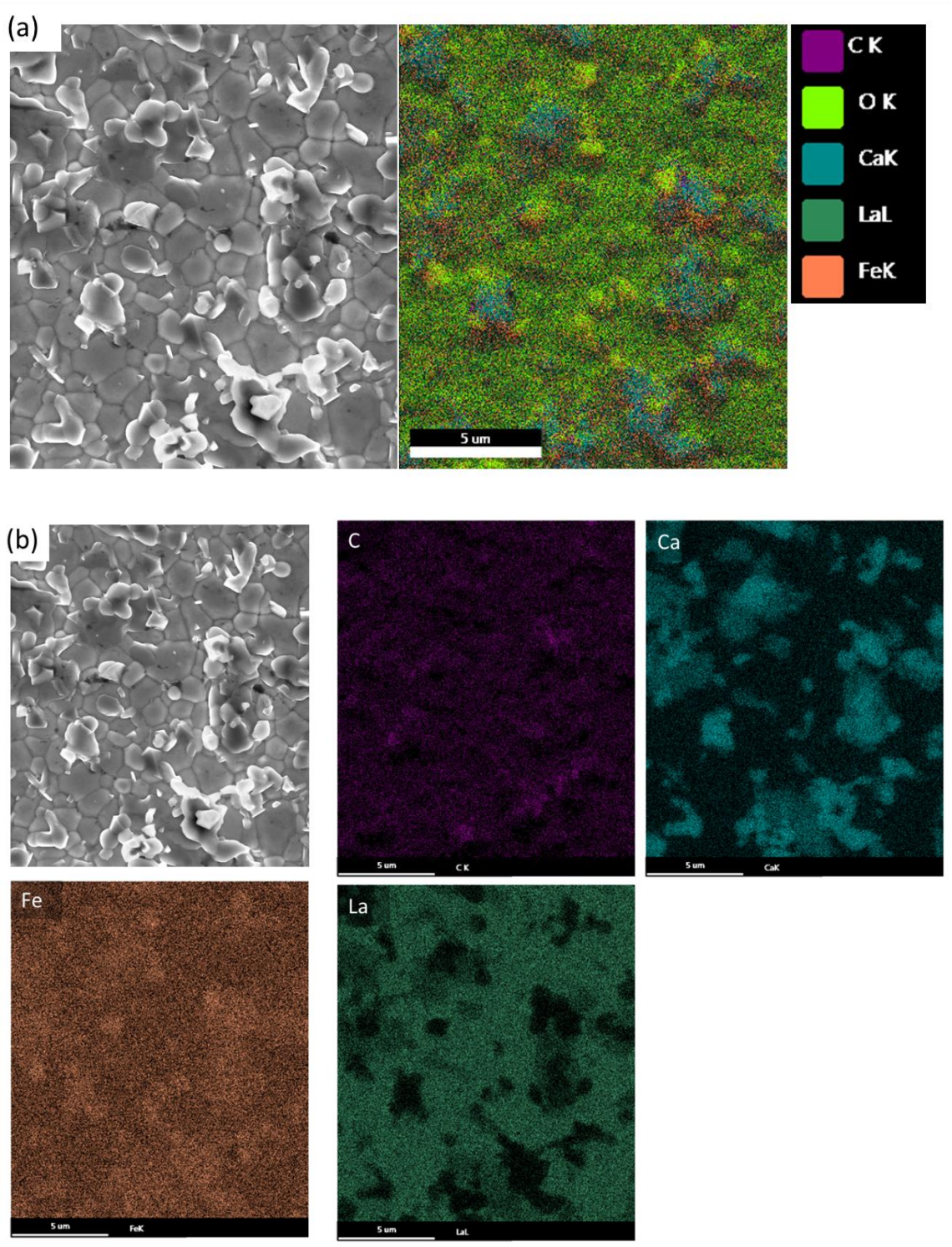

Figure 9.5 (a) The SEM and EDX images of the CO_2 feed side followed the splitting experiments, (b) The EDX images show different elements separately

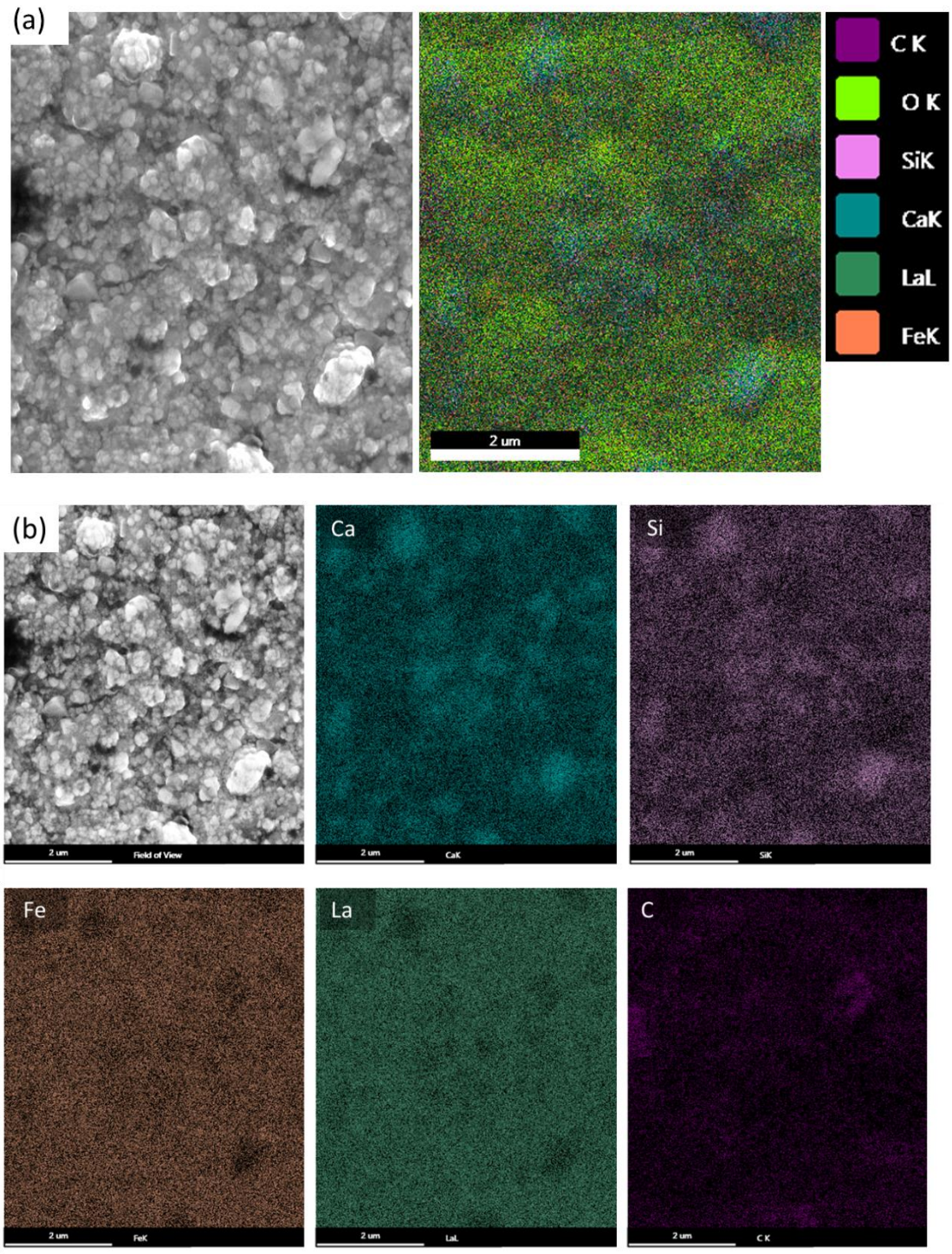

Figure 9.6 (a) The SEM and EDX images of the H_2O feed side followed the splitting experiments, (b) The EDX images show different elements separately

9.2 Thesis summary

This thesis aims at quantifying the oxygen transport process in the membrane-supported H_2O/CO_2 splitting processes and developing a framework for the reactor design. Experiments were carried out to investigate the dependency of the fuel production rate on membrane configurations and operating conditions. A resistant-network model was developed to model the oxygen transport process and the kinetic parameters were derived from the experimental data. The model predicted the limiting step(s) and then, modifications on those steps were implemented experimentally to study their effects on the performances. Finally, a monolith membrane reactor was modelled to show its advantages over the catalytic steam methane reformer and a sensitivity analysis revealed the important parameters on the reactor performances. The main results and findings from each chapter are summarized as follows.

Chapter 4 presents the study of H_2O splitting on a flat LCF-91 membrane with various sweep conditions (i.e., helium, hydrogen and methane). Water splitting rate is enhanced by the LCF-91 membranes compared to the homogeneous water thermolysis. The resistance-network model reveals that the limiting steps depend on both the oxygen sources and the sweep gases. For the water feed-fuel sweep case, the limiting step is the fuel oxidation reaction (either H_2 or CH_4) on the sweep side. As methane partial oxidation reaction has a lower rate constant than hydrogen oxidation, methane sweep leads to lower oxygen fluxes. Besides, the splitting rate is enhanced by increasing the fuel concentrations on the sweep side, as the surface reaction resistance on that side drops.

Chapter 5 investigates the improvements on the oxygen flux for the methane-sweep case by applying a porous layer on the sweep side. As a result, the hydrogen production rate from water splitting increases by two orders of magnitude. The addition of nickel catalyst to the porous layer further improves the performances by a factor of 2 with the maximum hydrogen production rate reaching 0.37 $\mu mol/cm^2 \cdot s$ at 990^oC (the methane concentration is 5% at the inlet on the sweep side). This Ni/LCF-91 porous layer also increases the syngas selectivity under our experimental conditions by a combination of surface and gas-phase reactions. Furthermore, hardly any solid carbon is found based on the carbon balance in the gas phase.

Chapter 6 carries out a detailed study on CO_2 splitting on the flat LCF-91 membrane and studies the dependences of oxygen fluxes on operating conditions (e.g., the CO_2 and fuel concentrations and temperatures). The maximum oxygen flux achieved in this work is 0.19 μmol/cm^2•s with 9.5% H_2 on the sweep side on a 1.3 mm thick LCF-91 membrane at 990^{o}C. The resistance-network model reveals that the rate limiting step changes from CO formation reaction on the feed side to fuel (i.e., H_2 and CO) oxidation on the sweep side at higher operating temperatures. Moreover, the transition temperature for H_2 is higher than that of CO (both used as fuels).

Chapter 7 reports the enhancement of the CO_2 splitting rate by applying porous LCF-91 layers on both the feed and sweep sides. The associated oxygen flux is raised by about 0.02 μmol/cm^2•s for the CO sweep cases. Arrhenius plots of the oxygen flux with different CO concentration on the sweep side also shows a transition in the limiting step from the CO formation reaction on the feed side to the CO oxidation reaction on the sweep side at higher temperatures.

Chapter 8 models the monolith membrane reactor to quantify the dependence of reactor performance on the operating conditions. This membrane reactor is compared with catalytic steam methane reforming, and the results show that the former has higher thermal efficiency to produce high-purity hydrogen (purity >99%) thanks to the *in situ* separation of H_2 from other non-condensable gases (e.g., CO_2 and CO). A sensitivity analysis for the reactor performances with respective to various design, operating and kinetic parameters is presented. The results show that the performance of the membrane reactor is very sensitive to the operating temperatures, the methane partial oxidation kinetics and the channel height. Therefore, for the best performance, it is crucial to have the effective thermal management and active and stable catalysts for methane partial oxidation.

9.3 Suggested future work

9.3.1 Micro-kinetics modelling of the surface reactions

The resistance-network model presented in Chapter 3 considers the oxygen direct-incorporation on the feed side and the Mars-van Krevelen for fuel oxidation on the sweep side. The model predicts the experimental results within ±25% error. Yet higher accuracy

may be achieved by adopting the micro-kinetics mechanism, similar to those for the fuel cells [185] and catalysis [214]. Careful design experiments [215] as well as numerical simulations are required to derive the micro-kinetics steps and parameters for H_2O/CO_2 splitting on a perovskite membrane.

9.3.2 *In situ* observation of the splitting process

H_2O/CO_2 splitting on a perovskite membrane is a complicated dynamic process. Properties derived from the bulk or under equilibrium conditions can be different from those under dynamics operations. The surface reconstruction [216], cation migration [217] and electric double-layers [218] can impact the splitting process during operations. Therefore, *in situ* observation is necessary to quantify both the reactions and transport during the splitting process.

For example, laser-assisted techniques such as planar laser-induced fluorescence (PLIF) have been applied to study the gas phase reactions during combustion processes [219]. Similarly, these techniques can be used to detect the gas species in the vicinity of the membrane such that the gas phase reactions near the membrane can be quantified. On the other hand, the gas-solid interactions can be examined by *in situ* X-ray spectroscopy. One example is that *in situ* X-ray absorption fine structure (XAFS) can give information about the crystal structure, surface atom configurations and electronic states of the transition metal during the splitting reactions [220]. The cation dislocations in the perovskite crystals can also be examined and the synergic effects between the oxygen vacancies and the transition metal cations in perovskite can be understood.

9.3.3 *Ab initio* calculations for better membranes

The oxygen permeability, surface activity and stability are among the major figures of merit (FOM) for an oxygen permeable membrane reactor. *Ab initio* calculations such as the density functional theory (DFT) have been applied to design materials for the fuel cell electrodes and catalysts, but very few studies have been carried out to explore better membrane materials for H_2O/CO_2 splitting. One example is that Michalsky et al. [97] compared the Gibbs free energy of reaction and enthalpy of metal oxide reduction in various binary metal oxides and perovskites using DFT.

$La_{0.5}Sr_{0.5}MnO_3$ and $La_{0.5}Sr_{0.5}Mn_{0.5}Co_{0.5}O_3$ are identified as the two best candidates for CO_2 splitting membrane materials with high oxygen permeability and fast surface kinetics. However, surface properties can be different from the bulk properties under the operating conditions. And membrane stability is another issue to be resolved. Further studies can identify and design better catalytic membranes for H_2O/CO_2 splitting.

9.3.4 Co-splitting of H_2O and CO_2

There are two pathways to produce fuels from H_2O and CO_2 [9]: 1) H_2O splitting followed by the Sabatier reaction to produce methane; 2) Co-splitting of H_2O and CO_2 to produce syngas. Thermodynamic analysis shows that co-splitting of H_2O and CO_2 has faster kinetics than CO_2 splitting thanks to the active H and –OH radicals in co-splitting. Several groups have studied co-electrolysis (electricity induced co-splitting) of H_2O and CO_2 in solid oxide electrolysis cell [221]. However, membrane-supported H_2O and CO_2 co-splitting has not been reported in the literature yet. Further studies are expected to combine H_2O and CO_2 splitting into one membrane reactor such that syngas can be produced on the feed side.

9.3.5 Techno-economic analysis of the H_2O/CO_2 splitting reactor system

As discussed in this thesis, H_2O/CO_2 splitting depends strongly on the operating conductions (e.g., temperatures, flow rates, H_2O/CO_2 concentrations and sweep gas species) and membrane characteristics (e.g., thickness, porous support and catalysts). Optimizations on the reactor designs and system integrations are required to achieve the best splitting performances close to the theoretical limits. Moreover, techno-economic analysis should also be carried out to design a cost-effective membrane reactor system.

Bibliography

1. Global Climate Report - March 2017. https://www.ncdc.noaa.gov/sotc/global/201703. Accessed April 23, 2017.
2. NASA, NOAA Data Show 2016 Warmest Year on Record Globally. https://www.nasa.gov/press-release/nasa-noaa-data-show-2016-warmest-year-on-record-globally. Accessed April 23, 2017.
3. IEA. Decoupling of global emissions and economic growth confirmed. http://www.iea.org/newsroomandevents/pressreleases/2016/march/decoupling-of-global-emissions-and-economic-growth-confirmed.html. Accessed April 23, 2017.
4. The Keeling Curve. 2016; https://scripps.ucsd.edu/programs/keelingcurve/. Accessed May 20 2016.
5. United nations conference on climate change. 2015; http://www.cop21.gouv.fr/en.
6. IEA, *World Energy Outlook*. 2012.
7. Rogelj, J., et al., *Halfway to Copenhagen, no way to 2^{o}C.* 2009(0907): 81-83.
8. Kleij, A.W., North, M., and Urakawa, A., *CO_2 Catalysis.* ChemSusChem, 2017. **10**(6): 1036-1038.
9. Nguyen, V.N. and Blum, L., *Syngas and Synfuels from H_2O and CO_2: Current Status.* Chemie Ingenieur Technik, 2015. **87**(4): 354-375.
10. Germany had so much renewable energy on Sunday that it had to pay people to use electricity. https://qz.com/680661/germany-had-so-much-renewable-energy-on-sunday-that-it-had-to-pay-people-to-use-electricity/. Accessed April 23, 2017.
11. New England Electricity Generation and Demand. https://www.iso-ne.com/. Accessed March 7 2017.
12. Ghoniem, A.F., *Needs, resources and climate change: Clean and efficient conversion technologies.* Progress in Energy and Combustion Science, 2011. **37**(1): 15-51.
13. Fuchs, G., et al. *Technology Overview on Electricity Storage: Overview on the potential and on the deployment perspectives of electricity storage technologies*. 2012. Available at: http://www.sefep.eu/activities/projects-studies/120628_Technology_Overview_Electricity_Storage_SEFEP_ISEA.pdf. Accessed March 27 2017
14. Rightor, E.G. and Tway, C.L., *Global energy & emissions reduction potential of chemical process improvements.* Catalysis Today, 2015. **258, Part 2**: 226-229.
15. Neuburger, A., *An article on the history of electrolysis of water.* Berichte Der Deutschen Chemischen Gesellschaft, 1903. **36**: 3572-3574.
16. Fujishima, A. and Honda, K., *Electrochemical Photolysis of Water at a Semiconductor Electrode.* Nature, 1972. **238**(5358): 37-38.
17. Fletcher, E.A. and Moen, R.L., *Hydrogen- and Oxygen from Water.* Science, 1977. **197**(4308): 1050-1056.
18. Browall, K.W. and Doremus, R.H., *Synthesis and Evaluation of Doped Y2O3-Stabilized ZrO2 for the Production of Hydrogen.* Journal of the American Ceramic Society, 1977. **60**(5-6): 262-267.

19. Hočevar, S. and Summers, W., *Hydrogen Production*, in *Hydrogen Technology*, A. Léon, Editor. 2008, Springer Berlin Heidelberg. 15-79.
20. Carmo, M., et al., *A comprehensive review on PEM water electrolysis.* International Journal of Hydrogen Energy, 2013. **38**(12): 4901-4934.
21. Ebbesen, S.D., et al., *High Temperature Electrolysis in Alkaline Cells, Solid Proton Conducting Cells, and Solid Oxide Cells.* Chemical Reviews, 2014. **114**(21): 10697-10734.
22. Wang, Z., et al., *Comparison of thermochemical, electrolytic, photoelectrolytic and photochemical solar-to-hydrogen production technologies.* International Journal of Hydrogen Energy, 2012. **37**(21): 16287-16301.
23. Moçoteguy, P. and Brisse, A., *A review and comprehensive analysis of degradation mechanisms of solid oxide electrolysis cells.* International Journal of Hydrogen Energy, 2013. **38**(36): 15887-15902.
24. Laguna-Bercero, M.A., *Recent advances in high temperature electrolysis using solid oxide fuel cells: A review.* Journal of Power Sources, 2012. **203**: 4-16.
25. Kang, P., et al., *Electrocatalytic Reduction of Carbon Dioxide: Let the Molecules Do the Work.* Topics in Catalysis, 2014. **58**(1): 30-45.
26. Smestad, G.P. and Steinfeld, A., *Review: Photochemical and Thermochemical Production of Solar Fuels from H_2O and CO_2 Using Metal Oxide Catalysts.* Industrial & Engineering Chemistry Research, 2012. **51**(37): 11828-11840.
27. Li, K.F., et al., *A critical review of CO_2 photoconversion: Catalysts and reactors.* Catalysis Today, 2014. **224**: 3-12.
28. Li, W., et al., *Mixed ionic-electronic conducting (MIEC) membranes for hydrogen production from water splitting.* International Journal of Hydrogen Energy, 2015. **40**(8): 3452-3461.
29. Thursfield, A., et al., *Chemical looping and oxygen permeable ceramic membranes for hydrogen production – a review.* Energy & Environmental Science, 2012. **5**(6): 7421 - 7459.
30. Jellinek, H.H.G. and Kachi, H., *The catalytic thermal decomposition of water and the production of hydrogen.* International Journal of Hydrogen Energy, 1984. **9**(8): 677-688.
31. Baykara, S.Z., *Experimental solar water thermolysis.* International Journal of Hydrogen Energy, 2004. **29**(14): 1459-1469.
32. Lede, J., et al., *Production of hydrogen by direct thermal decomposition of water: Preliminary investigations.* International Journal of Hydrogen Energy, 1982. **7**(12): 939-950.
33. Kogan, A., *Direct solar thermal splitting of water and on-site separation of the products—II. Experimental feasibility study.* International Journal of Hydrogen Energy, 1998. **23**(2): 89-98.
34. Dean, J.A., *Lange's Handbook of Chemistry, 15th edition*. 1990: Taylor & Francis.
35. Goodwin, D.G. Cantera. http://www.aresinstitute.org/Cantera/cantera-cxx.pdf. Accessed March 30 2017.
36. Smith, G.P., et al. GRI-Mech 3.0. http://www.me.berkeley.edu/gri_mech/. Accessed March 30 2017.
37. Cales, B. and Baumard, J.F., *Oxygen semipermeability and electronic conductivity in calcia-stabilized zirconia.* Journal of Materials Science, 1982. **17**(11): 3243-3248.
38. Kodama, T., *High-temperature solar chemistry for converting solar heat to chemical fuels.* Progress in Energy and Combustion Science, 2003. **29**(6): 567-597.
39. Sunarso, J., et al., *Mixed ionic–electronic conducting (MIEC) ceramic-based membranes for oxygen separation.* Journal of Membrane Science, 2008. **320**(1-2): 13-41.

40. Basile, A., et al., *Pd-based Selective Membrane State-of-the-Art*, in *Membrane Reactors for Hydrogen Production Processes*, M. De Falco, L. Marrelli, and G. Iaquaniello, Editors. 2011, Springer London. 21-55.
41. Hamakawa, S., et al., *Synthesis and hydrogen permeation properties of membranes based on dense $SrCe_{0.95}Yb_{0.05}O_{3-\alpha}$ thin films.* Solid State Ionics, 2002. **148**(1–2): 71-81.
42. Phair, J.W. and Badwal, S.P.S., *Review of proton conductors for hydrogen separation.* Ionics, 2006. **12**(2): 103-115.
43. Anderson, L.L., et al., *Advances in ion transport membrane technology for oxygen and syngas production.* Solid State Ionics, 2016. **288**: 331-337.
44. Kelly, S.M. *Praxair's oxygen transport membranes for oxy-combustion and syngas applications, presentation*. 2014.
45. Leo, A., Liu, S., and Costa, J.C.D.d., *Development of mixed conducting membranes for clean coal energy delivery.* International Journal of Greenhouse Gas Control, 2009. **3**(4): 357-367.
46. Cousin, P. and Ross, R.A., *Preparation of mixed oxides: a review.* Materials Science and Engineering: A, 1990. **130**(1): 119-125.
47. Naito, H. and Arashi, H., *Hydrogen production from direct water splitting at high temperatures using a ZrO_2-TiO_2-Y_2O_3 membrane.* Solid State Ionics, 1995. **79**(0): 366-370.
48. Park, C.Y., et al., *Hydrogen production from fossil and renewable sources using an oxygen transport membrane.* International Journal of Hydrogen Energy, 2010. **35**(9): 4103-4110.
49. Schmalzried, H., *Solid-State Reactions.* Angewandte Chemie International Edition in English, 1963. **2**(5): 251-254.
50. Jeon, S.-Y., et al., *A thermodynamically stable $La_2NiO_{4+\delta}$/$Gd_{0.1}Ce_{0.9}O_{1.95}$ bilayer oxygen transport membrane in membrane-assisted water splitting for hydrogen production.* Ceramics International, 2013. **39**(4): 3893-3899.
51. Jeon, S.Y., et al., *Oxygen ionic conductivity of $La_2NiO_{4+\delta}$ via interstitial oxygen defect.* Journal of Physics and Chemistry of Solids, 2012. **73**(5): 656-660.
52. Jiang, H., et al., *Simultaneous Production of Hydrogen and Synthesis Gas by Combining Water Splitting with Partial Oxidation of Methane in a Hollow-Fiber Membrane Reactor.* Angewandte Chemie International Edition, 2008. **47**(48): 9341-9344.
53. Evdou, A., Nalbandian, L., and Zaspalis, V., *Perovskite membrane reactor for continuous and isothermal redox hydrogen production from the dissociation of water.* Journal of Membrane Science, 2008. **325**(2): 704-711.
54. Park, C.Y., et al., *Oxygen permeation and coal-gas-assisted hydrogen production using oxygen transport membranes.* International Journal of Hydrogen Energy, 2011. **36**(15): 9345-9354.
55. Lee, T.H., et al., *Hydrogen Production by Steam Dissociation using Oxygen Transport Membranes.* ECS Transactions, 2008. **13**(26): 379-384.
56. Jiang, H., et al., *Hydrogen production by water dissociation in surface-modified $BaCo_xFe_yZr_{1-x-y}O_{3-\delta}$ hollow-fiber membrane reactor with improved oxygen permeation.* Chemistry, 2010. **16**(26): 7898-903.
57. Park, C.Y., et al., *$La_{0.7}Sr_{0.3}Cu_{0.2}Fe_{0.8}O_{3-x}$ as Oxygen Transport Membrane for Producing Hydrogen via Water Splitting.* ECS Transactions, 2008. **13**(26): 393-403.
58. Schiestel, T., et al., *Hollow fibre perovskite membranes for oxygen separation.* Journal of Membrane Science, 2005. **258**(1–2): 1-4.
59. Balachandran, U., et al., *Use of mixed conducting membranes to produce hydrogen by water dissociation.* International Journal of Hydrogen Energy, 2004. **29**(3): 291-296.

60. Wu, X.Y., Ghoniem, A.F., and Uddi, M., *Enhancing co-production of H_2 and syngas via water splitting and POM on surface-modified oxygen permeable membranes.* AIChE Journal, 2016. **62**(12): 4427-4435.
61. Balachandran, U., et al., *Dense ceramic membranes for partial oxidation of methane to syngas.* Applied Catalysis A: General, 1995. **133**(1): 19-29.
62. Zhu, N., et al., *Toward highly-effective and sustainable hydrogen production: bio-ethanol oxidative steam reforming coupled with water splitting in a thin tubular membrane reactor.* Chemical Communications, 2012. **48**(57): 7137-7139.
63. ten Elshof, J.E., Bouwmeester, H.J.M., and Verweij, H., *Oxidative coupling of methane in a mixed-conducting perovskite membrane reactor.* Applied Catalysis A: General, 1995. **130**(2): 195-212.
64. Wang, H., et al., *Mixed oxygen ion and electron conducting hollow fiber membranes for oxygen separation.* Solid State Ionics, 2006. **177**(26–32): 2255-2259.
65. Jiang, H., et al., *A Coupling Strategy to Produce Hydrogen and Ethylene in a Membrane Reactor.* Angewandte Chemie International Edition, 2010. **49**(33): 5656-5660.
66. Jiang, H., et al., *Improved water dissociation and nitrous oxide decomposition by in situ oxygen removal in perovskite catalytic membrane reactor.* Catalysis Today, 2010. **156**(3–4): 187-190.
67. Chang, X., et al., *A Comparative Study of the Performance of Symmetric and Asymmetric Mixed-conducting Membranes.* Chinese Journal of Chemical Engineering, 2009. **17**(4): 562-570.
68. Franca, R.V., Thursfield, A., and Metcalfe, I.S., *$La_{0.6}Sr_{0.4}Co_{0.2}Fe_{0.8}O_{3-\delta}$ microtubular membranes for hydrogen production from water splitting.* Journal of Membrane Science, 2012. **389**(0): 173-181.
69. Nalbandian, L., Evdou, A., and Zaspalis, V., *$La_{1-x}Sr_xMO_3$ (M = Mn, Fe) perovskites as materials for thermochemical hydrogen production in conventional and membrane reactors.* International Journal of Hydrogen Energy, 2009. **34**(17): 7162-7172.
70. Im, H.-N., et al., *Chemical expansion of water splitting oxygen separation membranes of $La_{0.7}Sr_{0.3}Cu_{0.2}Fe_{0.8}O_{3-\delta}$.* Journal of Ceramic Processing Research, 2012. **13**(5): 579 - 585.
71. Polfus, J.M., et al., *Oxygen permeation and creep behavior of $Ca_{1-x}Sr_xTi_{0.6}Fe_{0.15}Mn_{0.25}O_{3-\delta}$ (x=0, 0.5) membrane materials.* Journal of Membrane Science, 2016. **499**: 172-178.
72. Wu, X.Y., et al., *Toward enhanced hydrogen generation from water using oxygen permeating LCF membranes.* Physical Chemistry Chemical Physics, 2015. **17**(15): 10093-10107.
73. Balachandran, U., Lee, T., and Dorris, S., *Hydrogen production by water dissociation using mixed conducting dense ceramic membranes.* International Journal of Hydrogen Energy, 2007. **32**(4): 451-456.
74. Song, S.J., et al., *Non-galvanic hydrogen production by water splitting using cermet membranes.* Journal of Ceramic Processing Research, 2008. **9**(2): 123-125.
75. Wang, H., Gopalan, S., and Pal, U.B., *Hydrogen generation and separation using $Gd_{0.2}Ce_{0.8}O_{1.9-\delta}$–$Gd_{0.08}Sr_{0.88}Ti_{0.95}Al_{0.05}O_{3\pm\delta}$ mixed ionic and electronic conducting membranes.* Electrochimica Acta, 2011. **56**(20): 6989-6996.
76. Kniep, J., et al., *Electrical conductivity and oxygen permeation properties of $SrCoFeO_x$ membranes.* Solid State Ionics, 2010. **180**(40): 1633-1639.
77. Veldsink, J.W., et al., *The use of the dusty-gas model for the description of mass transport with chemical reaction in porous media.* The Chemical Engineering Journal and the Biochemical Engineering Journal, 1995. **57**(2): 115-125.

78. Webb, S.W. and Pruess, K., *The Use of Fick's Law for Modeling Trace Gas Diffusion in Porous Media.* Transport in Porous Media, 2003. **51**(3): 327-341.
79. Hong, J., Kirchen, P., and Ghoniem, A.F., *Numerical simulation of ion transport membrane reactors: Oxygen permeation and transport and fuel conversion.* Journal of Membrane Science, 2012. **407-408**: 71-85.
80. Hunt, A., et al., *Measuring the oxygen profile and permeation flux across an ion transport membrane and the development and validation of a multistep surface exchange model.* Journal of Membrane Science, 2014. **468**: 62-72.
81. Hunt, A., Dimitrakopoulos, G., and Ghoniem, A.F., *Surface oxygen vacancy and oxygen permeation flux limits of perovskite ion transport membranes.* Journal of Membrane Science, 2015. **489**: 248-257.
82. Dimitrakopoulos, G. and Ghoniem, A.F., *Developing a multistep surface reaction mechanism to model the impact of H_2 and CO on the performance and defect chemistry of mixed-conductors.* Journal of Membrane Science, 2017. **529**: 114-132.
83. NETL. Syngas optimized for intended products. 2015; http://www.netl.doe.gov/research/coal/energy-systems/gasification/gasifipedia/syngas-optimization. Accessed April 6 2017.
84. Dimitrakopoulos, G.T., *Experimental study and modeling analysis of ion transport membranes for methane partial oxidation and oxyfuel combustion*, 2017, Massachusetts Institute of Technology, PhD Thesis
85. Gärtner, C.A., van Veen, A.C., and Lercher, J.A., *Oxidative Dehydrogenation of Ethane: Common Principles and Mechanistic Aspects.* ChemCatChem, 2013. **5**(11): 3196-3217.
86. Ren, T., Patel, M., and Blok, K., *Olefins from conventional and heavy feedstocks: Energy use in steam cracking and alternative processes.* Energy, 2006. **31**(4): 425-451.
87. Li, W., et al., *High-rate hydrogen separation using an MIEC oxygen permeable membrane reactor.* AIChE Journal, 2017. **63**(4): 1278-1286.
88. Fang, W., et al., *A Highly Efficient Sandwich-Like Symmetrical Dual-Phase Oxygen-Transporting Membrane Reactor for Hydrogen Production by Water Splitting.* Angewandte Chemie International Edition, 2016. **55**(30): 8648-8651.
89. Li, W., et al., *H_2S-tolerant oxygen-permeable ceramic membranes for hydrogen separation with a performance comparable to those of palladium-based membranes.* Energy & Environmental Science, 2017. **10**(1): 101-106.
90. Nigara, Y. and Cales, B., *Production of Carbon Monoxide by Direct Thermal Splitting of Carbon Dioxide at High Temperature.* Bulletin of the Chemical Society of Japan, 1986. **59**(6): 1997-2002.
91. Jin, W., et al., *Efficient catalytic decomposition of CO_2 to CO and O_2 over Pd/mixed-conducting oxide catalyst in an oxygen-permeable membrane reactor.* Environmental Science & Technology, 2008. **42**(8): 3064-3068.
92. Itoh, N., et al., *Application of a membrane reactor system to thermal decomposition of CO_2.* Journal of Membrane Science, 1993. **77**(2–3): 245-253.
93. Jin, W., et al., *Thermal decomposition of carbon dioxide coupled with POM in a membrane reactor.* AIChE Journal, 2006. **52**(7): 2545-2550.
94. Zhang, C., et al., *Improving Performance of a Dense Membrane Reactor for Thermal Decomposition of CO2 via Surface Modification.* Industrial & Engineering Chemistry Research, 2007. **46**(7): 2000-2005.
95. Zhang, C., et al., *Decomposition of CO_2 coupled with POM in a thin tubular oxygen-permeable membrane reactor.* Catalysis Today, 2009. **148**(3–4): 298-302.

96. Zhang, K., et al., *Enhanced stability of membrane reactor for thermal decomposition of CO_2 via porous-dense-porous triple-layer composite membrane.* Journal of Membrane Science, 2014. **471**(0): 9-15.
97. Michalsky, R., Neuhaus, D., and Steinfeld, A., *Carbon Dioxide Reforming of Methane using an Isothermal Redox Membrane Reactor.* Energy Technology, 2015. **3**(7): 784-789.
98. Efimov, K., et al., *Ca-containing CO_2-tolerant perovskite materials for oxygen separation.* Journal of Membrane Science, 2012. **389**(0): 205-215.
99. Fan, Y., et al., *Reactor and Technical Feasibility Aspects of a CO_2 Decomposition-Based Power Generation Cycle, Utilizing a High-Temperature Membrane Reactor.* Industrial & Engineering Chemistry Research, 2003. **42**(12): 2618-2626.
100. Zhang, K., et al., *Highly Stable External Short-Circuit-Assisted Oxygen Ionic Transport Membrane Reactor for Carbon Dioxide Reduction Coupled with Methane Partial Oxidation.* Energy & Fuels, 2013. **28**(1): 349-355.
101. Xu, S.J. and Thomson, W.J., *Oxygen permeation rates through ion-conducting perovskite membranes.* Chemical Engineering Science, 1999. **54**(17): 3839-3850.
102. Liu, Y., Tan, X., and Li, K., *Mixed Conducting Ceramics for Catalytic Membrane Processing.* Catalysis Reviews, 2006. **48**(2): 145-198.
103. Geary, T.C. and Adler, S.B., *Oxygen nonstoichiometry and defect chemistry of the mixed conductor $La_{0.9}Ca_{0.1}FeO_{3-\delta}$ at low oxygen partial pressure.* Solid State Ionics, 2013. **253**(0): 88-93.
104. Wang, S., et al., *Electrical and Ionic Conductivity of Gd-Doped Ceria.* Journal of The Electrochemical Society, 2000. **147**(10): 3606-3609.
105. Katsuki, M., et al., *The oxygen transport in Gd-doped ceria.* Solid State Ionics, 2002. **154–155**: 589-595.
106. Ma, B., et al., *Electrical Transport Properties and Defect Structure of $SrFeCo_{0.5}O_x$.* Journal of The Electrochemical Society, 1996. **143**(5): 1736-1744.
107. Park, C.Y., Azzarello, F.V., and Jacobson, A.J., *The oxygen non-stoichiometry and electrical conductivity of $La_{0.7}Sr_{0.3}Cu_{0.2}Fe_{0.8}O_{3-\delta}$.* Journal of Materials Chemistry, 2006. **16**(36): 3624-3628.
108. Wackerl, J., et al., *Correlation of thermal properties and electrical conductivity of $La_{0.7}Sr_{0.3}Cu_{0.2}Fe_{0.8}O_{3-\delta}$ material for solid oxide fuel cells.* Journal of Applied Electrochemistry, 2009. **39**(8): 1243-1249.
109. Stevenson, J.W., et al., *Electrochemical Properties of Mixed Conducting Perovskites $La_{1-x}M_xCo_{1-y}Fe_yO_{3-\delta}$ (M = Sr, Ba, Ca).* Journal of The Electrochemical Society, 1996. **143**(9): 2722-2729.
110. Tai, L.W., et al., *Structure and electrical properties of $La_{1-x}Sr_xCo_{1-y}Fe_yO_3$. Part 1. The system $La_{0.8}Sr_{0.2}Co_{1-y}Fe_yO_3$.* Solid State Ionics, 1995. **76**(3–4): 259-271.
111. Hong, J., Kirchen, P., and Ghoniem, A.F., *Analysis of heterogeneous oxygen exchange and fuel oxidation on the catalytic surface of perovskite membranes.* Journal of Membrane Science, 2013. **445**: 96-106.
112. Bidrawn, F., et al., *The Effect of Ca, Sr, and Ba Doping on the Ionic Conductivity and Cathode Performance of $LaFeO_3$.* Journal of The Electrochemical Society, 2008. **155**(7): B660-B665.
113. Hung, M.-H., Rao, M.V.M., and Tsai, D.-S., *Microstructures and electrical properties of calcium substituted $LaFeO_3$ as SOFC cathode.* Materials Chemistry and Physics, 2007. **101**(2–3): 297-302.

114. Pecchi, G., et al., *Relation between defects and catalytic activity of calcium doped LaFeO3 perovskite.* Solid State Ionics, 2011. **187**(1): 27-32.
115. Dimitrakopoulos, G. and Ghoniem, A.F., *A two-step surface exchange mechanism and detailed defect transport to model oxygen permeation through the $La_{0.9}Ca_{0.1}FeO_{3-\delta}$ mixed-conductor.* Journal of Membrane Science, 2016. **510**: 209-219.
116. Tan, X. and Li, K., *Modeling of air separation in a LSCF hollow-fiber membrane module.* AIChE Journal, 2002. **48**(7): 1469-1477.
117. Merkle, R. and Maier, J., *How Is Oxygen Incorporated into Oxides? A Comprehensive Kinetic Study of a Simple Solid-State Reaction with $SrTiO_3$ as a Model Material.* Angewandte Chemie International Edition, 2008. **47**(21): 3874-3894.
118. Benson, S.J., Waller, D., and Kilner, J.A., *Degradation of $La_{0.6}Sr_{0.4}Fe_{0.8}Co_{0.2}O_{3-\delta}$ in carbon dioxide and water atmospheres.* Journal of The Electrochemical Society, 1999. **146**(4): 1305-1309.
119. Zhao, Z., et al., *Redox Kinetic Study of Fuel Reduced Ceria for Chemical-Looping Water Splitting.* The Journal of Physical Chemistry C, 2016. **120**(30): 16271 - 16289.
120. Zhang, R., Alamdari, H., and Kaliaguine, S., *Water vapor sensitivity of nanosized $La(Co, Mn, Fe)_{1-x}(Cu, Pd)_xO_3$ perovskites during NO reduction by C_3H_6 in the presence of oxygen.* Applied Catalysis B: Environmental, 2007. **72**(3–4): 331-341.
121. Kovalevsky, A.V., et al., *Oxygen permeability and stability of asymmetric multilayer $Ba_{0.5}Sr_{0.5}Co_{0.8}Fe_{0.2}O_{3-\delta}$ ceramic membranes.* Solid State Ionics, 2011. **192**(1): 677-681.
122. Ravkina, O., Klande, T., and Feldhoff, A., *Investigation of carbonates in oxygen-transporting membrane ceramics.* Journal of Membrane Science, 2015. **480**: 31 - 38.
123. Chen, W., et al., *Oxygen-selective membranes integrated with oxy-fuel combustion.* Journal of Membrane Science, 2014. **463**(0): 166-172.
124. Voigts, F., Argirusis, C., and Maus-Friedrichs, W., *The interaction of CO_2 and CO with Fe-doped $SrTiO_3$(100) surfaces.* Surface and Interface Analysis, 2012. **44**(3): 301-307.
125. Tong, J., et al., *Investigation of ideal zirconium-doped perovskite-type ceramic membrane materials for oxygen separation.* Journal of Membrane Science, 2002. **203**(1–2): 175-189.
126. Yi, J., Weirich, T.E., and Schroeder, M., *CO_2 corrosion and recovery of perovskite-type $BaCo_{1-x-y}Fe_xNb_yO_{3-\delta}$ membranes.* Journal of Membrane Science, 2013. **437**(0): 49-56.
127. Yang, Z., et al., *Mechanism analysis of CO_2 corrosion on $Ba_{0.9}Co_{0.7}Fe_{0.2}Nb_{0.1}O_{3-\delta}$ cathode.* International Journal of Hydrogen Energy, 2016. **41**(3): 1997 - 2001.
128. Argirusis, C., et al., *Oxygen incorporation into strontium titanate single crystals from CO_2 dissociation.* Physical Chemistry Chemical Physics, 2009. **11**(17): 3152-3157.
129. Gozálvez-Zafrilla, J.M., et al., *Fluid dynamic modeling of oxygen permeation through mixed ionic–electronic conducting membranes.* Journal of Membrane Science, 2011. **378**(1–2): 290-300.
130. Liang, Y.Q., Di, N.L., and Cheng, Z.H., *Charge-disproportionation-induced magnetic glassy behavior in $La_{0.5}Ca_{0.5}FeO_{3-\delta}$.* Physical Review B, 2005. **72**(13): 134416.
131. Nadeev, A.N., et al., *Structural features of the formation of $La_{1-x}Ca_xFeO_{3-\delta}$ ($0 \leq x \leq 0.7$) hetero valent solid solutions.* Journal of Structural Chemistry, 2010. **51**(5): 891-897.
132. Shannon, R., *Revised effective ionic radii and systematic studies of interatomic distances in halides and chalcogenides.* Acta Crystallographica Section A, 1976. **32**(5): 751-767.
133. Wang, Z., et al., *Preparation and Oxygen Permeation Properties of Highly Asymmetric $La_{0.6}Sr_{0.4}Co_{0.2}Fe_{0.8}O_{3-\delta}$ Perovskite Hollow-Fiber Membranes.* Industrial & Engineering Chemistry Research, 2008. **48**(1): 510-516.

134. ten Elshof, J.E., Bouwmeester, H.J.M., and Verweij, H., *Oxygen transport through $La_{1-x}Sr_xFeO_{3-\delta}$ membranes. I. Permeation in air/He gradients.* Solid State Ionics, 1995. **81**(1–2): 97-109.
135. Qiu, L., et al., *Oxygen permeation studies of $SrCo_{0.8}Fe_{0.2}O_{3-\delta}$.* Solid State Ionics, 1995. **76**(3–4): 321-329.
136. Akin, F.T. and Lin, J.Y.S., *Oxygen permeation through oxygen ionic or mixed-conducting ceramic membranes with chemical reactions.* Journal of Membrane Science, 2004. **231**(1–2): 133-146.
137. ten Elshof, J.E., Bouwmeester, H.J.M., and Verweij, H., *Oxygen transport through $La_{1-x}Sr_xFeO_{3-\delta}$ membranes II. Permeation in air/CO, CO_2 gradients.* Solid State Ionics, 1996. **89**(1–2): 81-92.
138. Haile, S.M., Staneff, G., and Ryu, K.H., *Non-stoichiometry, grain boundary transport and chemical stability of proton conducting perovskites.* Journal of Materials Science, 2001. **36**(5): 1149-1160.
139. Szabo, V., et al., *Perovskite-type oxides synthesized by reactive grinding: Part IV. Catalytic properties of $LaCo_{1-x}Fe_xO_3$ in methane oxidation.* Applied Catalysis B: Environmental, 2003. **43**(1): 81-92.
140. York, A.P.E., Xiao, T.C., and Green, M.L.H., *Brief overview of the partial oxidation of methane to synthesis gas.* Topics in Catalysis, 2003. **22**(3-4): 345-358.
141. Christian Enger, B., Lødeng, R., and Holmen, A., *A review of catalytic partial oxidation of methane to synthesis gas with emphasis on reaction mechanisms over transition metal catalysts.* Applied Catalysis A: General, 2008. **346**(1–2): 1-27.
142. IEA, *Technology Roadmap: hydrogen and fuel cells*, 2015.
143. Luo, S., et al., *Shale gas-to-syngas chemical looping process for stable shale gas conversion to high purity syngas with a H_2 : CO ratio of 2 : 1.* Energy & Environmental Science, 2014. **7**(12): 4104-4117.
144. Deshpande, N., et al., *High-Pressure Redox Behavior of Iron-Oxide-Based Oxygen Carriers for Syngas Generation from Methane.* Energy & Fuels, 2015. **29**(3): 1469-1478.
145. Furler, P., Scheffe, J.R., and Steinfeld, A., *Syngas production by simultaneous splitting of H_2O and CO_2 via ceria redox reactions in a high-temperature solar reactor.* Energy & Environmental Science, 2012. **5**(3): 6098-6103.
146. Hao, Y., Yang, C.-K., and Haile, S.M., *High-temperature isothermal chemical cycling for solar-driven fuel production.* Physical Chemistry Chemical Physics, 2013. **15**(40): 17084-17092.
147. He, F. and Li, F., *Perovskite promoted iron oxide for hybrid water-splitting and syngas generation with exceptional conversion.* Energy & Environmental Science, 2015. **8**(2): 535-539.
148. Zhao, Z., et al., *Design of a rotary reactor for chemical-looping combustion. Part 1: Fundamentals and design methodology.* Fuel, 2014. **121**: 327-343.
149. Zink, P.A., et al., *Analysis of the Electronic and Ionic Conductivity of Calcium-Doped Lanthanum Ferrite.* Electrochemical and Solid-State Letters, 2009. **12**(10): B141-B143.
150. Yu, A.S., et al., *Decreasing interfacial losses with catalysts in $La_{0.9}Ca_{0.1}FeO_{3-\delta}$ membranes for syngas production.* Applied Catalysis A: General, 2014. **486**: 259-265.
151. Adler, S.B., *Factors Governing Oxygen Reduction in Solid Oxide Fuel Cell Cathodes.* Chemical Reviews, 2004. **104**(10): 4791-4844.
152. Ahmed, S., et al., *Decomposition of hydrocarbons to hydrogen and carbon.* Applied Catalysis A: General, 2009. **359**(1–2): 1-24.

153. Maneerung, T., Hidajat, K., and Kawi, S., *Co-production of hydrogen and carbon nanofibers from catalytic decomposition of methane over $LaNi_{1-x}M_xO_{3-\alpha}$ perovskite (where M = Co, Fe and x = 0, 0.2, 0.5, 0.8, 1).* International Journal of Hydrogen Energy, 2015. **40**(39): 13399-13411.
154. Dimitrakopoulos, G. and Ghoniem, A.F., *Role of gas-phase and surface chemistry in methane reforming using a oxygen transport membrane.* Proceedings of the Combustion Institute, 2017. ***36***(3): 4347-4354.
155. Rostrup-Nielsen, J. and Trimm, D.L., *Mechanisms of carbon formation on nickel-containing catalysts.* Journal of Catalysis, 1977. **48**(1): 155-165.
156. Kathiraser, Y. and Kawi, S., *$La_{0.6}Sr_{0.4}Co_{0.8}Ga_{0.2}O_{3-\delta}$ (LSCG) hollow fiber membrane reactor: Partial oxidation of methane at medium temperature.* AIChE Journal, 2013. **59**(10): 3874-3885.
157. Gür, T.M., *Comprehensive review of methane conversion in solid oxide fuel cells: Prospects for efficient electricity generation from natural gas.* Progress in Energy and Combustion Science, 2016. **54**: 1-64.
158. Ashik, U.P.M., Wan Daud, W.M.A., and Abbas, H.F., *Production of greenhouse gas free hydrogen by thermocatalytic decomposition of methane – A review.* Renewable and Sustainable Energy Reviews, 2015. **44**: 221-256.
159. Yuan, R.-h., et al., *Partial oxidation of methane to syngas in a packed bed catalyst membrane reactor.* AIChE Journal, 2016: in press.
160. Dhakad, M., et al., *Low Cost, Ceria Promoted Perovskite Type Catalysts for Diesel Soot Oxidation.* Catalysis Letters, 2008. **121**(1-2): 137-143.
161. Xiao, P., et al., *CO and soot oxidation over macroporous perovskite LaFeO3.* Catalysis Today, 2015. **258, Part 2**: 660-667.
162. Hunt, A., *Experimental investigations of oxygen-separating ion transport membranes for clean fuel synthesis*, 2015, Massachusetts Institute of Technology, PhD thesis Thesis
163. Cowin, P.I., et al., *Recent Progress in the Development of Anode Materials for Solid Oxide Fuel Cells.* Advanced Energy Materials, 2011. **1**(3): 314-332.
164. Schefold, J., et al., *Long Term Testing of Short Stacks with Solid Oxide Cells for Water Electrolysis.* ECS Transactions, 2011. **35**(1): 2915-2927.
165. Park, K., et al., *Fast performance degradation of SOFC caused by cathode delamination in long-term testing.* International Journal of Hydrogen Energy, 2010. **35**(16): 8670-8677.
166. Freund, H.J. and Roberts, M.W., *Surface chemistry of carbon dioxide.* Surface Science Reports, 1996. **25**(8): 225-273.
167. Beller, M., Centi, G., and Sun, L., *Chemistry Future: Priorities and Opportunities from the Sustainability Perspective.* ChemSusChem, 2017. **10**(1): 6-13.
168. Graves, C., et al., *Sustainable hydrocarbon fuels by recycling CO_2 and H_2O with renewable or nuclear energy.* Renewable and Sustainable Energy Reviews, 2011. **15**(1): 1-23.
169. Jhong, H.-R.M., et al., *A Nitrogen-Doped Carbon Catalyst for Electrochemical CO_2 Conversion to CO with High Selectivity and Current Density.* ChemSusChem, 2017. **10**(6): 1094-1099.
170. Mulmi, S., et al., *Thermochemical CO_2 splitting using double perovskite-type $Ba_2Ca_{0.66}Nb_{1.34-x}Fe_xO_{6-\delta}$.* Journal of Materials Chemistry A, 2017.
171. Barton, E.E., Rampulla, D.M., and Bocarsly, A.B., *Selective Solar-Driven Reduction of CO_2 to Methanol Using a Catalyzed p-GaP Based Photoelectrochemical Cell.* Journal of the American Chemical Society, 2008. **130**(20): 6342-6344.

172. Lin, F., et al., *First demonstration of direct hydrocarbon fuel production from water and carbon dioxide by solar-driven thermochemical cycles using rhodium-ceria.* Energy & Environmental Science, 2016. **9**(7): 2400-2409.
173. Belimov, M., Metzger, D., and Pfeifer, P., *On the temperature control in a microstructured packed bed reactor for methanation of CO/CO_2 mixtures.* AIChE Journal, 2017. **63**(1): 120-129.
174. van Leeuwen, P.W.N.M. and Freixa, Z., *Carbon Monoxide as a Chemical Feedstock: Carbonylation Catalysis*, in *Activation of Small Molecules*. 2006, Wiley-VCH Verlag GmbH & Co. KGaA. 319-356.
175. Jin, F.M., et al., *Highly efficient and autocatalytic H_2O dissociation for CO_2 reduction into formic acid with zinc.* Scientific Reports, 2014. **4**.
176. Gálvez, M.E., et al., *CO_2 Splitting via Two-Step Solar Thermochemical Cycles with Zn/ZnO and FeO/Fe_3O_4 Redox Reactions: Thermodynamic Analysis.* Energy & Fuels, 2008. **22**(5): 3544-3550.
177. Gálvez, M.E., et al., *Physico-chemical changes in Ca, Sr and Al-doped La-Mn-O perovskites upon thermochemical splitting of CO_2 via redox cycling.* Physical Chemistry Chemical Physics, 2015. **17**(9): 6629-6634.
178. Venstrom, L.J., et al., *Efficient Splitting of CO_2 in an Isothermal Redox Cycle Based on Ceria.* Energy & Fuels, 2014. **28**(4): 2732-2742.
179. Muhich, C.L., et al., *Efficient Generation of H_2 by Splitting Water with an Isothermal Redox Cycle.* Science, 2013. **341**(6145): 540-542.
180. Chroneos, A., et al., *Oxygen diffusion in solid oxide fuel cell cathode and electrolyte materials: mechanistic insights from atomistic simulations.* Energy & Environmental Science, 2011. **4**(8): 2774-2789.
181. Zhang, H.L., et al., *Concentrated solar power plants: Review and design methodology.* Renewable and Sustainable Energy Reviews, 2013. **22**: 466-481.
182. Wu, Q., et al., *Understanding the Interactions of CO_2 with Doped and Undoped $SrTiO_3$.* ChemSusChem, 2016. **9**(14): 1889-1897.
183. McFarland, E.W. and Metiu, H., *Catalysis by Doped Oxides.* Chemical Reviews, 2013. **113**(6): 4391-4427.
184. Shen, P., et al., *Reaction mechanism on reduction surface of mixed conductor membrane for H_2 production by coal-gas.* Applied Surface Science, 2010. **256**(16): 5094-5101.
185. Janardhanan, V.M. and Deutschmann, O., *CFD analysis of a solid oxide fuel cell with internal reforming: Coupled interactions of transport, heterogeneous catalysis and electrochemical processes.* Journal of Power Sources, 2006. **162**(2): 1192-1202.
186. Mac Dowell, N., et al., *The role of CO_2 capture and utilization in mitigating climate change.* Nature Clim. Change, 2017. **7**(4): 243-249.
187. Furler, P., et al., *Solar Thermochemical CO_2 Splitting Utilizing a Reticulated Porous Ceria Redox System.* Energy & Fuels, 2012. **26**(11): 7051-7059.
188. Ong, K., Hanna, J., and Ghoniem, A.F., *Investigation of a Combined Hydrogen and Oxygen Spillover Mechanism for Syngas Electro-Oxidation on Ni/YSZ.* Journal of The Electrochemical Society, 2017. **164**(2): F32-F45.
189. Lee, W.Y., Wee, D., and Ghoniem, A.F., *An improved one-dimensional membrane-electrode assembly model to predict the performance of solid oxide fuel cell including the limiting current density.* Journal of Power Sources, 2009. **186**(2): 417-427.
190. Ni, M., *Modeling of a solid oxide electrolysis cell for carbon dioxide electrolysis.* Chemical Engineering Journal, 2010. **164**(1): 246-254.

191. Shi, Y., et al., *Experimental characterization and modeling of the electrochemical reduction of CO_2 in solid oxide electrolysis cells.* Electrochimica Acta, 2013. **88**: 644-653.
192. Udagawa, J., Aguiar, P., and Brandon, N.P., *Hydrogen production through steam electrolysis: Model-based steady state performance of a cathode-supported intermediate temperature solid oxide electrolysis cell.* Journal of Power Sources, 2007. **166**(1): 127-136.
193. Koumi Ngoh, S. and Njomo, D., *An overview of hydrogen gas production from solar energy.* Renewable and Sustainable Energy Reviews, 2012. **16**(9): 6782-6792.
194. Sheu, E.J. and Ghoniem, A.F., *Receiver reactor concept and model development for a solar steam redox reformer.* Solar Energy, 2016. **125**: 339-359.
195. Sheu, E.J. and Ghoniem, A.F., *Sensitivity analysis for a solar steam redox reformer.* Solar Energy, 2016. **134**: 23-31.
196. Kelly, S.M., et al., *Oxygen transport membrane system and method for transferring heat to catalytic/process reactors*. patent, US 8623241 B2, 2014
197. Ahmed, P., et al., *CFD (computational fluid dynamics) analysis of a novel reactor design using ion transport membranes for oxy-fuel combustion.* Energy, 2014. **77**: 932-944.
198. Michelsen, F.A., et al., *A distributed dynamic model of a monolith hydrogen membrane reactor.* Energy Conversion and Management, 2013. **67**: 160-170.
199. Wang, H., Hao, Y., and Kong, H., *Thermodynamic study on solar thermochemical fuel production with oxygen permeation membrane reactors.* International Journal of Energy Research, 2015. **39**(13): 1790-1799.
200. gPROMS. https://www.psenterprise.com/products/gproms (work carried out with collaboration and license from Tsinghua Unviersity).
201. Bao, C., Cai, N., and Croiset, E., *A multi-level simulation platform of natural gas internal reforming solid oxide fuel cell–gas turbine hybrid generation system – Part II. Balancing units model library and system simulation.* Journal of Power Sources, 2011. **196**(20): 8424-8434.
202. Luo, Y., et al., *Reversible solid oxide fuel cell for natural gas/renewable hybrid power generation systems.* Journal of Power Sources, 2017. **340**: 60-70.
203. EU and BP Renewable Electricity Accounting Methodologies. http://euanmearns.com/eu-and-bp-renewable-electricity-accounting-methodologies/. Accessed April 25, 2017.
204. Wang, W., Gorte, R.J., and Vohs, J.M., *Analysis of the performance of the electrodes in a natural gas assisted steam electrolysis cell.* Chemical Engineering Science, 2008. **63**(3): 765-769.
205. Boyano, A., et al., *Exergoenvironmental analysis of a steam methane reforming process for hydrogen production.* Energy, 2011. **36**(4): 2202-2214.
206. Jechura, J. Hydrogen from natural gas via steam methane reforming (SMR). http://inside.mines.edu/~jjechura/EnergyTech/07_Hydrogen_from_SMR.pdf. Accessed April 26, 2017.
207. Mills, A.F., *Heat Transfer, 2nd ed.* 1998, Englewood Cliffs, NJ: Prentice Hall.
208. Fuller, E.N., Schettler, P.D., and Giddings, J.C., *New method for prediction of binary gas-phase diffusion coefficients.* Industrial & Engineering Chemistry, 1966. **58**(5): 18-27.
209. Zheng, Y., et al., *Investigation of 30-cell solid oxide electrolyzer stack modules for hydrogen production.* Ceramics International, 2014. **40**(4): 5801-5809.
210. Whiston, M.M., et al., *Exergy and economic comparison between kW-scale hybrid and stand-alone solid oxide fuel cell systems.* Journal of Power Sources, 2017. **353**: 152-166.

211. Achenbach, E. and Riensche, E., *Methane/steam reforming kinetics for solid oxide fuel cells.* Journal of Power Sources, 1994. **52**(2): 283-288.
212. Aguiar, P., Adjiman, C.S., and Brandon, N.P., *Anode-supported intermediate temperature direct internal reforming solid oxide fuel cell. I: model-based steady-state performance.* Journal of Power Sources, 2004. **138**(1–2): 120-136.
213. Liu, Y., et al., *Degradation and stabilization of perovskite membranes containing silicon impurity at low temperature.* Journal of Membrane Science, 2015. **492**: 173-180.
214. Karakaya, C. and Deutschmann, O., *Kinetics of hydrogen oxidation on Rh/Al2O3 catalysts studied in a stagnation-flow reactor.* Chemical Engineering Science, 2013. **89**(0): 171-184.
215. Ovesen, C.V., et al., *A Microkinetic Analysis of the Water–Gas Shift Reaction under Industrial Conditions.* Journal of Catalysis, 1996. **158**(1): 170-180.
216. Hammami, R., Batis, H., and Minot, C., *Combined experimental and theoretical investigation of the CO_2 adsorption on $LaMnO_{3+y}$ perovskite oxide.* Surface Science, 2009. **603**(20): 3057-3067.
217. Sharma, V.I. and Yildiz, B., *Degradation Mechanism in $La_{0.8}Sr_{0.2}CoO_3$ as Contact Layer on the Solid Oxide Electrolysis Cell Anode.* Journal of The Electrochemical Society, 2010. **157**(3): B441-B448.
218. Paz-Garcia, J.M., et al., *Modeling of Electric Double-Layers Including Chemical Reaction Effects.* Electrochimica Acta, 2014. **150**: 263-268.
219. Hong, S.H., *Towards Predicting Dynamics in Turbulent Premixed Combustion Using PIV-PLIF Measurements of Flow-Flame Microstructure*, 2014, Massachusetts Institute of Technology, PhD Thesis
220. van Bokhoven, J.A. and Lamberti, C., *XAS Techniques to Determine Catalytically Active Sites in Zeolites: The Case of Cu-Zeolites*, in *XAFS Techniques for Catalysts, Nanomaterials, and Surfaces*, Y. Iwasawa, K. Asakura, and M. Tada, Editors. 2017, Springer International Publishing: Cham. 299-316.
221. Gaudillere, C., Navarrete, L., and Serra, J.M., *Syngas production at intermediate temperature through H_2O and CO_2 electrolysis with a Cu-based solid oxide electrolyzer cell.* International Journal of Hydrogen Energy, 2014. **39**(7): 3047-3054.